Lattice dynamics and spin-phonon coupling in the multiferroic oxides $Eu_{1-x}Ho_xMnO_3$ and $ACrO_2$

Dissertation zur Erlangung des
naturwissenschaftlichen Doktorgrades der
Julius-Maximilians-Universität Würzburg

vorgelegt von

Sebastian Elsässer
aus Singen

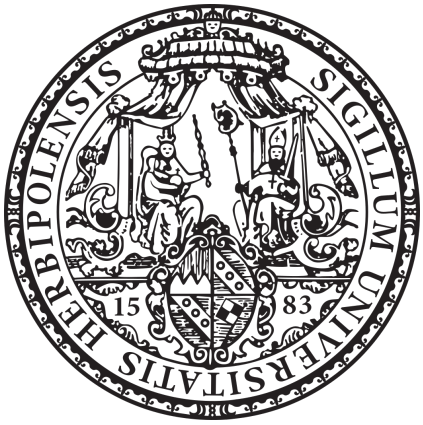

Würzburg, 2018

Eingereicht am: .....
bei der Fakultät für Physik und Astronomie

1. Gutachter: Prof. Dr. J. Geurts
2. Gutachter: Prof. Dr. M. Sing
3. Gutachter: .....
der Dissertation

Vorsitzende(r): .....

1. Prüfer: Prof. Dr. J. Geurts
2. Prüfer: Prof. Dr. M. Sing
3. Prüfer: Prof. Dr. B. Trauzettel
im Promotionskolloquium

Tag des Promotionskolloquiums: .....

Doktorurkunde ausgehändigt am: .....

Inhaltsübersicht

Thematik und Zielsetzung

Mit der Entdeckung des Riesenmagnetoelektischen Effekts (*Giant Magnetoelectric Effect*) in $TbMnO_3$ durch Kimura *et al.* im Jahre 2003, erlebte das Forschungsgebiet der multiferroischen Seltenerdmanganate $RMnO_3$ einen neuen Aufschwung durch die neuen Möglichkeiten, die sich durch diese Entdeckung offenbarten. [1] Der Effekt besteht darin, dass sich durch ein bestimmtes Muster der magnetischen Ordnung eine direkt an dieses Muster gekoppelte ferroelektrische Polarisation ergibt. Die Kopplung von magnetischer und ferroelektrischer Ordnung bewirkt, dass stets beide Parameter simultan beeinflusst werden, wenn ein externes elektrisches oder magnetisches Feld angelegt wird: Wird das Magnetisierungsmuster durch ein externes Magnetfeld beeinflusst, wirkt sich dies direkt auf die elektrische Polarisation aus. Umgekehrt, wenn die Polarisation durch ein elektrisches Feld beeinflusst wird, ist die magnetische Ordnung entsprechend betroffen. Dies erlaubt die vollständige Umordnung der elektrischen Polarisation durch ein magnetisches Feld oder der magnetischen Ordnung durch ein elektrisches Feld. Materialien, die mindestens zwei ferroische Eigenschaften, in diesem Fall eine spontane Magnetisierung und spontane elektrische Polarisation, in der gleichen Phase aufweisen, werden als Multiferroika bezeichnet. Diese allgemeine Klassifikation ist noch zu unterteilen in Typ-I und Typ-II Multiferroika. Zu Typ-I Multiferroika zählen Systeme wie $BiFeO_3$, bei denen die ferroelektrische und die magnetische Ordnung weitestgehend unabhängig voneinander und daher bei verschiedenen Temperaturen einsetzen ($T_C = 1100$ K für die ferroelektrische, $T_N = 643$ K für die magnetische Ordnung [2]). Dementsprechend sind Magnetisierung und Polarisation in diesem System kaum miteinander gekoppelt. Demgegenüber stehen die hier betrachteten Systeme der orthorhombischen $RMnO_3$ Seltenerdmanganate und der $ACrO_2$ Delafossite, die der Gruppe der Typ-II Multiferroika angehören. Hier ist die magnetische Ordnung die direkte Ursache der ferroelektrischen Polarisation, d.h. beide Phänomene treten simultan ab der gleichen Ordnungstemperatur auf.

Das Ziel von Forschungsbemühungen auf diesem Gebiet der Multiferroika ist zum Einen, neue Materialien zu finden, die solcherlei Kopplungseffekte zeigen. Zum Anderen gilt es, den Effekt besser nutzbar zu machen, sei es durch eine größere Kopplungsstärke oder durch höhere mögliche Ordnungstemperaturen. Um dies zu erreichen ist es von essentieller Bedeutung die zu Grunde liegenden mikroskopischen Mechanismen zu ergründen, diese zu studieren und schließlich ein besseres Verständnis der multiferroischen Kopplungsmechanismen zu erlangen.

In dieser Dissertation liegt der Fokus auf der systematischen Untersuchung von Kopplungseffekten zwischen der magnetischen Ordnung und der Dynamik des Kristallgitters mittels Ramanspektroskopie. Insbesondere werden Renormalisierungseffekte der Frequenzen der Gitterschwingungen untersucht, die sich durch die Ausbildung der magnetischen Ordnung und Kopplung derselben an die Gitterdynamik ergeben, die sogenannte Spin-Phonon Kopplung (SPC). Zu diesem Zweck werden die spektroskopischen Experimente mit Augenmerk auf die Polarisations-, Temperatur- und Magnetfeldabhängigkeit der ramanaktiven Moden durchgeführt. Dabei werden Serien von Proben zweier Materialsysteme untersucht, bei denen sich die multiferroische Phase durch unterschiedliche Mechanismen ausbildet: Zum Einen das System $Eu_{1-x}Ho_xMnO_3$ ($0 \leq x \leq 0.5$), welches zu den orthorhombischen RMnO$_3$ Systemen zählt und sowohl multiferroische als auch nicht-multiferroische Proben umfasst. Hierbei beruht der magnetoelektrische Effekt auf der inversen Dzyaloshinskii-Moriya Wechselwirkung. Im Vergleich dazu wird außerdem das System der ACrO$_2$ Delafossite mit A= Cu, Ag, Pd untersucht. Dieses System ist im Kontext der Multiferroika noch als relativ neu anzusehen. Hier kann die inverse Dzyaloshinskii-Moriya Wechselwirkung aus Symmetriegründen ausgeschlossen werden, sodass ein neuartiger magnetoelektrischer Kopplungsmechanismus vorliegt. Durch die Spin-Bahn Kopplung verschiebt sich die Gewichtung der Ladungsverteilung der Bindungen und führt dadurch zur Entstehung der elektrischen Polarisation. Im Vergleich der beiden Systeme, werden die Unterschiede der Spin-Phonon Kopplungsstärken und der Einfluss von lokalen Ordnungseffekten diskutiert. Die wesentlichen Ergebnisse sind im Folgenden zusammengefasst.

Ergebnisse: $Eu_{1-x}Ho_xMnO_3$

Einfluss des Ho-Gehalts auf die Gitterdynamik

In einem ersten Schritt wird der Einfluss der partiellen Substitution von Eu^{3+} mit Ho^{3+} auf die Gitterdynamik in $Eu_{1-x}Ho_xMnO_3$ für $0 \leq x \leq 0.5$ untersucht. Um dabei die Effekte der Spin-Phonon Kopplung, die durch das Auftreten der magnetischen Ordnung verursacht werden, ausschließen zu können, werden hierzu die Messungen bei Raumtemperatur durchgeführt, d.h. bei Temperaturen weit oberhalb der magnetischen Ordnungstemperatur, welche typischerweise im Bereich von 40-50 K liegt. Für eine weitergehende Analyse der Spektren müssen zunächst die beobachteten Moden im Ramanspektrum den einzelnen Auslenkungsmustern der Moden zugeordnet werden. [3] Dies geschieht anhand der berechneten Modenfrequenzen von Smirnova für $LaMnO_3$ sowie dem Vergleich mit bereits veröffentlichten Spektren, die für zahlreiche stöchiometrische $RMnO_3$ Verbindungen verfügbar sind [4]. Durch Ausnutzung der optischen Auswahlregeln lassen sich die beobachteten Moden im Ramanspektrum entsprechend ihrer Modensymmetrie trennen und zuordnen. Eine besondere Rolle wird in dieser Betrachtung der $A_g(4)$ Mode zuteil, die eine periodische Verkippung der MnO_6 Oktaeder beschreibt und einen linearen Zusammenhang zwischen der Modenfrequenz und dem Mn-O-Mn Bindungswinkel ϕ aufweist. Beim Vergleich der anhand der $A_g(4)$ Modenfrequenzen bestimmten Bindungswinkel für die $Eu_{1-x}Ho_xMnO_3$ Serie mit den Bindungswinkeln der stöchiometrischen $RMnO_3$ konnte bestätigt werden, dass das magnetische $T-x$ Phasendiagramm von $Eu_{1-x}Ho_xMnO_3$ exakt in das allgemeine $T-\phi$ Phasendiagramm für stöchiometrische $RMnO_3$ übergeht. [5, 6] Die Übergangstemperaturen sowie die magnetischen Grundzustände von $Eu_{1-x}Ho_xMnO_3$ entsprechen genau jenen, die man erhält, wenn man das stöchiometrische $T-\phi$ Phasendiagramm für die entsprechenden Werte von ϕ interpolieren würde. Im Allgemeinen ist eine Verschiebung der Frequenzen aller beobachteten Moden im Ramanspektrum hin zu höheren Frequenzen mit steigendem Ho-Gehalt x zu beobachten, die sich aus der zunehmenden orthorhombischen Verzerrung der ursprünglich kubischen Perowskitstruktur ergibt. Insbesondere kann hier der Einfluss der größeren Masse des Ho-Ions im Vergleich zu Eu ausgeschlossen werden, da dies zum Einen einen gegenläufigen Effekt hätte, und zum Anderen die Ionen an den R-Plätzen nicht an diesen Schwingungen teilnehmen. Die Stärke der Frequenzverschiebung unterscheidet sich von Mode zu Mode und lässt sich auf die spezifischen Auslenkungsmuster der Moden zurückführen.

Spin-Phonon Kopplung

Mit temperaturabhängigen Ramanexperimenten wird die Spin-Phonon Kopplung (SPC), sprich der Einfluss der magnetischen Austauschwechselwirkung durch Superaustausch über Mn-O-Mn auf die Rückstellkraft der Gitterschwingungen untersucht. Die Spin-Phonon Kopplung äußert sich durch eine Renormalisierung der Phononenfrequenz, wenn sich die magnetische Ordnung ausbildet. Die Stärke dieser Frequenzverschiebung ist direkt mit den zunehmenden magnetischen Korrelationen bei sinkender Temperatur verknüpft. Auch hier unterscheidet sich die Ausprägung des Effekts je nach Auslenkungsmuster der Moden. Jene Schwingungen, welche hauptsächlich die Mn-O-Mn Bindungen modulieren, reagieren hierbei besonders sensitiv auf magnetische Korrelationen und eignen sich daher hervorragend als lokale Sonden für Korrelationseffekte. Die $B_{2g}(1)$ Mode, die eine Atemschwingung der Sauerstoffionen in der MnO_2 Ebene (*ac*-Ebene in der *Pnma* Orientierung) darstellt wurde auch in der Vergangenheit bereits genutzt um mittels SPC den Einfluss magnetischer Korrelationen zu untersuchen [7]. Ein mathematischer Formalismus, entwickelt von Granado *et al.* erlaubt es, durch Messen der Frequenzverschiebung durch SPC auf die ferromagnetische Kopplungsstärke $\frac{\partial^2 J_{ac}}{\partial u^2}$ in der *ac* Ebene zu schließen und diese zu quantifizieren [8]. Eine bisher noch nicht identifizierte Anregung im Ramanspektrum konnte in dieser Arbeit eindeutig der $B_{3g}(1)$ Mode zugewiesen werden. Diese ist der $B_{2g}(1)$ Mode recht ähnlich, allerdings enthält ihr Auslenkungsmuster eine zusätzliche Bewegung der apikalen Sauerstoffionen entlang der *b*-Richtung. In diesem Zusammenhang wurde der Formalismus von Granado *et al.* auf diese neue Mode erweitert um damit erstmals Zugang zur Evaluierung der Kopplungsstärke $\frac{\partial^2 J_b}{\partial u^2}$ senkrecht zur *ac*-Ebene zu erlangen. Dadurch wird eine vollständige Quantifizierung aller beteiligten Kopplungsstärken für nächste Nachbarn ermöglicht.

Um das Bild der Gitterdynamik der ramanaktiven Moden zu vervollständigen, wurde auch der Effekt der SPC im externen Magnetfeld untersucht. Während die infrarotaktiven Moden sehr empfindlich für die ferroelektrische Ordnung bzw. deren Umorientierung im externen Feld sind, sollten die ramanaktiven Moden unabhängig davon sein, da die SPC Effekte der ramanaktiven Moden in erster Linie auf der Austauschwechselwirkung beruhen. [9, 10] Bei diesen Untersuchungen wurde klar gezeigt, dass die Auswirkungen des externen Magnetfeldes zwar durchaus klein, jedoch nicht vernachlässigbar sind.
Ein Punkt, der in der bisherigen Diskussion in der Literatur nur unzureichend erklärt wird besteht darin, dass SPC bereits bei Temperaturen weit oberhalb

der magnetischen Ordnungstemperatur zu beobachten ist. Durch die Vorstellung eines neuen Modells, welches die Entwicklung der Spinstruktur als Ordnungs-Unordnungs Übergang aus lokal korrelierten Spin Zykloiden als "Pseudospins"beschreibt, konnte diese Diskrepanz ausgeräumt werden. Die Umorientierung eines solchen Zykloids auf lokaler Ebene ist in diesem Modell mit einer Energiebarriere verbunden, welche überwunden werden muss. Diese entspricht in etwa 100 K und wurde durch ein gemeinsames Bestreben durch die Messung der Aktivierungsenergie in dielektrischen Messungen, der Aktivität des Elektromagnons in der THz-Spektroskopie und das Auftreten von SPC in der Ramanspektroskopie bestätigt. [11]

Im Zuge der detaillierten Untersuchungen zur Temperaturabhängigkeit der Spin-Phonon Kopplung wurde außerdem eine Verletzung der Raman Auswahlregeln in $Eu_{1-x}Ho_xMnO_3$ beobachtet, welche bisher in noch keinem der orthorhombischen $R\mathrm{MnO}_3$ nachgewiesen wurde. Diese Verletzung der Auswahlregeln tritt in einem sehr engen Temperaturintervall nahe der ferroelektrischen Übergangstemperatur auf und äußert sich durch eine starke Zunahme der Intensität der verbotenen Moden. Ein Deutungsansatz ergibt sich aus einer Besonderheit von $Eu_{1-x}Ho_xMnO_3$, da sich die Rotationsebenen der Spin Zykloide im Gegensatz zu den stöchiometrischen $R\mathrm{MnO}_3$ abhängig von x und der Temperatur T spontan umorientieren und damit 90° Domänen mit reduzierter Symmetrie in den Domänengrenzen zulassen. Anhand des typischen kritischen Verhaltens nahe der Übergangstemperatur, welches durch erhöhte Fluktuationen und kritisch verlangsamter Dynamik der Ordnung gekennzeichnet ist, konnte dadurch eine Erklärung für das Phänomen der Auswahlregelverletzung gefunden werden. [12]

Als weiteres Argument für die Plausibilität dieser neue Modellvorstellung bestätigen Monte Carlo Simulationen der Spin Dynamik, die für verschiedene Temperaturen durchgeführt wurde,n qualitativ die hervorgebrachten Argumente und Ideen, insbesondere, dass bei Temperaturen oberhalb des Multiferroischen Zustands zwar die makroskopische ferroelektrische Ordnung verloren geht, jedoch lokal Spin Zykloide erhalten bleiben.

Ramanaktivität des Elektromagnons

Während das Elektromagnon und die Elektromagnon-Phonon Kopplung im Ferninfrarot- bzw. THz-Spektrum von $R\mathrm{MnO}_3$ bereits in zahlreichen Studien belegt ist, sind experimentelle Hinweise für die Ramanaktivität des Elektromagnons noch spärlich gesät und werden kontrovers diskutiert. [7, 13, 14] Mit fortschreitenden Erkenntnissen über die Dynamik des Elektromagnons,

zeigte sich, dass das spektrale Gewicht der Anregung sich nicht nur aus der Kopplung elektromagnetischer Strahlung mit seinem Dipolmoment ergibt, sondern dass es zusätzlich zu diesem elektrischen Charakter noch einen magnetischen Beitrag zum spektralen Gewicht gibt. [15, 16] In der Infrarot- bzw. THz Spektroskopie sind jedoch lediglich polare Phononen zugänglich und damit kann nur der polare Anteil der Elektromagnon-Phonon Kopplung untersucht werden. Es ist daher von höchstem Interesse, ob sich diese elementare Anregung der multiferroischen Phase auch im Ramanspektrum beobachten lässt um auch die Elektromagnon-Phonon Kopplung durch unpolare Phononen zu erfassen. Als erster Schritt in diesem Unterfangen wurde in dieser Arbeit ein möglicher Nachweis über die Aktivität erbracht und das Verhalten der Anregung im externen Magnetfeld untersucht. Hierbei zeigten sich einige interessante Beobachtungen, die sich von dem bereits bekannten Verhalten des EM im Infrarotspektrum unterscheiden. So hängt die Intensität des EMs im Ramanspektrum kaum vom angelegten Magnetfeld ab, während es sich im Infrarotspektrum vollständig unterdrücken lässt. Die Anregung eines EM im Infrarotspektrum ist nur mit einer Polarisation entlang einer bestimmten Kristallachse möglich. Diese ändert sich nicht, auch wenn die Rotationsebene der Spin Zykloide von der *ac* zur *ab* Ebene umgeklappt wird und ist daher nicht an den Zykloid, sondern an das Kristallgitter gebunden. In der Ramanspektroskopie zeigt sich keine solche ausgezeichnete Achse für die Anregung. Anhand der beobachteten Auswahlregeln werden verschiedene mögliche Ursachen der Ramanaktivitä diskutiert.

Ergebnisse: $A\mathrm{CrO}_2$

Einfluss des *A*-ions auf die Gitterdynamik

Die Systematik der Untersuchungen der $A\mathrm{CrO}_2$ Delafossite verläuft analog zu den Untersuchungen an $\mathrm{Eu}_{1-x}\mathrm{Ho}_x\mathrm{MnO}_3$. Zuerst wurde der Einfluss des Ionenradius auf die Gitterdynamik von $A\mathrm{CrO}_2$ untersucht, welcher in der Reihenfolge von A= Cu, Pd und Ag zunimmt. In Analogie zu den Seltenerdmanganaten und zusätzlich unterstützt durch core-shell Berechnungen der Phononenfrequenzen mittels GULP ergab sich die Erwartungshaltung, dass die Frequenz der Gitterschwingungen mit zunehmendem Ionenradius abnehmen sollte. Die Ergebnisse zeigten jedoch zunächst keinen systematischen Zusammenhang der beobachteten Frequenzen in der Gegenüberstellung von Atommasse, Bindungswinkel oder Ionenradius der drei verschiedenen Verbindungen, jedoch ließ sich PdCrO_2 als Ausreißer der Probenserie identifizieren. Eine mögliche Ursache für die Abweichung der Modenfrequenzen von

der Erwartung könnte in der sich von Cu^+ und Ag^+ unterscheidenden Valenzelektronenkonfiguration des Pd^+-Ions begründet liegen. Während erstere über abgeschlossene 3d- respektive 4d-Schalen verfügen, teilen sich die Valenzelektronen von Pd^+ in 4d- und 5s-Orbitale ($4d^8\ 5s^1$) auf. Auch in der Literatur wurden bereits noch weitaus drastischer abweichende Werte der Modenfrequenzen beobachtet, was im Gesamten auf noch ungelöste Probleme in der Synthetisierung der $PdCrO_2$ Proben hindeutet. Das Ausräumen dieser Probleme ist von besonderer Wichtigkeit, da $PdCrO_2$ auch als Kanditat für eine andere exotische magnetische Phase, die Spin-Flüssigkeit gehandelt wird. [17–21]

Spin-Phonon Kopplung

Die Spin-Phonon Kopplung der $ACrO_2$ Verbindungen zeigte sich im Vergleich zu $Eu_{1-x}Ho_xMnO_3$ bzw. generell zu den $RMnO_3$ Systemen deutlich weniger stark ausgeprägt. Während sich der Effekt der Frequenzverschiebung durch SPC in $Eu_{1-x}Ho_xMnO_3$ auf etwa 1% der intrinsischen Modenfrequenz für die $B_{2g}(1)$ Mode beläuft, ist der Effekt in $ACrO_2$ um eine Größenordnung geringer und liegt im Bereich von 0.1%. Die Empfindlichkeit der beiden ramanaktiven Moden auf SPC kehrt sich darüber hinaus in dieser Probenserie mit A= Cr→ Pd→ Ag um: Zeigt in $CuCrO_2$ noch die E_g Mode die stärkere Frequenzverschiebung durch SPC, wird der Einfluss auf diese Mode schwächer und in $AgCrO_2$ schließlich erfährt die A_{1g} Mode die stärkere Spin-Phonon-Kopplung der beiden Moden. Einen Ansatz zur Erklärung liefern die Auslenkungsmuster der beiden Moden. Abhängig vom Bindungswinkel wird der Überlapp des Austauschintegrals durch die Schwingungen unterschiedlich stark moduliert, so dass sich je nach konkretem Bindungswinkel die Sensitivität der Moden für SPC ändern kann. Auch hier zeigen sich erste Effekte der SPC durch eine Frequenzverschiebung der Moden bereits bei deutlich höheren Temperaturen als der magnetischen Ordnungstemperatur.

Im Ramanspektrum von $CuCrO_2$ erscheint ein weiteres Feature bei tiefen Temperaturen als Satellit der E_g Mode, dessen Ursprung rege diskutiert wird. Zum Einen könnte es sich hierbei um einen Zwei-Magnonen Prozess handeln, wie z.B. für einen ähnlichen Peak in $LiCrO_2$ argumentiert wird [22]. Zum Anderen könnte es sich um eine Deformation des Gitters, welche an die Spin-Struktur gekoppelt ist handeln. [23] Die Temperaturabhängigkeit der Frequenz dieses Satellitenpeaks wurde in dieser Arbeit eingehend untersucht und es konnte gezeigt werden, dass der Peak nicht nur mit sinkender Temperatur an Intensität gewinnt, sondern sich zusätzlich kontinuierlich zunehmend von der E_g Mode separiert. Bei Raumtemperatur sind die Frequen-

zen des Satelliten und der E_g Mode so nahe zusammengerückt, dass sie im Spektrum nicht mehr zu unterscheiden sind. Die aktuelle Tendenz neigt sich zunehmend der Interpretation als Spin-induzierte Deformation des Gitters zu, welche durch die Beobachtungen der temperaturabhängigen Spin-Phonon Kopplung und durch druckabhängige Ramanspektren untermauert wird. [24] Die Vorstellung der Gitter- und Spindynamik von $A\mathrm{CrO_2}$ bei Annäherung an die magnetisch geordnete Phase kann dabei auf eine ähnliche Art und Weise wie in $\mathrm{Eu_{1-x}Ho_xMnO_3}$ durch eine lokale magnetische Ordnung verstanden werden, deren Domänen sich mit sinkender Temperatur zunehmend ausdehnen, wobei hier von den sechs möglichen Domänen letztendlich zwei aufgrund der magnetischen Ordnung favorisiert werden.

Im Vergleich zu den sehr schwachen Frequenzverschiebung durch SPC von 0.1% der intrinschischen Modenfrequenz, welche in den temperaturabhängigen Messungen beobachtet wurden, zeigte sich eine recht starke Magnetfeldabhängigkeit der Schwingungsfrequenzen von bis zu ca. 1%. Vor allem $\mathrm{CuCrO_2}$ zeigte hier im Bereich bis $B \leq 3$ T eine Frequenzverschiebung beider Moden und des Satelliten um etwa 5 $\mathrm{cm^{-1}}$. Interessanterweise verhalten sich die Schwingungsmoden und der Satellitenpeak für Felder $B \geq 3$ T unterschiedlich. Gerade das Verhalten des Satellitenpeaks im Magnetfeld könnte auf eine weitergehende Deformation des Gitters durch das magnetische Feld hindeuten.

Fazit

Sowohl die orthorhombischen $\mathrm{Eu_{1-x}Ho_xMnO_3}$ ($0 \leq x \leq 0.5$) als auch die $A\mathrm{CrO_2}$ Delafossite (A=Cu, Pd, Ag) zeigen in ihrer temperaturabhängigen Gitterdynamik Effekte der Spin-Phonon Kopplung, hervorgerufen durch die Modulation der Austauschintegrals durch die Schwingung der am magnetischen Austausch beteiligten Ionen, hauptsächlich der Sauerstoff Ionen. Die Ausprägung des Effekts hängt stark von dem spezifischen Schwingungsmuster der jeweiligen Moden ab, wobei die durch SPC verursachte Frequenzverschiebung in den Delafossiten um eine Größenordnung geringer ausfällt als in den untersuchten Manganaten. Das Verständnis der multiferroischen Phase und SPC in den Manganaten ist schon weit vorangeschritten und konnte in dieser Dissertation um weitere wichtige Punkte ergänzt werden. Insbesondere die Verbesserung des Formalismus zur quantitativen Analyse der Kopplungsstärken und das verbesserte Verständnis der Rollen von lokaler und globaler Ordnung der Spin Zykloide ermöglichen es, ein breiteres Feld an Beobachtun-

gen konsistent in einem Modell zu vereinen. Dazu gehören das Auftreten von Spin-Phonon Kopplung sowohl bei Raman- als auch Infrarot-aktiven Moden, die Aktivität von Elektromagnonen im Infrarot Spektrum und die Erhaltung der Richtung der elektrischen Polarisation gepolter Proben, selbst wenn diese auf Temperaturen weit oberhalb der magnetischen Ordnungstemperatur erwärmt werden. Die für die Manganate gewonnenen Erkenntnisse können teilweise auf das $A\mathrm{CrO}_2$ System übertragen werden und so die Diskussion um die Entstehung der magnetisch geordneten Phasen mit sinkender Temperatur bereichern.

In diesem Zusammenhang bietet die Dynamik der Domänengrenzen vielversprechende Ansätze für weitere Untersuchungen und potenzielle Anwendungen. Abhängig davon welche Domänen aufeinandertreffen, bilden sich Domänengrenzen mit erhöhter, neutraler oder verringerter Ladungsträgerdichte im Vergleich zum Restvolumen aus. Durch Ausrichten der Domänen lassen sich so beispielsweise Schaltkreise nach Belieben erstellen, bearbeiten und wieder löschen. [25–27]. Genaue Kenntnisse über die Dynamik der multiferroischen Domänen, bezüglich Stabilität, Mobilität und die Strärke der magnetoelektrischen Kopplung werden daher für beide Materialsysteme eine entscheidende Rolle für weitere Entwicklungen spielen.

Contents

1 Introduction **1**
1.1 The magneto-electric effect and multiferroicity 1
1.2 Scope and organization of this thesis 3

2 Fundamentals of Raman spectroscopy and lattice dynamics **7**
2.1 Classical description of the Raman effect 7
2.2 Quantum mechanical description of the Raman effect 10
2.3 Raman selection rules 13
2.4 Anharmonic phonon damping: The Klemens model 15
2.5 Spin-phonon coupling 18
2.6 The electromagnon - an introduction 23
2.7 Raman activity of the electromagnon 24
2.7.1 First-order magnon scattering 24
2.7.2 Second-order magnon scattering 25

3 Experimental setups **29**
3.1 Micro-Raman setup 29
3.2 Magnet cryostat with triple monochromator 31

I The orthorhombic perovskites $Eu_{1-x}Ho_xMnO_3$ **33**

4 Introduction to the orthorhombic RMnO$_3$ perovskites **35**
4.1 Crystal structure 35
4.1.1 Impact of the R-site ionic radius 36
4.1.2 Jahn-Teller effect 38
4.2 Magnetic order in RMnO$_3$ 41
4.2.1 Goodenough-Kanamori-Anderson rules 41
4.2.2 The A-type antiferromagnetic order 43
4.2.3 Incommensurable magnetic order 45
4.3 General introduction to multiferroicity 49

4.4 Multiferroicity by cycloidal spin order 51
4.4.1 Influence of the magnetic moment of the R-site ion in $R\mathrm{MnO_3}$ 54

5 Results and discussion - $\mathbf{Eu_{1-x}Ho_xMnO_3}$ 57
5.1 Mode assignment 57
5.2 Impact of Ho-content on the lattice dynamics of $\mathrm{Eu_{1-x}Ho_xMnO_3}$ 63
5.3 Temperature dependence and spin-phonon coupling 70
5.3.1 Mode dependence of SPC 71
5.3.2 Composition dependence of SPC 76
5.4 SPC coupling parameters 78
5.5 Magnetic-field dependence of SPC 81
5.6 Impact of local order to SPC above T_N 84
5.6.1 Experimental results 84
5.6.2 Order-disorder limit: The pseudospin model 87
5.7 Transient violation of Raman selection rules in $\mathrm{Eu_{1-x}Ho_xMnO_3}$ at the cycloid reorientation temperature 91
5.7.1 Possible scenarios of DW-induced disorder 96
5.7.2 Pseudospin model and the strength of the effect 98
5.8 Monte Carlo simulation of the $R\mathrm{MnO_3}$ spin system 100
5.8.1 Basic FM and AFM model for nearest neighbors 100
5.8.2 Next-nearest neighbor interactions and cycloidal order 102
5.9 Electromagnon activity 105
5.10 Summary 108

II The delafossite $\boldsymbol{A}\mathbf{CrO_2}$ 111

6 Introduction to the delafossite $\boldsymbol{A}\mathbf{CrO_2}$ 113
6.1 Crystal structure 113
6.2 Magnetic properties of $A\mathrm{CrO_2}$ 117
6.3 Multiferroicity by proper-screw type order in $A\mathrm{CrO_2}$ 119

7 Results and discussion - $\boldsymbol{A}\mathbf{CrO_2}$ 125
7.1 Characterization of $A\mathrm{CrO_2}$ 125
7.2 Temperature dependence and spin-phonon coupling 132
7.3 Satellite peak of the E_g mode 136
7.4 Magnetic-field dependence 141
7.5 Summary 144

8 Conclusion 147

9 Zusammenfassung **151**

Appendices **155**

A Hubbard model **157**

B Basic principles of Monte Carlo simulation **161**
B.1 Detailed balance and ergodicity 161
B.2 Metropolis algorithm 162

C Shell-model calculations with GULP **165**
C.1 Energy minimization 165
C.2 Long-range potential 166
C.3 Interatomic potentials 166
C.4 Setting up a GULP input file 168

Bibliography **171**

List of publications and conference contributions **185**

Danksagung **189**

Chapter 1

Introduction

1.1 The magneto-electric effect and multiferroicity

The material class of multiferroics has attracted interest of scientists for decades due to its peculiar properties. As is well known, in a solid, the application of an electric field **E** induces an electric polarization **P** and in a similar fashion, the application of a magnetic field **H** leads to a magnetization **M**. If the polarization is created spontaneously due to a reduction of the crystal symmetry, i.e., if the invariance under spatial inversion is broken, the material is called a ferroelectric. On the other hand, if a spontaneous magnetization occurs by breaking time inversion symmetry, this is termed a (anti-)ferromagnet. A multiferroic material, accordingly, is a material, in which spatial- and time inversion symmetry are broken within the same phase and therefore both, ferroelectric and ferromagnetic order are present. The two reductions of symmetries might occur completely independent of each other when magnetic and electric properties are uncoupled. If, however, a coupling between both degrees of freedom exists, electric properties like the polarization can be influenced with magnetic fields and vice versa. This kind of cross-coupling is called the Magneto-Electric Effect.

The first precursor of the Magneto-Electric (ME) Effect marks the discovery made by Röntgen in 1888: a dielectric moving through an electric field became magnetized [28]. From the theoretical side, P. Curie predicted on the basis of symmetry considerations that crystals which show an intrinsic ME effect could exist, i.e., without the necessity of the crystal being in motion. The name "magnetoelectric" was termed in the 1926 by Debye, after the first attempts to show the ME effect in experiments in the 1920s were unsuccess-

ful [29]. It was not until 1960 where the ME effect was demonstrated in the antiferromagnet Cr_2O_3 by electric-field induced magnetization and magnetic-field induced polarization [9, 30, 31]. This breakthrough triggered a surge of research in this field, peaking in the early 1970s [32]. However, only few materials were found at that time. Several factors need to be considered in the search for magnetoelectric materials [33]. The crystal symmetry must allow spontaneous electric polarization *and* spontaneous magnetization, which reduces the possible crystal structures. Furthermore, conventional ferroelectric materials are insulators with empty *d*-shells, as otherwise the application of an external electric field would not lead to an electric polarization, but would cause an electric current to flow. On the other hand, many ferromagnets like Fe or Ni are metals with partially filled *d*-shells and therefore conducting. A promising approach is therefore to search for magnetoelectric materials in weak ferromagnets or antiferromagnets, which are often insulators. The interest declined for the time being, as the observed, very weak ME coupling was not sufficient for promising technical applications. As an example, the ME coupling in Cr_2O_3 would only flip five spins out of 10^6 with an applied electric field of 1 $\mathrm{MV\,cm^{-1}}$: a shortcoming imposed by the aforementioned prerequisites for conventional magnetoelectrics [32]. Thus started the search for unconventional mechanisms of ferroelectricity.

Research on the ME effect was revived in the late 1990s with advances in the understanding of microscopic origins of magnetically-induced polarization. At its core stands that under specific circumstances, in particular distinct patterns in the magnetic order, the arrangement of spins leads to a shift of ions in the crystal [32–39]. If this shift of ions has a uniform component, the magnetic structure is the driving factor of the ferroelectric transition. Also the inverse is possible: inducing magnetic order by electric polarization. In this way the magnetic ordering pattern and the polarization pattern are directly coupled. Modification of one via applied magnetic or electric fields will inevitably affect the other, down to the local level. In this magnitude, it is also referenced as the *Giant Magneto-Electric Effect* and was first discovered in $TbMnO_3$ by Kimura *et al.* [1]. This approach is interesting for both scientific as well as technological reasons. From the scientific point of view, a plethora of new directions of investigation is opened up. The involved patterns of magnetic order which can induce a uniform electric polarization are "exotic", as they are not merely simple (anti-)ferromagnets with (anti-)parallel spin orientations but show rather complex structures, for example cycloidal or spiral spin arrangements. To achieve these complex spin structures, magnetically frustrated spin systems are necessary. This puts the multiferroic systems in close proximity to other

vigorously researched topics like unconventional spin-induced superconductivity or spin-liquids. All these magnetic systems bring forth their own "exotic" quasiparticles like skyrmions, Cooper Pairs, spinons and, in the case of multiferroics, the electrical-dipole active magnon, the electromagnon.

From the technological point of view, multiferroic materials are interesting as electromagnetic switches or for the application as memory devices. The outlook being that multiferroic memory could be switched electrically and reversibly at high speed, like modern DRAM, but with the advantage that the magnetic degrees of freedom would preserve the stored information once the device is turned off, as conventional but slow magnetic hard drives do. Other possible applications include filters for spin-polarized currents for the use in spintronic devices or magnetic sensing [38, 40], but also optical applications as electrical-field controlled polarizers in the THz range [41]. Recently the multiferroic domain walls themselves are gaining attention: depending on the type of domain wall, the charge carrier density is heightened or lowered and thus, the domain walls can acquire a conductive or insulating behavior, which is different from the rest of the material. With the demonstration that multiferroic domains can be easily written and erased, this opens up the path to rewritable circuits.
For a complete understanding, which is key for the progress of these versatile materials, it is important to investigate how spin, electronic and lattice degrees of freedom participate and couple with each other, which coupling mechanisms are at play and how they can be exploited to achieve the desired effects in multiferroic materials.

1.2 Scope and organization of this thesis

The focus of this thesis is the investigation of the lattice dynamics and the coupling of magnetism and phonons in two different multiferroic model systems. The first system, which constitutes the main part in this work is the system of multiferroic manganites $R\mathrm{MnO_3}$, in particular $\mathrm{Eu_{1-x}Ho_xMnO_3}$ with $0 \leq x \leq 0.5$. Its cycloidal spin arrangement leads to the emergence of the ferroelectric polarization via the inverse Dzyaloshinskii-Moriya interaction. This system is special among $R\mathrm{MnO_3}$ as with increasing Ho content x, $\mathrm{Eu_{1-x}Ho_xMnO_3}$ does not only become multiferroic, but due to the exchange interaction with the magnetic Ho-ion, the spin cycloid (and with it the electric polarization) is also flipped for higher Ho contents. This makes it one of the first compounds, where the cycloidal reorientation happens sponta-

neously, rather than with the application of external fields.
On the other hand, there is the delafossite $A\mathrm{CrO}_2$ system. Here, due to symmetry reasons, the spin-spiral pattern can not induce the polarization according to the inverse Dzyaloshinskii-Moriya interaction mechanism. Instead, it is thought that another way of magnetoelectric coupling is involved, which affects the charge distribution in the $d-p$ hybridized orbitals of the bonds.[42]

The lattice vibrations as well as the quasi-particle of the multiferroic phase, the electromagnon, are studied by Raman spectroscopy. Lattice vibrations like the B_{3g} mode, which involves vibrations of the Mn-O-Mn bonds modulate the exchange interaction and serve as a powerful tool for the investigation of magnetic correlations effects with high frequency accuracy. Raman spectroscopy acts as a local probe as even local magnetic correlations directly affect the phonon vibration frequency, revealing coupling effects onto the lattice dynamics even in the absence of global magnetic order. By varying the temperature, the coupling is investigated and unveils a renormalization of the phonon frequency as the magnetic order develops. For $\mathrm{Eu}_{1-x}\mathrm{Ho}_x\mathrm{MnO}_3$, the analysis of this spin-induced phonon frequency renormalization enables the quantitative determination of the in-plane spin-phonon coupling strengths. This formalism, introduced by Granado *et al.*, is extended here to evaluate the out-of-plane coupling strengths, which is enabled by the identification of a previously elusive feature as a vibrational mode. The complete picture is obtained by studying the lattice- and electromagnon dynamics in the magnetic field. Further emphasis is put towards the development of the cycloidal spin structure and correlations with temperature. A new model of describing the temperature-dependent behavior of said spin correlations is proposed and can consistently explain ordering phenomena which were until now unaddressed. The results are underscored with Monte Carlo based simulations of the spin dynamics with varying temperature.
Furthermore, a novel effect of a tentative violation of the Raman selection rules in $\mathrm{Eu}_{1-x}\mathrm{Ho}_x\mathrm{MnO}_3$ was discovered. While the phonon modes can be separated and identified by their symmetry by choosing appropriate polarization configurations, in a very narrow temperature range, $\mathrm{Eu}_{1-x}\mathrm{Ho}_x\mathrm{MnO}_3$ shows an increase of phonon intensities in polarization configurations where they should be forbidden. This is interpreted as a sign of local disorder, caused by 90° domain walls and could be explained within the model framework.

This course of action is followed with the material system of delafossites $A\mathrm{CrO}_2$. Being a relatively new class of multiferroic materials, the investi-

gations on $A\mathrm{CrO}_2$ are also of characterizing nature. For this, shell model calculations are performed as a reference to compare the vibrational frequencies obtained by the Raman experiments to. A renormalization of the vibrational frequencies is observed in this system as well and systematically analyzed across the sample series of A=Cu, Pd and Ag. Eventually, the effect of applying an external magnetic field is studied. A particularly interesting feature specific for CuCrO_2 is a satellite peak which appears at lower temperatures. It is presumably related to a deformation of the lattice and therefore going to be discussed in further detail.

The thesis is thus organized as follows: chapter 2 introduces the basic concepts of Raman spectroscopy and further details needed for the evaluation of the experiments as the anharmonic decay of optical phonons (*Klemens model*), spin-phonon coupling (SPC) and an introduction to the Raman activity of magnons. A short overview over the employed experimental techniques is given in chapter 3. The main part of the thesis is divided into two blocks. While Part I covers the $\mathrm{Eu}_{1-x}\mathrm{Ho}_x\mathrm{MnO}_3$ system, Part II is reserved for the $A\mathrm{CrO}_2$ system. Each of the two parts is organized in a similar manner: At first, an introduction to the crystallographic and magnetic structure of the material class is given, followed up by the presentation and discussion of results with respect to compositional and temperature-dependent dependent aspects. Specific considerations arising from the respective observations are discussed in further detail. The presentation of results is completed with investigations of electromagnons and lattice dynamics with applied magnetic fields. Eventually, the results are summarized in section 5.10 ($\mathrm{Eu}_{1-x}\mathrm{Ho}_x\mathrm{MnO}_3$) and section 7.5 ($A\mathrm{CrO}_2$). In chapter 8 the results of both investigated systems are compared and an outlook for further research is given.

Chapter 2

Fundamentals of Raman spectroscopy and lattice dynamics

Optical spectroscopy is a very powerful and versatile technique which enables the investigation of a multitude of physical properties of mechanic, electronic or magnetic origin. Typically, these observations are based upon the absorption, emission or scattering of photons by an excitation of the sample. Such excitations include, but are not limited to, excitations of electrons between atomic- or molecular levels or, in the case of a solid state material, quasiparticles like phonons, polarons, excitons or magnons. Optical methods excel at determining these properties with respect to their energy- or equivalently frequency dependence although, due to the small, yet non-zero photon momentum it is also possible to investigate the **k**-dependence. Various photon sources are available, spanning an energy range among several orders of magnitude: from the "quasi-optical" microwave and THz range, over infrared and the visible range up to the ultraviolet range and beyond. This corresponds to photon wavelengths of the order of 1 mm down to several hundreds of nanometers, or energies of $\approx 1\,\mathrm{meV}$ to several eV. It is common among spectroscopists to use the unit of wavenumber $[\tilde{\nu}] = \mathrm{cm}^{-1}$ as the unit of energy. With the speed of light c and the frequency ν, it is defined as $\tilde{\nu} = \nu/c$.

2.1 Classical description of the Raman effect

If a photon with the initial energy $\hbar\omega_i$ is inelastically scattered within the sample volume, this is called Raman scattering. During the scattering process, the system with the initial state $|i\rangle$ with energy E_i is excited to "virtual" state with energy E_v. This state decays under photon emission and creation or annihilation of a quasiparticle into the final state $|f\rangle$ with energy E_f.

Therefore, the emitted (scattered) photon is of different energy $\hbar\omega_s$ than the initial photon according to:

$$\hbar\omega_i + E_i = E_f + \hbar\omega_s. \tag{2.1}$$

The energy difference of the photons $\Delta E = \hbar(\omega_i - \omega_s) = E_f - E_i$ corresponds directly to the energy of the created or annihilated quasiparticle. The Raman

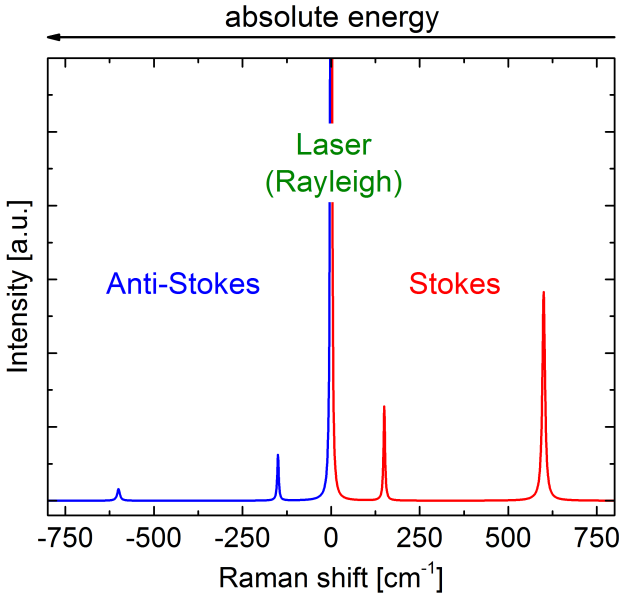

Figure 2.1: Simulated Raman spectrum for $T = 300$ K, consisting of the elastically scattered laser line (Rayleigh scattering), two features corresponding to the creation of two phonons on the Stokes side (positive Raman shift, less energy) and their counterpart on the Anti-Stokes side, corresponding to the annihilation of two preexisting phonons (negative Raman shift, higher energy).

process is further classified corresponding to the sign of energy shift of the inital photon. If a quasiparticle is created, then $\Delta E > 0$ and the scattered photon has a reduced energy with respect to the initial photon. The energy shift towards lower energies is termed Stokes shift. In the opposite scenario, an already existing quasiparticle is annihilated and its energy is transferred to the scattered photon, resulting in $\Delta E < 0$. Accordingly, this shift towards higher energies is called Anti-Stokes shift. If neither a quasiparticle is created nor annihilated in the scattering process the photon is scattered elastically and is emitted with the same energy as the initial photon. This process is called Rayleigh scattering. A simulated Raman spectrum displaying the laser

line at zero Raman shift (Rayleigh scattered), two phonons on the Stokes side (positive Raman shifts, lesser absolute energy) and their counterparts on the Anti-Stokes side (negative Raman shift, larger absolute energy) is shown in Fig.2.1. Note, that the positions of the Raman features of the Stokes and Anti-Stokes sides are symmetric, but the intensities are not (see section 2.2).

In the classical description, one considers an incident wave of light with the electric field $\mathbf{E} = \mathbf{E}_0 \cos \omega t$. This electric field induces a electric dipole moment proportional to the polarizability α of the material:

$$\mathbf{p} = \mu + \alpha \mathbf{E} \tag{2.2}$$

where μ denotes a potentially already present permanent dipole moment. For small displacements of the atomic cores from their equilibrium positions, one can perform a Taylor expansion of μ and α with the eigenmodes q_n

$$\mu(q) = \mu(0) + \sum_n \left(\frac{\partial \mu}{\partial q_n} \right)_0 q_n, \tag{2.3}$$

$$\alpha_{ij}(q) = \alpha_{ij}(0) + \sum_n \left(\frac{\partial \alpha_{ij}}{\partial q_n} \right)_0 q_n. \tag{2.4}$$

We can express the time dependence of the eigenmode q_n as

$$q_n(t) = A_n \cos \omega_n t \tag{2.5}$$

with the amplitude A_n and the eigenfrequency ω_n. Inserting 2.5 and 2.4 into 2.2, we obtain

$$\mathbf{p}(t) = \mu(0) + \sum_n \left(\frac{\partial \mu}{\partial q_n} \right)_0 A_n \cos \omega_n t + \alpha_{ij}(0) \mathbf{E_0} \cos \omega t \tag{2.6}$$

$$+ \frac{E_0}{2} \sum_n \left(\frac{\partial \alpha_{ij}}{\partial q_n} \right)_0 A_n \left(\cos(\omega - \omega_n)t + \cos(\omega + \omega_n)t \right). \tag{2.7}$$

The terms can now be interpreted according to their frequency with which they are oscillating: the first term is static and describes the permanent dipole moment. The second term oscillates with the frequency ω_n of the eigenmode q_n which gives rise to the infrared spectrum. The third one oscillates with the initial photon frequency ω is responsible for the Rayleigh scattering. The final term oscillates with frequencies of $\omega \mp \omega_n$ and describes the Stokes (-) and Anti-Stokes (+) Raman scattering. The Stokes scattering process corresponds to a creation of a phonon, which leads to a reduction of the energy of the scattered photon, while the Anti-Stokes scattering corresponds to the annihilation of an already existing phonon, thus leading to an increase of the energy of the scattered photon.

With the resulting equation 2.7, one can already deduce principal properties of infrared- and Raman-active modes. A given mode is infrared active, if $\frac{\partial \mu}{\partial q_n} \neq 0$, i.e. if the elongation pattern carries a dipole moment. Conversely, a mode is Raman active if the elongation pattern leads to a change of the polarizability $\alpha \left(\frac{\partial \alpha_{ij}}{\partial q_n} \neq 0 \right)$. While this classical approach explains the observed Raman shifts very well, a quantum mechanical approach, introduced in the upcoming section, is necessary to properly explain the observed intensities.

2.2 Quantum mechanical description of the Raman effect

To describe the scattering process, we can think of it as scattering of interacting particles happening in three steps:

1. The initial photon with ω_i is absorbed by an electron in the sample volume via the interaction operator $\mathbf{H}_{\text{e-rad}}$. This electron is now in an excited intermediate state $|a\rangle$.

2. The excited electron interacts with the lattice via an interaction Hamiltonian $\mathbf{H}_{\text{e-lattice}}$. In this process, a phonon is created and the electron is scattered into an intermediate state $|b\rangle$.

3. The electron decays back into its ground state by emitting the scattered photon with ω_s via $\mathbf{H}_{\text{e-rad}}$.

Note: since the electron's state is unchanged after the scattering process, it is conceivable, that a similar process without participation of an electron could be possible. However, it turns out that this interaction strength alone is very weak, unless photon and phonon energy are very close to each other. This is not the case for excitation with visible light and can therefore be neglected. To describe the Raman scattering process, we need to apply perturbation theory and find an appropriate expansion for the scattering probability. It is very helpful to consider the Feynman diagram in Figure 2.2, which shows the aforementioned scattering sequence. Note, that all six permutations of the three vertices of Fig. 2.2 are valid scattering processes and need to be summed up to reach the most general expression of the scattering probability. Since the scattering process shown in Fig. 2.2 is the dominant contribution to the Raman scattering process in typical semiconductor materials, we are going to focus on this single term. The scattering probability can now easily be written down according to Fermi's Golden Rule, as each vertex of the Feynman diagram corresponds to an interaction with the respective interaction

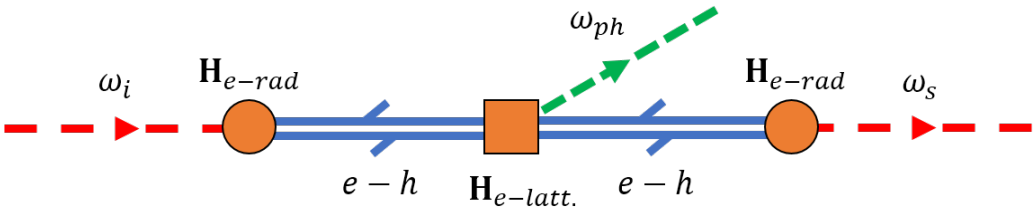

Figure 2.2: Feynman diagram of the dominant Raman scattering process. Note, that also all perturbations of phonon and photon propagators (lines) with their associated interaction vertices are valid scattering processes. Therefore, a total of six diagrams are conceivable.

Hamilton operator:

$$P(\omega_s) = \left(\frac{2\pi}{\hbar}\right) \left| \sum_{a,b} \frac{\langle i| \mathbf{H}_{\text{e-rad}} |b\rangle \langle b| \mathbf{H}_{\text{e-lattice}} |a\rangle \langle a| \mathbf{H}_{\text{e-rad}} |i\rangle}{[\hbar\omega_i - (E_a - E_i)]\,[\hbar\omega_i - \hbar\omega_0 - (E_b - E_i)]} \right|^2 \times \delta\left[\hbar\omega_i - \hbar\omega_0 - \hbar\omega_s\right] \tag{2.8}$$

where $|f\rangle = |i\rangle$ was already considered, as the electronic state is unchanged after the scattering process and therefore the final state of the electronic system should be identical with the initial state. This expression can be simplified further by summing over ω_s to remove the δ function. This summation is only nonzero for $\hbar\omega_i - \hbar\omega_0 = \hbar\omega_s$. Additionally, we can assume the initial state $|i\rangle$ as the ground state $|0\rangle$ with E_i=0 as the reference energy:

$$P(\omega_s) = \left(\frac{2\pi}{\hbar}\right) \left| \sum_{a,b} \frac{\langle 0| \mathbf{H}_{\text{e-rad}} |b\rangle \langle b| \mathbf{H}_{\text{e-lattice}} |a\rangle \langle a| \mathbf{H}_{\text{e-rad}} |0\rangle}{(\hbar\omega_i - E_a)\,(\hbar\omega_s - E_b)} \right|^2 . \tag{2.9}$$

When the Raman scattering experiment is conducted under resonant conditions, i.e. either $\hbar\omega_i$ or $\hbar\omega_s$ is in close vicinity to the energy of a real transition in the system, the denominator becomes very small. When the summation over all intermediary states $|a\rangle$ and $|b\rangle$ is carried out, this resonant term will be by far the largest in the sum and all other contributions can be regarded as some constant background. Let the resonant state be $|c\rangle$ with energy E_c, then the transition probability can be approximated as

$$P(\omega_s) \approx \left(\frac{2\pi}{\hbar}\right) \left| \frac{\langle 0| \mathbf{H}_{\text{e-rad}} |c\rangle \langle c| \mathbf{H}_{\text{e-lattice}} |c\rangle \langle c| \mathbf{H}_{\text{e-rad}} |0\rangle}{(\hbar\omega_i - E_c)\,(\hbar\omega_s - E_c)} \right|^2 . \tag{2.10}$$

Interestingly, since the phonon energy is small compared to $\hbar\omega_i$ and therefore $\hbar\omega_i \approx \hbar\omega_s$, Eq. 2.10 shows, that if the denominator is small for $(\hbar\omega_i - E_c)$,

also the term with $(\hbar\omega_s - E_c)$ is small. Therefore, the term with $a, b = c$ in Eq. 2.10 diverges nearly as if it consisted of two resonant denominators. All other terms in the sum of Eq. 2.9 will contain at most one resonant term (if $a \veebar b = c$), which further justifies the approximation. Since the Raman scattering efficiencies are orders of magnitude lower than direct processes like absorption of infrared light, it is desirable to perform the Raman scattering experiment under resonant conditions or close to resonant conditions by choosing an appropriate discrete laser line for excitation or if applicable a continuously tunable light source, such as for example dye lasers.
For the case of $(\hbar\omega_i - E_c) = 0$ or $(\hbar\omega_s - E_c) = 0$, Eq. 2.10 would lead to an unphysical infinite scattering probability. The situation can be avoided by adding an imaginary term $i\Gamma$ to the denominators. This can be justified either by the finite lifetime of the resonant state, where $\Gamma \propto 1/\tau_c$ corresponds to the inverse lifetime of the excited state, or by interpreting it as the damping constant of the scattered phonon ω_{ph}. Note, that a nonzero damping will change the observed phonon frequency. Since the damping constant is in general temperature-dependent, the observed phonon frequency will also be temperature dependent. This will be further discussed in section 2.4.

For the sake of completeness, but without a detailed deduction, the intensity ratio of the Stokes and Anti-Stokes Raman scattering processes is addressed. In the Stokes process, a phonon is created. This process can happen spontaneously, i.e., in the absence of any preexisting phonon in the considered state, or can be stimulated for $T \neq 0$, when the phononic state is already populated by thermal excitation, proportional to the Bose-Einstein factor $n(\omega_{ph}, T) = \left[e^{\hbar\omega_{ph}/k_B T} - 1\right]^{-1}$ and therefore the Intensity I_{Stokes} is proportional to $(n(\omega, T) + 1)$. On the other hand, the Anti-Stokes process is only possible if there already exists a phonon, which can be annihilated and therefore $I_{Anti-Stokes} \propto n(\omega_{ph}, T)$ [43]. As a result, for a given phonon frequency ω_{ph}, the intensity ratio of the Stokes and Anti-Stokes processes is

$$\frac{I_{Stokes}}{I_{Anti-Stokes}} = \frac{n(\omega_{ph}, T) + 1}{n(\omega_{ph}, T)} = e^{\hbar\omega_{ph}/k_B T}. \tag{2.11}$$

Therefore, the two peaks on the Anti-Stokes side of Fig. 2.1 do not show the same intensity ratio with respect to each other as on the Stokes side because the higher-energy phononic state is less populated due to thermal excitation than the lower state and the scattering intensity is reduced much further than for the lower state with the larger population. With increasing temperature, also the intensity of the Anti-Stokes spectrum is increased. The relation of Eq. 2.11 can in principle be used to determine the actual temperature in the sample. Note, however, that for $T = 0$ there is no Anti-Stokes spectrum.

Since the Raman scattering experiments conducted in this thesis are mostly performed at low temperatures, the Anti-Stokes scattering processes are not further considered in the data analysis.

2.3 Raman selection rules

While the expression in Eq. 2.8 describes the Raman scattering probability accurately, it is often difficult to evaluate it quantitatively due to the amount of necessary parameters which are not known in detail. In spectroscopy it is often sufficient to know if the probability for a specific scattering event, which includes also different possible polarization configurations of incident scattered light is zero or nonzero, even when the exact probability is not known. This is achieved by considering the symmetries of the wavefunctions and operators in Eq. 2.8. In the Raman scattering process there are three matrix elements to be considered. The first and the last interaction in the scattering process, expressed by the matrix elements $\langle \ldots | \mathbf{H}_{\text{e-rad}} | \ldots \rangle$ describe the excitation of the electronic wavefunction by an incident photon or the relaxation of the electronic wavefunction from an excited state via an emission of a real photon. As is well known, a transition of this kind is mediated by the application of the dipole operator [44]. In a crystal with a center of inversion the dipole operator changes the parity of the state it is acting upon, which is the consequence of applying the dipole operator $\hat{\mathbf{p}}$ to the spherical harmonics of the atomic electron wavefunction. For example, a state of even (g) parity would be converted to odd (u) parity. For the matrix element to be nonzero, the final state must therefore be also of odd parity, as the spherical harmonics form a complete set of orthogonal basic function and thus the product of two functions with different parity vanishes. In conclusion, this matrix element is only nonzero when the initial and the final state were of different parity. This leads to the selection rule of $\Delta L = \pm 1$ for an optical dipole transition, as the parity of the spherical harmonics is $(-1)^L$. Since this process occurs for the incident and also for the scattered photon and the electronic wavefunction returns to its original parity, it becomes clear that the matrix element $\langle b | \mathbf{H}_{\text{e-lattice}} | a \rangle$ is not allowed to change the parity. Therefore the interaction Hamiltonian $\mathbf{H}_{\text{e-lattice}}$ has to project the intermediate state $|a\rangle$ into an intermediate state $|b\rangle$ with the same parity, which corresponds to the selection rule $\Delta L = 0, 2, \ldots$. The whole Raman scattering process does therefore not change the parity of the electronic wavefunction, in contrast to direct excitation with infrared light, which changes the parity from u $\rightarrow$ g or from g $\rightarrow$ u. This shows that the infrared and the Raman spectrum of a crystal with inversion symmetry must be mutually exclusive. Besides parity

considerations, which is a direct consequence of the presence of a center of inversion in the crystal structure, further constraints can be imposed onto the scattering process by the crystal lattice symmetry, especially considering the polarization of the incident and scattered photons. The phonon excitation in $\langle b| \mathbf{H}_{\text{e-lattice}} |a\rangle$ is described by the Raman tensor $\underline{\mathbf{R}}$. The polarization selection rules are then obtained by multiplying the polarization vectors $\hat{\mathbf{e}}$ of the incident and scattered photon with the Raman tensor:

$$I_s \propto \left| \hat{\mathbf{e}}_\mathbf{s} \underline{\mathbf{R}} \hat{\mathbf{e}}_\mathbf{i}{}^T \right|^2 . \tag{2.12}$$

The Raman tensor is determined by the symmetry of the crystal lattice and by the symmetry of the specific mode for which it is considered. It can be determined by analyzing the point groups and allowed symmetry operations. This has been performed by Loudon [45], where all Raman tensors for all 32 pointgroups are tabulated. Note, that Raman tensors are always given in the crystallographic axis system for which they are defined.
We see, that the Raman selection rules depend on the polarization configurations, which are chosen for $\hat{\mathbf{e}}_{i,s}$. However, also the directions of the wavevectors of incident and scattered photons play a part in determining the selection rules. It is therefore convenient to write the scattering geometry and polarization configuration in an abbreviated form, known as Porto's Notation

$$\mathbf{k}_i(\mathbf{e}_i, \mathbf{e}_s)\mathbf{k}_s \tag{2.13}$$

where $\mathbf{k}_i, \mathbf{k}_s$ are the wavevectors and $\mathbf{e}_i, \mathbf{e}_s$ are the polarization vectors of the incident and scattered photon, respectively. They are typically written down by using the letter of the respective crystallographic axis. In this thesis, all Raman experiments are conducted in backscattering geometry, i.e. $\mathbf{k}_i = -\mathbf{k}_s$. As an example, incident light with wavevector parallel to the crystallographic a-axis with linear polarization parallel to the b-axis is scattered into the direction -a and with polarization parallel to c would read $a(b,c)\bar{a}$. This allows to efficiently write down different polarization configurations.
Since two material systems with distinct crystallographic symmetries are considered in this thesis, the Raman selection rules will not be presented at this point. Instead, it is referred to section 5.1 for $R\text{MnO}_3$ or section 7.1 for $A\text{CrO}_2$, where the specific Raman tensors and selection rules will be introduced for the mode assignment in the Raman spectrum.

2.4 Anharmonic phonon damping: The Klemens model

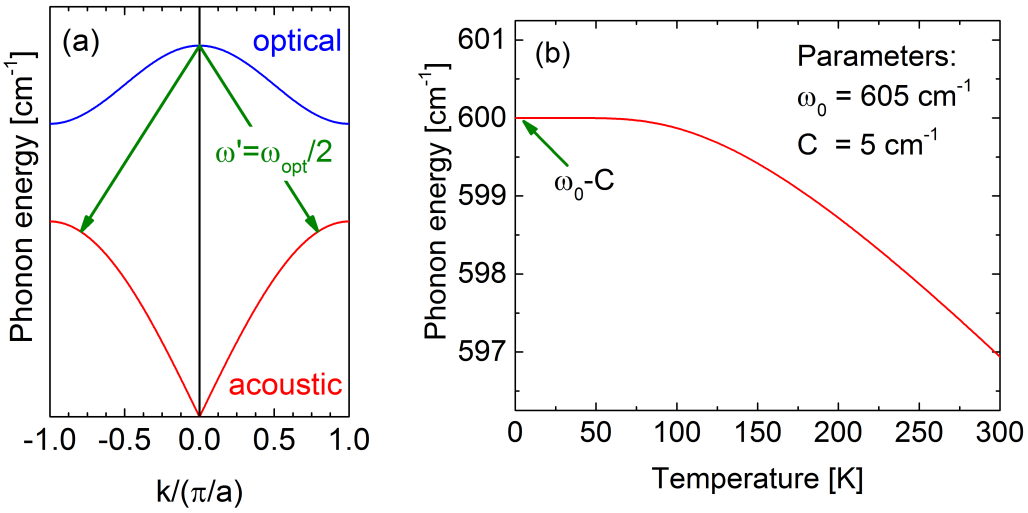

Figure 2.3: (a) Schematic illustration of the phonon decay process according to the Klemens model [46]. The optical phonon decays into two acoustic phonons of opposite wavevectors. The frequency of the acoustic phonon is $\omega' = \omega_{opt}/2$. (b) Simulated data for $\omega(T)$ according to the Klemens model Eq. (2.18) with typical values. For low temperatures the function becomes nearly constant and converges towards the value $\omega_0 - C$.

The major focus of this thesis is the observation of the temperature-dependent, magnetically induced shift of the phonon frequencies caused by spin-phonon coupling (SPC, see section 2.5). In order to separate the intrinsic contribution of the damping-induced frequency shifts from the SPC-induced frequency shift in the data analysis, this section will briefly discuss the influence of the intrinsic temperature-dependent damping $\Gamma(T)$ onto the phonon frequency.
The model which will be discussed here, was developed by Klemens and later extended by Balkanski *et al.* and is referred to as *Klemens model* in the following [46, 47]. As is well known, the phonon frequency and linewidth depend on the temperature, which is attributed to the anharmonic terms in the vibrational potential [44]. The anharmonicity of the potential couples the optical modes to other vibrational modes of the lattice and therefore allows an optical mode to decay. Klemens considers the decay of a single optical mode ω_{opt} at the Γ-point ($\mathbf{k}_{opt} = 0$) into two acoustic modes with frequencies

ω', ω'' and wave vectors $\mathbf{k}', \mathbf{k}''$, with the relaxation rate $\hbar/\tau = \Gamma$.[1] Due to conservation of energy and momentum, the relations

$$\omega_{opt} = \omega' + \omega'' \tag{2.14}$$

and

$$\mathbf{k}_{opt} = \mathbf{k}' + \mathbf{k}'' = 0 \tag{2.15}$$

must be fulfilled. Since the full discussion of the interaction Hamiltonians and perturbation theory calculation is beyond the scope of this thesis, we are going to focus on the results and refer to the original publications of Klemens [46] and Balkanski *et al.* [47].
The probability for the decay increases with increasing occupation numbers N' and N'' of the acoustic states and the derived relaxation rate is proportional to the factor $(1 + N' + N'')$, which is the only temperature-dependent factor in the expression for the relaxation rate. In turn, in thermal equilibrium, the occupation numbers are proportional to the Bose-Einstein factor $n(\omega_{opt}, T) = \left[e^{\hbar\omega_{opt}/k_B T} - 1\right]^{-1}$. As an approximation, a decay process as shown in the dispersion relation $\omega(\mathbf{k})$ in Fig. 2.3 is considered, with the creation of two identical acoustic phonons $\omega'_{ac} = \omega''_{ac} = \omega_{opt}/2$ with opposite wave vectors $\mathbf{k}'_{ac} = -\mathbf{k}''_{ac}$. Then, also $N' = N''$ and the final expression for the relaxation rate is

$$\frac{\hbar}{\tau(T)} = \Gamma(T) = \Gamma(0) \cdot \left(1 + \frac{2}{e^x - 1}\right) \tag{2.16}$$

where $\Gamma(0)$ is the damping at T=0, and contains all temperature-independent terms and $x = \hbar\omega_{opt}/2k_B T$ [46]. The temperature-dependent phonon frequency

$$\omega(T) = \omega_0 + \Gamma(T) \tag{2.17}$$

where ω_0 is the pure harmonic phonon frequency, i.e., without anharmonic terms, can then be expressed as

$$\omega(T) = \omega_0 - C\left[1 + \frac{2}{e^x - 1}\right] \tag{2.18}$$

where the constant C describes the strength of the anharmonic decay [46, 47]. For our purposes, C is chosen to be positive, hence the minus sign. An

[1] The extended model, which includes three- and four-phonon processes is known as the Klemens-Hart-Aggarwal-Lax model.[46–48]

example of Equation 2.18 with typical values is shown in Figure 2.3. Note that for $T \to 0$, $\omega(T) \to \omega_0 - C$. Therefore it is emphasized that ω_0 is not the *observed* extrapolated frequency for $T = 0$, but rather the bare mode frequency if no anharmonic terms would be considered for the lattice potential. The formula in Eq. (2.18) will be used to fit the experimental data of $\omega(T)$ with ω_0 and C as optimization parameters for the fit. Only the data obtained for temperatures $T \geq 100$ K are used for the fitting procedure, since at lower temperatures SPC comes into play. The difference between the experimental data for $T \leq 100$ K and the Klemens model fit is then ascribed to spin-phonon coupling.

2.5 Spin-phonon coupling

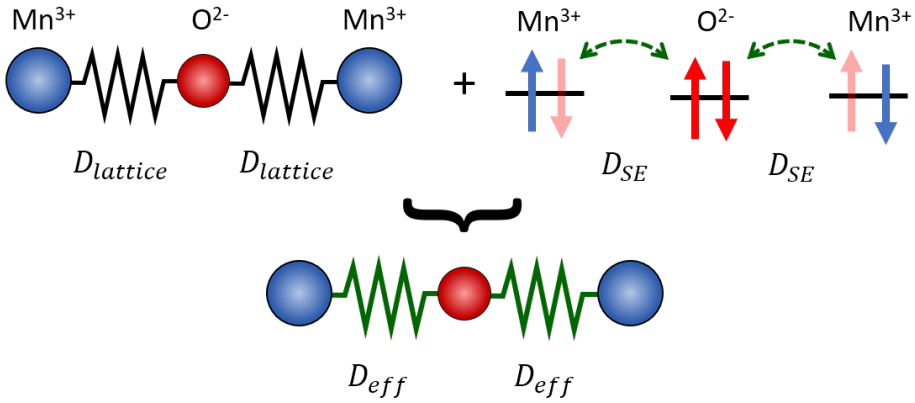

Figure 2.4: Illustration of a simple model for SPC: a Raman-active mode modulates the Mn-O-Mn bond lengths, coupled by the spring constant $D_{lattice}$. Since this modulates the exchange integral for the superexchange as well, the effective spring constant can be expressed as $D_{eff} = D_{lattice} + D_{SE}$.

The hallmark feature of spin-phonon coupling (SPC) is a renormalization of phonon frequencies relative to the intrinsic temperature dependence of the frequency of each phonon. The intrinsic behavior caused by the decay of optical phonons into acoustic phonons is caused by the anharmonicity of the lattice potential and was introduced in the previous section 2.4 in the framework of the Klemens model. When magnetic ions are involved in the lattice vibration, as in the vibrations of oxygen ions in the Mn-O-Mn bonds in $Eu_{1-x}Ho_xMnO_3$, also spin degrees of freedom need to be considered, as also the superexchange integral is modulated by the vibration. In section 4.4 we explore how the inverse DM interaction in $RMnO_3$ couples the spin ordering pattern closely together with the electric polarization, which is created by a uniform displacement of the oxygen ions in the Mn-O-Mn superexchange path. But also other mechanisms like charge order induced by magnetostriction can couple spin degrees of freedom with lattice degrees of freedom. All these additional effects may contribute to the frequency renormalization of the phonon, which becomes evident in the experimental results as a deviation of the expected frequency behavior from the Klemens model when the long range magnetic order develops. This frequency renormalization is called spin-phonon-coupling (SPC) and constitutes the main tool of investigation employed in this thesis.

For a basic understanding, we consider two magnetic ions, which in the case of $R\mathrm{MnO_3}$ would be $\mathrm{Mn^{3+}}$, connected by an intermediate oxygen ion. The methodology is also applicable for $A\mathrm{CrO_2}$, where two different magnetic ions are connected via oxygen, such as Cu-O-Cr as in $\mathrm{CuCrO_2}$. The chemical bond is abstracted as a mechanical spring with spring constant D, which mediates the restoring forces if the ions are displaced from their equilibrium positions (see Fig. 2.4). As a first step, we consider the situation in the paramagnetic state, where the magnetic moments are disordered and uncorrelated. Then, the restoring force is solely determined by the lattice potential $D = D_{lattice}$. At lower temperatures, when the magnetic moments are correlated, the magnetic superexchange comes into play. If the oxygen ion is displaced from its equilibrium position, the superexchange interaction is also subject to change due to the modulated interionic distances. In the mechanical model, the effective spring constant is then a combination of the lattice potential and the superexchange potential $D = D_{lattice} + D_{SE}$. As $\omega = \sqrt{D/m}$ in the classical mechanical model, the phonon frequency ω also changes with this additional contribution.

For a more quantitative approach, there exist quantum-mechanical models which aim to describe the spin-phonon coupling due to superexchange. In the following, we will review the model which was developed for SPC in the A-type AFM $\mathrm{LaMnO_3}$ by Granado *et al.*, based on the work of Baltensperger and Helman for EuO [8, 49]. The temperature-dependent frequency change $\omega_\alpha(T) - \omega_\alpha(T_0) \equiv \Delta\omega_\alpha(T)$ of a phonon mode enumerated by the index α is decomposed as:

$$\Delta\omega_\alpha(T) = (\Delta\omega_\alpha)_{latt} + (\Delta\omega_\alpha)_{anh} + (\Delta\omega_\alpha)_{ren} + (\Delta\omega_\alpha)_{SPC}. \tag{2.19}$$

The first term, $(\Delta\omega_\alpha)_{latt}$ is the change of phonon frequency due to lattice expansion or contraction because of change in the ionic binding energies. The second, $(\Delta\omega_\alpha)_{anh}$ is the intrinsic, anharmonic frequency shift at constant volume. This term is very important in the higher temperature range $T \gg T_N$ and described by the Klemens model (see section 2.4). The term $(\Delta\omega_\alpha)_{ren}$ describes effects of frequency renormalizations close to critical temperatures, when electronic states might change due to a phase transition. Eventually, $(\Delta\omega_\alpha)_{SPC}$ is the spin-phonon coupling, introduced by the modulation of the exchange integral between magnetic sites by lattice vibrations. To proceed, we need a model Hamiltonian which describes the magnetic interaction, an expression how the exchange integral is modulated by the ion displacements of the phonon modes and finally, how this is connected with the phonon

frequency. The Hamiltonian considered by Granado *et al.* is

$$H_{spin} = -\sum_{i,j>i} J_{ij} \langle \mathbf{S_i} \cdot \mathbf{S_j} \rangle, \tag{2.20}$$

with the superexchange integral J_{ij} and the spin correlation function $\langle \mathbf{S_i} \cdot \mathbf{S_j} \rangle$. The sum in j runs over the the nearest neighbors of the ith Mn ion. The effect of the superexchange modulation by the displacement $\mathbf{u}_k^\alpha(t)$ of the kth oxygen ion from its equilibrium position is approximated by a Taylor expansion up to second order of J_{ij}. The change ΔJ_{ij}^α is then given by:

$$\Delta J_{ij}^\alpha(\mathbf{u}_k^\alpha(t)) = \left[\mathbf{u}_k^\alpha(t) \cdot \nabla_k\right] J_{ij} + \frac{1}{2}\left[\mathbf{u}_k^\alpha(t) \cdot \nabla_k\right]^2 J_{ij}. \tag{2.21}$$

The potential energy of an harmonic oscillator is

$$U = \frac{1}{2} D_{eff} u(t)^2 = \frac{1}{2} m\omega^2 u(t)^2. \tag{2.22}$$

We substitute now $\omega = \omega_0 + \Delta\omega_{SPC}$ and $D_{eff} = D + D_{SPC}$ in Eq. (2.22) to decompose the SPC of D_{SPC} and the associated change to the phonon frequency $\Delta\omega_{SPC}$ from the other contributions, which are all absorbed into D and ω_0. Considering only the linear terms in $\Delta\omega_{SPC}$, we arrive at $(\Delta\omega_\alpha)_{SPC} = \frac{D_{SPC}}{2m\omega_0}$. This consideration of an harmonic oscillator of a single particle needs now to be adapted to the phonon at hand. The mass is replaced by the reduced mass μ_α which is relevant for the phonon mode α and we need to account for the individual directions of oxygen movements by writing D_{SPC} in tensor form:

$$(\Delta\omega_\alpha)_{SPC} = \frac{1}{2\mu_\alpha\omega_\alpha} \sum_k \hat{\mathbf{u}}_k^\alpha \mathbf{D}_{SPC} \hat{\mathbf{u}}_k^\alpha, \tag{2.23}$$

with $\hat{\mathbf{u}}_k^\alpha$ the unit vector of the elongation of the kth oxygen ion of the mode α. Now we can write down the final expression for the SPC-induced frequency shift identifying the Hamiltonian (2.20) with expression (2.22) and inserting it into equation (2.23) we obtain:

$$(\Delta\omega_\alpha)_{SPC} = -\frac{1}{2\mu_\alpha\omega_\alpha} \sum_k \left(\langle S_i \cdot S_j \rangle \left[\hat{\mathbf{u}}_k^\alpha(t) \cdot \nabla_k\right]^2 J_{ij} \right) \tag{2.24}$$

To obtain quantitative results, Granado *et al.* consider stretching modes of the oxygen octahedron, where all six oxygen ions vibrate along their Mn-O-Mn bond axis:

$$\begin{aligned}(\Delta\omega_\alpha)_{SPC} = -\frac{N}{2\mu_\alpha\omega_\alpha} \big(& 2\langle S_i \cdot S_j \rangle_{ac} \left[\hat{\mathbf{u}}_{O(1)}^\alpha(t) \cdot \nabla_{O(1)}\right]^2 J_{ac} \\ & + \langle S_i \cdot S_j \rangle_b \left[\hat{\mathbf{u}}_{O(2)}^\alpha(t) \cdot \nabla_{O2}\right]^2 J_b \big)\end{aligned} \tag{2.25}$$

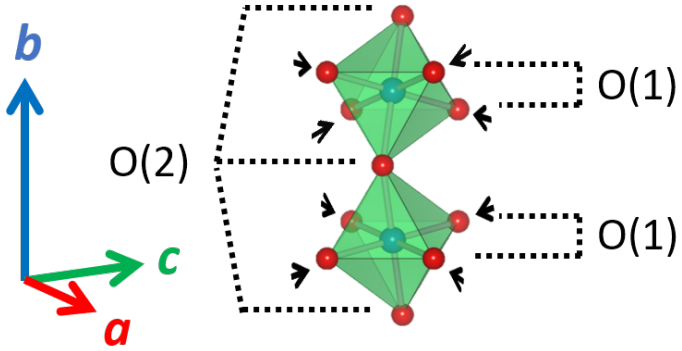

Figure 2.5: Mode pattern of the $R\mathrm{MnO}_3$ octahedron breathing mode $\mathrm{B}_{2g}(1)$. Only the oxygen ions of the octahedron labeled "O(1)" are in motion. The elongation vectors are within the ac-plane. The apical oxygen ions (along the b direction) are referred to as "O(2)".

where O(1) and O(2) are the in-plane and apical oxygen ions of the octahedron and the indices a, b, c are the crystal axis. The corresponding exchange constants are the ferromagnetic J_{ac} in the ac-plane and the antiferromagnetic J_b in the perpendicular direction [50]. They specifically consider the $\mathrm{B}_{2g}(1)$ mode (see Fig. 2.5). In this mode, only the O(1) oxygen ions of the ac-plane vibrate, which simplifies equation (2.25) to

$$(\Delta\omega_{B_{2g}(1)})_{SPC} = -\frac{1}{\mu_{B_{2g}(1)}\omega_{B_{2g}(1)}}\left(\langle S_i \cdot S_j\rangle_{ac}\frac{\partial^2 J_{ac}}{\partial u^2}\right). \tag{2.26}$$

This makes it possible to obtain quantitative values for $\frac{\partial^2 J_{ac}}{\partial u^2}$ by measuring $\omega(T)$ of the $\mathrm{B}_{2g}(1)$ mode over a large enough temperature range by Raman spectroscopy when some information is known about $\langle S_i \cdot S_j\rangle$. For LaMnO_3 considered in this article, which has a canted A-type AFM ground state, this is readily obtained through a mean-field approach via the sublattice magnetization within the ac plane [8, 51]

$$\langle S_0 \cdot S_1\rangle_{ac} \approx 4\left(\frac{M_{sublatt}(T)}{4\mu_B}\right)^2. \tag{2.27}$$

This procedure is however only applicable to the (canted) A-type order. If the magnetic order is of the cycloidal type, the sublattice magnetization is also zero within the ac plane. Laverdière *et al.* [52] extended this approach to the incommensurable magnetic phases, where the spin-spin correlation function is given by

$$\langle \mathbf{S}_i \cdot \mathbf{S}_j\rangle = K(T)\cos(2\pi\mathbf{k}\cdot\mathbf{r_{ij}}). \tag{2.28}$$

Here, $\mathbf{k}$ is the cycloid propagation vector and $K(T)$ is a temperature-dependent prefactor. The summation of spins is extended until the next nearest-neighbor (NNN) Mn-ions, to include spins at positions $\mathbf{r} = \pm 0.5\mathbf{a} \pm 0.5\mathbf{c}$ ($J_1 < 0$) as well as $\mathbf{r} = \pm\mathbf{a}$ ($J_2 > 0$) and $\mathbf{r} = \pm\mathbf{c}$ ($J_3 > 0$). With the propagation vector given as $\mathbf{k} = (k_a, 0, 0)$, the SPC-induced frequency shift is given by

$$\Delta\omega_{SPC} = \frac{K(T)}{\mu\omega}\left[2D_1\cos(\pi k_a) + D_2\cos(2\pi k_a) + D_3\right] \tag{2.29}$$

where $D_i = \partial^2 J_i/\partial u^2$. For the A-type AFM order, $\mathbf{k} = 0$ and $K(T) \propto \mathbf{M}^2_{sublatt}$ and under the assumption that $|D_1| \gg |D_2 + D_3|$ the same result as in Eq. (2.27) is obtained for that case. These equations are useful to qualitatively discuss their Raman spectroscopy results of their stoichiometric samples ranging from R=Pr, Nd, Sm, Eu, Gd, Tb, Dy, Ho until Y and therefore spanning the sample range from the A-type AFM, over the multiferroic up until the E-type AFM ground states. They report a significant contribution of $\Delta\omega_{SPC}$ only for the A-type AFM samples and conclude by Eq. (2.29), that SPC is weak or absent in incommensurate and E-type AFM ($\mathbf{k}_a = 0.5$) ordered materials. However, their samples with R=Eu, ...Y were all polycrystalline. In more recent results with monocrystalline samples [7, 53–55], including in this thesis, showed that monocrystalline samples show a clearly detectable SPC-shift also for the incommensurably magnetically ordered samples. However, as SPC of the $B_{2g}(1)$ decreases with decreasing R-site ionic radius, their argumentation still holds for the E-type AFM samples. While equation (2.29) is certainly more comprehensive than equation (2.27), it introduces more challenges to produce quantitative output. Instead of the sublattice magnetization $\mathbf{M}_{sublatt}(T)$, a new parameter $K(T)$ is used, although it could be identified with $\left(\frac{M_{sublatt}(T)}{4\mu_B}\right)^2$ for A-type AFM materials and probably approximated to some degree by it for materials close to the A-type AFM to cycloidal transition. The larger concern is, that the number of SPC coupling constants have increased from one to three, which makes it impracticable to extract values for the SPC coupling constants from Raman experiments. This issue is going to be addressed in the discussion of section 5.4.

2.6 The electromagnon - an introduction

The intimate coupling of magnetic and electric properties gives rise to a new elementary excitation in the multiferroic phase, dubbed the electromagnon (EM). It was observed for the first time in $GdMnO_3$ in the THz regime by Pimenov *et al.* [56] Typical energies are in the range of several tens of wavenumbers, usually 20-80 cm^{-1} [15, 16]. It can be thought of as a derivation of a magnon in a conventional magnetic material: the excitation of a magnon leads to oscillations of the spin system. However, the magneto-electric coupling leads also to oscillations of electric polarization. Therefore, the electromagnon is dipole active. To further understand the nature of the dipole activity of the electromagnon, it is mandatory to identify the microscopic origin how the spins couple to the electric polarization, i.e. the dynamical magneto-electric effect. Since the inverse DM interaction is seen as the key mechanism for the multiferroic order in $R\mathrm{MnO}_3$, it seemed natural to model the dynamical magneto-electric coupling also on the basis of the inverse DM interaction. Katsura *et al.* put forward models based on the inverse DM interaction and could succesfully explain the dipole activity of the EM [57, 58] and is now refered to as the Katsura-Balatsky-Naganosa (KBN) mechanism. However, the calculated EM response was much weaker than in the original experiment and subsequent experiments on other $R\mathrm{MnO}_3$ compounds confirmed this result [59, 60]. In addition, experiments showed, that if the spin cycloidal plane (and with it the electric polarization, see 4.2) is flipped, the selection rules of the EM did not flip accordingly, as would be the case for an EM with the KBN mechanism. Instead, the selection rules seemed to be bound to the lattice, instead of the cycloid [15]. A model proposed by Valdés Aguilar *et al.*, based on Heisenberg exchange coupling could account for this and could also explain the strong EM response [61]. Even more recent experiments suggest, that both, the KBN mechanism and the Heisenberg mechanism could play a role. Shuvaev *et al.* found that a part of the spectral weight of the EM follows the selection rules according to the Heisenberg mechanism, but there exists a smaller contribution to the spectral weight, which follows the behavior according to the KBN mechanism, when the spin cycloid is flipped [15].

While the infrared activity of the electromagnon was demonstrated thoroughly in FIR and THz spectroscopy and its dipolar character was also confirmed by the spectral weight transfer from the lowest-lying infrared phonon [62], there existed no experimental evidence of its activity in Raman spectroscopy and only recently, scarce publications on the EM activity in Raman spectra showed up [53]. To get a basic understanding of the Raman activity

of electromagnons, we are going give an introduction to how conventional magnons gain their Raman activity.

2.7 Raman activity of the electromagnon

2.7.1 First-order magnon scattering

The conventional Raman effect is described with second-order perturbation theory, where the incident photon excites an electron, which in turn scatters inelastically with a phonon via the interaction Hamiltonian $\mathbf{H}_{\text{e-lattice}}$ (Equation 2.8). Essentially, the scattering process is described similar like in the Feynman diagramm of Fig. 2.2, however, the scattering Hamiltonian $\mathbf{H}_{\text{e-lattice}}$ must be replaced to couple to the electromagnon. While the electromagnon becomes infrared active due to its electric dipole moment, it seems natural to assume that the "magnon" part becomes Raman active like a regular magnon. This paragraph shall give a short summary of the magnon Raman activity as outlined in Fleury and Loudon [63]: Historically, a first treatment was proposed by Bass and Kaganov by considering the magnetic dipole interaction between the spin system, represented by $\mathbf{S}$ and the magnetic component of the incident electromagnetic wave $\mathbf{h}$ [64]:

$$\mathbf{H}_{MD} = -g\beta \sum_i \mathbf{h_i} \cdot \mathbf{S_i} \tag{2.30}$$

But it fell short, as it did not predict the observed selection rules correctly, and the observed scattering efficiency was too low, to explain the experimental findings.
A mechanism, that predicted a much larger scattering efficiency, is the electric dipole interaction

$$\mathbf{H}_{ED} = -e \sum_i \mathbf{E}_i \cdot \mathbf{r}_i \tag{2.31}$$

where $\mathbf{E}_i$ is the electric field at the position $\mathbf{r}_i$ of the ion i. Although a magnon would not couple directly to the electric field, one can consider the following scattering process of dipole-allowed transitions in a magnetic ion: the ion in the ground state $|L = 0, J_z = S\rangle$, where L denotes the value of the angular momentum ($L = S, P, D... \equiv 0, 1, 2...$) and J_z stands for the z component of the total angular momentum J, is excited to one of the intermediate states $|1, S-1\rangle$,$|1, S+0\rangle$ or $|1, S+1\rangle$. These states are separated by the spin-orbit coupling $\lambda \cdot J_z$ and act as the virtual intermediate state. In the second scattering transition, the ion relaxes back to $|0, S+0\rangle$, but in the process

a magnon is created, effectively leaving the ion in the state with reduced spin of $S-1$ and the scattered radiation is red-shifted, which corresponds to the magnon energy quantum. The first-order (in terms of λ/E_0) scattering matrix element of this process is proportional to the spin-orbit coupling λ [63]:

$$M_i = \frac{\pi\hbar e^2\lambda\sqrt{\omega_1\omega_2 S}}{n_1 n_2 V}\left[\frac{\epsilon_1^z\epsilon_2^+ - \epsilon_1^+\epsilon_2^z}{(E_0-\hbar\omega_1)^2} - \frac{\epsilon_1^z\epsilon_2^+ - \epsilon_1^+\epsilon_2^z}{(E_0+\hbar\omega_2)^2}\right] \times \langle 0, S+0|z|1, S+0\rangle\langle 1, S-1|x-iy|0, S+0\rangle. \quad (2.32)$$

Using the spin lowering operator $S^-|0,S\rangle = \sqrt{2S}|0,S-1\rangle$ this can be recast into the effective interaction Hamiltonian for a ferromagnetic magnon

$$\mathbf{H}_{eff,FM}^{Stokes} = \Gamma\sum_i \left(E_1^z E_2^+ - E_1^+ E_2^z\right) S_i^- \quad (2.33)$$

where the indices 1 and 2 refer to the incident and scattered photons, ϵ and E to the polarization or electric field vectors, respectively, the x, y, z superscripts to linear polarization parallel to x, y and z and $+, -$ to right- and left-circular polarization in the xy plane. In Γ, all the prefactors and remaining matrix elements $\langle ...\rangle$ of Eq. (2.33) are absorbed, as they do not depend on a specific ion. Note, that $\Gamma \propto \lambda$. While this result applies for a ferromagnetic magnon, along the same line a very similar expression is obtained for the case of an antiferromagnetic magnon. The antiferromagnetic magnon, in contrast to the ferromagnetic magnon, has of course now two branches, corresponding to an increase or decrease of total spin to $S+1$ or $S-1$, while the ferromagnetic magnon has only one branch corresponding to the reduction of total spin to $S-1$. When the magnon is excited with linearly polarized light, the scattered light would be circularly polarized, the two AFM magnon branches having opposite helicity. The main conclusion here is, that the magnon disappears in the Raman spectrum when the polarization of incident and scattered (detected) photons in the experiment is chosen to be parallel (i.e. $E_1 = E_2$), as the polarization plane of the circularly scattered light is orthogonal to the incident linear polarized light.

2.7.2 Second-order magnon scattering

As with conventional Raman scattering on phonons, the scattering process of magnons can also be extended to the second order, with the creation or annihilation of two magnons. Because of the conservation of momentum, the wavevectors of the two magnons must be approximately of equal magnitude

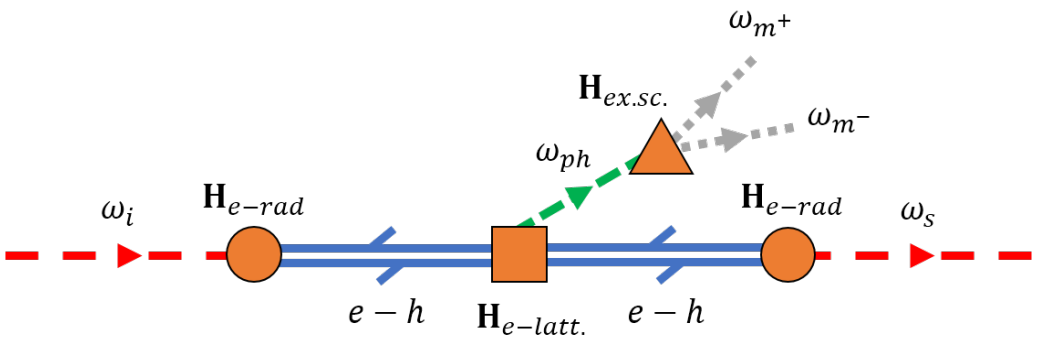

Figure 2.6: Exchange scattering mechanism mediated by a virtual phonon. The virtual phonon ω_{ph} is created like in first-order Raman scattering, but subsequently decays into two real magnons $\omega_{m^\pm}$.

with opposite sign, $\mathbf{k}_1 \approxeq \mathbf{k}_2$. Like with two-phonon scattering, it is more likely to occur for $\mathbf{k}$ vectors where the density of states is large. Thus, the two-magnon scattering occurs most likely for magnons close to the Brillouin zone boundary, where the dispersion relation is flat and the density of states is high. As this transition matrix element is of second order, it is proportional to $(\lambda/E_0)^2$ and because usually $\lambda \ll E_0$, the scattering probability should be much smaller. However, for an antiferromagnet there exists another mechanism, which is of second order, but unrelated to the electric dipole spin-orbit scattering. This mechanism is called exchange scattering and can be mediated in two different ways: with the participation of a virtual phonon or via an orbital excitation of the magnetic ion.

The phonon-mediated mechanism can be thought of as a two-step process. In the first step, the incident light undergoes a normal Raman scattering process, but with the creation of a *virtual* phonon. In the second step, this virtual phonon modulates the bonds between magnetic ions and therefore the exchange integral J and then decays into two magnons. The responsible term here is

$$\mathbf{H}_{ex.sc.} \propto \frac{\partial J}{\partial u} \Delta u S_i^- S_j^+ \tag{2.34}$$

with the normal coordinate of the vibration u and Δu the change in u introduced by the phonon. It is noted, that this effect is indeed of second order, as the created phonon is virtual, whereas in conventional first-order Raman scattering the created phonon is real. The scattering process involves an intermediate, virtual electronic state (as in first order Raman scattering), a virtual phononic state and eventually the real magnon pair, as illustrated in the Feynman diagram in Fig. 2.6. The second mechanism considers two

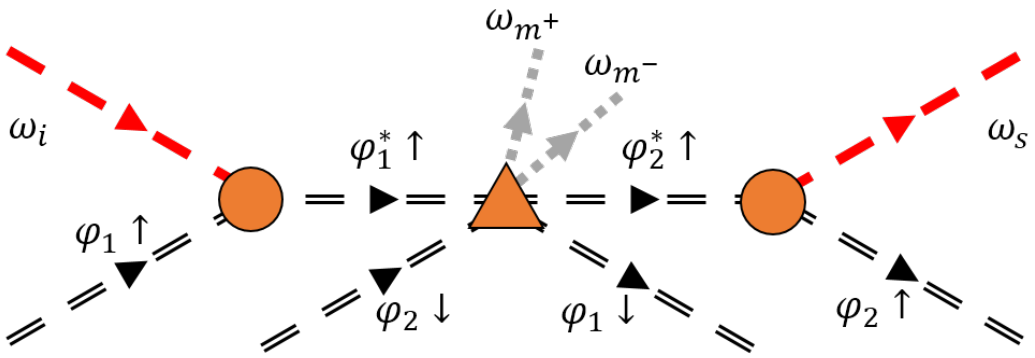

Figure 2.7: Exchange scattering mechanism mediated by electron hopping. In the beginning, the ion φ_1 is on the "spin up", the ion φ_2 on the "spin down" sublattice. Stars indicate that the ion is in an excited orbital state. On the second vertex, the electrons are exchanged between ions and two real magnons $\omega_{m\pm}$ are created.

magnetic ions in the antiferromagnet, illustrated in the Feynman diagram in Fig. 2.7. The first ion, φ_1, located on the "spin-up" sublattice is excited to a higher orbital state by the incident photon ω_i. The excited ion $\varphi_1^* \uparrow$ now interacts via exchange interaction with a second ion from the "spin-down" sublattice $\varphi_2 \downarrow$ by exchanging electrons so that φ_1 returns to the ground state orbital, while φ_2 is now excited. At the same time, because the spins of the respective sublattices are now flipped, two magnons $m^{\pm}$ are created. In the last vertex, $\varphi_2^* \uparrow$ relaxes to its ground state orbital under the emission of the scattered photon ω_s. It is noted, that the second-order two-magnon scattering process does not impose specific selection rules in contrast to the first-order one-magnon scattering process. However, selection rules might occur, depending on the symmetry of the magnetic ion(s) which is considered. This section gave an introduction to the Raman activity of conventional magnons, drawing a parallel to the electromagnon. It should be noted though, that the exact dynamics of the electromagnon are still not fully understood and different mechanisms might be at work. Recent publications on the infrared activity of the electromagnon draw a much more complicated picture of the infrared excitation mechanism [15, 16].

Chapter 3

Experimental setups

3.1 Micro-Raman setup

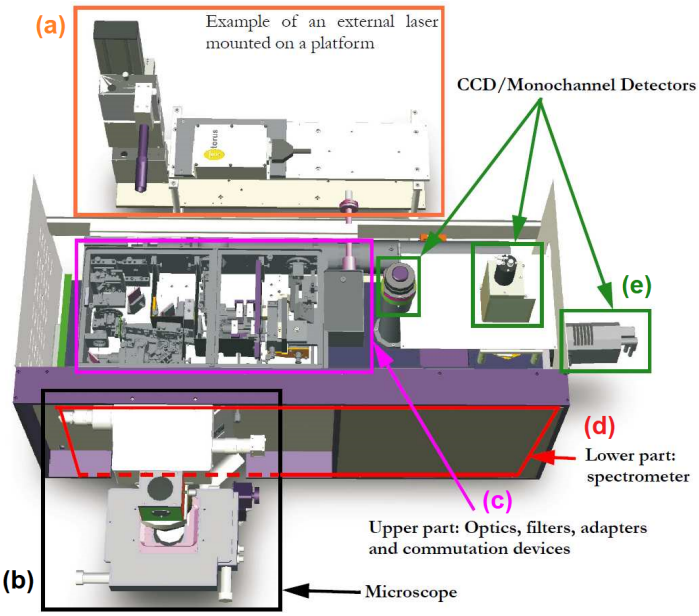

Figure 3.1: Illustration of the LabRAM HR800 spectroscopic apparatus. Adapted from [65].

During the course of this thesis, two setups for Raman spectroscopy were used. The first one, used for the temperature-dependent investigations, is the highly integrated Horiba LabRAM HR800 spectrometer. The spectrometer itself comprises of a housing which contains all necessary optics to guide the laser beam onto the sample, collect the scattered light and disperse the

signal with a single grating onto the detector. For excitation, a 20 mW HeNe laser with λ =632.8 nm and a frequency doubled, 80 mW Nd:YAG laser with λ=532.0 nm are available (Fig. 3.1(a)). The optical path (Fig. 3.1(c)) is equipped with a neutral density filter wheel, plasma-line cleanup filters and a $\lambda/2$ wave plate in the excitation path. The beam is directed into a modified confocal microscope (Fig. 3.1(b)), which focuses the exciting laser beam onto the sample and also collects the scattered light. As the microscope was used in conjunction with an LHe cold-finger optical cryostat, only the 50x ULWD (ultra-long working distance) objective could be used, to cover the relatively large distance between the objective lens and the sample surface through the cryostat windows. The cryostat is mounted to a motorized stage, which allows for manipulation with μm precision along the x-, y- and z-direction of the sample with respect to the focal point. The collected scattered light is guided through the Glan-analyzer (Fig. 3.1(c)) into the monochromator (Fig. 3.1(d)), which an achromatic Czerny-Turner monochromator with a focal length of 800mm. The grating is interchangeable, with gratings with groove densities of 1800 mm^{-1} and 600 mm^{-1} mounted on a motorized turret. In the last compartment (Fig. 3.1(e)), the spectroscopically fanned-out signal is focused onto a Peltier-cooled CCD detector with 1024x256 pixels of 26 μm edge length. As in any spectrometer with diffractive elements, the spectral resolution depends not only on the optical elements and the groove density of the grating, but also on the wavelength of the diffracted light. Long-wavelength light is diffracted stronger than short-wavelength light and therefore the spectral resolution per pixel is better for the 632.8 nm laser line than for the 532.0 nm line ($\approx$ 0.3 cm^{-1} versus $\approx$ 0.5 cm^{-1}) at the expense of a smaller spectral range per spectrum ($\approx$ 320 cm^{-1} versus $\approx$ 500 cm^{-1}).
To avoid local heating due to the high energy density in the focal point on the sample, the laser intensity is kept as low as reasonably possible by the application of neutral density filters. The measured laser power after the microscope, before entering the cryostat was always below 1 mW. Temperature control is achieved by maintaining a constant helium flow and applying the desired heat current provided by a heater close to the sample.

3.2 Magnet cryostat with triple monochromator

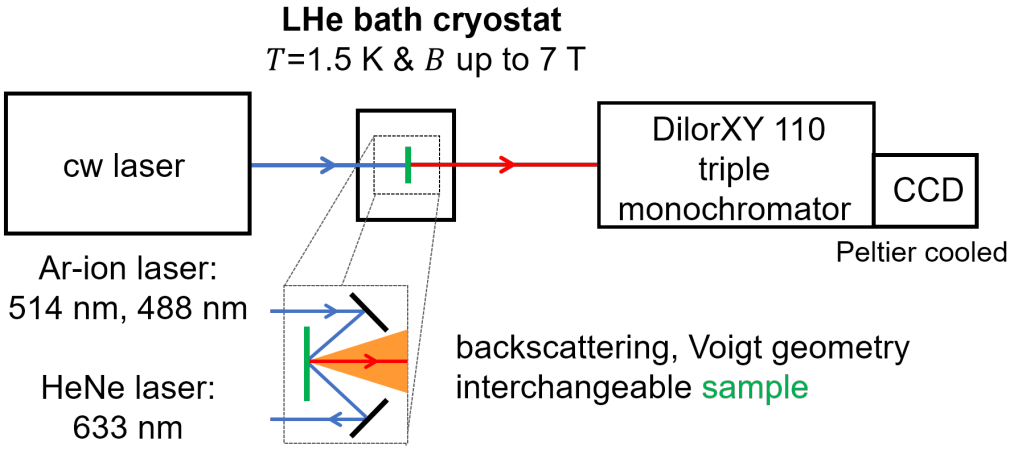

Figure 3.2: Magnetic-field liquid He bath cryostat with triple monochromator. The sample is mounted in the backscattering geometry, i.e. the incident and scattered light are approximately antiparallel.

The second setup used in this thesis for the magnetic-field dependent investigations consists of a Oxford Spectromag liquid-helium bath cryostat with achievable magnetic fields up to 7 T and a DilorXY 110 triple monochromator equipped with a Peltier cooled CCD camera. Amongst the choices for excitation are a 10mW HeNe laser with λ =632.8 nm and a tunable Ar-ion laser, which offers various discrete laser lines of which the 514.5 nm and the 488.0 nm lines were used. The output power depends on the intensity of the particular laser line, but range from several 10 mW to several watts. Plasmaline filters and neutral density filters are mounted onto an optical table and guided towards the backside windows of the cryostat. The sample holder inside the sample chamber is equipped with two mirrors. The first mirror reflects the beam onto the sample (see Fig. 3.2) in the so-called backscattering geometry, i.e. the incident and scattered light are approximately antiparallel. The second mirror redirects the beam which is directly reflected from the sample surface to reduce stray light being collected by the spectrometer. the Raman scattered light is collimated by a lens on the front side of the cryostat and guided to the spectrometer, where it is internally focused onto the entry slit.
The spectrometer is a DilorXY 110 triple monochromator, which means it

consists of three monochromators in series. The first two stages fulfill a different role depending on the mode of operation: in the additive mode, each monochromator stage disperses the light. The advantage of this mode is the strong effective dispersion of the spectrum, which results in high possible spectral resolution. In the subtractive mode, the first stage disperses the light. Then, the fanned-out image passes a slit, which cuts out a part of the spectrum. The second stage reverses the effect of the first stage. In effect, the first two stages thus act as a bandpass filter, with highly efficient extinction rate. Only the third stage is then responsible for the spectral dispersion. While the dispersion is thus lower than in the additive mode, the subtractive mode is crucial for experiments which require to observe Raman features very close to the laser line, as it allows highly efficient extinction of the laser, with steep flanks of the bandpass. Depending on the experimental situation, features shifted by as low as a few wavenumbers relative to the laser line can be observed, typically in the order of 5-10 cm^{-1}. This is by far better than commonly available longpass or bandpass Raman filters, which cut off the spectrum already at Raman-shifts in the order of 50 cm^{-1}.
The samples are mounted onto a sled, that allows to switch quickly between up to six samples without thermally cycling the system. The sample chamber is filled through a needle valve with liquid helium from the helium reservoir, which doubles as a cryopump to maintain in the insulating vacuum compartment a pressure lower than 10^{-7} mbar. As this is an optical experiment and the liquid helium in the sample chamber would constantly evaporate, a constant flux of bubbles would obstruct the experiment. Thus, the sample chamber is pumped to bring the helium into the suprafluid state below the lambda-point ($T_\lambda = 2.2K$). In this state, helium is a nearly ideal thermal conductor and the heat is distributed among the whole helium volume. A limited temperature control is possible by adjusting the vapor pressure within the sample chamber, with typical achievable temperatures of 1.2-2 K.

Part I

The orthorhombic perovskites $Eu_{1-x}Ho_xMnO_3$

Chapter 4

Introduction to the orthorhombic $R\mathrm{MnO_3}$ perovskites

In this chapter of the thesis, we will focus on the orthorhombically distorted perovskites with the chemical formula $\mathrm{ABX_3}$. More specifically, the A-site ion is a rare-earth ion R^{3+}, B is a manganese ion $\mathrm{Mn^{3+}}$ and X is an oxygen ion $\mathrm{O^{2-}}$. To understand the usefulness and versatility of the orthorhombic manganites as a model system for the research of multiferroic properties, an introduction to the crystallographic and magnetic structure will be given in the following. Starting from the undistorted cubic perovskite structure, the most important mechanisms at work in $R\mathrm{MnO_3}$ are introduced until we eventually arrive at the actual crystallographic structure of $\mathrm{Eu_{1-x}Ho_xMnO_3}$ (section 4.1). In the subsequent section, section 4.2, the magnetic structure is introduced, starting with the A-type antiferromagnetic order of $\mathrm{LaMnO_3}$ and finishing with the characteristic cycloidal spin order of the multiferroic $R\mathrm{MnO_3}$ compounds. After an introduction to multiferroicity in section 4.3, the connection between cycloidal spin order and multiferroicity in $R\mathrm{MnO_3}$ is established in section 4.4 by considering the mechanism of the inverse Dzyaloshinskii-Moriya interaction.

4.1 Crystal structure

The crystalline structure of $R\mathrm{MnO_3}$ is a derivate based of the cubic mineral Perovskite ($\mathrm{CaTiO_3}$). For a better understanding, we assume $R\mathrm{MnO_3}$ to be in this undistorted cubic perovskite structure (Figure 4.1), as it is realized in $\mathrm{SrTiO_3}$ and $\mathrm{BaTiO_3}$ as a starting point and apply the orthorhombic distortions step by step until we arrive at the orthorhombic "perovskite-like" structure of $R\mathrm{MnO_3}$. In this cubic unit cell, the Mn-ion is located in the

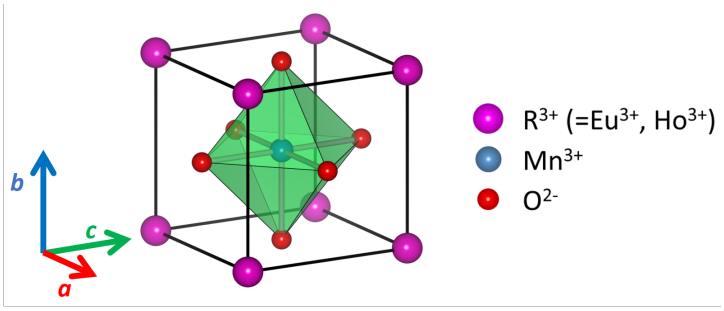

Figure 4.1: Unit cell of the undistorted, ideal cubic perovskite as realized in $SrTiO_3$ or $BaTiO_3$. The R-site cation is represented as purple, oxygen anions as red spheres and on the position of the titanium cation, manganese is located at the center, represented as a blue sphere. The green triangles emphasize the octahedron that is formed by the central Mn ion and the six nearest-neighbor oxygen ions.

center of the unit cell and surrounded by six oxygen ions, which form an octahedron around the Mn-ion. As the oxygen ions are centered on the faces of the unit cell, neighboring octahedra are sharing corners with each other, thus forming an three dimensional network. The R-site ions are located on the corners of the unit cell, therefore in-between the octahedra. This octahedron will be referred to as the MnO_6 octahedron, as Mn has a coordination number of 6. To arrive at the actual orthorhombic perovskite structure, the symmetry needs to be lowered. There are two main causes, which introduce distortions to the cubic structure: The first being the size of the R-site ion and the second being the Jahn-Teller distortion of the octahedron.

4.1.1 Impact of the R-site ionic radius

The distortion introduced to the lattice by size effects of the R-site ion is of purely geometric origin. Let us consider two distances in the cubic unit cell under the assumption that all ions touch each other: the face diagonal R-O-R which translates to $2(r_R + r_O) = \sqrt{2}a$, and the distance between opposing oxygen ions on the faces: O-Mn-O, i.e. $2(r_O + r_{Mn}) = a$, where r_i denotes the ionic radius of the respective ion and a is the lattice constant. Both equations are divided by each other to obtain:

$$t = \frac{r_R + r_O}{\sqrt{2}(r_{Mn} + r_O)}. \tag{4.1}$$

This is the Goldschmidt's tolerance factor t. It includes also the possibility that the respective ionic radii in the nominator and denominator do not add

up to a and therefore that the relation can lead to values of $t \neq 1$. With it, it can be estimated if given ions are compatible with the cubic crystal structure. If the radius of the R-site ion is reduced from the ideal value for $t = 1$, the tolerance factor is also decreased. The cubic structure is stable in the range of $0.89 < t \leq 1$. The orthorhombic structure is stable for $0.8 < t < 0.89$. For even lower values, the ilmenite structure becomes stable [66]. Below $t < 0.89$, the octahedra are going to tilt to fill space. The tilt operations consist of an in-phase tilt about the [010] axis and an out-of-phase tilt about the [101] axis as shown in Fig. 4.2. This kind of distortion from

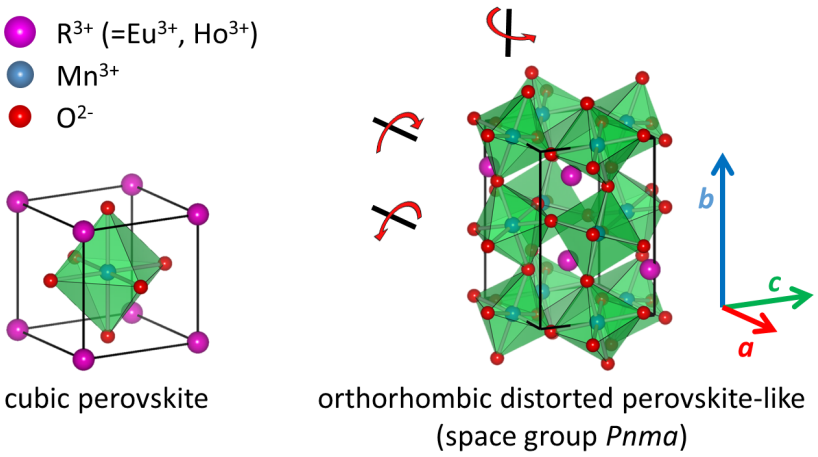

Figure 4.2: Symmetry reduction from the cubic to the orthorhombic *Pnma* structure by in-phase rotation of octahedra about the [010] axis and out-of-phase rotation about the [101] axis. The original cubic axes are rotated by 45 °. The a- and c- axes are elongated by a factor of $\sqrt{2}$, while the b-axis is elongated by a factor of 2.

the cubic perovskite to the orthorhombic perovskite is called $GdFeO_3$-like, as it shares the same kind of octahedron tilt. This symmetry reduction can be considered as a combination of four basic distortions according to Abrashev *et al.* [67]. The first two are related to the octahedron tilt caused by size effects of the R-site ion: an out-of-phase tilting of the neighboring MnO_6 octahedra around the cubic [101] axis $D_{[101]}$ and an in-phase tilt around the cubic [010] axis $D_{[010]}$. The third, the Jahn-Teller distortion D_{JT} is discussed in subsection 4.1.2 and eventually, a shift of the R^{3+} cations D_R. The new crystal axes can be obtained by a rotation of the cubic a- and c-axes by 45 °around the b-axis and multiplication by a factor of $\sqrt{2}$, while the b-axis is elongated by a factor of 2 (space group *Pnma*). The resulting unit cell has therefore a four times larger volume, containing 20 atoms. The strength of

the distortion is closely related to the ionic radius of the R^{3+} ion. Among the lanthanides, La^{3+} has the largest ionic radius with $r_{La} = 1.22$ Å and shows the weakest octahedron tilt, with a Mn-O-Mn bond angle of about 155 °. Proceeding through the lanthanides from La to Lu, the ionic radius shows a pronounced decrease due to the so-called *lanthanide contraction*. In the lanthanides, with increasing atomic number, electrons are added to the $4f$ shell, which have a low efficiency for screening the outer $5s$ and $5p$ shells from the nuclear charge. In the $R\mathrm{MnO_3}$ series, the orthorhombic structure crystallizes from $\mathrm{LaMnO_3}$ up until $\mathrm{DyMnO_3}$, corresponding to Goldschmidt factors of $t = 0.86$ to $t = 0.81$, respectively [68]. With even smaller ions, like Ho^{3+} ($t = 0.80$), the samples grow in the hexagonal crystal structure. However, with special preparation techniques under pressure, also $\mathrm{HoMnO_3}$ can be synthesized in the orthorhombic structure, as the orthorhombic unit cell has a smaller volume than the hexagonal unit cell [6, 69–71]. The dependence of the orthorhombic distortion on the ionic radius of the R^{3+} ion can be used to systematically choose suitable R-site ions to achieve the desired octahedron tilt or, conversely, the Mn-O-Mn bond angle ϕ. This can be done in discrete steps as, for example $\mathrm{LaMnO_3}$, $\mathrm{SmMnO_3}$, $\mathrm{EuMnO_3}$, $\mathrm{TbMnO_3}$, ... On the other hand, finer tuning is possible by partial substitution of the R-site ion A with another ion B, to form solid solutions of the type $\mathrm{A_{1-x}B_xMnO_3}$. The lattice is able to tolerate the foreign ions and incorporate them into the structure without additional unwanted lattice distortions. It behaves, as if there is an R-site ion with a single "average" radius, which is the weighted average of the employed ions A and B. The effective radius of the R-site ions can therefore be described as:

$$r_{eff} = (1 - x) \cdot r_A + x \cdot r_B \tag{4.2}$$

In this work, we consider the $\mathrm{Eu_{1-x}Ho_xMnO_3}$ system with $x \leq 0.5$, which covers a range of non-multiferroic ground states for $x \leq 0.15$ and multiferroic ground states with two distinct directions of spontaneous polarizations, depending on the Ho concentration x. This will be discussed further in section 4.4.

4.1.2 Jahn-Teller effect

The Jahn-Teller effect describes the elongation and/or contraction of bond lengths due to the geometry of the crystal field. Here, we consider the $3d$-shell of Mn in an octahedral crystal field created by the six nearest-neighbor oxygen ions, as depicted in Fig. 4.3. While in the free atom, the d-orbitals are fivefold degenerate, in the octahedral environment the degeneracy is partially

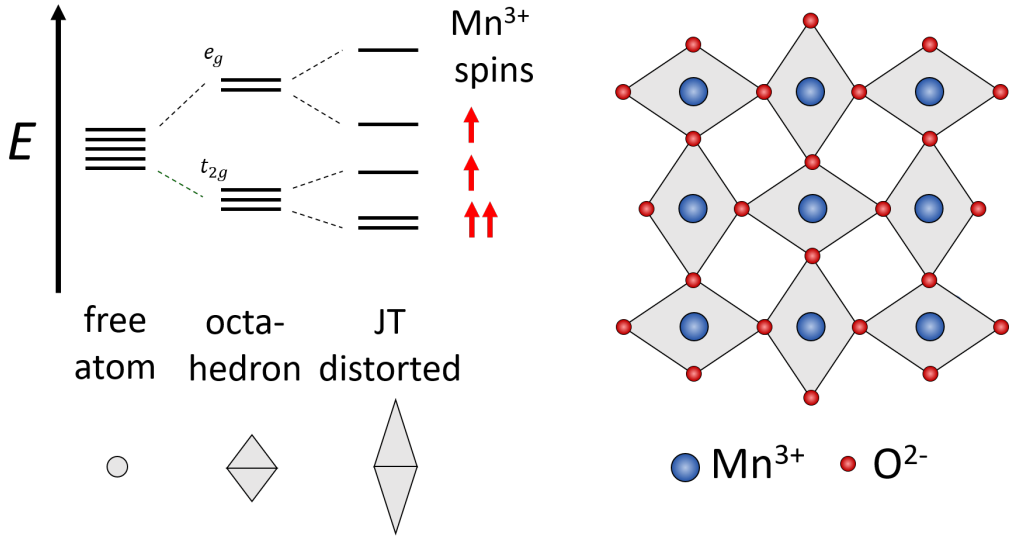

Figure 4.3: Effect of the Jahn-Teller distortion onto the MnO_6 octahedra. The cooperative Jahn-Teller distortion leads to a pattern of alternating MnO_6 octahedra orientation.

lifted and the orbitals split up into two groups of degenerate orbitals: the d_{xy}, d_{yz} and d_{xz} orbitals, which point in-between the oxygen positions and have a lower overlap with the oxygen $2p$ orbitals and the $d_{x^2-y^2}$ and d_{z^2} orbitals, which point towards the oxygen ions and therefore have a larger overlap with the oxygen orbitals. The former are grouped together to the threefold degenerate t_{2g} orbitals and the latter are grouped together to the twofold degenerate e_g orbitals. The t_{2g} orbitals are energetically more favorable than the e_g orbitals, because of the lower Coulomb repulsion of Mn^{3+}-$3d$-electrons by the O^{2-} $2p$ electrons (see Fig. 4.3). In the case of partially filled orbitals, it is possible to reduce the total energy by further reducing the symmetry. In the $R\mathrm{MnO_3}$ systems considered here, the manganese ion Mn^{3+} has four valence electrons, which need to be distributed among the $3d$ orbitals. In general, this can be done in two different ways: in the high-spin configuration, all spins are aligned in parallel, which means every occupied orbital is only occupied by one electron: The first three electrons occupy the three t_{2g} orbitals, while the fourth electron occupies one of the two e_g orbitals. The other possibility is the low-spin configuration. In this case, the energetically lower t_{2g} orbitals are filled first, before occupation of the e_g starts. This means all four electrons are located in the t_{2g} orbitals, with one orbital being doubly occupied with antiparallel spins. Which of the two spin configurations is realized depends on two competing interactions. On the one hand, there is

an energy cost associated to the Coulomb repulsion between electrons when a second electron is introduced into an already occupied orbital. On the other hand, there is an energy cost associated to the crystal-field splitting if one electron is placed in the higher e_g orbitals instead of the lower t_{2g} orbitals. This is also referred to as Hund's coupling. If Hund's coupling is dominant, this results in Hund's first rule: orbitals are filled up at first by single occupation of electrons with parallel spin before orbitals are doubly occupied with antiparallel spin. Whichever energy scale is dominant, decides if the ion is in the high-spin or low-spin configuration. In the rare-earth manganites, the Hund's coupling strength J_H is usually a factor of about 2 larger than the crystal-field splitting energy ($J_H \approx 2 - 3\,eV, \Delta_{cf} \approx 1.5\,eV$[72, 73]) and therefore Mn^{3+} is in the high-spin state in $R\mathrm{MnO_3}$. Still, the thus obtained configuration is degenerate, as the last electron can be in either of the e_g orbitals. Degenerate ground states are in general susceptible to symmetry breaking. The reduction of symmetry allows to reduce the energy of the *occupied* states by shifting the energy levels in such a way, that the total energy of *all* states remains unchanged. Here, the reduction of symmetry is achieved by distorting the MnO_6 octahedron according to Fig. 4.3 by elongating the octahedron along one direction of O-Mn-O bonds and contraction along the other two directions of bonds. This splits the t_{2g} and e_g even further up and now the degeneracy of the ground state is fully lifted. Note, that when the splitting occurs, the energetic center of gravity is not changed. The t_{2g} orbitals splits into one upper level with $+2/3$ of the splitting energy and two lower orbitals with $-1/3$ of the splitting energy, relative to the original position of the t_{2g} orbitals. The same holds for the e_g orbitals with $\pm 1/2$ of the splitting energy. It becomes now clear, that the total energy of all orbitals combined remains unchanged. However, as the highest orbital is unoccupied, the resulting distorted ground state is energetically beneficial. Due to the staggered distribution of d orbitals in $R\mathrm{MnO_3}$ the cooperative Jahn-Teller distortion leads to the pattern of alternating octahedra orientations as shown in Figure 4.3, right hand side.

4.2 Magnetic order in $R\mathrm{MnO}_3$

Now, that the crystalline structure has been established, a discussion of the magnetic mechanisms that lead to the various patterns of magnetic order in the $R\mathrm{MnO}_3$ compounds is in order. This section will introduce the basic concepts of how the magnetic moments of the Mn^{3+} ions interact with each other. As the details of magnetic interactions and the resulting magnetic ground state can be arbitrarily complex, the explanation of the sign of magnetic exchange in $R\mathrm{MnO}_3$ in this work is going to be restricted to a set of rules, which are widely used and very successfully applied in the orthorhombic rare-earth manganites. This set of rules, termed the Goodenough-Kanamori-Anderson (GKA) rules, will enable us to achieve a qualitative understanding of the different exchange paths in $R\mathrm{MnO}_3$. We will see, that the $R\mathrm{MnO}_3$ systems (for example R= La, Sm, Eu, Gd, Tb, Dy, Ho) are frustrated magnetic systems, which can support exotic patterns of magnetic order. This, in turn, will lead us to the role of the Dzyaloshinksii-Moriya interaction and magneto-electric coupling that eventually determines the multiferroic properties in this class of material systems. Since this section considers electron hopping, it relies on terms and ideas of the Hubbard model. A detailed explanation of the Hubbard model is given in appendix A.

4.2.1 Goodenough-Kanamori-Anderson rules

To achieve a qualitative understanding of the magnetic interactions, a set of rules, termed the Goodenough-Kanamori-Anderson (GKA) rules has been established [74, 75]. By simply considering the crystal and orbital geometry, combined with the occupation configuration of the considered orbitals, it is possible to predict the sign of exchange interaction between two magnetic ions. The basic assumptions for the rules are as follows:

- During an electron transfer between orbitals, the spin is conserved.
- The Pauli exclusion principle is applied. Transfer of electrons between singly occupied orbitals with parallel spins is forbidden.
- The spin-spin exchange interaction within an ion is ferromagnetic ($= \hat{} J_H$).

The third rule implies that Hund's coupling is dominant, thus all spins in singly-occupied orbitals within one ion are aligned in parallel. Together with these basic principles, we examine two rules in particular, that apply to $R\mathrm{MnO}_3$. We consider two Mn^{3+} ions in the high-spin configuration. Their

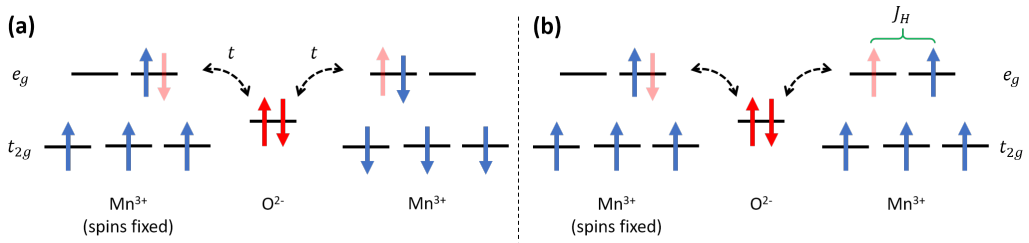

Figure 4.4: Visualization of the GKA rules for superexchange between two Mn^{3+} ions via an intermediate oxygen ion. The hopping is represented with the exchange integral t. The hopping electrons originating from the oxygen ion have to overcome the on-site Coulomb repulsion U on the manganese ion. (a): GKA rule for electron hopping between singly occupied or empty Mn-orbitals. This leads to an antiferromagnetic coupling between the Mn-ions. (b) GKA rule for electron hopping between one singly-occupied and one empty orbital. The additional ferromagnetic Hund's coupling J_H between the hopping electron and the right-hand-side Mn-spin leads to an ferromagnetic superexchange coupling between the Mn-ions.

spins interact by superexchange interaction via an intermediate O^{2-} ion. We are always going to assume that the spin of the first manganese ion is fixed and then we establish how the spin of the second ion would be aligned.
First, we consider the GKA rule that applies for the superexchange between two singly occupied Mn^{3+} orbitals, visualized in Fig. 4.4(a). Note, that the same rule applies also for the superexchange between two empty orbitals. The system's energy can be lowered by virtual hopping of O^{2-} ions into orbitals of the Mn^{3+} ions. The orbitals of both ions are thus shared by the electron, which leads to an admixture of both orbitals into this electron's wavefunction (hybridization). The kinetic energy of the electron is reduced. This is represented by the transfer integral t. On the other hand, the electron gains potential energy to overcome the Coulomb repulsion on the manganese site (represented by U). Only the electron with antiparallel spin with respect to the fixed manganese spin can hop to the fixed spin. In order for the second hopping electron to be able to be transferred into the orbital of the other manganese ion, that ions spin must align antiparallel to the fixed manganese spin. The energy gained is $\Delta E = -\frac{2t^2}{U}$.

The second GKA rule visualized in Fig. 4.4(b) applies to hopping between one singly occupied orbital and one empty orbital. The electron hopping to the singly occupied target orbital with fixed spin needs to be the electron with antiparallel spin. Since the target orbital is now unoccupied, the sec-

ond electron is allowed to hop independently of the spin alignment of the second manganese ion. However, if the spin of the second manganese ion aligns parallel to the hopping electron's spin, the Coulomb repulsion is reduced by Hund's coupling J_H due to the ferromagnetic intra-atomic coupling. Therefore, in this case, ferromagnetic alignment of the manganese spin is favored, with an energy reduction of $\delta E = -\frac{2t^2}{U-J_H}$. In the specific case of the Mn-O-Mn superexchange in $R\mathrm{MnO_3}$ the occupation (or non-occupation) of face-to-face orbitals of neighboring Mn ions determines whether case (a) or case (b) of Figure 4.4 is applies.

4.2.2 The A-type antiferromagnetic order

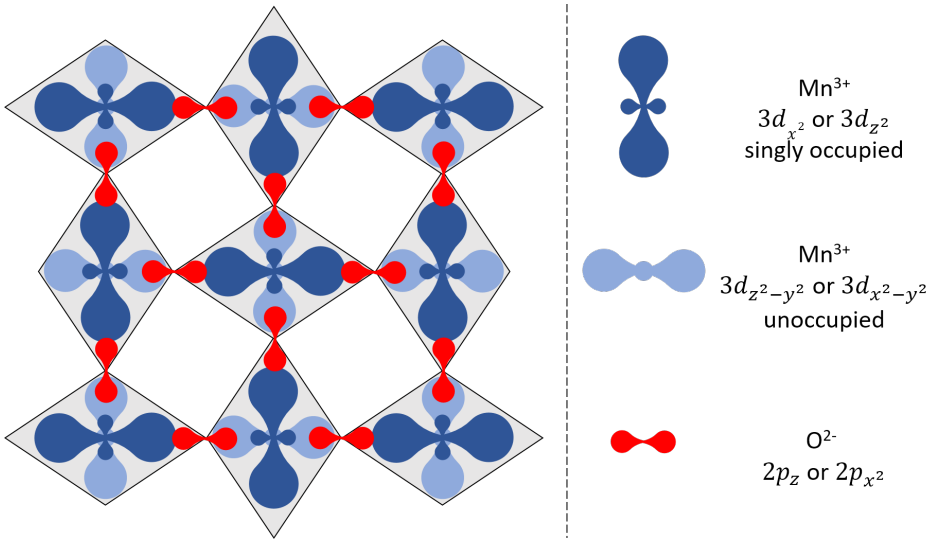

Figure 4.5: Octahedron- and orbital orientation in the ac-plane of $R\mathrm{MnO_3}$. The Mn-O-Mn bonds are alternating between singly occupied $3\mathrm{d}_{x^2}$ ($3\mathrm{d}_{z^2}$) and an unoccupied $3\mathrm{d}_{z^2-y^2}$ ($3\mathrm{d}_{x^2-y^2}$) orbitals. The superexchange is FM.

The GKA rules established in subsection 4.2.1 can now be applied to the unit cell of the orthorhombic $R\mathrm{MnO_3}$ family. We recall, that the cooperative Jahn-Teller distortion of the $\mathrm{MnO_6}$ octahedra leads to a pattern, where the octahedra are oriented in an alternating fashion as shown in Fig. 4.3. As a consequence, within the ac-plane, the Mn-O-Mn bonds are also alternating between one singly occupied $3\mathrm{d}_{x^2}$ ($3d_{z^2}$) and an unoccupied $3\mathrm{d}_{z^2-y^2}$ ($3\mathrm{d}_{x^2-y^2}$) orbital. This is visualized in Fig. 4.5. Along the a- and c-direction, the GKA rule for superexchange between singly occupied and unoccupied orbitals applies and therefore the superexchange interaction along those directions is

ferromagnetic. Along the b direction, the Mn $3d_{y^2}$ orbitals are always singly occupied. The superexchange interaction is antiferromagnetic. This is further visualized in the three-dimensional depiction in Fig. 4.6. The resulting

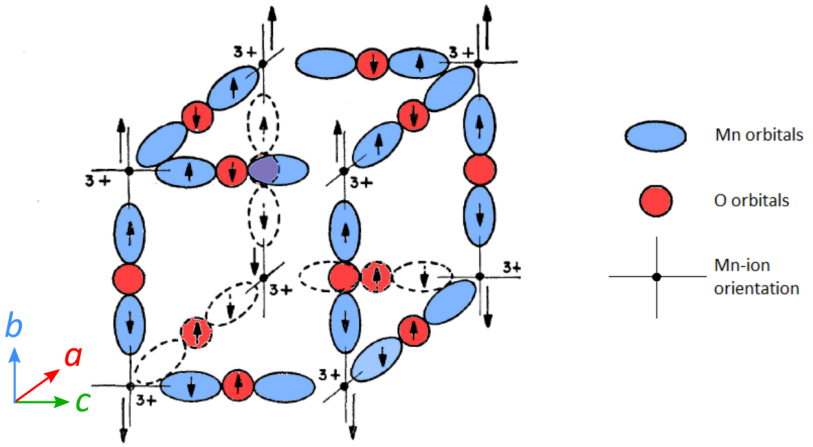

Figure 4.6: Three-dimensional orbital orientation adapted from [74] for orthorhombic $R\mathrm{MnO_3}$. Along the b direction, the Mn-orbitals are always oriented identically and the superexchange takes place between two singly occupied orbitals. The resulting interaction is antiferromagnetic. Within the ac plane the Mn orbital orientation alternates, so that one singly occupied Mn orbital interacts via superexchange with an unoccupied Mn orbital. The interaction is therefore ferromagnetic.

situation is therefore as follows: within the ac-plane, the spins are ferromagnetically coupled, favoring parallel in-plane alignment, while the plane-to-plane coupling along b is antiferromagnetic in nature, favoring antiparallel alignment. The resulting magnetic structure is the so-called A-type antiferromagnetic order shown in Fig. 4.7 with ferromagnetically ordered layers of spins stacked antiferromagnetically on top of each other.

Beside the exchange which was discussed up to now, a further type has to be considered, which is referred to as antisymmetric exchange. Although this is discussed in more detail in section 4.4, it will be anticipated here briefly. For this, we consider the cluster of two magnetic ions connected via a ligand ion as shown in Figure 4.8. The bond angle is $\neq 180°$. The antisymmetric exchange originates from spin-orbit coupling and its Hamiltonian can be written as

$$H_{DM} = \mathbf{D}_{ij} \cdot (\mathbf{S}_i \times \mathbf{S}_j) \tag{4.3}$$

where the Dzyaloshinskii-Moriya vector $\mathbf{D}_{ij}$ is proportional to $\mathbf{r}_i \times \mathbf{r}_j$. This can also be rewritten as $\mathbf{D}_{ij} \propto \mathbf{r}_{ij} \times \mathbf{x}$, see Figure 4.8. For $\mathbf{D}_{ij} \neq 0$ the

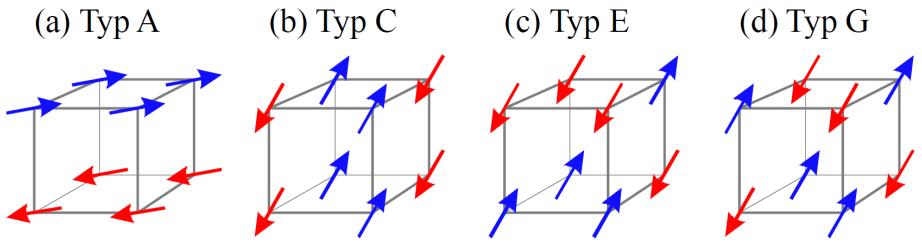

Figure 4.7: Several possible antiferromagnetic order patterns for a simple cubic lattice: (a) A-type, layer- ("**a**rea"-) like; (b) C-type, **c**hain-like (c) E-type, zig-zag pattern (d) G-Type, antiferromagnetic in every direction. Adapted from Ref. [76].

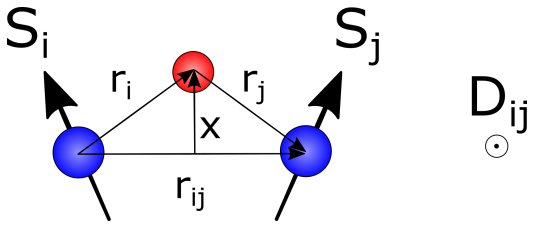

Figure 4.8: Illustration of the orientation of spin- and spatial vectors used in Eq. (4.9) and the accompanying text. In this example, the Dzyaloshinskii-Moriya (DM) vector D_{ij} points into the image plane.

term $\mathbf{S}_i \times \mathbf{S}_j$ obviously favors orthogonal alignment of spins. This leads to a canting of the spins away from their (anti-)parallel (anti-)ferromagnetic orientation. The result is the canted A-type antiferromagnetic structure (often abbreviated as c-AFM) as it is realized for example in $LaMnO_3$, $SmMnO_3$ or $EuMnO_3$ [6].

4.2.3 Incommensurable magnetic order

Until now, we have discussed the magnetic properties for $R\mathrm{MnO}_3$ with relatively large R-site ions like La^{3+}, Pr^{3+}, Nd^{3+}, Sm^{3+} and Eu^{3+}, which corresponds to a relatively small orthorhombic distortion. As the orthorhombic distortion increases for smaller R-site ions like Gd, Tb or Dy, the FM superexchange interaction in the ac plane is weakened as the transfer integral is reduced due to the inclination, while the AFM superexchange along the b-direction is strengthened by reducing the Mn-O-Mn bond angle, bringing the Mn ions closer together with respect to that interaction path. However, according to [6], a simple consideration of nearest neighbor (NN) superexchange is not sufficient to appropriately describe the magnetic structure in

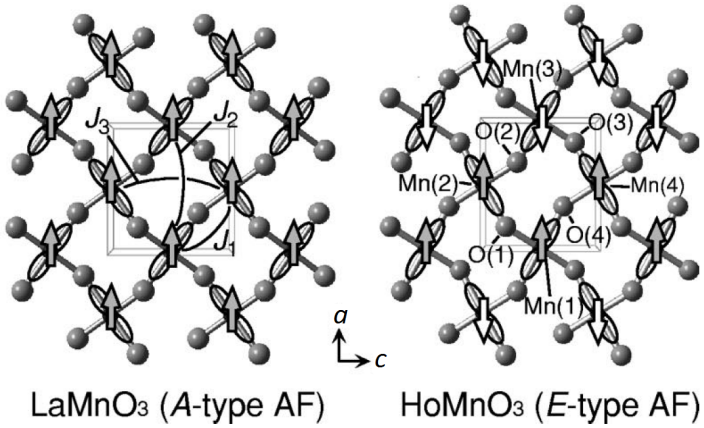

Figure 4.9: Nearest- and next-nearest neighbor interactions in the ac plane. Due to the increased octahedron tilt the balance of NN and NNN interactions is altered, which eventually turns the A-type FM order into the E-type AFM order with "zig-zag" patterns in the ac plane. Adapted from [6].

the multiferroic range for small R-site ions between Eu^{3+} and Ho^{3+}, which show a considerable orthorhombic distortion. In Fig. 4.9, it becomes clear, that due to the orthorhombic distortion, the distance between O(2) and O(4) is reduced from ≈ 3.4 Åfor $LaMnO_3$ to ≈ 3.0 Åfor $HoMnO_3$ [77]. Due to the staggered orientation of orbitals, the AFM next-nearest-neighbor (NNN) Mn-O-O-Mn interactions become inequivalent. The interaction between the Mn(1) and Mn(3) ion in Fig. 4.9 becomes stronger than the interaction between the Mn(2) and Mn(4) ion. It is therefore the Mn(1)-O-O-Mn(3) NNN AFM superexchange, which introduces spin frustration into the otherwise FM NN interaction within the ac plane. This is substantiated by experimental results, which show, that the Néel-temperature T_N is reduced from ≈ 140 K in $LaMnO_3$ to ≈ 50 K in $EuMnO_3$. If we recall section 4.1.1, with smaller R-site ionic radius, the Mn-O-Mn bond angle is also subject to change. From the $T-\phi$ phase diagram of $RMnO_3$ in Figure 4.10 we can see, that this angle decreases from 155° in $LaMnO_3$ to 147° in $EuMnO_3$. It is therefore possible to tune the magnetic interactions within the $RMnO_3$ system by appropriately choosing the R-site ion.
We already saw, that for larger R-site ions (La^{3+} to Eu^{3+}), the magnetic ground state is the A-type AFM pattern ($T = 0$), where in the ac-plane the FM interaction is dominant. On the other hand, for very small R-site ions like Ho^{3+}, the in-plane NNN AFM interaction is strong enough to drive the system into the E-type AFM (a type of "up-up-down-down" AFM order) order. Now, within the ac-plane the spins form "zig-zag" lines of parallel

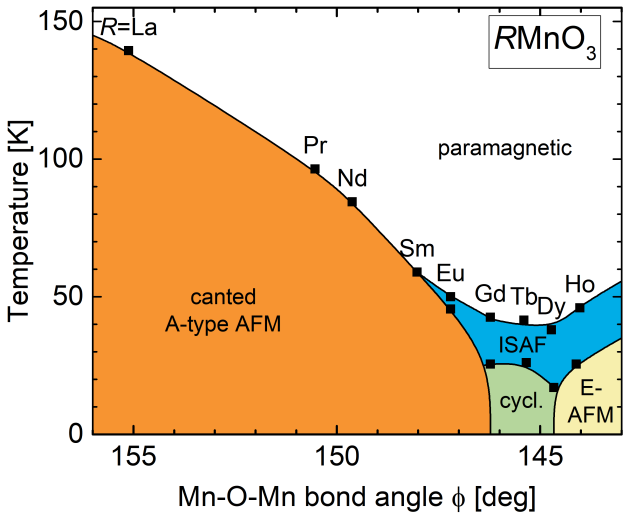

Figure 4.10: Phase diagram of $R\mathrm{MnO_3}$ with respect to the temperature T and the Mn-O-Mn bond angle ϕ. Adapted from Kimura *et al.*

spins stacked antiferromagnetically next to each other (see also Fig. 4.7). In-between $\mathrm{EuMnO_3}$ and $\mathrm{HoMnO_3}$ the spin frustration is the most pronounced, which is exemplified by the fact, that T_N shows a minimum between those two compounds. The magnetic ground state in this range of ionic radii is incommensurable. This means, that the periodicity of the magnetic ordering pattern does not match with the periodicity of the lattice (or an integer multiple of it), it is therefore incommensurable with the lattice. The angle between two adjacent spins is then of course also not an integer fraction of 2π. This is in contrast of conventional ferromagnetic (2π) or antiferromagnetic (π) spin order. There are several possible ways of incommensurable magnetic order. Typical examples are displayed in Fig. 4.11. In Fig. 4.11b), the rotation axis of the spins is parallel to their modulation vector q. They form a spin-screw pattern. Fig. 4.11c) shows a cycloidal arrangement. Here, the rotation axis is perpendicular to the modulation vector. It is noteworthy, that for these two cases also commensurable examples exist. For example a 120° arrangement of spins, which corresponds to $q = 2\pi(0, 0, 1/3)$, which is for example the ground state of an perfectly isotropic 2D triangular lattice of spins. Fig. 4.11a) shows the so-called sinusoidal spin arrangement. Here, the incommensurability is not reflected by the angle between the spins. This can be understood as a spin-density wave (SDW), where the periodicity of the spin density does not coincide with the lattice periodicity. For a spin $S(\mathbf{x_i})$ at the site $\mathbf{x_i}$ a collinear sinusoidal pattern can be described as $S(x_i) = S_0 \cdot \sin(\mathbf{q} \cdot \mathbf{x_i})$ with modulation vector $\mathbf{q}$.

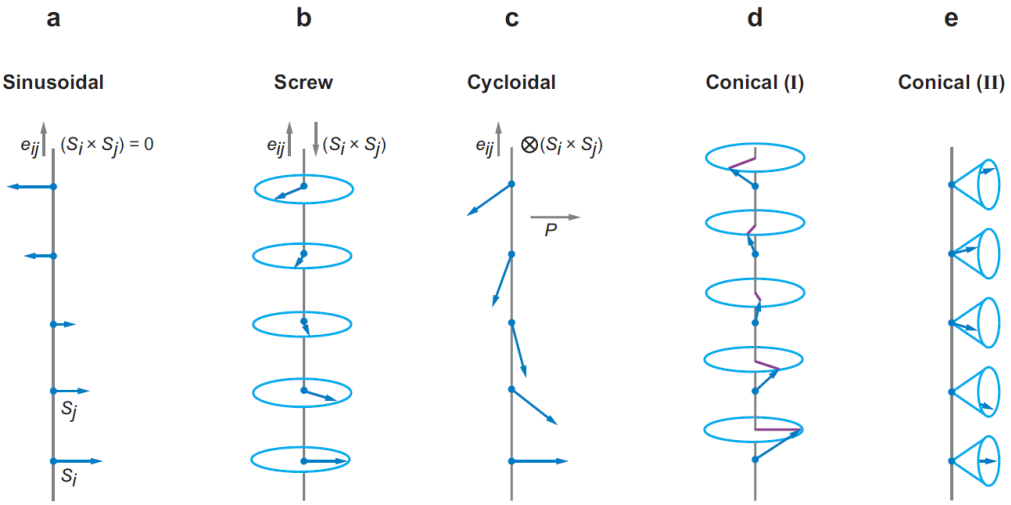

Figure 4.11: Several possible ways of incommensurable magnetic order. Adapted from [35].

In the orthorhombic $R\mathrm{MnO_3}$ compounds with ϕ <147°, the commonly accepted phase diagram consists of two major types of incommensurable magnetic order patterns. According to this understanding, upon cooling down, the system enters at first an inncommensurate sinusoidal antiferromagnetic (ISAF) phase, with transition temperatures around T_N = 45-50 K [5, 6]. This phase is assumed to be paraelectric, with a temperature-dependent modulation vector **q**. At even lower temperatures, a second phase transition occurs at $T_{lock} = 20 - 40\,K$, the so-called "lock-in temperature", where the temperature-dependent modulation vector of the preceding ISAF phase "locks" to a temperature-independent value. With decreasing Mn-O-Mn bond angle ϕ, this is either an A-type AFM state (for example in $\mathrm{EuMnO_3}$), a cycloidal state (R= Gd, Tb, Dy), which is multiferroic, or, for orthorhombic $\mathrm{HoMnO_3}$ an E-type AFM state. The interesting range of ϕ is thus between $\mathrm{EuMnO_3}$ and $\mathrm{HoMnO_3}$ where multiferroicity occurs. After a general introduction to multiferroicity in section 4.3, the specific considerations for multiferroicity in $R\mathrm{MnO_3}$ are treated in section 4.4.

4.3 General introduction to multiferroicity

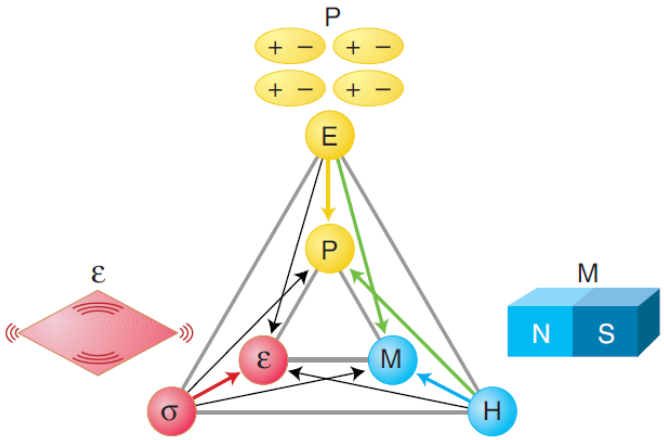

Figure 4.12: The multiferroic triangle, illustrating the cross-coupling of the fields E, H and σ with the macroscopic properties P, M and ε. The magnetoelectric coupling $M(E)$ and $P(H)$ is emphasized by green arrows. Adapted from [34].

Although multiferroicity is a very intensively studied topic with a prospective vast amount of new technological applications and also serves as a catalyst for novel scientific directions of investigation, the definition of multiferroism is surprisingly simple and can apply to a vast amount of materials. First, we recall the meaning of "ferroic" behavior: In the most general sense, ferroic behavior denotes a spontaneous symmetry break, accompanied with a change of the material response. The response can be an electric polarization P in a ferroelectric, where inversion symmetry is broken, magnetization M in an (anti-)ferromagnet with broken time inversion symmetry or the lattice deformation ε in a ferroelastic, with a reduction of the lattice symmetry. All three macroscopic response functions have a conjugated field, that plays the role of a potential in the free energy: the electric field E, the magnetic field H and the stress σ. In the linear theory, these material properties are simply connected by a response function χ with their respective fields, such as $P = \chi_e E$, where χ_e is the electric susceptibility. Multiferroism is then nothing more than a *coexistence* of at least two ferroic properties within the same phase (see Figure 4.12). An exemplary material would be $BiFeO_3$, which undergoes a phase transition to a ferroelectric state below $T_{FE} = 1100\,K$ and then a phase transition to a magnetically ordered state below $T_N = 643\,K$. Thus, it shows magnetization and electric polarization within the same phase. The properties are however completely unrelated to

each other. These materials with negligibly weak cross-coupling belong to the so-called type-I multiferroics. A much more interesting class of multiferroic materials are therefore the type-II multiferroics, which show a considerable cross-coupling of their ferroic properties. A systematic approach is to expand the free energy $F(\mathbf{E}, \mathbf{H})$ to at least the second order with respect to $\mathbf{E}$ and $\mathbf{H}$:

$$F(\mathbf{E}, \mathbf{H}) = F_0 - \sum_i P_i^0 E_i - M_i^0 H_i \\ - \sum_{i,j} \frac{1}{2}\varepsilon_{ij} E_i E_j - \frac{1}{2}\mu_{ij} H_i H_j - \alpha_{ij} E_i H_j - \dots \tag{4.4}$$

where the terms of zeroth order are the spontaneous polarization and magnetization. The field-dependence of the electric polarization is then obtained in the usual way by differentiation of F with respect to the electric field

$$P_i(\mathbf{E}, \mathbf{H}) = -\frac{\partial F}{\partial E_i} = P_i^0 + \varepsilon_{ij} E_j + \alpha_{ij} H_j + \dots \tag{4.5}$$

and in the same way the magnetization is obtained by differentiation with respect to the magnetic field:

$$M_i(\mathbf{E}, \mathbf{H}) = -\frac{\partial F}{\partial H_i} = M_i^0 + \mu_{ij} H_j + \alpha_{ij} E_i + \dots \tag{4.6}$$

We see that the second-order term of the free energy $\alpha_{ij} E_i H_j$ introduces a cross-coupling between electric polarization and applied magnetic field on the one hand and between magnetization and applied electric field on the other hand via the magnetoelectric coupling tensor α. This is called the linear magnetoelectric (ME) effect. While the ME coupling appears naturally from the serial expansion of F, its particular origin in a specific material system is crucial for the understanding of ME effects.

4.4 Multiferroicity by cycloidal spin order in $R\mathrm{MnO}_3$

As discussed in subsection 4.2.3, multiferroicity in $R\mathrm{MnO}_3$ is the simultaneous appearance of electric polarization (i.e., the breaking of the inversion symmetry) with the onset of cycloidal magnetic order. In this section we are going to discuss some possible ways of breaking inversion symmetry by magnetic order and the principles behind their origin. It is underscored that in the following consideration the breaking of spatial inversion symmetry (and the corresponding appearance of electric polarization) is purely caused by magnetic interactions.

There exist various scenarios where the breaking of time inversion symmetry can lead to a breaking of spatial inversion symmetry. The two main effects discussed for the $R\mathrm{MnO}_3$ compounds are magnetostriction (or exchange striction), i.e., a reduction (elongation) of bonds lengths to increase (decrease) the overlap of orbitals for favorable (unfavorable) spin orientations and the spin-current model (or inverse Dzyaloshinskii-Moriya model). Magnetostriction creates a polarization which is proportional to the scalar product of spins S_i and S_j . The dipole induced by a pair of spins is then:

$$\mathbf{p}_{ij} \propto (\mathbf{S}_i \cdot \mathbf{S_j}) \tag{4.7}$$

As an example, a linear up-up-down-down arrangement of spins with alternating atoms is considered in Fig. 4.13(a). The inequivalent strength of exchange striction between parallel and antiparallel spins favors a closer overlap of wavefunctions for the stronger exchange interaction. If we assume that the AFM exchange striction is stronger than the FM, sites with antiparallel spin move closer together from their equillibrium positions (marked as empty circles) which leads to a uniform polarization along the direction of the spin chain [35, 78]. This type of inversion symmetry breaking can occur for collinear as well as non-collinear spin arrangements, given a suitable lattice geometry.

The other possible form of magnetically induced electric polarization is explained by the spin-current or inverse Dzyaloshinskii-Moriya model. The Dzyaloshinskii-Moriya (DM) interaction favors canting of spins, if they are connected by a superexchange mechanism and the connecting ion is not completely in line with the other two ions. The Hamiltonian is written as

$$H_{DM} \propto \mathbf{D}_{ij} \cdot (\mathbf{S}_i \times \mathbf{S}_j) \tag{4.8}$$

with the Dzyaloshinskii-Moriya vector $\mathbf{D}_{ij} = \mathbf{r}_i \times \mathbf{r}_j$. Within the inverse DM model this idea is turned around: For a noncollinear spin arrangement, the

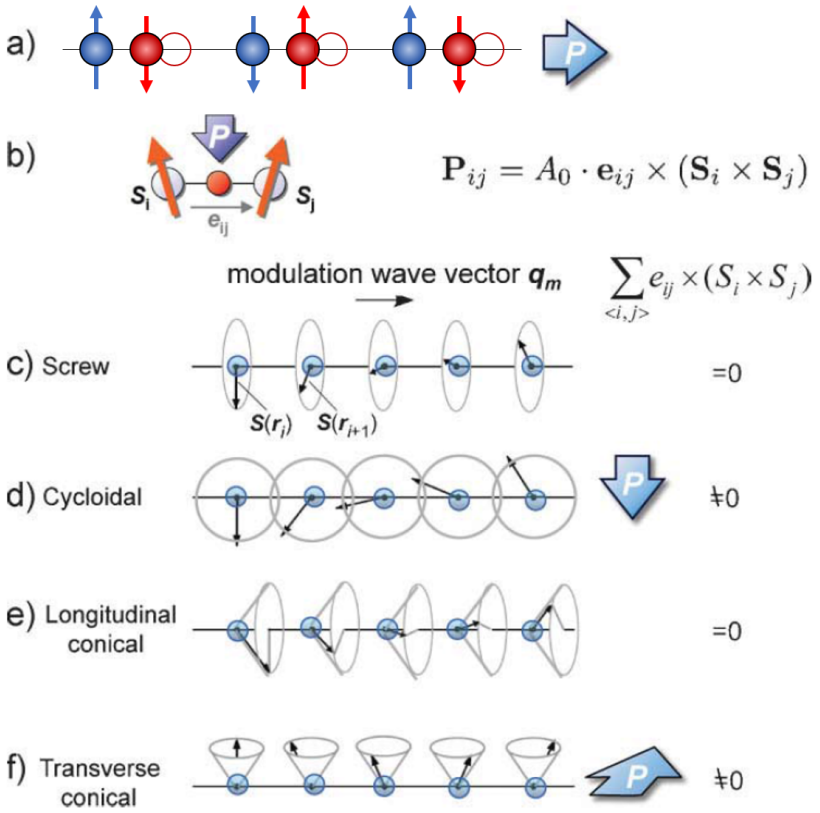

Figure 4.13: Illustration of electric polarization induced by magnetic order. (a): magnetistriction mechanism. (b) Polarization induced via the inverse DM mechanism. (c) Proper-screw spin order, where the screw axis is parallel to the modulation vector $\mathbf{q}$. The resulting polarization is zero (d) cycloidal order with the spin rotation axis perpendicular to $\mathbf{q}$. Clockwise and counter-clockwise cycloids induce polarization of opposite sign. (e) The longitudinal conical order is a combination of the proper-screw and a constant spin component (f) The transverse conical order is a combination of a constant spin component ($\hat{=}$ no polarization) and a cycloid. Since the cycloidal plane is rotated by 90°, so is the induced polarization. Adapted from [35].

inverse DM interaction leads to a transverse shift of the intermediate ion of the superexchange mechanism. Therefore the resulting dipole moment can be expressed as

$$\mathbf{p}_{ij} = q \cdot \mathbf{x} \propto \hat{\mathbf{e}}_{\mathbf{ij}} \times (\mathbf{S_i} \times \mathbf{S_j}) \tag{4.9}$$

where $\hat{\mathbf{e}}_{\mathbf{ij}}$ is the unit vector connecting the two spins S_i and S_j, q the ionic charge and $\mathbf{x}$ is the displacement of the intermediate ion, see also Fig. 4.13b). If this mechanism is applied to the canted AFM structure, it produces local dipole moments, however no macroscopic polarization. The alternating canting to opposite sides leads to alternating antiparallel dipole moments and thus they cancel out. To create a macroscopic polarization with this mechanism, the spin must rotate consecutively as in a spiral. Figures 4.13(c)-(f) show different possible spin spirals, together with the resulting net polarizations. Figure 4.13(c) shows a "proper-screw" pattern, where the screw axis and the modulation vector are antiparallel. No dipoles occur, since the spin rotation vector $(\mathbf{S_i} \times \mathbf{S_j})$ is antiparallel to $\hat{\mathbf{e}}_{\mathbf{ij}}$ and therefore expression (4.9) is zero for each pair of spins. Figure 4.13d) shows a cycloidal pattern. The spin rotation vector is now perpendicular to the modulation vector, giving the maximum value for equation (4.9). In figure 4.13e), there is no net polarization for the longitudinal conical pattern. This can be understood as a combination of a proper screw like in Fig. 4.13c) and a uniform spin component along the modulation vector, which both result in zero dipole moments in the inverse DM mechanism. Eventually, Fig. 4.13f) shows a transverse conical pattern. This can be separated in a similar way into a uniform spin component pointing upwards and a cycloidal rotation. Compared to Fig. 4.13c), the spin rotation vector is rotated by 90° and - most notably - the polarization is rotated along with it in the same way.

If we compare the different patterns, the cycloidal patterns gives the maximum possible net polarization in the inverse DM mechanism from a geometric point of view. Furthermore, if the spin rotational plane is rotated around the modulation vector (i.e., the normal vector is rotating perpendicular to the modulation vector), the polarization is also rotated by the same angle. If the spin rotational normal vector is rotated towards the modulation vector, the induced polarization is gradually diminished until it vanishes when the spin rotational normal vector is (anti-)parallel to the modulation vector. This situation corresponds to the proper screw order pattern. The most striking effect though is the inverse effect: instead of rotating the spin rotational plane by a magnetic field and changing the polarization accordingly, one might also apply an electric field to manipulate the electric polarization. By means of the DM interaction, the spins will now adjust for the new polarization state and the spin rotational plane will change accordingly. The result is therefore

a system, where the magnetization can also be controlled by an electric field and, vice versa, the electric polarization can be controlled by a magnetic field. This is indeed the case in the multiferroic $R\mathrm{MnO_3}$ compounds and was shown for example for $\mathrm{TbMnO_3}$ [1].

4.4.1 Influence of the magnetic moment of the *R*-site ion in $R\mathrm{MnO_3}$

Until now we have discussed how the $\mathrm{Mn^{3+}}$ spins interact with each other, mediated by superexchange over the $\mathrm{O^{2-}}$ ions. The R-site ion was only considered as a placeholder between the $\mathrm{MnO_6}$ octahedra as a means of tuning the Mn-O-Mn bond angle. However, many compounds involve an ion with a magnetic moment, for example R=Dy, Tb, ... As Tb shows the most pronounced ME coupling, it is of interest, if R-site 4f spins also influence the magnetic properties of $\mathrm{Mn^{3+}}$ in any way. A first step was to determine if the magnetic moment of the R-site spins are necessary for the multiferroic properties. To investigate this issue, a substitutional approach was employed. The $\mathrm{Eu_{1-x}Y_xMnO_3}$ series are prime candidates for this, as with substitution content $0 \leq x \leq 0.5$, the Mn-O-Mn bond angles ϕ in the range from the stoichiometric $\mathrm{EuMnO_3}$ to $\mathrm{TbMnO_3}$ can be accessed. In addition, $\mathrm{Eu^{3+}}$ with a half-filled 4f shell has zero total angular momentum and $\mathrm{Y^{3+}}$ is non-magnetic. Due to the very weak interaction between the $4f$ orbitals of adjacent R-sites spins are still disordered when the multiferroic phase occurs at $T \approx 25\,\mathrm{K}$: their ordering temperature T_R is usually about 5 K ($\mathrm{TbMnO_3}$: 7 K [36], $\mathrm{DyMnO_3}$: 7.5 K [79], $\mathrm{HoMnO_3}$: 5 K [32]). It was shown, that the multiferroic phase occurs in the same way and with the same dependency as in the stoichiometric compounds [5, 7, 80, 81]. While the R-site ions are not required for the formation the cycloidal spin structure, Ivanov *et al.* showed for $\mathrm{Eu_{1-x}Ho_xMnO_3}$, that the R-site ions do have another important influence onto the magnetic properties [5]. For this purpose, $\mathrm{Y^{3+}}$ of $\mathrm{Eu_{1-x}Y_xMnO_3}$ was replaced by $\mathrm{Ho^{3+}}$, which has an ionic radius nearly identical to $\mathrm{Y^{3+}}$, but is magnetic: In the crystal field, the $\mathrm{Ho^{3+}}$ spins are in a quasi-doublet state, i.e., the difference in energy of "up" and "down" orientation of the spin system is negligible. Due to the Ho-Mn exchange interaction this doublet splits, but only if there is a spin component of the $\mathrm{Mn^{3+}}$ spins along the b-axis. This introduces another contribution to the effective anisotropy constant which lowers the anisotropy energy along the b-axis, while leaving contributions along the other two axes unaffected. As a result, with increasing Ho-content, the cycloidal plane is expected to be reoriented from the ca- to the ba-plane. This is explained by the anisotropic

free energy density Φ_A of the form

$$\Phi_A \approx \frac{1}{2}K_{ca}^{Mn}A_x^2 + \frac{1}{2}K_{ba}^{Mn}A_z^2 - NT\ln\left[2\cosh(\Delta/k_BT)\right] \tag{4.10}$$

with the anisotropy constants K_{ca}^{Mn} and K_{ba}^{Mn} acting on the Mn-spins in the ca- and ba-plane respectively, where $K_{ca}^{Mn} < K_{ba}^{Mn}$ so that in the absence of Ho, the cycloid is oriented within the ca-plane, N is the concentration of rare-earth ions, A_x and A_z are respective components of the antiferromagnetism vector $\mathbf{A}$ and Δ is the total Ho-doublet splitting, including the crystal field splitting and the anisotropic Ho-Mn exchange. When $\Delta \ll k_BT$ or the

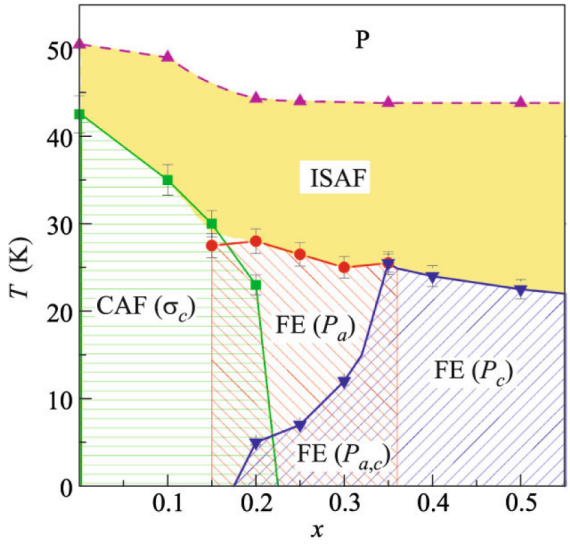

Figure 4.14: Magnetic phase diagram of $Eu_{1-x}Ho_xMnO_3$, experimentally determined by Ivanov *et al.* [5]. With $x \geq 0.2$, the spin cycloid is succesively reoriented. *Note:* The crystallographic axes are given in the *Pbnm* orientation. The conversion from *Pbnm*↔*Pnma* is performed by replacing (*abc*) ↔(*cab*).

Ho concentration N is small, the system should behave like $Eu_{1-x}Y_xMnO_3$, while at lower temperatures and increasing Ho content, the behavior should start to differ by reorientation of the spin cycloids. This is indeed the case, and the resulting phase diagram of $Eu_{1-x}Ho_xMnO_3$ (see Fig. 4.14) shows the expected similarity to the $Eu_{1-x}Y_xMnO_3$ compounds.

Chapter 5

Results and discussion - $Eu_{1-x}Ho_xMnO_3$

5.1 Mode assignment

As a first step before delving deeper into the analysis of the $Eu_{1-x}Ho_xMnO_3$ compounds, a basic understanding of the phonon eigenmodes needs to be established. With 20 atoms in the unit cell, there exist 57 optical phonon modes plus 3 acoustic ones. Due to the presence of a center of symmetry, the phonon modes are exclusively either infrared- or Raman active. Of the 57 optical modes, 24 are Raman active. Grouped according to their symmetry (*Pnma* notation), these modes are: 7 A_g + 5 B_{1g} + 7 B_{2g} + 5 B_{3g}. They are enumerated according to their eigenfrequency within their respective group as $A_g(1)$, $A_g(2)$, ... with $A_g(1)$ being the mode with the highest energy. Furthermore, by applying appropriate settings for polarizer and analyzer in the setup, each of this four groups of phonon modes can be probed individually. This can be seen by examining the corresponding Raman tensors given by [45]:

$$A_g : \begin{pmatrix} a & 0 & 0 \\ 0 & b & 0 \\ 0 & 0 & c \end{pmatrix}, \quad B_{1g} : \begin{pmatrix} 0 & d & 0 \\ d & 0 & 0 \\ 0 & 0 & 0 \end{pmatrix},$$
$$B_{2g} : \begin{pmatrix} 0 & 0 & e \\ 0 & 0 & 0 \\ e & 0 & 0 \end{pmatrix}, \quad B_{3g} : \begin{pmatrix} 0 & 0 & 0 \\ 0 & 0 & f \\ 0 & f & 0 \end{pmatrix}. \tag{5.1}$$

With polarizer and analyzer set parallel, e.g., in the scattering configuration $b(a,a)\bar{b}$, only the modes with A_g symmetry are detectable. As the Raman tensor for the A_g modes has only entries along the main diagonal, also par-

allel scattering configurations with polarization along the b- and c- would be equivalent. If it is desired to detect exclusively the modes of B-symmetry, the polarizer and analyzer need to be set to a perpendicular configuration. If the wavevector of the incoming light is parallel to one of the crystal's main axes, for each axis, one of the three B-modes is excited. We focus here on b- and a-cut samples, giving access to the B_{2g} modes in $b(c,a)\bar{b}$ geometry and the B_{3g} modes for $a(c,b)\bar{a}$. We utilize the enumeration of modes according to [4], where the enumeration is performed in the order how the modes appear in the spectrum of $LaMnO_3$. As some modes show a strong composition dependence of the phonon frequency, the order in which modes appear in spectra of other samples can and will deviate from $LaMnO_3$. Corresponding elongation patterns are readily available in literature, for example as calculated by Smirnova and are displayed in figure 5.1 [3]. For an overview, the modes can be classified into three categories, with typical frequency ranges in which they appear:

1. Motions of the heavy R^{3+} and the Mn^{3+} ions: $\tilde{\nu} < 300\,\mathrm{cm}^{-1}$.

2. Tilting, rotating and buckling motions of the MnO_6 octahedra: $300\,\mathrm{cm}^{-1} < \tilde{\nu} < 500\,\mathrm{cm}^{-1}$.

3. Stretching and breathing of the MnO_6 octahedra: $500\,\mathrm{cm}^{-1} < \tilde{\nu} < 700\,\mathrm{cm}^{-1}$.

With this knowledge, a qualitative statement about the expected Raman intensities can be made: the low frequency modes will have a very low Raman intensity, as the heavy R^{3+}-ions barely move and therefore the polarizability change $\frac{\partial\alpha}{\partial q}$ of the R-O bonds is expected to be small, thus giving also small Raman intensity according to 2.7. On the other hand, the modes with higher frequencies, which involve oxygen movements and thus modulations of the Mn-O bonds will result in a much larger change in polarizability and produce the strongest Raman signal in the spectra. However, the modes of B_{1g} and B_{3g} symmetry show such low, if any, Raman intensities that they are generally neglected in the literature. Therefore, in the following the focus of the discussion will be on the A_g and B_{2g} modes. With spectra of similar $RMnO_3$ compounds readily available in literature [54, 81, 82], the assignments of modes to individual Raman peaks is straightforward. We use the data for $EuMnO_3$ recorded by Iliev *et al.*, listed in table 5.1. Typical Raman spectra are shown in figure 5.2. For the modes with A_g symmetry, the spectra are recorded in $b(a,a)\bar{b}$ scattering geometry, while the modes with B_{2g} symmetry are recorded in $b(a,c)\bar{b}$ geometry. There exist two pairs of modes, that demand further clarification in the naming scheme: the $A_g(1)$ and the $A_g(3)$

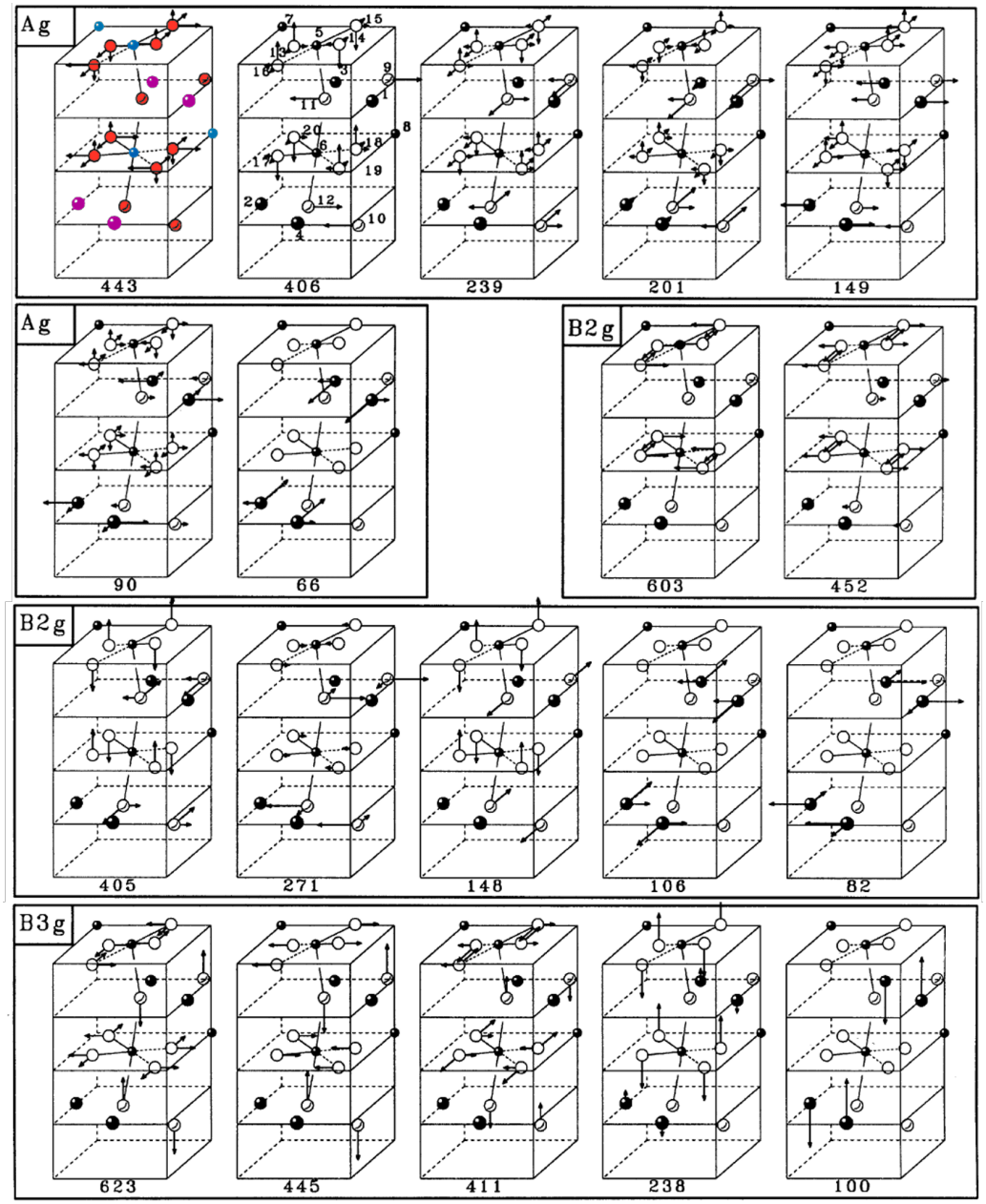

Figure 5.1: Elongation patterns of the Raman-active phonon modes with A_g, B_{2g} and B_{3g} symmetry of $LaMnO_3$. The ions in the first elongation pattern follow the color code as before. Mn: blue, O: red and R: purple. Adapted from [3].

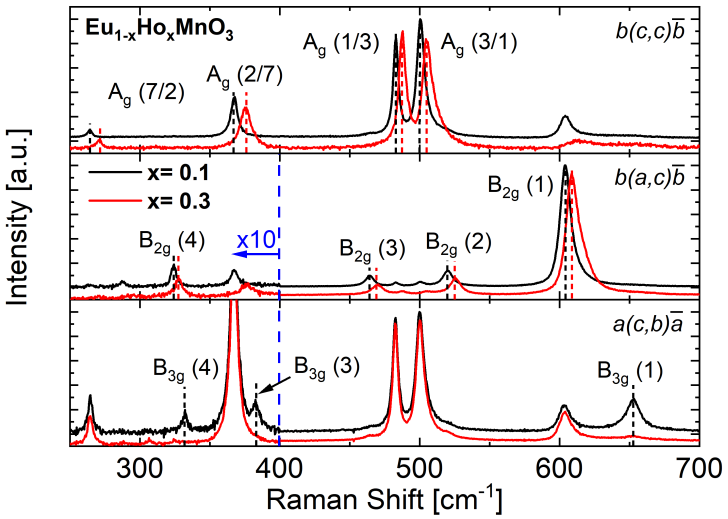

Figure 5.2: Typical polarized Raman spectra of $Eu_{1-x}Ho_xMnO_3$ ($x = 0.1$ and 0.3). The modes are labeled according to [82]. The first two panels show spectra with incident light parallel to the b-axis in parallel (A_g) and crossed (B_{2g}) polarization configuration, the third panel shows spectra with incident light in a direction in crossed configuration (B_{3g}).

modes, as well as the $A_g(2)$ and the $A_g(7)$ modes. For $LaMnO_3$, the enumeration is clear. However, the $A_g(3)$ and the $A_g(7)$ mode frequency strongly depends on the R-site ionic radius, while the the $A_g(1)$ and the $A_g(2)$ frequencies are nearly independent of the R-ion. When the R-site ionic radius is decreased, the $A_g(3)$ and $A_g(7)$ mode frequencies increase. When they reach the vicinity of the $A_g(1)$ and $A_g(2)$ frequencies, respectively, the mode frequencies follow the typical behavior of coupled oscillators according to $\omega_{1,2} = \frac{\omega'+\omega''}{2} \pm \sqrt{\frac{(\omega'-\omega'')^2}{4} + \frac{V^2}{4}}$. Here, ω' and ω'' are the frequencies of the uncoupled modes and V is a coupling constant [83]. The coupling between these modes leads to the typical anticrossing behavior and to the hybridization of the modes. In the considered $Eu_{1-x}Ho_xMnO_3$ compounds, we find ourselves in the range of strong mixing of the $A_g(1)$ and the $A_g(3)$ modes. The modes are thus more aptly referred to as $A_g(1/3)$ and $A_g(3/1)$, whereas $A_g(1/3)$ means that the mode has a stronger admixture of the $A_g(1)$ mode and vice versa. The observed relative intensities and linewidths of the Raman modes match very well to other observed spectra in the $RMnO_3$ series in the literature, specifically the stoichiometric parent compound $EuMnO_3$. Apart from the known phonon modes in the spectra, most publications show or mention a broad feature at around 650 cm^{-1}, the origin of which was ambiguous until now. This was either ascribed to an oxygen defect mode [84], an additional

Mode	Basic distortion	$\tilde{\nu}(300\,\mathrm{K})$ in $EuMnO_3$ [cm^{-1}]
$A_g(1/3)$	JT + [010], [101]	501.0
$A_g(3/1)$	[101], JT + [010]	479.0
$A_g(4)$	[101]	360.8
$A_g(2/7)$	[010], R-shift	
$A_g(7/2)$	R-shift, [010]	
$B_{2g}(1)$	JT	609.5
$B_{2g}(2)$	[010]	518.4
$B_{2g}(3)$	[101]	464.6
$B_{2g}(7)$	R-shift	323.8

Table 5.1: Observed Raman modes of A_g and B_{2g} symmetry in $EuMnO_3$ and their corresponding basic distortion(s) according to Iliev *et al.* [4].

mode of A_g symmetry [3], a single-phonon excitation at the Brillouin zone boundary or a two-phonon mode [85]. On the other hand, the close proximity to the $B_{2g}(1)$ mode bears semblance as a Fano lineshape of the $B_{2g}(1)$ mode. In this thesis however, we present strong arguments which indicate that this is a misconception of this feature in the $RMnO_3$ spectra. To elucidate this matter, we consider the spectrum shown in figure 5.2. It shows the Raman spectrum at 5 K of the a-cut sample of $Eu_{0.7}Ho_{0.3}MnO_3$, which grants access to the B_{3g} symmetry modes in the $a(b,c)\bar{a}$ scattering configuration. Not only can we see how the modes with B_{2g} symmetry are suppressed, but also that the feature at $\approx 650\,\mathrm{cm}^{-1}$ is now more pronounced compared to the $b(c,a)\bar{b}$ configuration. Upon closer inspection, as shown in Figure 5.3, new features with Lorentzian lineshapes are observed at lower frequencies, with typical linewidths for phonons in these materials. A comparison with phonon

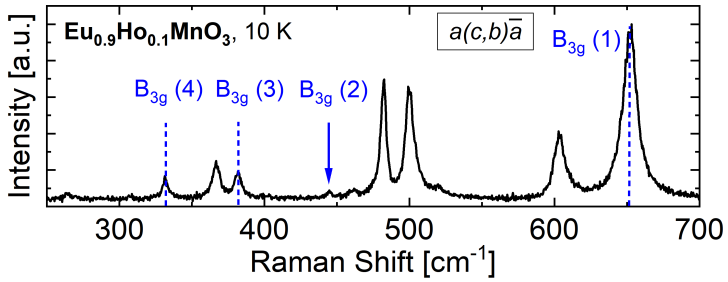

Figure 5.3: Closer examination of the B_{3g} spectra of $Eu_{0.9}Ho_{0.1}MnO_3$. Four out of the five possible modes with B_{3g} symmetry are identified.

frequencies calculated by Smirnova shows, that the observed features could match the calculated frequencies of B_{3g} modes within a reasonable margin

of error between experimental and calculated values [3]. Another argument which supports this notion can be found in the temperature-dependent behavior of $\omega(T)$ for this feature, which is going to be discussed in section 5.3.2 and 5.4. In short, we will see that the temperature dependence of this feature shows two typical phenomena related to phonons: the frequency shift caused by anharmonic decay of the optical phonon into two acoustic ones (Klemens model, see Sec. 2.4) at higher temperatures $T \gg T_N$ and the SPC-induced frequency shift at lower temperatures. Being the mode of highest frequency in this scattering configuration, we will refer to it from now on as the $B_{3g}(1)$ mode and identify it with a mode of the octahedron where not only the O2 oxygen ions of the MnO_2 plane are in motion (as in the $B_{2g}(1)$ breathing mode), but also an additional antiphase motion of the two apical O1 ions occurs.

This marks the first time that this feature was consistently explained and identified as the $B_{3g}(1)$ mode in the $R\mathrm{MnO}_3$ family. Its observation and interpretation of the new information supplemented by this mode opens up new paths in investigation of the lattice dynamics and SPC in this material class, which is going to be discussed in detail in section 5.3.1 and 5.4 [55]. In the following section 5.2, the effect of R-site substitution onto the lattice dynamics is investigated before we turn our attention to spin-phonon coupling (SPC) effects in section 5.3. Spin-phonon coupling is examined with respect to the temperature dependence and mode symmetry (5.3.1), compositional dependence (5.3.2) and behavior in an external magnetic field (5.5).

5.2 Impact of Ho-content on the lattice dynamics of $Eu_{1-x}Ho_xMnO_3$

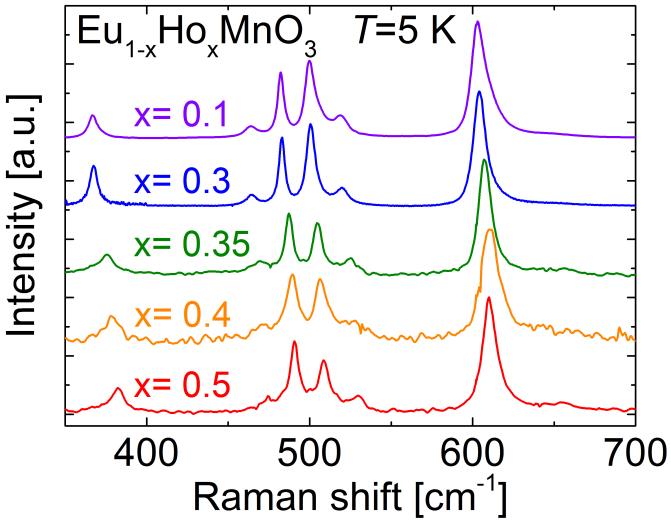

Figure 5.4: Unpolarized Raman spectra for various $Eu_{1-x}Ho_xMnO_3$ compounds with $0.1 \leq x \leq 0.5$. The mode frequencies are shifted to higher values as the Ho content x is increased. The strength of this shift is specific for each mode.

Now that the mode patterns are assigned to the individual peaks in the Raman spectrum, the analysis of the obtained data is in order. The first step is to analyze the impact of the Ho-content onto the lattice dynamics of the various $Eu_{1-x}Ho_xMnO_3$ compounds. Samples are available with Ho concentrations of $x = 0.1$, 0.3, 0.35, 0.4 and 0.5. All samples are high-quality single crystal platelets of the order of 100 μm thickness and a few millimeters width and length. The surface is perpendicular the b-axis (referred to as b-cut). One additional specimen of the x =0.1 sample is available with a c-cut surface. Note, that for $x > 0.5$ the manganites can crystallize with admixtures of the hexagonal crystal structure. $HoMnO_3$ in particular crystallizes naturally in the hexagonal phase. However, the orthorhombic phase can be stabilized when pressure is applied during the growth process [71]. If the crystals would either grow in a mixed structure consisting of orthorhombic and hexagonal partitions, or the crystals would grow in clusters of $EuMnO_3$ and $HoMnO_3$ instead of the solid solution $Eu_{1-x}Ho_xMnO_3$, this would be clearly visible as a splitting of the modes or at the very least a significant broadening. Figure 5.4 shows the unpolarized spectra of all investigated $Eu_{1-x}Ho_xMnO_3$ compounds. For an easier distinction of the individual modes, the spectra

at T =5 K are displayed. The absence of any such observations as excessive broadening or splitting confirms the high quality and homogeneity of the single crystals.

For the analysis of the lattice dynamics with respect to the Ho content x,

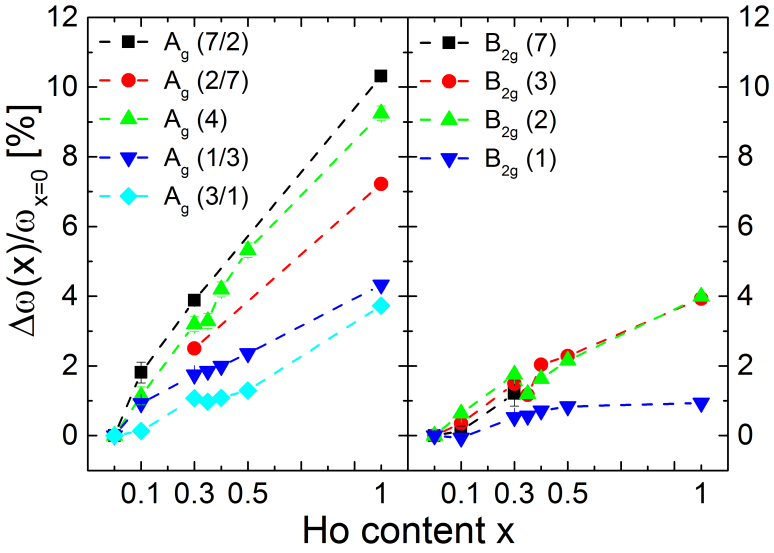

Figure 5.5: Composition dependence of the percentual shifts of the room temperature phonon frequencies in $Eu_{1-x}Ho_xMnO_3$ relative to $EuMnO_3$. Data for x =0 and x =1 added from Issing *et al.* and Iliev *et al.*, respectively [4, 7].

it is important that no effects due to the magnetic properties of the system are interfering. Therefore we extract the phonon frequencies from the Raman spectra at room temperature by fitting the peaks with Lorentzian lineshapes. The Ho-induced phonon frequency shifts obtained in this way, are plotted versus the Ho-content x in Fig. 5.5. For a better comparison, data from pure $EuMnO_3$ (corresponding to $x = 0$) and orthorhombic $HoMnO_3$ (x =1.0) are added to the graph from literature [4, 7]. The values shown denote the relative shift compared to pure $EuMnO_3$. All observed modes show an increase of frequency with increasing Ho-content x. That the general trend is towards higher phonon frequencies can be explained with the simple model of an harmonic oscillator with frequency

$$\omega = \sqrt{\frac{D}{\mu}}. \tag{5.2}$$

Two mechanisms that affect the phonon frequency can be expected from this equation. The first mechanism would be the change of frequency due to a

different reduced mass μ, when the Eu-ions are replaced with Ho-ions. This is, however, not the case. Because the Ho-mass (164 u) is larger than the Eu-mass (152 u), the phonon frequencies should decrease with increasing Ho-content, which is clearly in contrast to the observed behavior. In addition, the Raman modes of higher frequency ($> 300\,\mathrm{cm}^{-1}$) consist mainly of vibrations of the oxygen ions and Ho does not participate in the elongation patterns.
The second mechanism could be a change in the force constant D, which depends on the strength and length of the chemical bonds and is influenced by the lattice constants. Indeed, with smaller R-site radius (and therefore stronger octahedron tilt), the lattice constants are also decreasing, see section 4.1.1. This leads to an increase of the coupling constant and thus also to an increase of the phonon frequency. With the global trend of increasing phonon frequencies of Raman active modes explained, a more detailed analysis based on the elongation pattern of the individual modes is in order to understand their individual strength of frequency shift with increasing Ho-content. In general, the A_g modes experience a stronger relative shift than the modes of B_{2g} symmetry. The strength of the shift is also specific for each mode. This is caused by their individual elongation patterns: We recall from section 4.1, that the orthorhombic distortion of the cubic perovskite is caused by four basic distortions $D_{[101]}, D_{[010]}, D_{JT}$ and D_R. This reduction of symmetry is also reflected in the phonon elongation patterns. While there can not be any Raman-active mode in the cubic lattice with inversion symmetry, the phonon modes become active because of the reduction of symmetry caused by these basic distortions of the lattice. According to Iliev *et al.*, most modes are activated by a single one of those four basic distortions. The modes with their corresponding distortion(s) are listed in Table 5.1. The composition dependent behavior at room temperature can be fully understood with this knowledge.
The $B_{2g}(1)$ breathing mode, which is activated by D_{JT}, is very insensitive to the Ho-content. Among the modes with B_{2g} symmetry, the $B_{2g}(2)$ and $B_{2g}(3)$ modes depend much stronger on the Ho-content, because they are activated by the octahedron tilt- and rotation operation $D_{[101]}$ and $D_{[010]}$ respectively, which is a direct effect of varying the R-site ionic radius and the resulting octrahedron tilt.

	ω [cm^{-1}]	Mn-O-Mn bond angle ϕ (Raman)
$EuMnO_3$ [1, 4]	360.8	147.22°
$Eu_{0.9}Ho_{0.1}MnO_3$	366.5	146.65°
$GdMnO_3$	370.5	146.21°
$Eu_{0.7}Ho_{0.3}MnO_3$	374.0	145.91°
$Eu_{0.65}Ho_{0.35}MnO_3$	374.3	145.88°
$Eu_{0.6}Ho_{0.4}MnO_3$	377.6	145.55°
$TbMnO_3$	378.2	145.38°
$Eu_{0.5}Ho_{0.5}MnO_3$	381.7	145.15°
$DyMnO_3$	386.0	144.72°
$HoMnO_3$	395.9	144.10°

Table 5.2: Mn-O-Mn bong angle ϕ calculated via Eq. 5.3 from the $A_g(4)$ mode frequency with $EuMnO_3$ as reference. Data for the stoichiometric compounds are extracted from Ref. [6].

In a similar way, one would expect the modes with A_g symmetry to behave. Let us at first consider the case without coupling between modes, i.e. without mode-mixing. The $A_g(1)$ mode is mainly activated by the Jahn-Teller distortion D_{JT} and additionally a smaller contribution of the rotation $D_{[010]}$. It would be expected to have only a minor dependence on the R-site ionic radius. On the other hand, the modes $A_g(2)$-$A_g(4)$, activated by $D_{[101]}$ and $D_{[010]}$ should show a strong dependence on r_R and finally the mode $A_g(7)$, activated by the R-shift D_R, should show only small effects. In the R^{3+}-radius range at hand, this behavior is altered by the coupling of modes to mixed modes. The $A_g(1)$ mode acquires its dependence on r_R by coupling with the $A_g(3)$ mode, hence the nomenclature $A_g(1/3)$. On the other hand, due to the anticrossing behavior of coupled excitations, the sensitivity of the $A_g(3)$ mode is reduced by mixing with the $A_g(1)$, hence it is referred to as $A_g(3/1)$. In a similar fashion, this holds for the other pair of mixed modes $A_g(2/7)$ and $A_g(7/2)$.
The last mode in the A_g spectrum is the $A_g(4)$ mode, which is also activated by the octahedron tilt operation $D_{[101]}$. Because this mode mimics the octahedron tilt introduced by reducing the R-site radius and, at the same time, it does not mix with other modes, it is a prime candidate to investigate the octahedron tilt for varied ionic radii of R. Not only does this mode allow us to investigate qualitative properties of how the octahedron tilt is affected by R-site substitution.

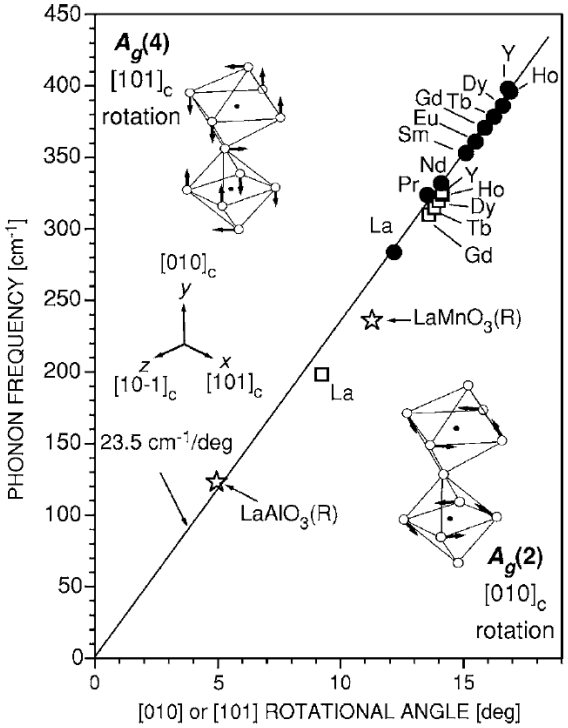

Figure 5.6: Frequency dependence of the $A_g(4)$ mode, associated with the octahedron-tilt operation $D_{[101]}$ (full circles) and the $A_g(2)$ mode, associated with the octahedron-rotation operation $D_{[010]}$ (empty squares). Adapted from [4].

Detailed spectroscopic Raman studies of Iliev *et al.*, see Fig. 5.6, on stoichiometric compounds ranging from $LaMnO_3$ ($r_{La^{3+}} = 1.22$Å) to $YMnO_3$ ($r_{Y^{3+}} = 1.08$Å) revealed a linear relationship between the $A_g(4)$ mode frequency and the angle Ψ_{101} of the octahedron tilt operation D_{101} [4]:

$$\frac{\partial \omega_{A_g(4)}}{\partial \Psi_{[101]}} \approxeq 23.5 \frac{\mathrm{cm}^{-1}}{\mathrm{deg}}. \tag{5.3}$$

In a way, this mode can be thought of a "soft mode" of the octahedron tilt, as $\omega(\Psi_{[101]}) \to 0$ for $\Psi_{[101]} \to 0$. This angle refers to the angle $\Psi_{[101]}$ of an individual octahedron. As the $D_{[101]}$ operation is applied out-of-phase to adjacent octahedra, an increase of one degree in $\Psi_{[101]}$ amounts to a reduction of the Mn-O-Mn bond angle ϕ by two degrees away from the cubic 180° bond angle. Concerning the Mn-O-Mn bond angle, the relation for the $A_g(4)$ mode frequency is therefore $\frac{\partial \omega_{A_g(4)}}{\partial \phi} \approxeq -11.8 \frac{cm^{-1}}{\mathrm{deg}}$. With this information it is possible to deduce an angular accuracy of ϕ in the order of a few 0.01°

by evaluating the Raman spectrum of this particular mode. The obtained Raman frequencies are listed in table Table 5.2 together with the Mn-O-Mn bond angles calculated with Eq. 5.3.

For improved consistency with the $T-\phi$ phase diagram, we use the values ω =360.8 cm^{-1} and ϕ = 147.22° for $EuMnO_3$ (see Refs. [4, 6]) as reference values. Table 5.2 is supplemented with values for ϕ extracted from Ref. [6]. The dataset of table 5.2 is also plotted in Fig. 5.7, which shows the $A_g(4)$ frequency $\omega(\phi)$ for the angles ϕ obtained via Raman spectroscopy with literature values of Raman- and XRD data for stoichiometric compounds. The linear relation 5.3, represented by the grey dotted line is well fulfilled. The $Eu_{1-x}Ho_xMnO_3$ datapoints show, that the increase in Ho-concentration x leads to a proportional increase in the $A_g(4)$ frequency ω. The one exception is the x =0.35 sample, which should fall right in-between the x=0.3 and x=0.4 values, but it appears to be too close to the x=0.3 specimen. This might be due to an inaccurate determination of the Ho content x. We see, that the $Eu_{1-x}Ho_xMnO_3$ series with $x \leq 0.5$ spans a range of $144.1° \leq \phi \leq 146.7°$. We can now compare the $T-\phi$ phase diagram of Kimura *et al.* for stoichiometric $RMnO_3$ with the $T-x$ phase diagram obtained by Ivanov *et al.* for $Eu_{1-x}Ho_xMnO_3$.

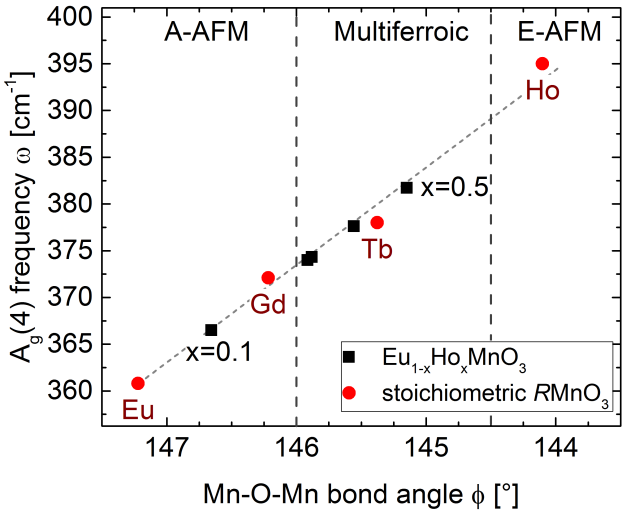

Figure 5.7: Frequency of the $A_g(4)$ mode at room temperature versus the Mn-O-Mn bond angle ϕ. red: data of stoichiometric $RMnO_3$ extracted from XRD [6] and Raman experiments [4]. black: values calculated via Eq. 5.3 and Raman measurements of $Eu_{1-x}Ho_xMnO_3$. The linear relation of ω and ϕ is indicated by the dotted grey line. Vertical broken lines separate the areas of different magnetic ground states for the various ranges of ϕ.

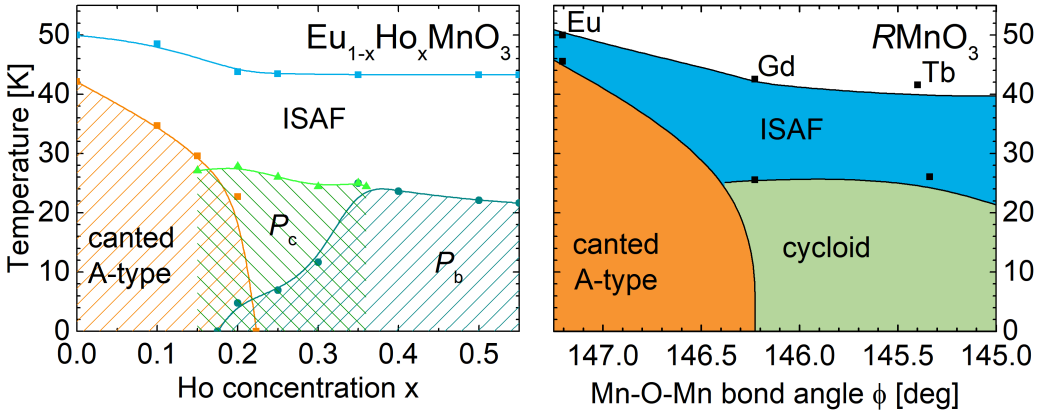

Figure 5.8: left panel: $T - x$ phase diagram for $Eu_{1-x}Ho_xMnO_3$ adapted from Ivanov *et al.*. P_c, P_b denote the directions of electric polarization which is induced by the cycloidal order in the multiferroic phase. Right panel: $T - \phi$ phase diagram of $R\mathrm{MnO}_3$. The ϕ-scale of 4.10 is chosen to display the ϕ values obtained from Raman spectroscopy for x=0 until x=0.5. Note the excellent agreement.

The comparison in Fig. 5.8 shows a phase diagram of $Eu_{1-x}Ho_xMnO_3$ determined by pyrocurrent measurements by Ivanov *et al.* in the left panel, while the right panel shows a magnified version of Fig. 4.10, where the T- and ϕ-scales have been set accordingly to cover the same range as the axis on left-hand-side panel, i.e., from $EuMnO_3$ (x=0) until $Eu_{0.5}Ho_{0.5}MnO_3$. The angular values are the ones evaluated from the results of Raman spectroscopy (see Table 5.2). In the left panel, $P_{c,b}$ denote the direction of electric polarization, which is induced by the cycloidal order of spins. Note the excellent agreement of both panels. It becomes clear that the $A_g(4)$ mode frequency is a very useful and accurate tool to determine where in the $T - \phi$ phase diagram of $R\mathrm{MnO}_3$ a sample is located. In particular, one can determine directly that a sample is within the multiferroic range if the $A_g(4)$ frequency is between 370 and 390 cm^{-1}.

5.3 Temperature dependence and spin-phonon coupling

All previous considerations were focused around the influence of R^{3+} substitution onto the lattice at room temperature, i.e. in the absence of magnetic order and far above the magnetic ordering temperature $T_N \approx$ 40-50 K to rule out any influence of magnetic effects. In the following, the temperature-dependent behavior of the $Eu_{1-x}Ho_xMnO_3$ Raman modes will be explored in the full temperature range from 300 K down to 5 K. As before, all phonon eigenfrequencies have been obtained by fitting the phonon peaks for each spectrum with a Lorentzian lineshape. Depending on the intensity of each individual peak and also its proximity to other peaks, the accuracy of the phonon frequency determination can vary widely. To give an idea of the accuracy of the fitting procedure, the error bars are based on the statistical error given by the fitting algorithm. As the raw values of statistical error usually underestimates the real error, the raw values have been multiplied by a factor of 10. This results in error bar values of 1 cm^{-1} for the weaker modes and values around 0.1 cm^{-1} for the stronger modes, which are realistic values for the frequency reproducibility capabilities of the spectroscopic apparatus. Note, some error bars are thus smaller than the plotted datapoint symbols. The results are shown in Figure 5.9 for the modes of A_g symmetry and in Figure 5.10 for the modes of B_{2g} symmetry.

As a general observation, in the temperature range of about 300 K> T >100 K, all modes show an increase of their frequency as the temperature is reduced. Once the magnetically ordered phases are approached, most modes show a pronounced softening (decrease of frequency) which continues well into the low-temperature magnetic phases. This applies both for the c-AFM phase in $Eu_{0.9}Ho_{0.1}MnO_3$ ($T \leq$35 K) as well as the multiferroic cycloidal phases from $Eu_{0.7}Ho_{0.3}MnO_3$ to $Eu_{0.5}Ho_{0.5}MnO_3$ ($T \leq$ 27 K). This softening is unanimously ascribed to spin-phonon coupling (SPC) [7, 8, 52]. To perform a quantitative analysis of the temperature-dependent impact of SPC onto the phonon frequency, it is mandatory to separate the SPC effect from the intrinsic temperature dependence of the frequency which every phonon, even in the absence of magnetic order shows as we have seen in section 2.4. The dominant contribution to $\omega(T)$ is the anharmonic decay of an optical phonon into two acoustic ones, described by the Klemens model [46, 47]. The formula Eq. 2.18 is used to fit the datapoints for $T \geq$100 K for all observed modes since at these temperatures one can assume that there should not be any influence of magnetic correlations. As Eq. 2.18 approaches

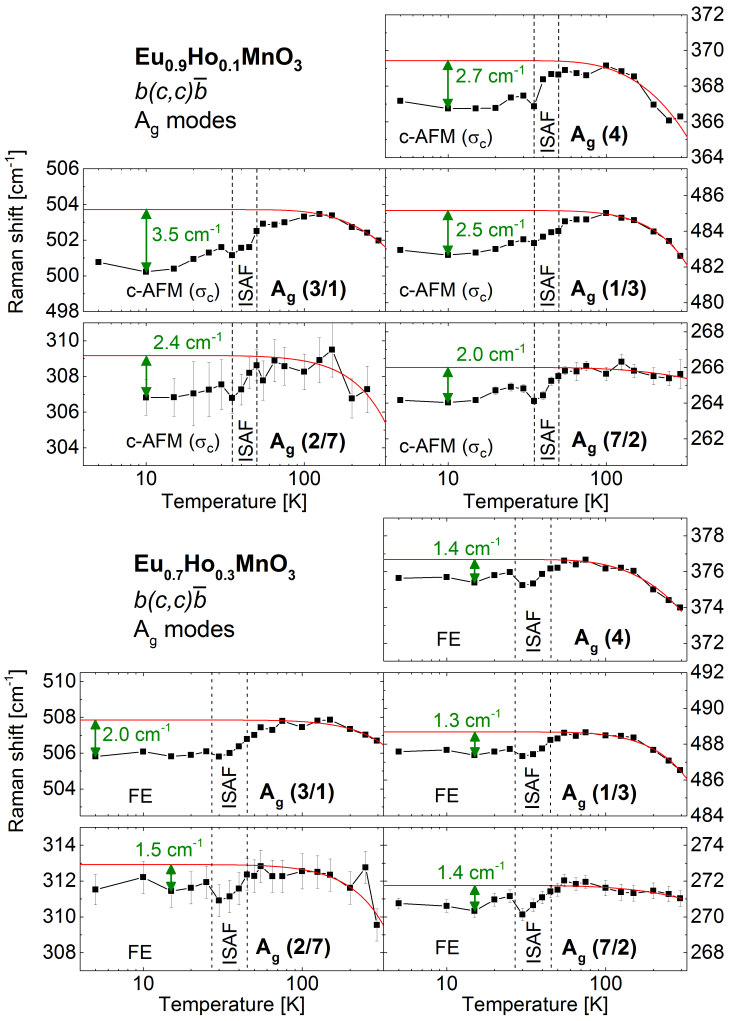

Figure 5.9: Temperature dependence for each individual mode frequency of A_g symmetry. The panels show the data for Ho contents x=0.1 and x=0.3.

a constant value for low temperatures, it becomes obvious that the experimental frequency values show a clear deviation from the Klemens-fit. This deviation is therefore not due to the purely decay-induced frequency shift behavior, but rather reflects the aforementioned spin-phonon coupling.

5.3.1 Mode dependence of SPC

In section 2.5 we have seen, that the SPC-induced frequency shift depends on the spin correlations $\langle \mathbf{S}_i \cdot \mathbf{S}_j \rangle$. Among the orthorhombic $R\mathrm{MnO_3}$ compounds, one would expect to see the most pronounced SPC effects for the A-type AFM

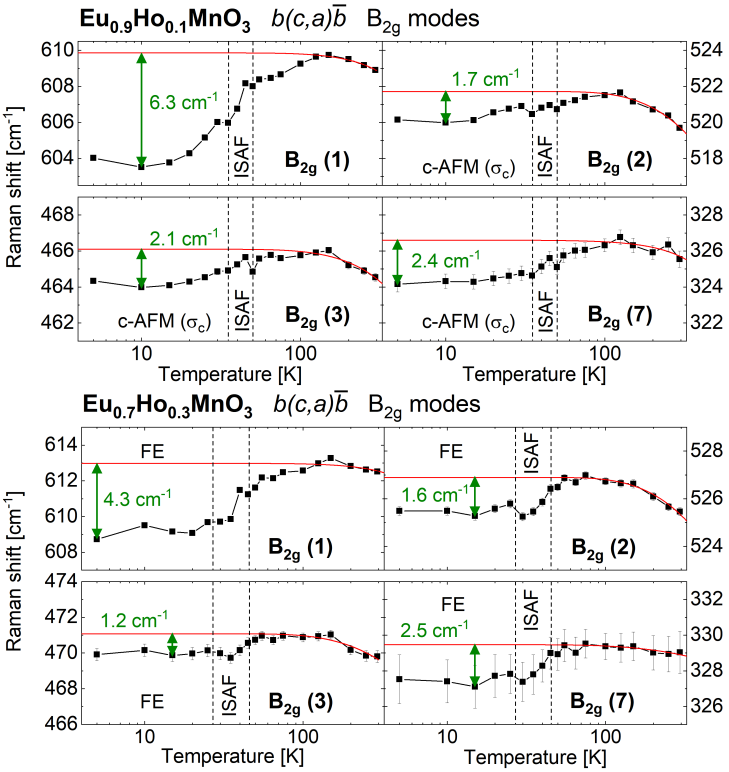

Figure 5.10: Temperature dependence for each individual mode frequency of B_{2g} symmetry. The panels show the data for Ho contents x=0.1 and x=0.3.

order where $\langle \mathbf{S}_i \cdot \mathbf{S}_j \rangle$ is maximal. As the ferromagnetic planes lie within the ac-planes, an additional expectation would be, that modes with oxygen displacements within the MnO_2 plane would be the most sensitive to magnetic correlations, as they directly alter the exchange integral between the in-plane Mn ions. Therefore, among the modes of B_{2g} and A_g, the $B_{2g}(1)$ and the $A_g(1)$ mode should show the strongest SPC-induced shift. For a comparison, the relative SPC shift is plotted in Fig. 5.11. The relative shift is calculated by subtracting the measured values for $\omega(T)$ from the values obtained by the fit according to the Klemens model with Eq. 2.18. This difference is then divided by the asymptotic value of the fit for $\omega(T \to 0)$, which corresponds to $\omega_0 + C$. Fig. 5.11 shows only $Eu_{0.9}Ho_{0.1}MnO_3$ and $Eu_{0.7}Ho_{0.3}MnO_3$, supplemented with data for pure $EuMnO_3$ from Issing *et al.*, as only for these samples reliable data for all modes of A_g, B_{2g} and B_{3g} symmetry could be obtained [7]. The samples with $x \geq 0.35$ suffered from inferior surface quality, which strongly diminishes the intensity of the modes in the spectra. Thus, the weaker modes could not be evaluated anymore.

The $B_{2g}(1)$ mode shows clearly the strongest SPC-induced relative shift, with

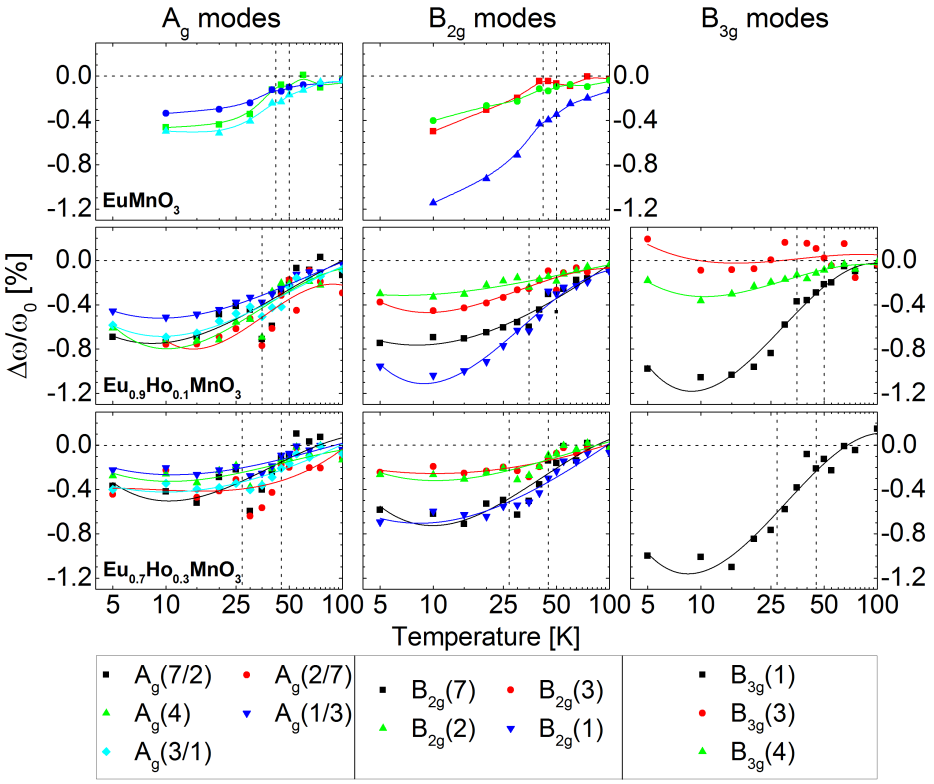

Figure 5.11: Raman shift relative to the zero-temperature frequency, determined as $\omega_0 + C$ in the Klemens-model. Broken lines indicate the magnetic transition temperatures according to Figure 5.8. The horizontal broken line is a guide to the eye for the reference frequency. With increasing Ho concentration, the SPC-induced shift is reduced for the A_g and B_{2g} modes, as the exchange interaction in the ac plane is weakened. For the $B_{3g}(1)$ mode, this is compensated by the increasing interaction along the b direction.

values up to -1.2%, which is in agreement with the expected strong dependence on the spin correlations for this mode. The maximum SPC shift is reached and saturates in the low-temperature magnetic phase. However, despite the $A_g(1)$ mode having a similar elongation pattern, it does not stand out from the other A_g modes. This can again be explained with the coupling of the $A_g(1)$ mode to the $A_g(1/3)$ mode, as the $A_g(3)$ mode shows oxygen displacements mainly perpendicular to the ac plane. Similarly like with the compositional dependence of the phonon frequency, a mode with strong dependence is mixed with a mode with weak dependence, resulting in a merely "intermediate" strength of the SPC shift like the other modes of A_g symmetry. A further differentiation of the other modes with respect to the magnetic correlations $\langle \mathbf{S}_i \cdot \mathbf{S}_j \rangle$ with symmetry arguments is rather challenging, as they involve elongation patterns that are neither solely within the ac plane nor solely parallel to the b axis. Among the A_g and B_{2g} modes, the $B_{2g}(1)$ mode is therefore the prime candidate to further investigate magnetic correlations via SPC effects. There is however another feature in the spectrum of $Eu_{1-x}Ho_xMnO_3$, the modes of B_{3g} symmetry, which have not been discussed in detail before. In the bottom panel of Figure 5.2, the spectra of $Eu_{0.9}Ho_{0.1}MnO_3$ and $Eu_{0.7}Ho_{0.3}MnO_3$ are shown for the $a(c,b)\bar{a}$ scattering configuration, which gives rise to the modes with B_{3g} symmetry. The necessary a-cut sample was available for x=0.1, for x=0.3 the b-cut crystal plate was intentionally tilted to improve the visibility of the B_{3g} modes. Several new modes appear in this configuration, the most intense of which is located around 650 cm^{-1}, identified as the $B_{3g}(1)$ mode in section 5.1.

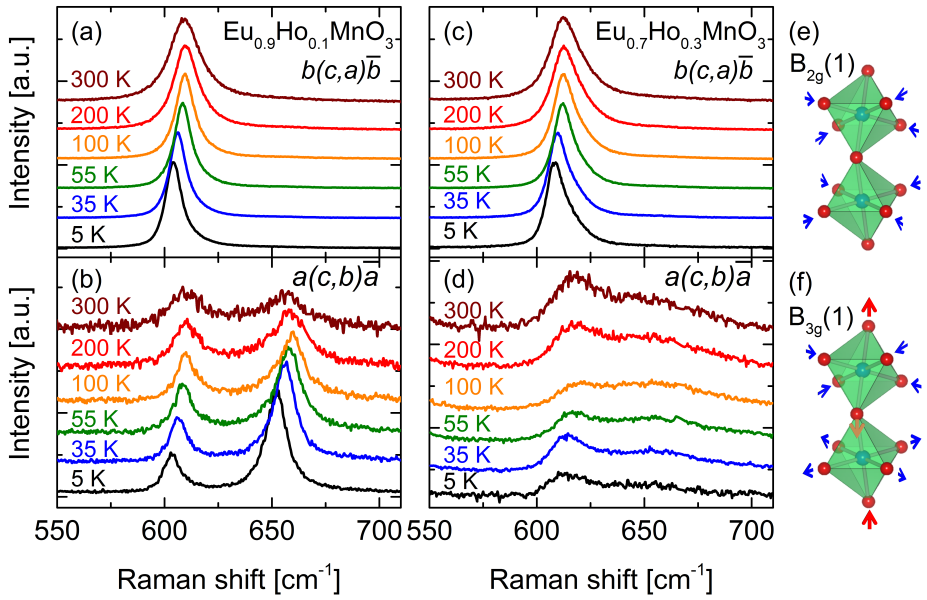

Figure 5.12: A more detailed comparison of the temperature-dependent spectra of the $B_{2g}(1)$- (panels (a,c):$\approxeq$ 610cm^{-1}) and the $B_{3g}(1)$ modes (panels (b,d)$\approxeq$ 650cm^{-1}). Note, that in panel (d), the $B_{3g}(1)$ mode appears only weakly as a shoulder to the $B_{2g}(1)$ mode. Panels (e) and (f) show the elongation patterns of the $B_{2g}(1)$ and the $B_{3g}(1)$ modes.

A more detailed comparison of the $B_{2g}(1)$ and the $B_{3g}(1)$ mode spectra is shown in Fig. 5.12. The frequency is slightly higher than of the $B_{2g}(1)$ mode and shows a good agreement with calculated values for the out-of-phase breathing mode of the MnO_6 octahedra (Fig. 5.12(f)) [3]. The temperature-dependent spectra show, that this feature shows a very similar behavior as the other phonon modes. In fact, it shows a similar SPC induced frequency shift as the $B_{2g}(1)$ mode, which triggers the assumption, that this mode should also be related to oxygen displacements between the manganese ions and therefore modulate the exchange integral. The displacement pattern of the $B_{3g}(1)$ mode is partially similar to the $B_{2g}(1)$ mode, as it involves oxygen displacements within the *ac*-plane. As an additional displacement, the apical oxygen ions are also in motion, parallel to the *b*-axis. This will prove crucial in the quantitative discussion of the SPC effects, as also the AFM interaction along the *b* direction comes into play with this elongation pattern. It is already obvious in this plot, that this additional interaction term plays a great role in the dynamics of this mode, as the SPC shift is nearly unchanged between x=0.10 and x=0.30, despite the decrease of SPC for the $B_{2g}(1)$ mode. This aspect will be discussed in the following sections 5.3.2 and 5.4.

Eventually, a small increase in frequency at the lowest investigated temperature of 5 K is observed for most modes, which is ascribed to the ordering of Ho^{3+} moments ($T_{Ho} \approxeq 6.5$ K in orthorhombic $HoMnO_3$[86]), as it is not observed for $Eu_{1-x}Y_xMnO_3$ where Y^{3+} is non-magnetic.

5.3.2 Composition dependence of SPC

As the SPC behavior of most lower-energy modes is not very differentiated, we are going to focus in the following mainly on the octahedron-breathing mode $B_{2g}(1)$ and the similar $B_{3g}(1)$ mode, which are the most interesting modes when magnetic effects are concerned. First, let us consider the SPC behavior of the $B_{2g}(1)$ mode for the various compositions of $Eu_{1-x}Ho_xMnO_3$. Figure 5.13 shows the temperature-dependent data of the frequency of this

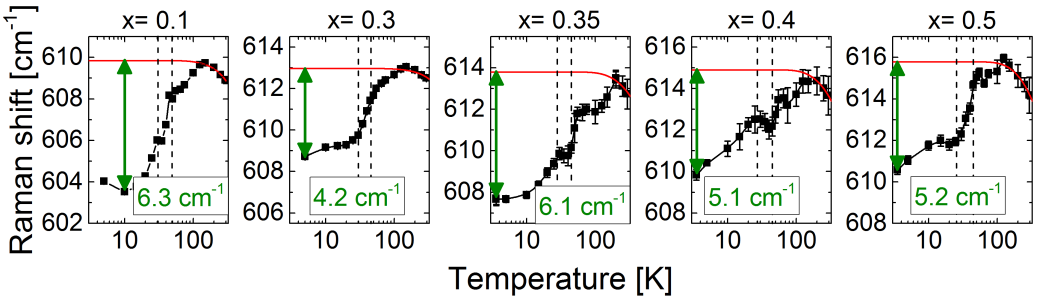

Figure 5.13: Temperature dependence of the $B_{2g}(1)$ mode in $Eu_{1-x}Ho_xMnO_3$. The expected phonon behavior due to anharmonic decay of phonons is fitted to the high-temperature data (red). The deviation from this behavior is attributed to spin-phonon coupling due to magnetization effects. Green numbers display the absolute value of the maximum SPC shift. The dashed lines correspond to the transition temperatures to the ISAF and cycloidal phases, as in the magnetic phase diagram of Figure 5.8.

mode for all samples. Like before, fits with the Klemens model according to Eq. 2.18 are drawn as red lines. The absolute value of the maximum amount of SPC shift relative to the Klemens model fit is shown as green numbers and arrows. Starting with $Eu_{0.9}Ho_{0.1}MnO_3$ and $Eu_{0.7}Ho_{0.3}MnO_3$, the maximum SPC-shift is first decreased as expected. With the decreasing Mn-O-Mn bond angle ϕ, induced by the incorporation of more and more of the smaller Ho^{3+} ions, the FM interaction in the ac plane is reduced and thus also the SPC is reduced. This is the analogous effect like in the $Eu_{1-x}Y_xMnO_3$ system, with the similarly sized Y^{3+} ion. However, in stark contrast to the behavior of the $Eu_{1-x}Y_xMnO_3$ system, $Eu_{0.65}Ho_{0.35}MnO_3$ shows again a particularly strong SPC shift and it eventually decreases again to an intermediate strength for

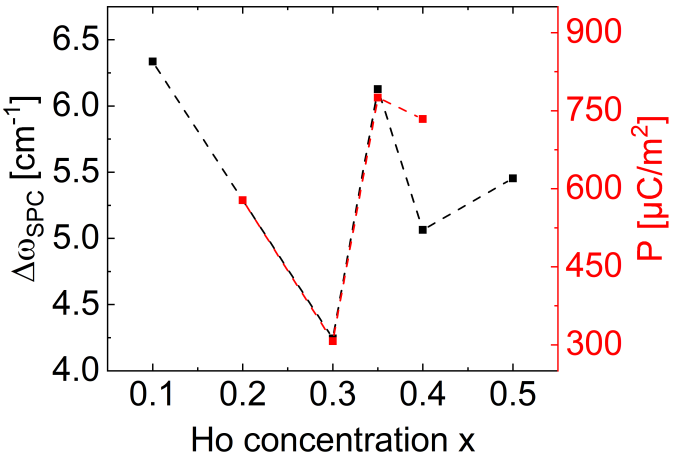

Figure 5.14: Comparison of the maximum SPC-induced frequency shift and the electric polarization for different Ho content. Both, $\Delta\omega_{SPC}$ and P show the same behavior with regard to the Ho content. The values for the total polarization P are calculated from the data of Ivanov *et al.*

the remaining two specimen $Eu_{0.6}Ho_{0.4}MnO_3$ and $Eu_{0.5}Ho_{0.5}MnO_3$, while in $Eu_{1-x}Y_xMnO_3$, the SPC shift nearly vanishes for Y-contents of x=0.4 and x=0.5 [80, 81]. It stands to reason that this is related to the presence of the magnetic moment of Ho^{3+} in some way. Considering the $T-x$ phase diagram of Fig. 5.8, we see that the x=0.35 sample is the sample where both directions of polarization, P_c and P_b appear at a similar strength. To examine this further, let us consider the graph shown in Fig. 5.14. This graph shows the values of the maximum SPC-induced frequency shift, as shown by the green arrows in Fig. 5.13 on the left y-axis and compares it with the total electric polarization, plotted with the right ordinate. The datapoints for the graph were calculated from the data extracted from Figure 3 of Ref. [5] by calculating the effective total polarization $P_{tot} = \sqrt{P_b^2 + P_c^2}$ [5]. Although there is no data for x=0.1, since it does not exhibit multiferroicity (and therefore $P = 0$), it can be seen that the polarization follows the same trend as the SPC strength of the $B_{2g}(1)$ mode. A possible explanation can be found in the additional exchange path introduced by the Ho-magnetic moment, which ultimately reorientates the spin cycloid from the ac to the ab plane due to the additional anisotropy energy for spins with a component parallel to the b-direction (see subsection 4.4.1). This would amount to an additional contribution in the SPC coupling parameters, resulting in the observed increased SPC-induced shift. This could explain the approximately constant SPC-shift for x=0.4 and x=0.5, where the SPC should decrease due to the R-ion size effect (decreased Mn-O-Mn bond angle ϕ and therefore lower J_{ac}), which

competes with the increasing contribution introduced by the Ho-spins.
Data for the $B_{3g}(1)$ could only be obtained for the x=0.1 and x=0.3 sample. Here, we see that the SPC-induced frequency shift is very similar for both samples. The in-plane interaction J_{ac} is reduced when going from $Eu_{0.9}Ho_{0.1}MnO_3$ to $Eu_{0.7}Ho_{0.3}MnO_3$, as evidenced by the behavior of the $B_{2g}(1)$ mode. Once again, we need to consider the elongation patterns: For the $B_{2g}(1)$ mode, only the oxygen ions within the ac plane participate. The $B_{3g}(1)$ mode features an additional displacement of the apical oxygen ions along the b-direction, which makes it mandatory to take the plane-to-plane interaction J_b into consideration. As discussed in 4.4.1, the plane-to-plane interaction J_b should increase with decreasing Mn-O-Mn bond angle ϕ and therefore with increasing Ho-content. The nearly constant SPC of the $B_{3g}(1)$ mode in $Eu_{0.9}Ho_{0.1}MnO_3$ and $Eu_{0.7}Ho_{0.3}MnO_3$ can then be understood as a superposition of two opposing trends: the decrease of J_{ac}, counteracted by the increase in strength of J_b. In the next section, we strive to achieve a more quantitative understanding of this phenomenon, by evaluating the SPC coupling parameters.

5.4 SPC coupling parameters

A quantitative expression with experimentally accessible parameters for the SPC shift of the $B_{2g}(1)$ mode was derived by Granado *et al.* and a short summary of the model was given in section 2.5. The final result was the expression in Eq. 2.26, which allows to calculate the FM coupling constant $\partial^2 J_{ac}/\partial u^2$ by evaluating the $B_{2g}(1)$ mode frequency, when also details about the spin correlations $\langle S_i \cdot S_j \rangle$ are known. We recall Eq. 2.25 here, but already evaluate the differential operators:

$$(\Delta\omega_\alpha)_{SPC} = -\frac{N}{2\mu_\alpha\omega_\alpha}\left(2\langle \mathbf{S}_i \cdot \mathbf{S}_j\rangle_{ac}\frac{\partial^2 J_{ac}}{\partial u^2} + \langle \mathbf{S}_i \cdot \mathbf{S}_j\rangle_b \frac{\partial^2 J_b}{\partial u^2}\right) \tag{5.4}$$

Granado *et al.* considered solely the $B_{2g}(1)$ mode, where only the oxygen ions in the ac-plane participate in the elongation pattern of the mode and thus the last term would vanish. In contrast, when considering the $B_{3g}(1)$ mode, the full equation 5.4 needs to be applied to calculate the SPC induced shift for the $B_{3g}(1)$ mode and the AFM exchange J_b enters the equation. The formalism of Granado *et al.* is therefore expanded to this mode with the aim of finding a relation for the SPC coupling strength $\frac{\partial^2 J_b}{\partial u^2}$. To do this, we multiply $((\Delta\omega_\alpha)_{SPC}$ by $\mu_\alpha \cdot \omega_\alpha$ and consider the difference of the equations for $\alpha = B_{3g}(1)$ and $B_{2g}(1)$. As the term with $\frac{\partial^2 J_{ac}}{\partial u^2}$ is the same for both modes,

it cancels out in the subtraction and the result simplifies to:

$$\mu_{B_{3g}}\omega_{B_{3g}} \cdot \left(\Delta\omega_{B_{3g}}\right)_{SPC} - \mu_{B_{2g}}\omega_{B_{2g}} \cdot \left(\Delta\omega_{B_{2g}}\right)_{SPC} = -\frac{N}{2}\left\langle \mathbf{S}_i \cdot \mathbf{S}_j \right\rangle_b \frac{\partial^2 J_b}{\partial u^2} \tag{5.5}$$

where the "(1)" enumeration was omitted as we are solely considering the $B_{2g}(1)$ and $B_{3g}(1)$ modes in this section. This equation can either be evaluated right away by measuring the frequencies ω_α and calculating their respective SPC shift ($\Delta\omega_\alpha$) as demonstrated in 2.5 under the assumption, that the reduced masses $\mu_{B_{3g}} : \mu_{B_{2g}}$ are in the ratio 3:2 (which corresponds to six versus four oxygen per octahedron which participate in the displacement pattern) and that the spins along b are aligned antiparallel, thus giving always the maximum but negative value for $\langle \mathbf{S}_i \cdot \mathbf{S}_j \rangle_b$. The latter is obviously fulfilled in the A-type AFM order, as this is the defining characteristic of an A-type AFM. But this also holds in the cycloidal phase, as the modulation vector of the cycloid is parallel to the a-axis while the antiparallel alignment of spins along b still stays intact in the cycloidal phase. [1] This equation can be processed further to include only numerical values which are often widely available in literature or can directly be measured. In the fully aligned (i.e., not canted) A-type AFM case, $\langle \mathbf{S}_i \cdot \mathbf{S}_j \rangle_b = -\langle \mathbf{S}_i \cdot \mathbf{S}_j \rangle_{ac}$ holds and can be used as an approximation for the A-type AFM case, as long as the spins are not canted too much. For the canted or cycloidal case a prefactor of $\cos^{-1}(\pi k)$ needs to be added to the ac-term. In the case of a cycloidal spin pattern, $\mathbf{k} = k_a$ is the cycloid modulation vector, whose only nonzero component is parallel to the a-axis. This yields

$$\mu_{B_{3g}}\omega_{B_{3g}} \cdot \left(\Delta\omega_{B_{3g}}\right)_{SPC} - \mu_{B_{2g}}\omega_{B_{2g}} \cdot \left(\Delta\omega_{B_{2g}}\right)_{SPC} = +\frac{N}{2}\cos^{-1}(\pi k_a)\left\langle \mathbf{S}_i \cdot \mathbf{S}_j \right\rangle_{ac} \frac{\partial^2 J_b}{\partial u^2}. \tag{5.6}$$

This equation can now be compared with Eq. 5.4 for $\alpha = B_{2g}$, where we can see, that

$$\frac{N}{2}\left\langle \mathbf{S}_i \cdot \mathbf{S}_j \right\rangle_{ac} = -\frac{1}{2}(\omega_{B_{2g}} \cdot \Delta\omega_{B_{2g}} \cdot \mu_{B_{2g}})/\frac{\partial^2 J_{ac}}{\partial u^2}. \tag{5.7}$$

Inserting Eq. 5.7 into Eq. 5.6 and solving for $\frac{\partial^2 J_b}{\partial u^2}$ yields

$$\frac{\partial^2 J_b}{\partial u^2} = 2\cos(\pi k_a)\frac{\partial^2 J_{ac}}{\partial u^2}\left(1 - \frac{3}{2} \cdot \frac{\omega_{B_{3g}}\Delta\omega_{B_{3g}}}{\omega_{B_{2g}}\Delta\omega_{B_{2g}}}\right) \tag{5.8}$$

[1] Note, that the sense of clockwise/counter-clockwise propagation of neighboring cycloidal planes along b is not affected by this, as it represents merely a phase shift of 180°.

	$\frac{\partial^2 J_{ac}}{\partial u^2}$ [mRy/Å^2]	$\frac{\partial^2 J_b}{\partial u^2}$ [mRy/Å^2]
$EuMnO_3$ [80]	13.4	-
$Eu_{0.9}Ho_{0.1}MnO_3$	12.2	-12.7
$Eu_{0.7}Ho_{0.3}MnO_3$	8.2	-18.6
$Eu_{0.65}Ho_{0.35}MnO_3$	12.7	-
$Eu_{0.6}Ho_{0.4}MnO_3$	10.6	-
$Eu_{0.5}Ho_{0.5}MnO_3$	10.9	-

Table 5.3: Spin-phonon coupling strength values $\frac{\partial^2 J_{ac}}{\partial u^2}$ (MnO_2-planes) and $\frac{\partial^2 J_b}{\partial u^2}$ (plane-to-plane) calculated with Eq. 2.26 and Eq. 5.8.

whereat the reduced masses have already been evaluated. This allows the quantitative evaluation of the plane-to-plane SPC coupling strength $\frac{\partial^2 J_b}{\partial u^2}$: $\frac{\partial^2 J_{ac}}{\partial u^2}$ is either well-documented in literature [8, 52, 81] or calculated in the usual way directly from measurements of the $B_{2g}(1)$ mode frequency and its SPC shift. The cycloidal modulation vector value k_a is also readily available in literature for all relevant stoichiometric compounds or can be measured for example in neutron diffraction experiments. The resulting coupling strengths are listed in table 5.3 The data in table 5.3 quantifies the behavior outlined in section 5.4. The in-plane coupling strength values decrease with increasing Ho-content until $x = 0.3$ in a very similar manner like in the $Eu_{1-x}Y_xMnO_3$ system from 13.4 mRy/Å^2 to 8.2 mRy/Å^2 [62, 81]. Although no absolute values for $\frac{\partial^2 J_b}{\partial u^2}$ are given in the reference for $Eu_{1-x}Y_xMnO_3$ with $x = 0.4$ and 0.5, it is clear from the temperature-dependent data, that it is continuously reduced even further. In contrast, $Eu_{0.65}Ho_{0.35}MnO_3$ shows a strong increase to 12.7 mRy/Å^2 in the coupling strength and it remains large for $Eu_{0.6}Ho_{0.4}MnO_3$ and $Eu_{0.5}Ho_{0.5}MnO_3$ with values of 10.6 mRy/Å^2 and 10.9 mRy/Å^2, respectively. Clearly, the presence of the Ho spins increases the SPC coupling strength also in the *ac*-plane. We like to recall the expression for the anisotropic free energy density Eq. 4.10 at this point:

$$\Phi_A \approx \frac{1}{2}K_{ac}^{Mn}A_x^2 + \frac{1}{2}K_{ab}^{Mn}A_z^2 - NT\ln\left[2\cosh(\Delta/k_BT)\right]. \qquad (5.9)$$

With increasing Ho content, the second term with the anisotropy constant K_{ab} for the *ab*-plane is strengthened. Since K_{ab} does not only act along the *b*-direction but within the *ab*-plane, the increase of SPC for $\frac{\partial^2 J_{ac}}{\partial u^2}$ for $x \geq 0.35$ can be understood with the increase of importance of the K_{ab} anisotropy term. Even the sudden increase for x =0.35 can be qualitatively understood. Due to the reorientation of the spin cycloid from the *ac* to the *ab* plane, the component A_z of the antiferromagnetic vector becomes larger as the new

energy minimum with the new cycloidal orientation is established in order for the system to optimize the K_{ab} contribution.

5.5 Magnetic-field dependence of SPC

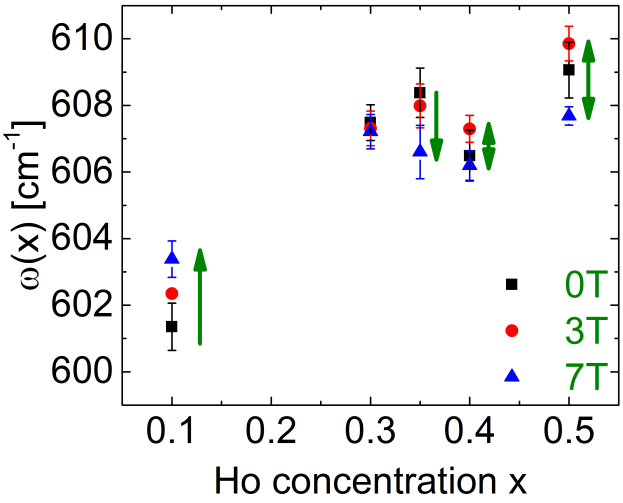

Figure 5.15: The $B_{2g}(1)$ mode frequency for all investigated $Eu_{1-x}Ho_xMnO_3$ compounds in the magnetic field. Green arrows act as a guide to the eye how the mode frequency shifts when the magnetic field is increased.

All previous experiments have dealt with the temperature-dependent behavior of SPC. However, a magnetic-field dependent characterization of SPC in Raman spectroscopy is still missing. For this, the samples were mounted in a liquid helium bath cryostat at a constant temperature of 2 K, with magnetic fields B_{ext} up to 7 T in Voigt geometry. In this geometry, it is possible to investigate SPC effects with incident radiation $E \parallel a, c, B \parallel c, a$ (where B is the magnetic component of the electromagnetic wave) and an external magnetic field $B_{ext} \parallel a, c$. It is noted, that Raman spectra were recorded in all combinations of mentioned polarization and magnetic field orientations. As the crystallographic axes a and c are nearly equivalent, no significant difference was observed in the spectra when the sample or the polarization was rotated by 90°. As a first observation, the spectra with magnetic field were practically identical to the spectra at 0 T. If any shifts of phonon frequencies or line broadening would occur, most of them are below the experimental resolution. Only the $B_{2g}(1)$ mode showed small noticeable effects and will once more be considered in more detail. Figure 5.15 shows the obtained phonon

frequency of the $B_{2g}(1)$ mode for the five $Eu_{1-x}Ho_xMnO_3$ compounds for a selection of magnetic fields. Only the non-multiferroic sample with x=0.10 shows an increase of the phonon frequency with magnetic field. Recalling the Klemens-fits from Fig. 5.13, this indicates a decrease of SPC strength, as the difference towards the Klemens model fit is decreased. The first multiferroic sample with x=0.30 shows no observable shift with magnetic field at all. The $x = 0.35$ sample, which is the first sample where the spin cycloid is spontaneously reoriented due to the Ho moments, shows a decrease of phonon frequency with magnetic field, which means that the SPC is actually strengthened. The latter two samples with x=0.40 and x=0.50 both show a behavior, which is different from the former ones: First, the phonon frequency is slightly increased and then decreases again for larger magnetic fields. This intriguing reversal of $\partial\omega/\partial B_{ext}$ is illustrated in Fig. 5.16. The

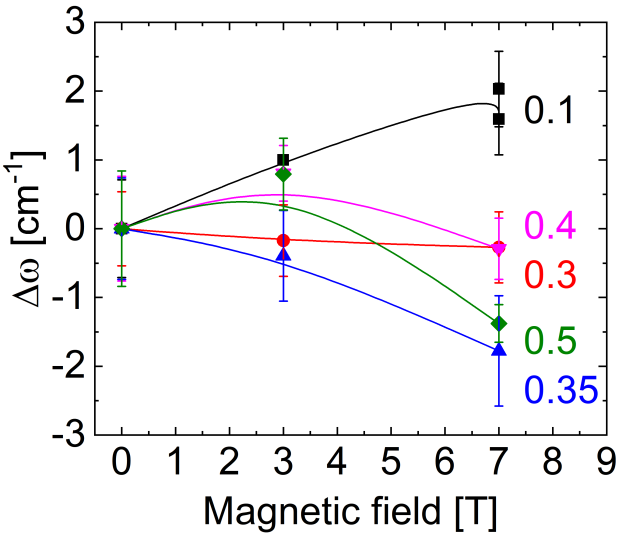

Figure 5.16: Shift of the $B_{2g}(1)$ mode frequency relative to $\omega(B_{ext} = 0)$. Interesting is the reversal of slope from positive (for x=0.10) to negative for $x \geq$0.35.

lack of any pronounced trend is not unexpected: While the infrared-active phonons carry an electric dipole moment, it is expected and observed that the infrared modes are affected by the multiferroic order. Most notably the spectral weight transfer from the lowest-lying phonon mode towards the electromagnon [62]. If the multiferroic order is suppressed or the rotational plane of the spin cycloid is flipped by the application of the magnetic field, this has direct consequences for the modes in the spectra, as the EM disappears or changes selection rules, while the phonon regains its spectral weight

[15, 16, 41, 87, 88]. In Raman spectroscopy, the SPC coupling should only depend on the superexchange integral between Mn sites and should therefore be determinded by the crystal lattice. One possible explanation for a B-field dependence could be that the external magnetic field would affect the crystal lattice and therefore would change the superexchange intergral. However, this should in turn also show up as a shift of the $A_g(4)$ phonon frequency if the Mn-O-Mn bond angle ϕ would be affected, which is either not the case or the effect is too small to be observed. For the x=0.10 sample with c-AFM order, the decrease of SPC could originate from a possible slight rotation of the canted, ferromagnetically ordered ac layers of Mn-spins towards the magnetic field. Another approach could be that the Ho moments *increase* the SPC if they are aligned with the magnetic field. This could explain why the x=0.10 sample, which contains the fewest Ho-ions, shows a weakening of SPC. With x=0.30 the effects of weakening and strengthening by Ho cancel out and reach the maximum effect for x=0.35. Unfortunately, the explanation does not hold for $x \geq 0.40$. The results show, that the effects of the external magnetic field may be small compared to the overall SPC strength, but are not negligible. The magnetic-field dependent behavior in itself reveals an interesting dynamics, which was not expected. Clearly, further research and theoretical input is needed to fully clarify the effects of incorporating Ho into this system.

5.6 Impact of local order to SPC above T_N

In the previous discussion of the magnetic properties of the multiferroic $R\mathrm{MnO_3}$ compounds the magnetic phases (as depicted in Fig. 5.8) start in the cycloidal phase below $T_{cycl} \approxeq 28$ K as ground state and with increasing temperature, go through an intermediate sinusoidal collinear phase ($T_{cycl} < T < T_N$) before arriving in the paramagnetic state ($T > T_N \approxeq$ 40-50 K). However, a static sinusoidal order does not agree with the fact that the Mn^{3+} ion should exhibit a Heisenberg spin with constant magnitude of $S = 2$. A more satisfying approach is to view the sinusoidal order as a time-averaged mixture of cycloidal phases, as suggested by model calculations and by recent analysis of dielectric relaxation [89, 90]. The question arises, what comprises the underlying nature of the intermediate magnetic order above T_{cycl} and how the low-temperature cycloidal phase proceeds towards the transition into the paramagnetic phase.

5.6.1 Experimental results

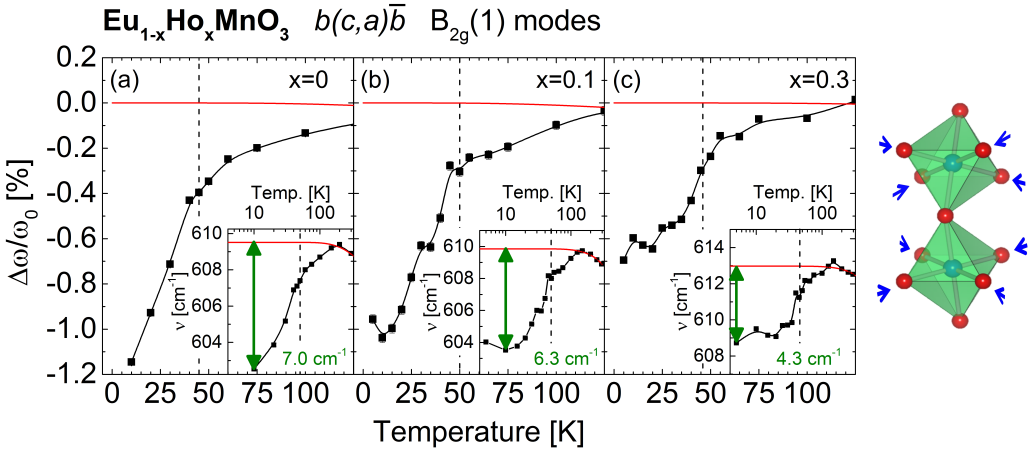

Figure 5.17: Phonon frequency renormalization of the $B_{2g}(1)$ mode of $Eu_{1-x}Ho_xMnO_3$ for (a) x=0, (b) x=0.10, and (c) x=0.30, relative to the extrapolated frequency $\omega(T \to 0)$ of the Klemens model (Eq. 2.18). The deviation from the Klemens fit (red curves), caused by SPC starts already at about 100 K. Dashed lines indicate T_N.

An important result of the temperature-dependent Raman studies is that SPC is not confined only to the magnetically ordered phases below T_N. Already far above T_N, up to temperatures of about 100 K, the SPC-induced deviation from the Klemens model fit is observed. Figure 5.17 shows this

	T_N [K]	T_{SPC} [K]
$EuMnO_3$	50	100-130
$Eu_{0.9}Y_{0.1}MnO_3$	48	100-120
$Eu_{0.8}Y_{0.2}MnO_3$	47	100
$Eu_{0.7}Y_{0.3}MnO_3$	46	100-110
$Eu_{0.6}Y_{0.4}MnO_3$	46	50-60
$Eu_{0.5}Y_{0.5}MnO_3$	45	50-60
$GdMnO_3$	45	80
$TbMnO_3$	42	50-60

Table 5.4: Magnetic order temperatures T_N and approximate temperatures T_{SPC} for the onset of spin-phonon coupling obtained by Raman spectroscopy [80, 81]. Spin-correlations are present even at $T \gg T_N$.

clearly. The SPC-induced frequency shift $\Delta\omega_{SPC}(T) = (\omega_0 - C) - \omega(T)$ is proportional to the spin correlations

$$\Delta\omega_{SPC} \propto \langle \mathbf{S}_i \cdot \mathbf{S}_j \rangle \tag{5.10}$$

see also Eq. 2.24. Of course, Eq. 5.10 is not confined to a global cycloidal order. Therefore, it also occurs for non-multiferroics, such as $EuMnO_3$ (Fig. 5.17a) and $Eu_{0.9}Ho_{0.1}MnO_3$ (Fig. 5.17b), which show the A-type AFM order, and reflects magnetic correlations at a local level [81]. This indicates nonzero local spin correlations $\langle \mathbf{S}_i \cdot \mathbf{S}_j \rangle$, even at this elevated temperature, in contrast to an abrupt ordering of spins at $T_N \approxeq 50$ K or even at T_{cycl} of about 25 K. Similar results have been obtained for multiferroic $GdMnO_3$ and $TbMnO_3$ as well as for $Eu_{1-x}Y_xMnO_3$([80, 81]) and various other multiferroic $RMnO_3$ compounds, but are rarely discussed in detail. Examples for the onset temperature of SPC are given in table 5.4. The onset temperature of SPC exceeds T_N by far. For most of the compounds by a factor of two or even greater.

SPC at $T \ll T_N$ is shown in the Raman data of several other research groups and appears to be a more general feature of $RMnO_3$ compounds, but in none of these reports this observation is discussed in terms of Mn-spin order in this temperature range [52, 53, 91]. The existing results on the temperature dependence of SPC in $RMnO_3$ can be explained consistently by assuming that SPC is due to local, short-range order of the Mn spins, persisting far above T_N. In a collaborative effort we could show that also both, the high- and the low-energy electromagnon, which are the elementary excitations of the cycloid, persists beyond the cycloidal phase, which supports the interpretation given above. The corresponding THz- and infrared spectra are

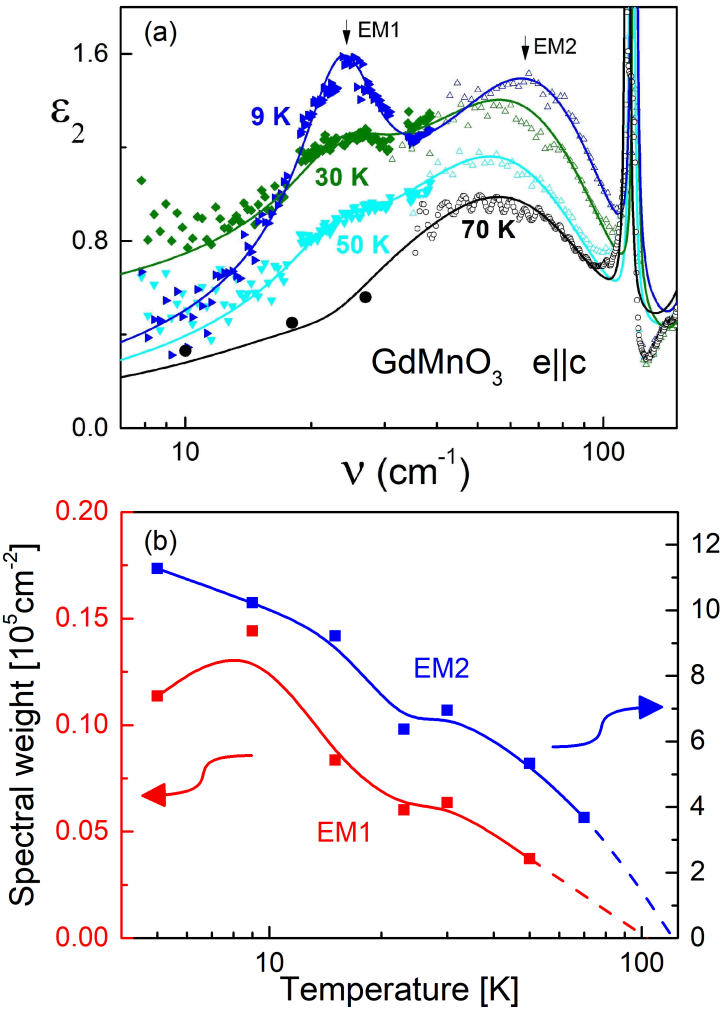

Figure 5.18: (a) Imaginary part of the THz- and infrared permittivity of $GdMnO_3$ below and above the magnetic ordering temperature $T_N \approxeq 40$ K. The two electromagnons are marked as EM1 and EM2. The strong feature at 120 cm^{-1} is an infrared phonon [59]. (b) Spectral weight of the two electromagnons of $GdMnO_3$ as obtained from the spectra in panel (a) [11]. Red symbols: EM1 at 25 cm^{-1} from the THz data, black symbols: EM2 at 80 cm^{-1} from the infrared data. Lines are guides to the eye. Their extrapolation demonstrates the characteristic energy scale of 100 K.

shown in Fig. 5.18(a). Interestingly, $GdMnO_3$ is a material with no clearly established cycloidal phase [56]. However, well-defined electromagnons at THz frequencies strongly suggest the existence of at locally correlated cycloids. In contrast to the similar compound $DyMnO_3$, the disorder does not allow the observation of static electric polarization. The electromagnons in $GdMnO_3$ are observed up to 70 K (Fig. 5.18a). For a better quantification, it is useful to consider the spectral weight

$$SW = \int_0^\infty Re(\sigma(\omega))d\omega \tag{5.11}$$

where $\sigma(\omega)$ is the complex optical conductivity. In the case of a Lorentzian lineshape the spectral weight is equal to

$$SW = \frac{\pi}{2}\varepsilon_0\Delta\varepsilon \cdot \omega_0^2 \tag{5.12}$$

with the vacuum permittivity ε_0 and $\Delta\varepsilon$ and ω_0 as the dielectric contribution and eigenfrequency of the Lorentzian, respectively. The results of this procedure are shown in Fig. 5.18b. Clearly, the EM are visible until 70 K, which is a temperature already above the ISAF phase. A polynomial extrapolation points also towards a temperature of about 100 K until the EM fully disappears. This is a strong indication for the persistence of spin cycloids.
Further evidence of cycloids above T_N showed up with an experiment by De and Sundaresan [92]. They aligned all cycloids by poling the sample in an electric field. Afterwards they measured the remaining electric polarization after heating up and cooling down the sample with the pyrocurrent method. They found, that the original polarization is recovered even if the sample is heated up to about 90 K. Since the polarization is directly coupled to the existence of the cycloids, this also points towards the existence of coupled cycloids up to this temperature, in line with the presented results of SPC in Raman spectroscopy and the electromagnon activity.
Therefore, instead of the commonly used description of the intermediate magnetic phase with a sinusoidal order, the idea of describing the magnetic structure with cycloids is extended to higher temperatures.

5.6.2 Order-disorder limit: The pseudospin model

A usfeul idea to describe the intermediate magnetic phase is the pseudo-spin model [90, 93]. Basically, to every pair of spins, an electric dipole is ascribed. This dipole is refered to as a "pseudospin", as it can only point either "up" or "down" corresponding to the polarization directions $\pm P_a$ in the multiferroic phase, which are caused by the clockwise or counter-clockwise rotation

of the cycloids. The macroscopic electric polarization is then proportional to the occupation difference of cycloids with opposite chiralities. The electric polarization can then be regarded as the primary order parameter. The two possible directions of electric dipoles, which are associated with the displacement of the O^{2-} ions between the magnetic Mn-ions, are assumed to be separated by an energy barrier E_A in a double-well potential and are coupled. This is illustrated in Fig. 5.19. The minima in the double-well po-

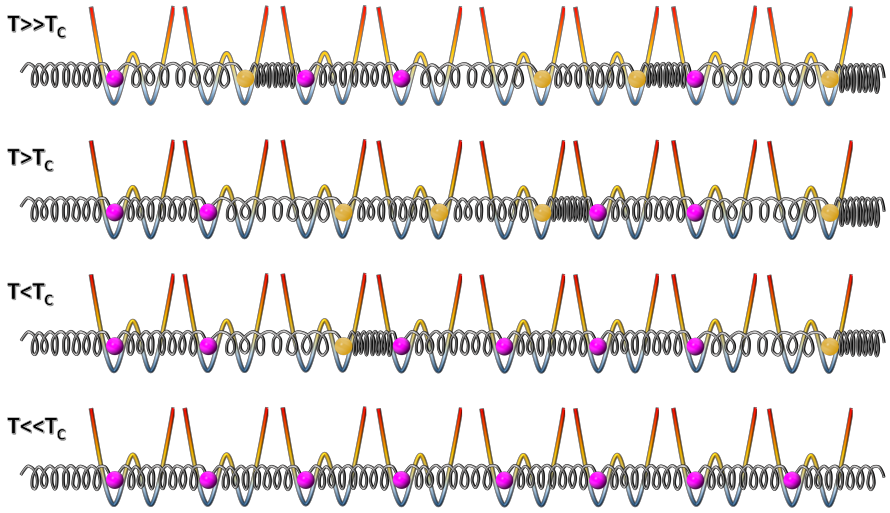

Figure 5.19: Sequence of ordering of atoms in a double-well potential in the order-disorder limit with a critical T_{cycl}. Magenta and yellow balls indicate ions in the left or in the right state of the potential. At high temperatures $T \geq T_{cycl}$ the positions of neighboring ions are not correlated in any significant way. Near the transition temperature a degree of short-range order is established. Below the transition temperature one side of the double-well potential is favored and a long-range order appears. Well below the transition temperature each ion occupies the same side of the double-well potential. Adapted from [11].

tential correspond to the two possible oxygen displacements introduced by the inverse DM interaction. If the chirality of the spin cycloid is reversed, the intermittent oxygen ion is displaced into the opposite direction, i.e. the other minimum in the double-well potential. The stability of a once-formed cycloid is ensured by the energy barrier, which separates the two energy minima. Each site is coupled with its neighbors, which leads to the correlated long-range order at low temperatures. Depending on the ratio E_A/k_BT_{cycl}, two limiting cases exist. For $E_A/k_BT_{cycl} \leq 1$ the transition of the displacive type. The ions can vibrate inside the double-well potential. At higher tem-

perature, the time-averaged displacement is zero. When the temperature is reduced, due to the interionic coupling, the vibrating ions start collectively to gradually shift their average position towards one of the potential minima. Also when a single ion is considered, the appearance of the electric dipole moment is thus continuous.
For $E_A/k_BT_{cycl} \geq 1$, we find ourselves in the so-called order-disorder limit. The energy barrier is now too large and the ions are confined to either one of the potential minima. In contrast to a phase transition of the displacive type, the local dipole moment is always nonzero and changes abruptly when the ion jumps into the other potential minimum [94–96]. This is indeed the case here [90, 93]. The coupling between the pseudospins can then be described as a Hamiltonian, which is similar to an Ising-type Hamiltonian:

$$H \propto -\sum_{R,R'} (\Delta x)^2 J_{R,R'} \cdot \sigma_R \sigma_{R'} \tag{5.13}$$

where Δx is the displacement of the oxygen ion, $J_{R,R'}$ is the coupling constant between the oxygen ions at the positions R and R' and σ_R is the pseudospin at position R with $\sigma_R = x_R/\Delta x$, which can take the values ± 1. E_A is the activation energy, which determines the characteristic energy scale and therefore the height of the energy barrier between the two possible pseudospin orientations. For the dynamics of the order parameter, the flips of pseudospins are of main interest, since a flip of a pseudospin corresponds to a motion of an oxygen ion. For $T < E_A$, the ions reside in one or the other side of the double-well potential and a local cycloidal spin order is present, due to the inverse DM interaction. The absence of macroscopic polarization is then merely a result of about equal occupation of "up" or "down" pseudospins in this temperature regime. On the other hand, only for $T > E_A$, the local potential does not force ions to stay in one side of the double-well potential. Instead, the ions vibrate around the average position and the shape of the double-well potential has only a small effect to modify the phonon frequency. The analysis of the dielectric relaxation characteristics of $DyMnO_3$ near the magnetically induced ferroelectric phase transition according to the pseudospin model confirmed an order-disorder type transition with an experimentally determined activation energy of $E_A \approxeq 100$ K [90].

In this framework, the evolution of the magnetic structure of a multiferroic compound with increasing temperature can be explained as a pseudospin system of two possible types of cycloids with opposing chirality. Instead of disappearing above T_{cycl}, they locally persist up to an energy scale of 100 K. Due to the local character, this should not be understood as a phase transition at 100 K, but rather as a gradual onset of local order, starting below

100 K. The vanishing polarization between T_{cycl} and 100 K is then simply a consequence of the model, when "up" and "down" pseudospins are occupied with equal occupation numbers, thus canceling out the macroscopic polarization.

5.7 Transient violation of Raman selection rules in $Eu_{1-x}Ho_xMnO_3$ at the cycloid reorientation temperature

As established in 2.3 and 5.1, when specific polarization configurations are used in a Raman experiment, the experimenter can choose which modes are detected in the Raman spectrum, while other modes are forbidden by the symmetry selection rules of incident and detected polarization. For the orthorhombic $R\mathrm{MnO_3}$, there are polarization configurations where modes of A_g and B_g symmetry are mutually exclusive. Such configurations on which we will focus in this section are, for b-cut samples, $b(a,a)\bar{b}$ or $b(c,c)\bar{b}$, where only modes of A_g symmetry are allowed, and $b(c,a)\bar{b}$ or $b(a,c)\bar{b}$ where only modes of B_{2g} symmetry are allowed. Although, in an actual experiment, small contributions of the symmetry forbidden phonon modes might occur. These leakages of forbidden modes into the spectrum are typically due to marginal misalignment of polarization in the optical setup or depend on the sample quality. Let us consider the spectra of $\mathrm{Eu_{0.7}Ho_{0.3}MnO_3}$ and $\mathrm{Eu_{0.9}Ho_{0.1}MnO_3}$ for the two complementary polarization configurations $b(c,c)\bar{b}$ and $b(c,a)\bar{b}$, shown in Figure 5.20 in a very narrow temperature range of about 5 K around the onset temperature of cycloidal order, $T_{\mathrm{onset}} \sim 31\,\mathrm{K}$.

The spectral range in the graphs shows the five octahedron stretching and bending modes of highest frequency: The two intermixed $\mathrm{A}_g(1/3)$ and $\mathrm{A}_g(3/1)$ modes and the $\mathrm{B}_{2g}(1)$, $\mathrm{B}_{2g}(2)$ and $\mathrm{B}_{2g}(3)$ modes. The selection rules are well fulfilled for most spectra. This applies for the whole temperature range of 5 K - 300 K (see also 5.3). Apart from small leakages, the A_g modes appear for $b(c,c)\bar{b}$ and the B_{2g} modes for $b(c,a)\bar{b}$. The results in Figure 5.20 show for every polarization configuration a group of up to six nearly identical spectra, which are superimposed on top of each other in black and illustrate the conventional polarization dependence. However, in this particular temperature range, a striking violation of selection rules is observed in very few anomalous spectra, which are also superimposed on top of each other in red. They show a strong enhancement of the modes with B_{2g} symmetry in the $b(c,c)\bar{b}$ spectra (Fig.5.20(a,c)) and conversely the A_g modes in the $b(c,a)\bar{b}$ configuration (Fig. 5.20(b,d)). The anomalous spectra always appear in the temperature range of the onset of the development of macroscopic polarization, T_{onset}. The symmetry-rule violation is most obvious for the strong octahedron stretching mode $\mathrm{B}_{2g}(1)$ ($\sim 610\,\mathrm{cm}^{-1}$) for the $\mathrm{Eu_{0.7}Ho_{0.3}MnO_3}$ sample (Fig. 5.20(a)). In this panel, also the forbidden $\mathrm{B}_{2g}(2)$ and $\mathrm{B}_{2g}(3)$ modes appear clearly on the shoulders of the two A_g modes at T_{onset}. In the same way, the forbidden mode pair $\mathrm{A}_g(1/3)$ and $\mathrm{A}_g(3/1)$ appears in the

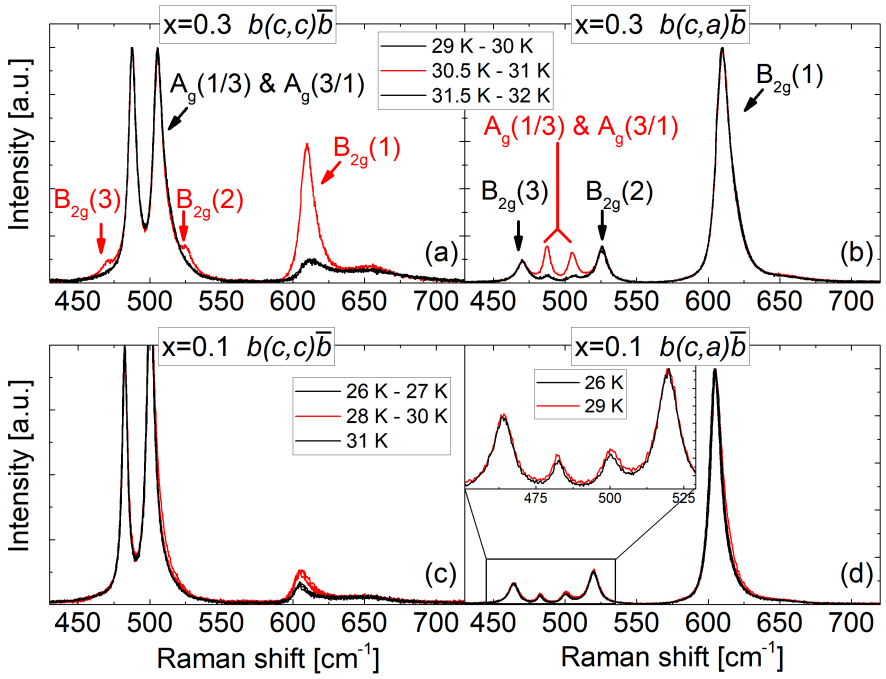

Figure 5.20: Polarized Raman spectra of the $Eu_{1-x}Ho_xMnO_3$ lattice vibration modes for x=0.3 (a,b) and x=0.1 (c,d) in the T-range of the onset of cycloidal order. The black spectra for different temperatures are virtually superimposable and show conventional symmetry behavior, while the red spectra show a violation of symmetry selection rules.

$b(c,a)\bar{b}$ spectra of Fig. 5.20(b) at this temperature. The effect is also observed for $Eu_{0.9}Ho_{0.1}MnO_3$, although it is far less pronounced as can be seen in panel (c) and in the inset of panel (d).

For a more quantitative treatment of the forbidden-phonon intensity which is induced by the selection-rules violation at T_{onset}, the following method is employed: The area of the various modes are integrated. Note, due to the close proximity of of the $B_{2g}(2)$, $B_{2g}(3)$ and the $A_g(1/3)$ and $A_g(3/1)$ modes, these four modes are integrated together as one group. The areas obtained from the spectra with conventional behavior are taken as a basis to compensate for the expected temperature behavior of photon scattering intensity with a fit according to References [46, 47]. This fit is defined as a reference to normalize to experimental area values to. The value obtained in this way is denoted as the enhancement factor. For the conventional spectra, this enhancement factor is therefore close to unity, which reflects the good fulfillment of selection rules. For the unconventional spectra, the enhancement factor is larger than one. The resulting temperature dependence for

the x =0.3 sample is shown in figure 5.21. The enhancement factor for the forbidden B_{2g} in the $b(c,c)\bar{b}$ scattering configuration is shown in figure 5.21(a) and the forbidden A_g modes in $b(c,a)\bar{b}$ scattering configuration are shown in 5.21(b). Obviously, the enhancement factors are close to unity, with only small statistical fluctuations due to the low residual intensity of the leaked peaks, which is a quantitative confirmation of the conventional behavior. The striking exception is at T_{onset}, where the factor increases abruptly in a step-like manner. On average the enhancement amounts to about 3.5 with values ranging from 2.5 to 4.5, depending on the individual phonon modes. Although the factor for the $A_g(1/3)$ and $A_g(3/1)$ modes is the largest one should note that this value is the least reliable due to the way of integration because of their close proximity. Repeated temperature scans confirmed the extremely narrow temperature window of the selection rule violation of about 1-2 K. The findings for the x=0.1 sample are qualitatively the same, with the enhancement factor being much lower at values of around 1.5.

To investigate, if the appearance of this phenomenon depends on the tem-

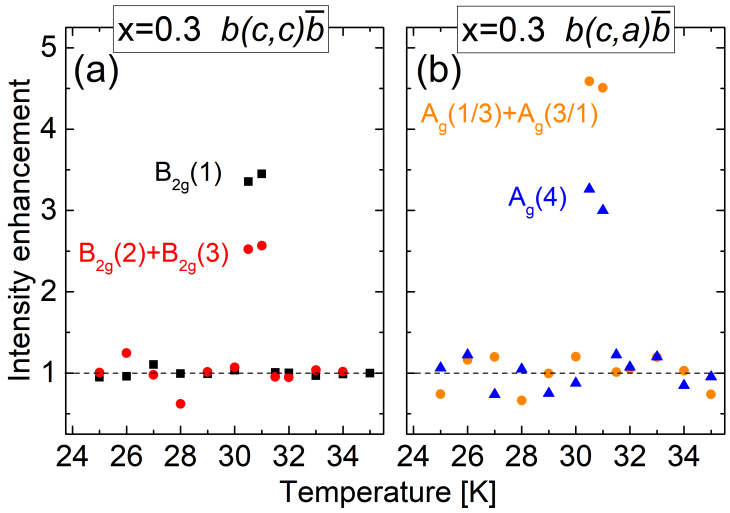

Figure 5.21: Temperature dependence of the intensity-enhancement factor of the symmetry-forbidden vibrational modes of $Eu_{0.7}Ho_{0.3}MnO_3$. A factor equal to one (indicated by the dashed line) corresponds to conventional behavior, whereas a factor > 1 indicates an increased intensity of the symmetry-forbidden modes. (a) Parallel polarization configuration, where the forbidden modes of B_{2g} symmetry appear and (b) orthogonal polarization configuration where the forbidden modes of A_g symmetry appear.

perature scanning procedure, several temperature cycles with different approaches were performed: cooling down from room temperature and while

warming up from 5 K, initial cooling to 5 K at slow and high cooling rates all showed this phenomenon. A more challenging task proved to be the effort to pinpoint whether the anomaly appears at a specific temperature or if it exhibits hysteresis. For this, several temperature runs in close proximity were performed, once the phenomenon was detected. As an example, a schematic cooling sequence is shown in Fig. 5.22. In this example, the sample is cooled

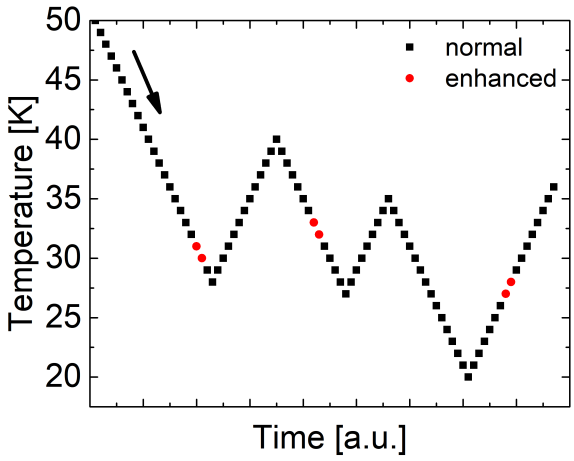

Figure 5.22: Schematic procedure of a temperature sequence to test for hysteresis. Each data point represents a spectrum acquisition at the corresponding temperature. Black points denote normal behavior of the intensity, red points indicate the appearance of the forbidden modes. While the enhancement does occur at different temperatures, the T values appear to be randomly shifted in the close vicinity of T_{onset} and therefore do not follow the typical behavior of hysteresis.

until the enhancement is detected (red data points). The temperature is then reduced even further until the modes recovered their conventional behavior. Afterwards, the temperature is increased again. If the phenomenon would show hysteresis effects, the temperature at which it appears would be at higher T-values when warming up and at lower values when cooling down. This is clearly not the case. Various temperature scans have revealed the relevance of the temperature scanning procedure around T_{onset}. When T_{onset} is crossed in a temperature scan and the normal selection rules have recovered, the violation of selection rules can only be observed from anew when T_{onset} was exceeded by several Kelvin, before scanning the temperature in the opposite direction. Furthermore, scanning the temperature back and forth closely around T_{onset} shows slight sequence-dependent shifts of a few Kelvin of the exact temperature at which the selection-rule violation occurs [12].

For an approach of explanation of this effect, we consider the Raman selection rules once more. The Raman scattering matrices are derived from the symmetry of the lattice [45]. Even when time-inversion symmetry is broken when the system enters a magnetically ordered phase, the selection rules still apply as long as the spatial symmetry remains unchanged. In multiferroic orthorhombic manganites, the spatial inversion symmetry is broken via the inverse DM interaction of Eq. 4.3 as the cycloidal spin order leads to the development of ferroelectric polarization. Yet, in all experimental results reported for a wide variety of $R\mathrm{MnO_3}$ compounds, it is shown that the selection rules still remain intact in the magnetically ordered phases [6–8, 52, 80, 81]. The transient violation of Raman selection rules at a specific temperature T_{onset} must have a different origin. The question is therefore: what mechanism can reduce the lattice symmetry at this particular temperature to account for the observed symmetry violation?

In the spirit of section 5.6.2, one possible cause could be based on the char-

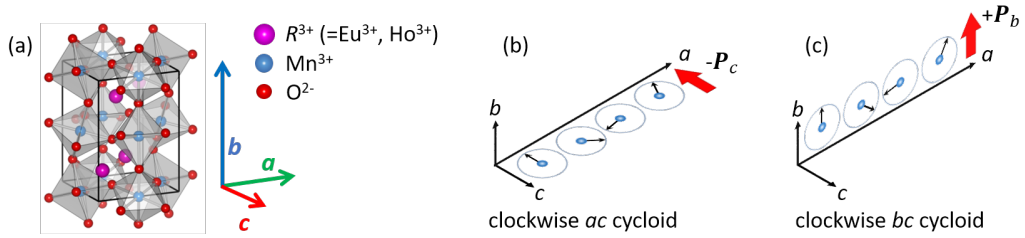

Figure 5.23: (a) Unit cell of the orthorhombic $R\mathrm{MnO_3}$ in *Pnma* notation. (b,c) Two of the four possible spin-cycloid patterns in $\mathrm{Eu_{1-x}Ho_xMnO_3}$ with the resulting electric polarization $\mathbf{P}$. If the cycloids rotate counter-clockwise, the respective polarization directions are inverted. Adapted from [12].

acteristic structure of domain walls (DWs) in $\mathrm{Eu_{1-x}Ho_xMnO_3}$, illustrated in Fig. 5.23. The stoichiometric compounds in the same multiferroic range (i.e. $\mathrm{GdMnO_3}$ or $\mathrm{TbMnO_3}$), but also the solid solutions of $\mathrm{Eu_{1-x}Y_xMnO_3}$ (x=0.1, 0.3) etc. show only one direction of polarization $\pm P_c$ (anti-)parallel to the c-axis in the ground state at low temperatures, which is reached by cooling at $B = 0\mathrm{T}$ (zero-field cooling, ZFC). Flipping the polarization to the b-axis is only possible by flipping the ac spin cycloid via the application of an external magnetic field to the ab-plane. Thus, in the ZFC ground state, only 180° DWs between $\pm P_c$ domains are possible. In the investigated material, $\mathrm{Eu_{1-x}Ho_xMnO_3}$, the situation at low temperatures is very different. Here, the magnetic moment of Ho leads to a spontaneous reorientation of the spin cycloids. This effect can either be facilitated by increasing the Ho concentration x or by lowering the temperature, as covered in section 4.4.1.

In particular, the pyrocurrent measurements by Ivanov *et al.* show that both polarization components P_c and P_b are nonzero and appear simultaneously around 30 K in $Eu_{0.7}Ho_{0.3}MnO_3$. This implies the presence of 90° DWs between $\pm P_c$ and $\pm P_b$ domains. This aspect could be crucial in understanding the transient violation of Raman selection rules. Domain walls of the 180° type are in general very thin, in a ferroelectric often as thin as a single atomic plane. They do not necessarily reduce the local symmetry in the DW volume. On the other hand, 90° DWs are typically much broader and the local symmetry can be lowered in several ways [97]. Two possible scenarios will be discussed in the following.

5.7.1 Possible scenarios of DW-induced disorder

The first scenario discusses the situation as found in the ferroelectric transition of $PbTiO_3$. The system is initially cubic with $a = b = c$. The ferroelectricity is induced by a structural cubic-to-tetragonal phase transition to $a = b \neq c$ with the electric polarization parallel to the c axis. Meyer and Vanderbilt discuss the formation of domain walls in $PbTiO_3$ as a formation of crystal twins, i.e. the ions on the interface of one domain must coincide with the ions of the other domain interface. The formation of 180° and 90° domain walls in this mechanism is shown in Fig. 5.24 The unit cell is abstracted as a rectangle. When the domain interfaces connect, the corners of the rectangles must connect to form coherent twins. The ferroelectric polarization is indicated with green arrows (Fig. 5.24a). For a 180° DW interface, this is easily done without any reduction in the lattice symmetry, as the long axes of both domains are parallel and of the same length (Fig. 5.24b). The case is different for the 90° DW interface in Fig. 5.24c, as now the long axis of the 90° domain is also rotated by 90° with respect to the reference domain. To connect the corners of the domains, it is necessary to incline the domains to a smaller angle ≠90°. Obviously, in the domain wall region, the symmetry is reduced due to the necessary bending of atomic rows. Although this effect is discussed for a structural phase transition in $PbTiO_3$, where the ferroelectric polarization is coupled to the long axis of the lower-symmetry unit cell, the argument still holds as long as there is a change of one of the lattice constants associated with the direction of electric polarization. While the crystal symmetry of $Eu_{1-x}Ho_xMnO_3$ at low temperatures is still orthorhombic, to this day there are no experimental studies on the dependence of the lattice constants on the direction of electric polarization in $Eu_{1-x}Ho_xMnO_3$, which would be a definite test of whether or not this mechanism of sterically induced disorder is of relevance for the $Eu_{1-x}Ho_xMnO_3$ system.

An additional reduction of symmetry by DWs can stem from the orien-

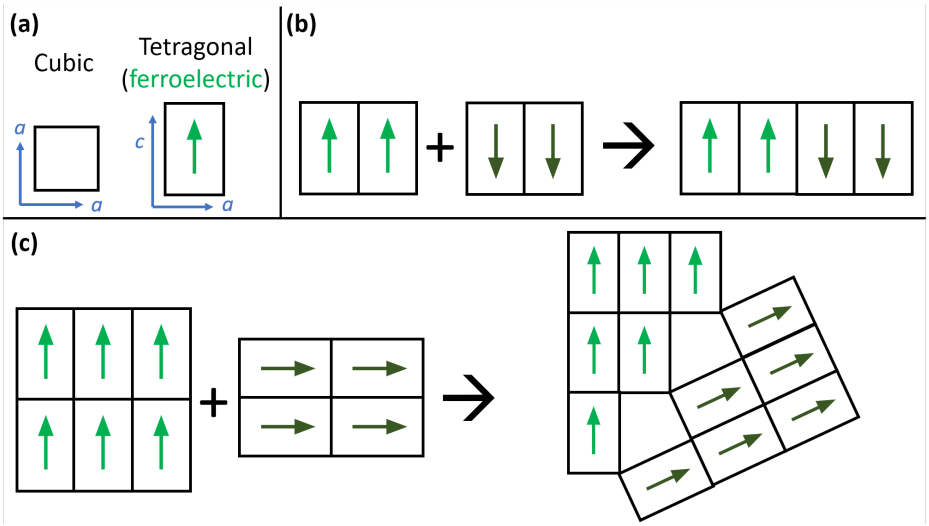

Figure 5.24: Ferroelectric domain wall formation in $PbTiO_3$ with tetragonal lattice constants $a = b \neq c$ and polarization parallel to c (a) [98]. To form consistent crystal twins, the ions of the two DW at the interface must coincide. (b): For a 180° DW, the interfaces can easily form twins, as the unit cells match of opposite polarization match perfectly. (c): For 90 ° DWs, the long axes are rotated by 90° with respect to each other. To form a crystal twin, the unit cells must rotate and form an angle ≠90°. The symmetry in the DW is thus lower than in the rest of the domain.

tation of polarization within P_c-to-P_b DW. Indeed, Kagawa *et al.* calculated the structure of a 90° DW of this type for $DyMnO_3$, as illustrated in Fig. 5.25 [99]. They found that the evolution of the polarization vector in the DW is continuously rotating from the c- to the b-axis, which is reminiscent of a Néel type wall. The symmetry is reduced, because the polarization is no longer confined to the principal c- or b-axis across the interface, but may assume arbitrary angles in-between, which is not in harmony with the lattice symmetry operations anymore. If the notion of DW-induced disorder is correct, this could also be tested independently by provoking a similar relaxation of selection rules in $TbMnO_3$ or $DyMnO_3$ by finely tuning an external magnetic field B_a parallel to the a-axis across the cycloidal-flop transition. The cycloidal flop transition takes place around 4-6 T for $TbMnO_3$, [6] and 1.5 - 2 T for $DyMnO_3$ [99].

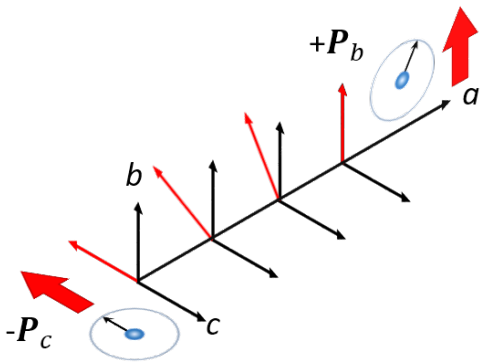

Figure 5.25: Illustration of a 90° P_c-to-P_b domain wall with a gradual tilt of the polarization vector from the c to the b direction. Adapted from [12].

5.7.2 Pseudospin model and the strength of the effect

The final question in this context is as to why the effect is so distinct but was not reported before. As a starting point serves again the model of a double well potential from subsection 5.6.2. Each potential well represented one state of polarization, either $+P_c$ or $-P_c$. Without Ho, the multiferroic ground state has only the component P_c, with one of the P_c potential minima being of lowest energy and the other wells are separated by an energy barrier. When the temperature is increased, the depths of the $\pm P_c$ wells are equalizing. As a consequence, pseudospins of the formerly lower-lying potential well minimum are transfered to the other one until both occupation numbers are equal. The result is a net polarization of zero they are equally occupied.
With the presence of Ho, this idea needs to be expanded to four potential wells in order to include also the polarizations $\pm P_b$, but the way of thought remains the same. Now, there is also a critical set of parameters where the polarization is spontaneously reorientating from P_c to P_b. In other words, close to the reorientation, the P_c and P_b potential wells are of similar depths. When shallow potential wells are involved and the phase transition is closely approached the dynamics of reorientation process is critically slowed down, as the potential gradient is too small to force the system into the new orientation. At the same time, fluctuations are enhanced as the potential barrier is small enough to be easily overcome at the phase transition. This means, that individual flops of polarization vectors are very probable, but the system as a whole only finds the new equilibrium arbitrarily slow. This produces a large DW density. This is also possible for the double-well case, but as we established, it is likely the 90° DW that introduces the reduction of lattice

symmetry and is only possible in $Eu_{1-x}Ho_xMnO_3$.[2] In this context, the weaker enhancement factor for x=0.1 is explained by (i) the weaker coupling to favor the $\pm P_b$ polarization or even (ii) that the reorientation is only local in the proximity to the Ho ions, as the concentration is very low.
Eventually, the fact that the transition temperature, at which a global electric polarization is observable is reported as $\sim 25\,\mathrm{K}$ does not contradict the observed symmetry violation at around $\sim 30\,\mathrm{K}$. As the pseudospin model suggests, the cycloids are still present even in the absence of global order, but macroscopically, the polarization vectors cancel out (see subsection 5.6.2 or [90, 93]). Therefore it is plausible that the reorientation process can already happen at a higher temperature than when a nonzero polarization in either direction shows up. In this context, the onset temperature T_{onset} is understood as a temperature where the occupation of one of the four possible polarizations starts to dominate, even by the slightest. Upon closer inspection of the $P(T)$ graphs for $Eu_{1-x}Ho_xMnO_3$ of Ivanov *et al.* show already a small nonzero contribution to the polarization at about 30 K
To summarize, $Eu_{1-x}Ho_xMnO_3$ shows a violation of Raman selection rules at T_{onset}. As a reason, a significant transient lowering of the lattice symmetry due to 90° domain walls is proposed, combined with an increase of domain wall density at T_{onset} resulting from a critical slowing down of the spin cycloid (and therefore the polarization) ordering process. Similar effects might be observed in other $R\mathrm{MnO}_3$ compounds by tuning the experimental parameters closely to the reorientation phase transition, for example by a B-field induced polarization reorientation in $TbMnO_3$ or $DyMnO_3$.

[2]The dependence of the defect density (here: DW density) on the way how closely and/or slowly the phase transition is approached is termed the Kibble-Zurek mechanism.[100, 101]

5.8 Monte Carlo simulation of the $R\mathrm{MnO}_3$ spin system

The findings of section 5.6 and 5.7 that the domains of different spin cycloids in $R\mathrm{MnO}_3$ play an important role in the dynamics of the magnetic system triggered the interest in visualizing the spin dynamics with an appropriate method. In a first step, basic ferro- and antiferromagnetic order should be reproduced by tuning the magnetic interaction strength and temperature. Then a cycloidal order should be reproduced with an appropriate set of interaction parameters. Furthermore varying the temperature, effects of rapid or slow cooling and heating should be visualized, with the ultimate goal to yield descriptive evidence if cycloids can persist locally when the temperature is raised above T_N and if these remaining domains are sufficient to reproduce the original magnetic pattern, once the temperature is lowered again. In order to achieve this, a program was developed in Qt, which uses the Monte Carlo method to simulate the spin dynamics. For an introduction to the fundamentals of Monte Carlo based simulations it is referred to appendix B.

5.8.1 Basic FM and AFM model for nearest neighbors

As a first test of the program, only nearest neighbor interactions are considered with all interaction parameters set equally and ferromagnetic, i.e., $J_{ij} < 0$. The spins are located in a 3D lattice and each spin's position is referenced with an x, y and z index. In $R\mathrm{MnO}_3$, the magnetic Mn^{3+} ion is located in an octahedral environment. Therefore, each spin in this simulation is interacting with the six nearest-neighbor spins in the $\pm x$, $\pm y$ and $\pm z$ directions. For an easier representation in the graph, an additional contribution proportional to S_z^2 is introduced, to force the spins into the xy plane, which is displayed by the program in the graphical window. Then, obviously, the energetically most favorable directions are the four diagonal directions in the xy plane. The effect of the cooling rate onto long-range magnetic order is investigated by randomly initializing the system at a high temperature $T \gg T_N$, perform Monte Carlo steps and then lower the temperature in steps. For each temperature, Monte Carlo steps are advanced at constant temperature. The cooling rate is now simulated by performing more intermediate temperature steps, which corresponds to a slower cooling rate, or less temperaure steps, which corresponds to a faster cooling rate. The number of Monte Carlo steps is constant at each temperature. To quantify the degree of magnetic order, the angles of all spins are returned by the program, which can be used to plot a distribution of spin angles in a histogram (Fig. 5.26). At $T \gg T_N$, all spin

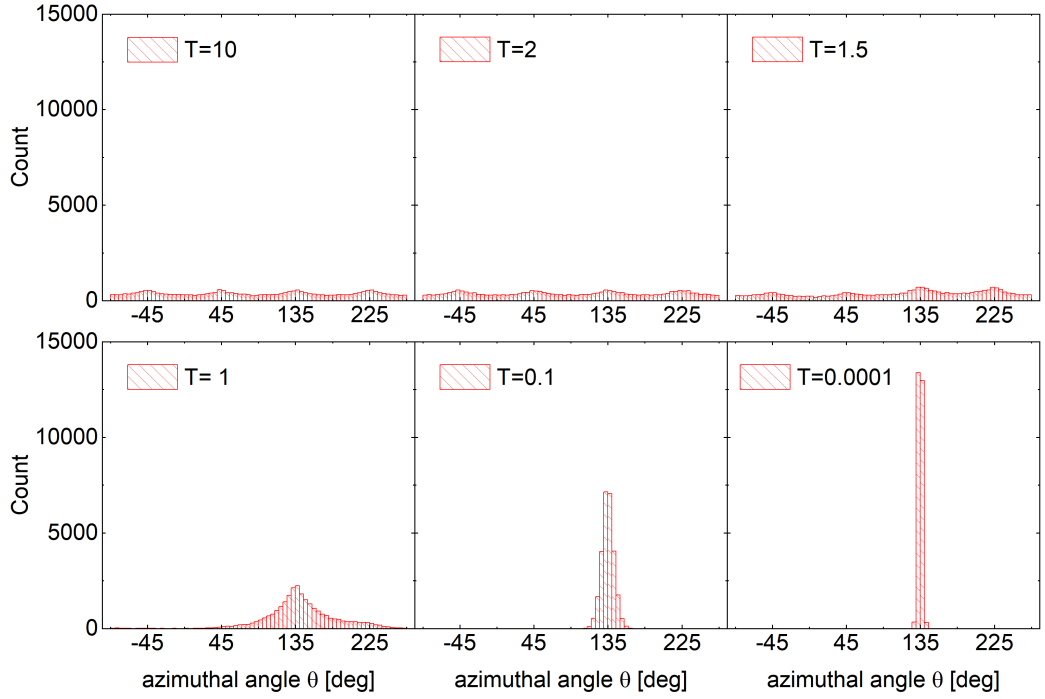

Figure 5.26: Distribution of angles for FM NN interactions with slow cooling rate. For $T \to 0$, the sample is practically in a single domain state, with most spins facing into the same direction.

orientations are present, as thermal fluctuations dominate. The weight in the distribution is equal for nearly all angles. Only for angles in the vicinity of the xy diagonals, there is a slight increase of probability of finding a spin oriented in this orientation. As the system is slowly cooled below T_N, one of the favored orientations starts to dominate. For $T \to 0$, nearly all spins are aligned towards a single direction, which is reflected in the histogram as a very narrow distribution of angles. The system is now practically in a single domain state. Now, the cooling procedure is performed with fewer intermediate temperatures and eventually with "instantly" cooling from T_N to 0 K, which is illustrated in Fig.5.27. With the intermediate cooling rate, the disorder is already enhanced, but the system can still manage to find a preferred spin alignment. The spontaneous macroscopic magnetization is now reduced compared to slow cooling. At the fastest cooling rate, the system ends up in a glass-like state. Small domains of local order can still be found, but the distribution of spins altogether results in a magnetization close to zero.

Similarly results are obtained, for the antiferromagnetic case $J_{ij} > 0$ (Fig. 5.27, lower row), with the main difference that now two angles remain

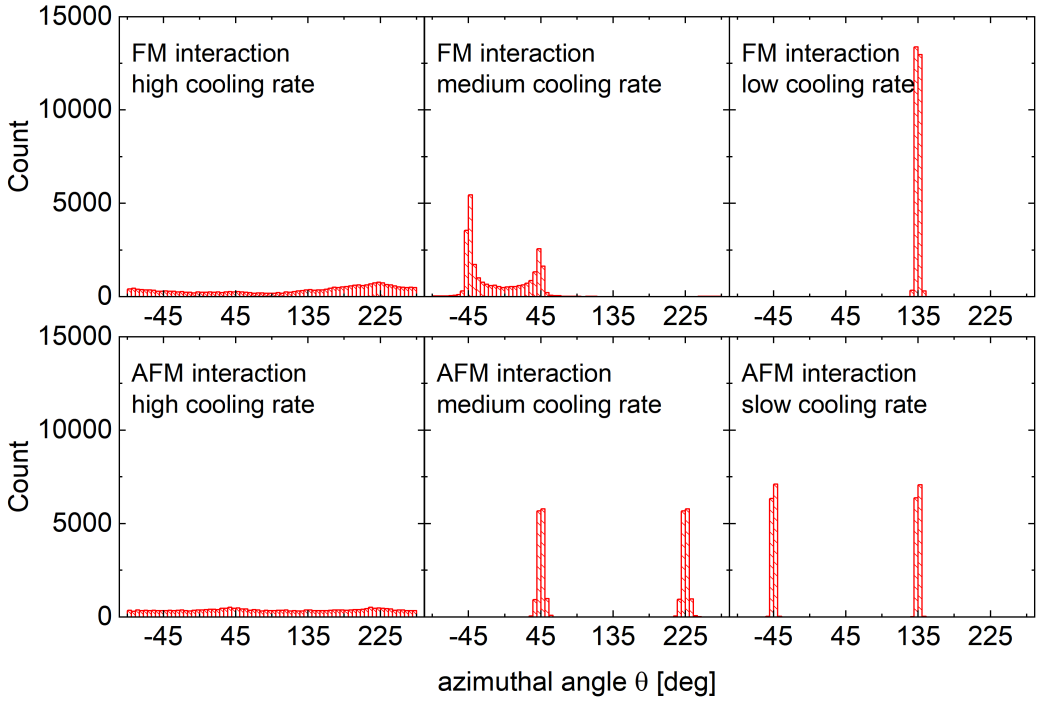

Figure 5.27: Distribution of angles for FM (top) and AFM (bottom) NN interactions by "instant", medium and slow cooling rates. With faster cooling, disorder is enhanced to a point, that the macroscopic magnetization is close to zero. The unitless temperature T is normalized to T_N.

in the ground state with an angular difference of 180°, which reflects of course the antiparallel alignment of the spins. The A-type AFM order is straightforwardly reproduced by setting the in-plane NN interaction to FM and the out-of plane NN interaction to AFM. Also the A-type AFM order is reproduced by choosing the interaction parameters ferromagnetic within a plane and antiferromagnetic in the perpendicular direction.

5.8.2 Next-nearest neighbor interactions and cycloidal order

The final step is to reproduce the cycloidal order. To achieve this, further interactions need to be considered. We recall Fig. 4.9 from section 4.2.3 at this point. Within the *ac*-plane, three interaction strengths need to be considered. The NN interaction J_1 and the NNN interactions $J_{2,3}$ via the Mn-O-O-Mn interaction path. Due to the orthorhombic distortion, $J_2 \neq J_3$

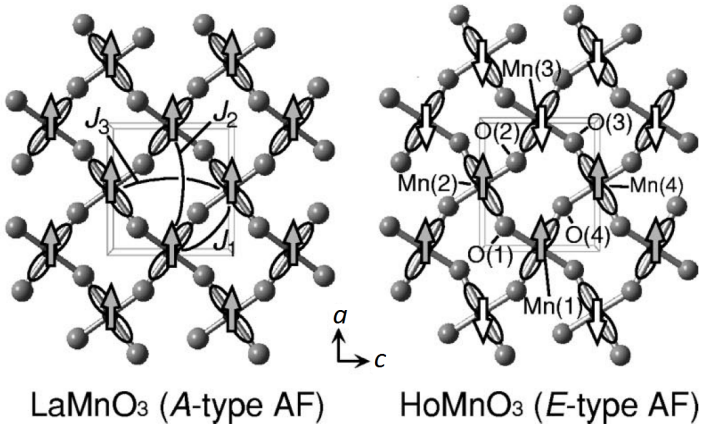

Figure 5.28: Nearest- and next-nearest neighbor interactions in the ac plane. Due to the increased octahedron tilt the balance of NN and NNN interactions is altered, which eventually turns the A-type FM order into the E-type AFM order with "zig-zag" patterns in the acplane. Adapted from [6].

and depending on the bond angle ϕ, even the sign of J_2 and J_3 is subject to change [6]. The cycloidal magnetic pattern is obtained when $J_1 \approxeq -J_2$. The exchange interaction J_3 is small and set to $J_3 = -0.01J_2$, resulting in a weakly FM NNN interaction [6]. The result of the slow cooling procedure can be seen in Fig. 5.29. With these parameters, the cycloidal structure with $q = 1/6$ is found. This value corresponds to the phase shift between adjacent lattice sites. From unit cell to unit cell this value would be the typical value of 1/3. This is reflected in the peaks in the first histogram of Fig. 5.29, which are 60° apart from each other. Eventually, we want to turn to the claims made and discussed in sections 5.6.2 and 5.7 which impose the questions: If the system is in the cycloidal phase with the full order established and the system is heated up above T_N, is the order still partially retained? And if the system is subsequently cooled down again, will the original ordering pattern be reestablished? In the initial state (Fig. 5.29a) the cycloid rotates counter-clockwise, when following the spins in the x-direction from left to right. The histogram shows the sixfold symmetry of the spin angles. Once the sample is heated up to 1.5 T_N (panel (b)), this sixfold symmetry vanishes. The disorder is strongly enhanced, however, a slight fourfold symmetry remains. Note, that the angles of the maxima are different than in panel (a). Subsequently, the temperature is brought down again and the cycloidal sixfold order is reestablished in panel (c). Note also here, that the angles are now different than in the original cycloidal order. There is an important observation to make in this procedure: While the distribution of

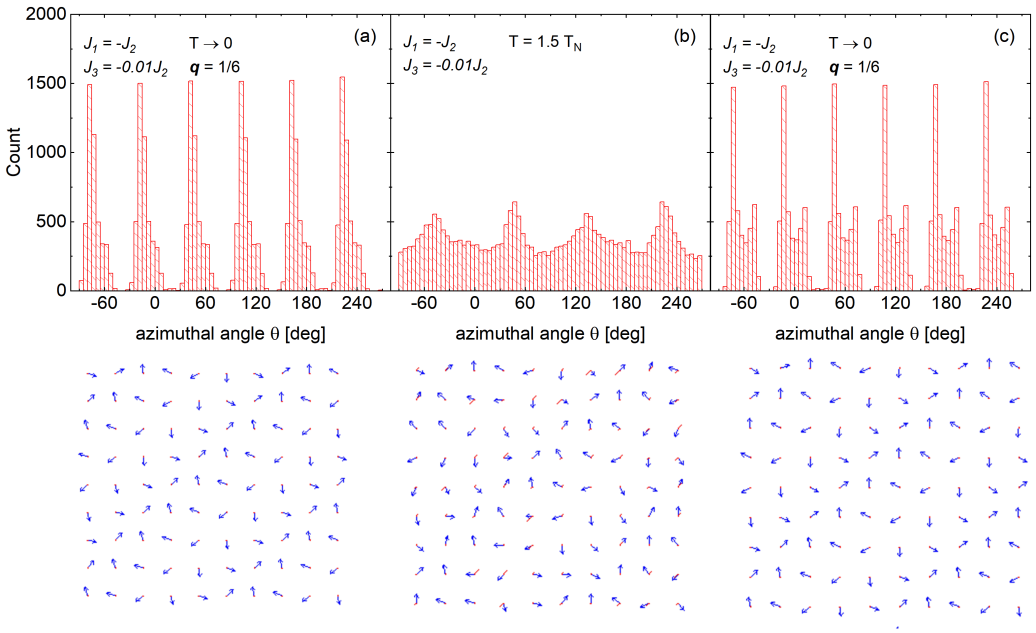

Figure 5.29: Conservation of cycloids above T_N: Starting from an ordered system at $T = 0$ (a), for $T > T_N$ the sixfold symmetry of the spins is lost on the macroscopic scale, the rotational sense of spins is conserved on the local level (b). When the system is brought back to $T < T_N$, the sixfold symmetry is restored (c). Despite the different absolute values for the spin angles, the rotational sense of the cycloids is unchanged in the procedure, as evident by the spin structure shown below each histogram.

angles shows a much larger disorder at higher temperatures, the rotational sense, i.e. the counter-clockwise rotation of spins remains intact. Even when the angles in the panel (c) are different than in the original structure of panel (a), the chirality of spins is the same as in the original pattern. In this way, domains of clockwise and counter-clockwise cycloids are stabilized above T_N. Another aspect could be the stabilization of individual spins, if they are aligned along the directions, which are energetically favored when only NN interactions are considered, i.e. the diagonal directions of the xy plane. This stabilization of cycloids does not even consider yet the energy barrier, which must be overcome to invert the cycloid helicity, as the oxygen ion in the Mn-O-Mn bonds needs to be displaced according to the inverse DM interaction.

5.9 Activity and magnetic field dependence of the electromagnon

While the electromagnon is routinely observed in $R\mathrm{MnO_3}$ with infrared- or THz-spectroscopy [7, 56, 88], the experimental data of observation with Raman spectroscopy was still lacking. The EMs appear in the infrared spectra of $R\mathrm{MnO_3}$ typically in the order of a few tens of $\mathrm{cm^{-1}}$. The temperature-dependent Raman setup (see 3.1) is unsuitable for this task, as it allows only for Raman spectra as close as about $50\,\mathrm{cm^{-1}}$ of Raman shift with respect to the laser line. The limiting factor is the notch filter used to block the laser in the detection path, which also cuts off the spectrum very close to the laser line. Razor-edge filters are commercially available, but still can not transmit the spectrum as close as a few $\mathrm{cm^{-1}}$ to the laser line. Because of this, the DilorXY 110 setup equipped with a triple monochromator in subtractive mode, as described in section 3.2, was used to record these spectra. Unfortunately, the liquid-helium bath cryostat does not allow for temperatures $>4\,\mathrm{K}$, so that all spectra are recorded at a constant temperature of $2\,\mathrm{K}$. To examine the magnon selection rules discussed in section 2.7, the spectra were tested for polarization dependence in $b(a,a)\bar{b}$, $b(c,c)\bar{b}$, $b(c,a)\bar{b}$ and $b(a,c)\bar{b}$ scattering configurations, and with the magnetic fields applied either $B \parallel a$ or $B \parallel c$ by rotating the sample.

The resulting spectra are shown in Fig. 5.30 for all five different Ho-contents of $\mathrm{Eu_{1-x}Ho_xMnO_3}$. Note that for the diagonal configurations only the spectra in the configuration $b(c,c)\bar{b}$ are shown, as the spectrum did not differ significantly between the $b(c,c)\bar{b}$ and $b(a,a)\bar{b}$ scattering configuration and the direction of the magnetic field. In orthogonal polarization ($b(a,c)\bar{b}$ and $b(c,a)\bar{b}$), the EMs are not observed. The $b(c,c)\bar{b}$ was chosen, as the same spectra contained also the $\mathrm{A}_g(4)$ mode at 350-380 $\mathrm{cm^{-1}}$. The spectra were all normalized to the area of the $\mathrm{A}_g(4)$ mode, so that also the EM intensities can be compared across different magnetic fields.

All spectra show two peaks around $20\,\mathrm{cm^{-1}}$ and $45\,\mathrm{cm^{-1}}$, indicated by arrows. The lower feature frequency corresponds very well to the lower-frequency EM, however, the higher-frequency EM was reported at higher frequency of $75\,\mathrm{cm^{-1}}$ [13, 53, 56, 60, 88] However, Chen *et al.* also observed an IR feature around $40\,\mathrm{cm^{-1}}$ in $\mathrm{Eu_{1-x}Ho_xMnO_3}$. On the other hand, Rovillain *et al.* report also lower EM frequencies in the Raman spectrum of $\mathrm{TbMnO_3}$ compared to the FIR spectrum, but argue, that the coupling mechanism is different for the two experiments, which results in the observed discrepancy of IR and Raman data. In the case of the x=0.1 sample, similar features are observed, However, as this sample has an A-type AFM ground state, these features

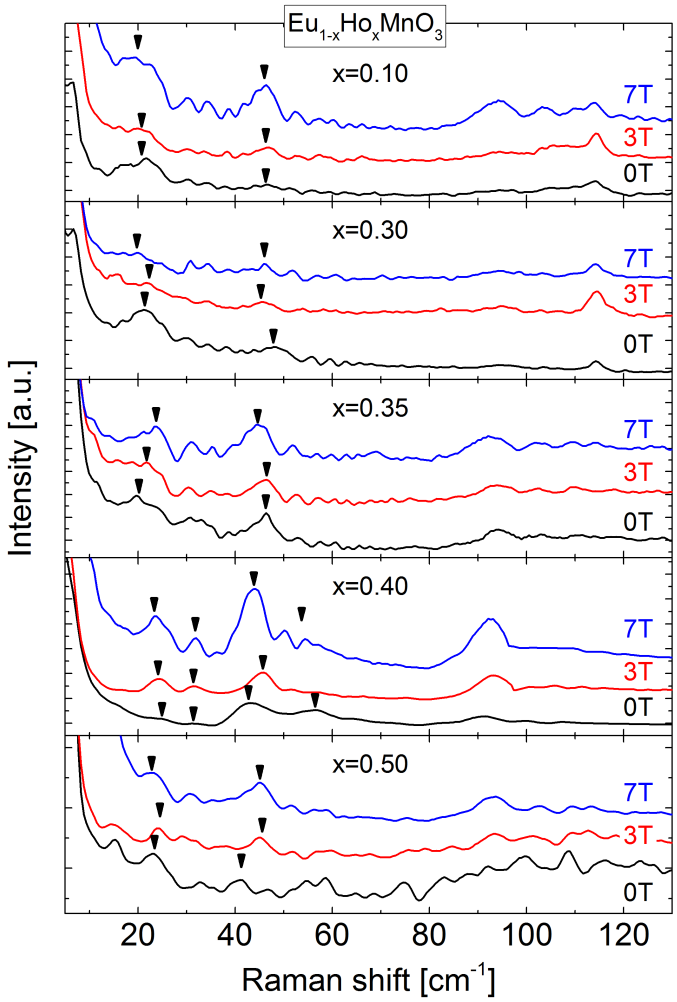

Figure 5.30: Raman spectra for $Eu_{1-x}Ho_xMnO_3$ $x \leq 0.5$ with varying magnetic felds at 2 K. The arrows indicate possible features. The (electro-)magnons are located around 20 cm^{-1} and 45 cm^{-1}

are ascribed to an ordinary antiferromagnetic resonance instead of EMs [88]. Across the whole series of samples, the EM intensity does not vary too much. This is interesting in itself, as in IR spectroscopy the AFM resonance is usually much stronger than the EM. Another key difference to FIR spectroscopy is the magnetic-field dependence of the intensity of the features. FIR shows a decrease of EM activity with increasing field, until it disappears at a certain critical field (for example 2 T in $GdMnO_3$, 8 T in $TbMnO_3$ [13]). The situation is very different in the results of Raman spectroscopy: For x=0.10 and x=0.30, the EM activity is first decreased slightly for 3 T and regains the full intensity again at 7 T, the highest achievable magnetic field with the

setup. Similar observations were made for the electromagnons in the Raman spectrum of $TbMnO_3$ where the electromagnons are still observed for magnetic fields up to 10 T, the maximum magnetic field in the cited articles [53, 102]. For the other samples, the intensity does not change except for the x=0.4 sample, where the intensity at 7 T is higher than at 0 T. In this sample, the two peaks appear to be split, as they are each accompanied by a smaller satellite. In contrast to the very similar $TbMnO_3$, an additional broad structure around 100 cm^{-1} is observed, which might consist of three broadened sub-features, as can be seen in Fig. 5.30 best for x=0.10. This could most likely be related to crystal-field excitations of the Ho $5f$ energy levels.

According to the model for Raman activity of magnons by Fleury and Loudon, which consider spin-orbit coupling as dominant coupling mechanism and was surmised in section 2.7.1, the magnon intensity should vanish when the polarization vectors of polarizer and analyzer are parallel. This is clearly not the case in $Eu_{1-x}Ho_xMnO_3$, as all shown spectra of Fig. 5.30 are recorded with $E_i \parallel E_s$. This is in line with results of $TbMnO_3$, which were published in parallel to these measurements [53]. This would rule out a first-order Raman scattering of a magnon in this mechanism. On the other hand, the observed frequencies appear too small to originate from a second-order magnon scattering process as in section 2.7.2, where two magnons are created in the scattering process, as the frequency would be about twice as high. From this point of view, this would lead to the conclusion that the EM is neither coupled via magnetic dipole interaction, nor via spin-orbit coupling or that a completely different coupling mechanism is much stronger. Other approaches in literature focus on a Heisenberg exchange mechanism or on magnetostriction with spin-orbit coupling, but do not point out any specific Raman selection rules [61, 103]. An additional striking difference to the IR-data is, that the Raman activity is not coupled to the incident polarization being parallel to a specific crystal axis. Also remarkable is the absence of any signature of the reorientation of the cycloidal spin order neither due to the applied magnetic field nor due to the spontaneous reorientation by the influence of Ho-spins. Further questions arise due to observed selection rules, which do not correspond to conventional magnon scattering theory. It is also not fully clear if the feature around 45 cm^{-1} is indeed an EM response, where the lower frequency compared to IR experiments is possibly explained by a different coupling mechanism to the incident radiation, or, if it is an entirely different feature altogether, which is assumed in the FIR studies performed by Chen *et al.* [88].

5.10 Summary

We have seen that at room temperature, the phonon modes of $Eu_{1-x}Ho_xMnO_3$ show a shift towards higher frequencies as the Ho content x is increased. The magnitude of this shift is very similar as it was observed before in $Eu_{1-x}Y_xMnO_3$ as the Ho^{3+} and Y^{3+} have a nearly identical ionic radius. This shows that the mass and magnetic moment of the R-site ion does not influence the room temperature properties of the observed modes (Sec. 5.2). As nearly every mode is activated by a single one of the four basic distortions, which transform the cubic perovskite into the orthorhombically distorted perovskite, particular modes could be used to investigate specific properties (Sec. 5.1). In this context, three modes are of especial importance:

- The $A_g(4)$ mode, activated by the $D_{[101]}$ distortion (rotation of the octahedra about [101]), was successfully employed to follow the evolution of Mn-O-Mn bond angle with varying Ho-content. Its frequency can be used as an alternative to structural analysis methods like e.g. XRD to locate any given $R\mathrm{MnO}_3$ in the $T-\phi$ phase diagram (Fig. 4.10).

- The $B_{2g}(1)$ mode, activated by the D_{JT} distortion, which modulates the Mn-O bonds within the ac plane. As the magnetic exchange J_{ac} in this plane is ferromagnetic, this mode allows to study the in-plane ferromagnetic interaction strength by analyzing the frequency shift introduced to this mode via spin-phonon coupling at low temperatures.

- The $B_{3g}(1)$ mode, which is also activated by D_{JT}. Like the $B_{2g}(1)$ mode, the displacement pattern shows a modulation of the ac-plane Mn-O bonds. However, the apical oxygen ions of the octahedra do also participate in the motion and modulate the bonds along the b-axis. The exchange J_b is of antiferromagnetic nature.

The latter mode, $B_{3g}(1)$ was not observed or at the very least not properly assigned in literature before. In this work, the Raman selection rules and the characteristic temperature-dependent behavior of a phonon made it possible to assign this feature in the spectrum to this mode for the first time [55]. In a quantitative analysis of the temperature-dependent SPC of the $B_{2g}(1)$ mode, the SPC coupling strengths $\frac{\partial^2 J_{ac}}{\partial u^2}$ were calculated, enabled by a formalism derived by Granado *et al.* [8]. To include the $B_{3g}(1)$ in the quantitative analysis, the formalism was extended in this work, arriving at an expression to evaluate $\frac{\partial^2 J_b}{\partial u^2}$ (Sec. 5.4). With the additional SPC-data provided by the $B_{3g}(1)$ mode, it is not only possible to quantitatively analyze the ferromagnetic in-plane interaction, but also the antiferromagnetic interaction along

the b-axis. This is crucial for a more detailed understanding of the magnetic interactions in the $R\mathrm{MnO_3}$ system, as both interactions compete and introduce frustration to the system, which is needed to support unconventional magnetic phases, as the cycloidal one. This might trigger further interest to evaluate also this mode if it is experimentally accesible.
The maximum SPC strength across the $\mathrm{Eu_{1-x}Ho_xMnO_3}$ series reveals a key difference to the $\mathrm{Eu_{1-x}Y_xMnO_3}$ series: Both series behave very similar for Ho- or Y-concentrations, respectively, until x=0.30. The SPC strength decreases with increasing x. While this trend continues for the $\mathrm{Eu_{1-x}Y_xMnO_3}$ series, $\mathrm{Eu_{0.65}Ho_{0.35}MnO_3}$ showed a particularly strong SPC shift and remains strong for x=0.40 and x=0.50. This could be attributed to the contribution to the anisotropy energy in the ba plane introduced by the Ho magnetic moments, which lowers the the anisotropy energy within this plane and leads eventually to the flip of the cycloidal plane from the ac to the ab plane.
The effect of a magnetic field onto SPC was expected to be negligible, however, the $\mathrm{B_{2g}}(1)$ mode nevertheless showed a particular behavior in the magnetic field. Depending on Ho concentration, the frequency would shift to higher or lower frequencies with increasing field and for a particular concentration, even the change in frequency can reverse its sign as the magnetic field is increased. This might be related to opposite effects taking place: weakening of SPC due to rotation of the Mn-spins towards the magnetic field and strengthening of SPC due to orientation of Ho-spins. However, clearly further investigations and theoretical input is needed in this point.
The electromagnon spectrum remains still elusive. The polarization dependence did neither follow conventional magnons nor a behavior similar as observed in infrared spectroscopy, where the electromagnon is only excited along one crystallographic axis, which does not change if the cycloid is flipped. The observed frequency of the high-frequency electromagnon does not agree too well with the infrared results. However, similar effects were reported in references [14, 53, 102] for $\mathrm{TbMnO_3}$ and was explained with the difference in activation of the electromagnon in Raman and infrared spectroscopy.
Great progress has been made in the understanding of SPC at temperatures reaching even into the paramagnetic phase and the evolution of the cycloidal magnetic structure as the temperature is increased. In the framework of a pseudospin model, instead of transitioning into a sinusoidal phase above T_{cycl}, the single-domain phase splits up into domains of cycloids with opposite chirality. As the temperature increases, the occupation numbers for both cycloids equalize and eventually lead to the disappearance of the macroscopic electric polarization. Since the cycloids are still coupled in the model, this gives a natural explanation for SPC, even in the absence of long-range order. The onset of SPC, the electromagnon activity and the activation energy de-

rived from dielectric relaxation experiments point to a characteristic energy scale of around 100 K.
An additional argument, that the spin cycloids persist is delivered by Monte Carlo simulations. It was shown, that the disorder increases drastically above T_N and the distinct correlation of spin angles is lost, however, when examining the spin domains, the chirality of the spins remains largely intact. Once the system is cooled down again, the spin angles may be different than after the initial cooling, but since the chirality is conserved at higher temperatures, the original polarization direction of the domain is restored. In addition, if spins are aligned along the energetically favored directions in an unfrustrated scenario, they are more stable against thermal fluctuations and can act as anchorpoints for the cycloids.
A novel effect was discovered in the Raman spectra around 30 K, where the Raman selection rules are violated in a very narrow temperature range. This could be succesfully explained within the same framework: As $Eu_{1-x}Ho_xMnO_3$ does not only allow the two directions of spontaneous polarization $\pm P_c$, but also $\pm P_b$, this leads to the presence of 90° domain walls. Within the 90° domain wall, the lattice symmetry is reduced and leads to the relaxation of Raman selection rules, observable by the strong leaking of forbidden modes into the spectrum. Due to the strength of the observed effect, we could deduce that the DW density must be large in this small temperature range, very closely to the cycloidal phase, before one of the four possible eventually starts to dominate at lower temperatures. When this point is carefully approached, the fluctuation dynamics are strongly enhanced, while on the other hand the dynamics of reorientation or long-range order are critically slowed down, as the potential landscape is not steep enough to force the system into one of the possible four cycloidal orientations.

Part II

The delafossite $ACrO_2$

Chapter 6

Introduction to the delafossite $A\mathrm{CrO}_2$

6.1 Crystal structure

The crystal structure of the delafossite $A\mathrm{CrO}_2$ is typically described with two different but equivalent unit cells. The first one which we are going to consider consists of only one formula unit of $A\mathrm{CrO}_2$ as a basis, with a rhombohedral lattice ($\alpha, \beta, \gamma \neq 90°$, Fig.6.1). The basis consists of a Cr^{3+}

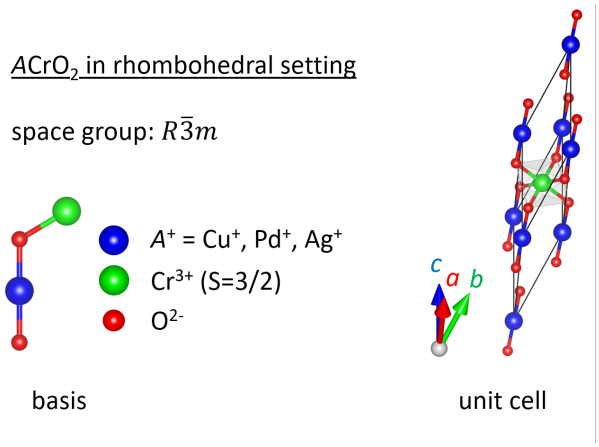

Figure 6.1: Basis and rhombohedral unit cell of $A\mathrm{CrO}_2$, which consists of only one formula unit of $A\mathrm{CrO}_2$. The magnetic Cr^{3+} ion is coordinated within a distorted octahedral environment by the O^{2-}ions.

ion, which is in an octahedral environment of six O^{2-} ions. These layers of edge-sharing CrO_6 octahedra are connected via the A^+ ion to the next CrO_6 layer, thus forming a linear O^{2-}-A^+-O^{2-} dumbbell (Fig. 6.1). This

unit cell is convenient to visualize the vibrational modes: With four atoms in the unit cell, there is a total of 9 optical modes. In addition, due to the inversion symmetry, the modes are either exclusively Raman- or infrared active. The group theoretical treatment according to Pellicer-Porres *et al.* [104, 105] yields

$$\Gamma_{opt} = A_{1g} + E_g + 2A_{2u} + 2E_u. \tag{6.1}$$

Thus, there are only two Raman active modes A_{1g} and E_g, whereas the modes of E-symmetry are doubly degenerated. The elongation patterns of all optical phonon modes are displayed in Figure 6.2 [104]. The A_{1g} mode consists of oxygen displacements perpendicular to the Cr- or A- layers and can thus be thought of as a movement of two oxygen layers against each other. For the E_g mode, the oxygen displacements are parallel to the Cr- or A-layers, also moving in opposite directions. The degeneracy is explained, because the same elongation pattern, rotated by 90° is an equivalent elongation pattern. With these displacement patterns, the frequency of the A_{1g} mode is expected to be higher than that of the E_g mode. The general Raman spectra

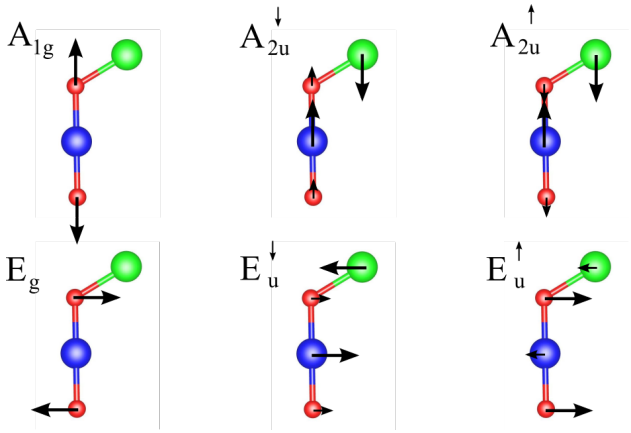

Figure 6.2: Elongation patterns of the $ACrO_2$ optical phonon modes, adapted from [104]. Due to the presence of a center of inversion, the modes are either even (g) and Raman-active, or odd (u) and infrared active. modes of E-symmetry are doubly degenerate.

of crystals with delafossite structure is well-known. For example, Bruesch and Schuler reported polarized room-temperature Raman spectra for various isostructural $NaBX_2$ compounds and confirmed the intuitive trend, that the vibrational mode frequencies depend dominantly on the bond strength of the involved ions in the elongation patterns and therefore of the interionic distances. Thus, the frequencies of $ACrO_2$ are expected to be similar as in

the studies of Bruesch and Schuler with X=O [106]. However, Raman investigations of the $A\mathrm{CrO}_2$ system are still scarce in literature. The spectrum in Fig. 6.3 shows a recent Raman spectrum by Aktas *et al.* for CuCrO_2, which allows us to specify the expected mode frequencies for the investigated $A\mathrm{CrO}_2$ further by about 710 cm^{-1} for the A_{1g} and 450 cm^{-1} for the E_g mode at room temperature [107]. While some temperature-dependent stud-

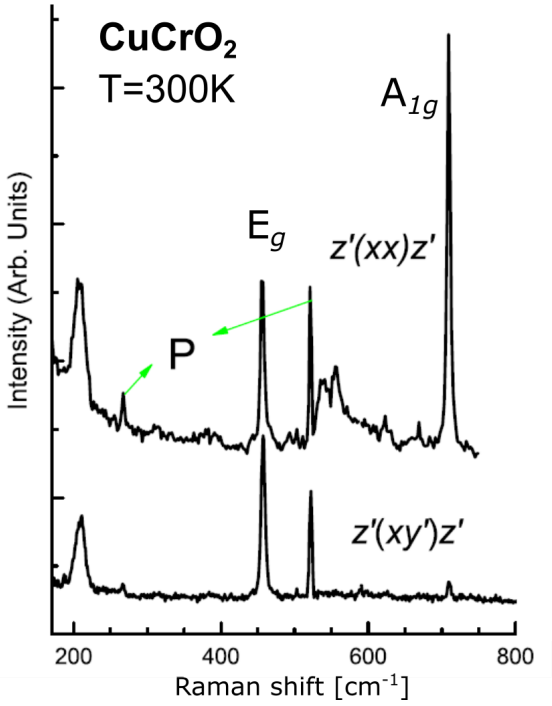

Figure 6.3: Room-temperature Raman spectrum of CuCrO_2. The two expected Raman modes, E_g and A_{1g} are well separated and show a narrow linewidth. Features labeled with "P" denote plasma lines of the Ar-ion laser. Adapted from [107].

ies of CuCrO_2 are available, they were often focused on a possible structural transition or lacked detail in the low-temperature data and no spin-phonon coupling effects were reported yet.

The second unit cell considered here is of higher symmetry, but of larger volume and is described in the hexagonal setting (Figure 6.4). The advantage of this larger unit cell is the more intuitive orientation of lattice vectors, which greatly facilitates discussions concerning the lattice. All references made to lattice vectors are going to use this hexagonal setting.
In particular, the layers of ions are now located in the *ab* plane and stacked

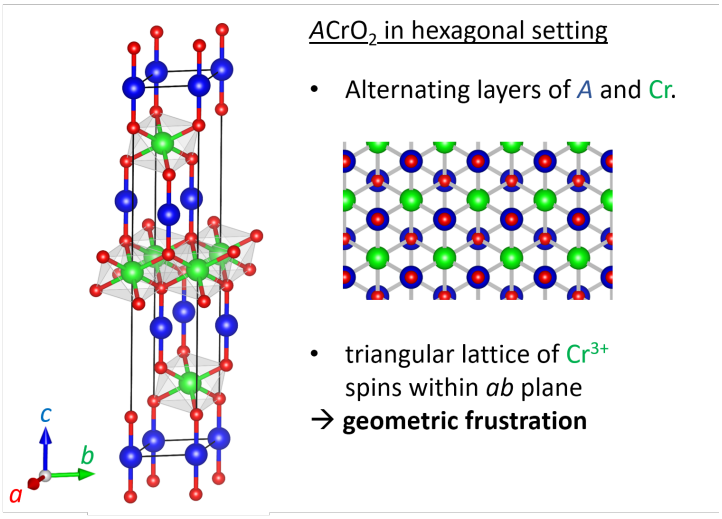

Figure 6.4: Hexagonal unit cell, equivalent to the rhombohedral setting in Figure 6.1. The Cr^{3+} ions form a triangular lattice within the hexagonal ab-plane.

along the c direction. The layers are shifted to one another in a three layer sequence (ABCABC stacking), with the space group $R\bar{3}m$. By viewing the structure as a top-down view (Figure 6.4) from the c-axis it becomes clearer now, that each layer of the A-site and Cr-ions, respectively, forms a triangular lattice with antiferromagnetic in-plane interaction.

Since the triangular arrangement of the magnetic ions plays a special role for the magnetic interactions in $ACrO_2$, the next section is going to address the main differences between $ACrO_2$ and $RMnO_3$ in the magnetic structure and interaction mechanisms that are responsible for the multiferroic behavior.

6.2 Magnetic properties of $A\mathrm{CrO}_2$

In order to discuss the magnetic properties, we are going to focus on CuCrO_2 as a representative of the investigated $A\mathrm{CrO}_2$ compounds. The Cu^+ and O^{2-} ions both have completely filled outer shells in this state of oxidation (Cu^+: $3d^{10}$, O^{2-}: $2s^2 2p^6$). The Cr^{3+} ion, with the valence electron configuration $3d^3 4s^0$ is therefore responsible for the magnetism in CuCrO_2. Due to the quenched orbital momentum, the magnetic properties of the Cr-ion are well represented by a $S = \frac{3}{2}$ Heisenberg spin with antiferromagnetic interaction within the triangular Cr-layers [108]. Contrary to the $R\mathrm{MnO}_3$ system, where the spin system is frustrated due to competing FM- and AFM interactions, the frustration in a triangular antiferromagnet is of geometric origin, thus also referred to as "geometric frustration". To further illustrate this, let us consider the three antiferromagnetically coupled spins on a single triangle as depicted in Figure 6.5. If the exchange interaction between all three of them

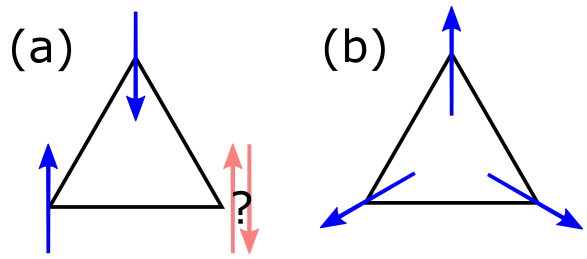

Figure 6.5: (a) Three antiferromagnetically coupled spins on a triangular plaquette. Two spins can align antiparallel to satisfy the AFM interaction. The third spin can obviously never align antiparallel with respect the other two. (b) For a perfectly isotropic triangular lattice, the spins in the ground state order in a 120° pattern.

is antiferromagnetic, then two spins could align antiparallel, but the third spin can not fully satisfy both AFM exchange interactions. It is noteworthy to mention, that if the triangular lattice is perfectly isotropic, and thus shows the strongest geometric frustration, i.e., all three exchange interactions are equal, it can be shown that in the ground state the spins order with a 120° pattern (Fig. 6.5(b)) [109]. However, the smallest deviation of the perfect isotropy, together with small spins (i.e. $S = 1/2$) leads to a whole plethora of new phenomena. For example the spins behave like Ising spins, and can only align either $\uparrow$ or $\downarrow$. Quantum fluctuations are of the order of the spins themselves and remain therefore relevant even for $T \to 0$, which might prevent long-range order even at $T = 0$ despite significantly higher Curie-Weiss temperatures of a few hundreds of Kelvin. Even in the absence of long-range

order due to the fluctuations, the spin are still strongly correlated even at long range: flipping one spin, causes a large amount of other spins to simultaneously flip accordingly. The ground state might be highly degenerate with different, superpositioned patterns to populate the lattice, which have the same total energy. This exotic magnetic state leads also to new exotic low-energy excitations with spin-charge separation (spinons). This is however not the scope of this thesis, but shows that we find ourselves in a very interesting and active area of research of magnetic phenomena. Returning back to $CuCrO_2$, we can understand now how the in-plane properties are affected by the crystal lattice: Due to the geometric frustration introduced by the triangular lattice, the spins tend to form noncollinear patterns. In the case of $CuCrO_2$, the system undergoes two successive phase transitions in close proximity at T_{N1}= 23.6 K and T_{N2}=24.2 K. Only at temperatures below T_{N1}= 23.6 K, the magnetic order is accompanied with the break of inversion symmetry, thus exhibiting the multiferroic state with an electric polarization [110–112]. The spin pattern within the ab-plane is a spin spi-

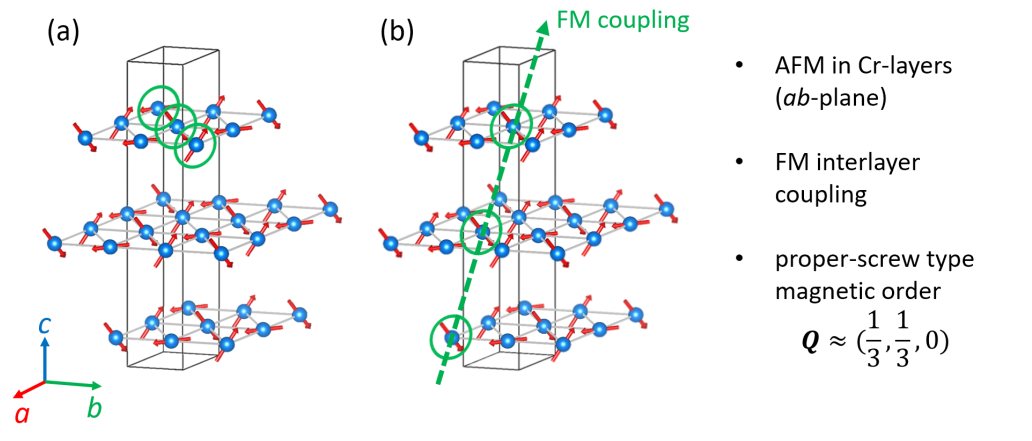

Figure 6.6: (a) Proper-screw magnetic order in $ACrO_2$ with wavevector $\mathbf{Q} = (q, q, 0)$. The screw axis is parallel to (q,q,0), the spin rotational plane is indicated by green circles. (b) Illustration of the direction of ferromagnetic interlayer coupling.

ral of the proper-screw type depicted in Figure 6.6(a), described with the modulation vector $\mathbf{Q} = (q, q, 0)$ where q is typically in close vicinity to $\frac{1}{3}$, i.e. the 120° case. Since here, the modulation vector is always within the ab plane, the third component is often omitted in literature and the abbreviated notation $\mathbf{Q} = (q, q)$ is used.

While the coupling within each Cr-layer in the ab plane is AFM, there exists also a long-range FM interlayer coupling. Since the stacked Cr-layers

are shifted horizontally with respect to each other, the direction of ferromagnetically coupled spins is not parallel to the c-axis, but tilted, as shown in Fig. 6.6(b). The full modulation vector for $CuCrO_2$ according to Frontzek *et al.* reads $\mathbf{Q} = (0.3298, 0.3298, 0)$, where $q_3 = 0$ represents the ferromagnetic coupling along c [110].

The phase between T_{N1} and T_{N2} is not yet fully understood: It was argued on the basis of neutron diffraction studies, that in this phase only the c-components of the spins order [112]. Below 23.6 K, also the order of spin components in the ab is established and is accompanied with the break of inversion symmetry, thus exhibiting the multiferroic state with an electric polarization [111, 112]. Newer neutron diffraction studies of Frontzek *et al.* for the intermediate phase between T_{N1} and T_{N2} suggest, that the spin spiral is already present in this phase with the same modulation vector as in the multiferroic phase, but with the spiral rotation plane lying within the ab-plane. As the full 3D correlations are not established yet, the lack of electric polarization is explained by the assumption that the spiral planes are not correlated and the polarization cancels out, though further research is suggested [110]. In the following, we are going to discuss only the low-temperature multiferroic phase and which mechanism drives the multiferroic phase transition. Because of this, and of the fact that the other investigated $A\mathrm{CrO}_2$ compounds (with A=Ag, Pd) show only a single transition, we are going to refer to the transition temperature to the multiferroic phase in $CuCrO_2$ also as T_N unless details of the intermediate phase are of importance.

6.3 Multiferroicity by proper-screw type order in $A\mathrm{CrO}_2$

In the previous section, 4.4, we have established that the proper-screw type magnetic order, where the modulation vector $\mathbf{q}$ is parallel to the spin cycloidal normal vector, can not induce an electric polarization with the inverse-DM mechanism. If $\mathbf{q} \parallel (\mathbf{S}_i \times \mathbf{S}_j)$, then $\mathbf{q} \times (\mathbf{S}_i \times \mathbf{S}_j) = 0$. The conventional magnetostriction term $\mathbf{S}_i \cdot \mathbf{S}_j$ can also be excluded, as the ferroelectric polarization by this mechanism occurs only, if the spin modulation is commensurate to the lattice. Nevertheless, the delafossite $CuFeO_2$ was found to exhibit multiferroicity with an incommensurate proper-screw type magnetic order. To advance to the origin of the electric polarization induced by a spin spiral pattern Arima proposed a model for the isostructural $CuFeO_2$ based on a change in bond valency, introduced by spin-orbit coupling [42]. First, he considers the allowed symmetry operations for the crystal lattice to find relations be-

tween the spin spiral modulation vector $\mathbf{Q}$ and the induced polarization. We consider an arrangement of ions as shown in Fig. 6.7: a layer of mag-

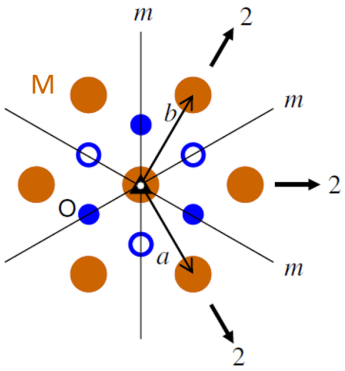

Figure 6.7: Layer of magnetic ion M (ocher) and the nearest layers of oxygen ions above (empty blue circles) and below (full blue circles) the M-layer. The allowed symmetry operations are: threefold rotation around c axis, space inversion, twofold rotations around [100], [010] and [110] directions and mirror planes, normal to the twofold rotation axes. Adapted from [42].

netic ions M in the ab-plane and the nearest layers of oxygen ions above and below the M-layer, represented by open and filled circles, respectively. In the absence of magnetic order, the allowed operations are: space inversion, twofold rotations around a, b and the [110] axes, mirror planes with normal vectors parallel to the twofold rotation axes and threefold rotations around the c-axis. Note, while the layer of M-ions would allow for a sixfold rotation symmetry, the alternating location of the oxygen ions above and below the M-layer reduces this rotation to only threefold. The proper-screw spin spiral, as shown in Figure 6.8a with $\mathbf{Q} = (q, q)$ breaks all of these symmetries, and only a 2' operation remains, which is a twofold rotation operation around [110] with consecutive time inversion. The only possible direction in which the ferroelectric polarization can appear is thus parallel to this [110] axis, as this rotation operation does not change the polarization direction. The polarization is therefore parallel to the spin-spiral modulation vector $\mathbf{Q}$.

Besides magnetostriction and the inverse DM interaction, Jia *et al.* [114, 115] considered a third term resulting from spin-orbit coupling, which affects the $p-d$ hybridization in order to explain the multiferroic behavior in $ACrO_2$. This term is expressed as

$$(\mathbf{S}_i \cdot \mathbf{e}_{ij})\,\mathbf{S}_i - (\mathbf{S}_j \cdot \mathbf{e}_{ij})\,\mathbf{S}_j \tag{6.2}$$

where the symbols have the same meaning as before. An illustration of this $p-d$ term is given in Figure 6.9. Arima [42] considers a two-ion cluster

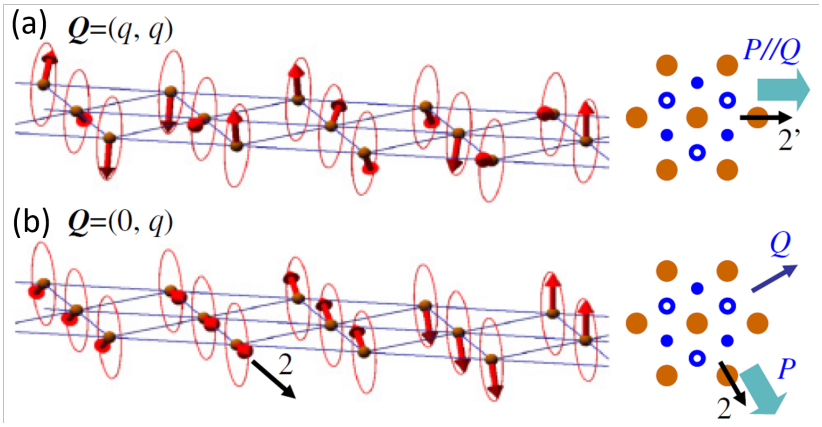

Figure 6.8: (a) The spin spiral order with $Q = (q, q)$ breaks all symmetries except a twofold rotation with time inversion. The ferroelectric polarization must appear parallel to this axis and is parallel to Q. (b) With $Q = (0, q)$, one twofold rotation operation remains. The polarization would appear perpendicular to Q. Adapted from [42].

model, consisting of a magnetic ion M (here M=Cr), which is connected via a ligand oxygen ion to the next magnetic ion of $ACrO_2$. The Hamiltonian, which describes the electron transfer between the two of them is given by

$$H_t = \sum_{\sigma} t_{pd}(d^{\dagger}_{1\sigma}p_{1\sigma} + d^{\dagger}_{-1\sigma}p_{-1\sigma}) + h.c. \tag{6.3}$$

Due to spin-orbit coupling, the degeneracy of the d- and p-orbitals is lifted. The energy differences Δ for the minority spins ($\sigma = \downarrow$) are then shifted by $\pm\lambda_{eff}S_z$, where λ_{eff} is the difference of the two spin-orbit interaction strengths of the M- and O-ion. As a result, the covalent mixing is estimated to change from t_{pd}/Δ to $t_{pd}/(\Delta \pm \lambda_{eff}S_z)$ as illustrated in Fig. 6.10. When H_t is considered as a perturbation, the ionic charge of the ligand ion O is changed by

$$t^2_{pd}\lambda^2_{eff}S^2\cos(2\theta)/\Delta^4 \tag{6.4}$$

where θ is the angle between the direction of the spin moments and the M-O bond direction. The task is now to apply this equation to the magnetic structure of $CuFeO_2$ to see, if it produces an uniform electric polarization. For this, we consider a cluster of Cr_4O_2, as depicted in Fig. 6.10(b). The Cr-ions are all located within the same plane, while the oxygen ion O1 is located above the Cr-plane and O2 is located below. This is further illustrated in the side view, with the corresponding angles between the Cr- and O-ions, θ_1

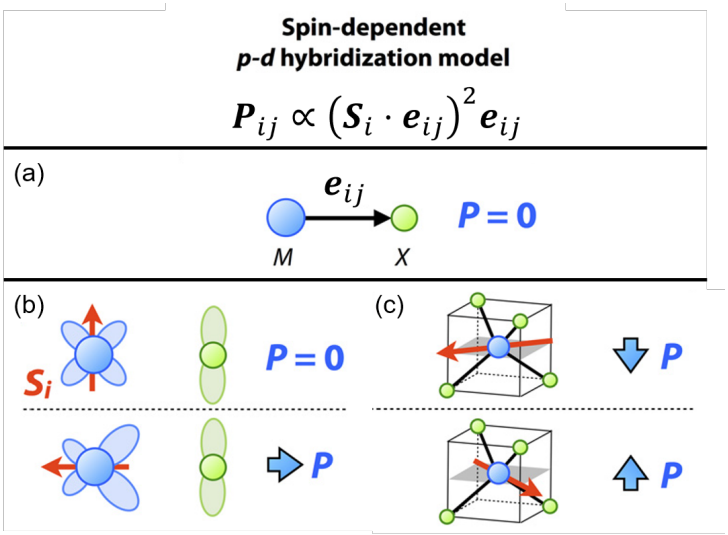

Figure 6.9: Illustration of electric polarization by $p-d$ hybridization according to Equation 6.2. (a): The vector $\mathbf{e}_{ij}$ is defined as the vector connecting the magnetic ion M with the ligand X. (b): Depending on the orientation of the spin to the M-X bond, the $p-d$ hybridization affects the charge distribution and induces a polarization. (c): For the total polarization, each ligand bond needs to be considered and depends on the orientation of the spin. Adapted from [113].

and θ_2. The modulation vector of the spin spiral is $\mathbf{Q} = (q, q)$. The phase relations between the spins on the four Cr-sites are then given by $\mathbf{Q}\cdot\mathbf{r} - q$ (Cr1), $\mathbf{Q}\cdot\mathbf{r}$ (Cr2,Cr3) and $\mathbf{Q}\cdot\mathbf{r} + q$ (Cr4). To calculate the charge transfer from the ion O1 to Cr1 with Eq. 6.4 (α-term), one has to consider the charge transferred from and to the O1 ion from the three Cr ions surrounding it, i.e. Cr2-O1 and Cr4-O1 (β- and γ-terms), which will be counted as negative, as well as that a stronger covalency of one bond, makes the other two less covalent, resulting in the mixed terms with $\alpha\beta$ and $\alpha\gamma$:

$$\begin{aligned}&[1 + a\cos 2(\mathbf{Q}\cdot\mathbf{r} - q - \theta_2)]\\ &\times [1 - \beta\cos 2(\mathbf{Q}\cdot\mathbf{r} - \theta_1) - \gamma\cos 2(\mathbf{Q}\cdot\mathbf{r} + q - \theta_2)]\,.\end{aligned} \tag{6.5}$$

The net electric dipole moment induced along the [110] direction is then given by the difference of charge transferred from Cr1-O1 and Cr4-O1[1]

$$\begin{aligned}p_{[110]} \propto \sin 2q\,[&\alpha\beta\sin 2(\theta_1 - \theta_2) - 2(\alpha+\gamma)\sin 2(\mathbf{Q}\cdot r - \theta_2)\\ &+\alpha\beta\sin 2(2\mathbf{Q}\cdot r - \theta_1 - \theta_2)]\end{aligned} \tag{6.6}$$

[1] In the original publication, the argument of the last sin term is given by $2(2\mathbf{Q}\cdot r + \theta_1 - \theta_2)$, which is supposedly a typo.

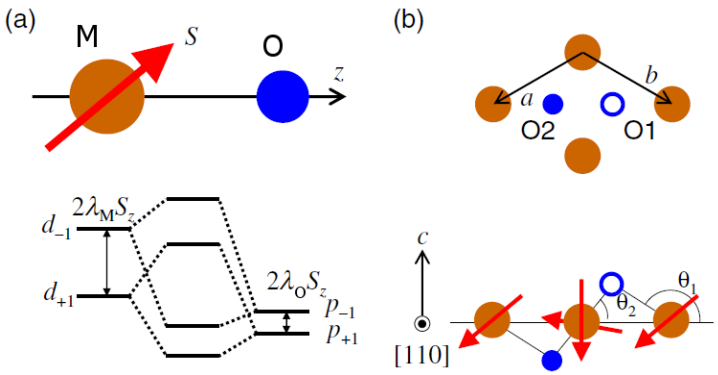

Figure 6.10: (a) Two-ion cluster model of a magnetic ion M (corresponding to Cr in our case) and an oxygend ligand ion for $ACrO_2$. The spin is tilted with an angle θ with respect to the M-O bond. The degeneracy in the d-orbitals of M and the p orbitals of O is lifted by spin-orbit interaction. (b) A cluster of Cr_4O_2. The full circle represents an O-ion below the Cr-plane, the empty circle an O-ion above the Cr plane. The proper-screw type spin pattern is shown below, with the modulation vector (q, q). Adapted from [42].

This electric moment is comprised of a part which depends on r and oscillates with wavevectors of $2\mathbf{Q}$ and $4\mathbf{Q}$ and a uniform part which depends only on $(\theta_1 - \theta_2)$. Similarly to the rare earth manganites, where the polarization is reversed together with the chirality of the cycloid, the induced dipoles in $ACrO_2$ are reversed when the spiral helicity is reversed. This corresponds to $q \to -q$, which reverses the sign of $\sin 2q \to -\sin 2q$ in the first sin factor in Eq. 6.6. As a peculiarity, due to this prefactor, this mechanism would not produce any polarization for q values with integer multiples of $q = \pi/2$.

Chapter 7

Results and discussion - $A\mathrm{CrO}_2$

In this chapter the experimental results and the analysis of the obtained data for the lattice dynamics in $A\mathrm{CrO}_2$ are presented and discussed. The organization of this chapter is similar as in chapter 5. First, the observed modes in the spectrum are assigned by considering the Raman spectra for different polarization configurations and the modes' Raman tensors (section 7.1). The behavior of phonon frequencies is analyzed with respect to the different A-site ions Cr, Pd and Ag. In addition, shell-model calculations with the GULP software package are performed in order to identify and supplement trends for the observed phonon frequency shift by A substitution. Details about the use of the GULP package can be found in C.
In the subsequent section, section 7.2, the temperature dependence of the phonon modes and SPC effects are studied. A feature specific for CuCrO_2, which appears as a satellite of the E_g mode, is discussed in higher detail in section 7.3, as it might be related to a lattice distortion and could act as a viable probe in further investigations. In section 7.4, the lattice vibrations, as well as the satellite peak are investigated under the influence of a magnetic field. A summary of the results of $A\mathrm{CrO}_2$ is given in section 7.5.

7.1 Characterization of $A\mathrm{CrO}_2$

To assign the Raman features to their corresponding modes, we representatively consider the room-temperature spectrum of the single crystal CuCrO_2 sample for different scattering configurations. To determine suitable polar-

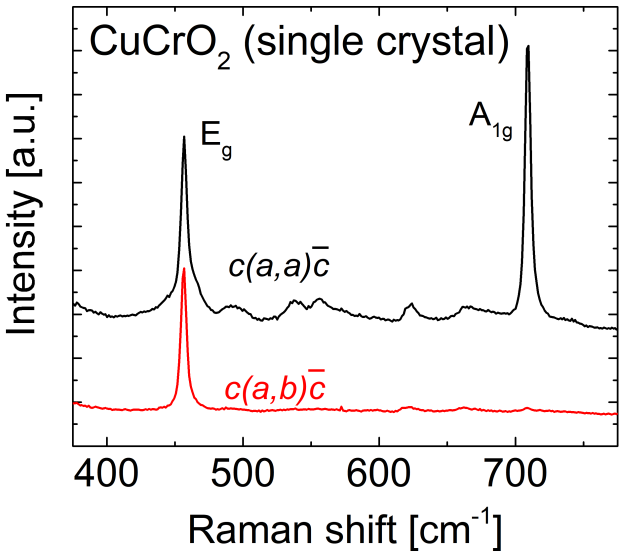

Figure 7.1: Raman spectrum of a single crystal of $CuCrO_2$ at room temperature. The mode around 710 cm^{-1} disappears in the orthogonal $c(a,b)\bar{c}$ scattering configuration is thus the A_{1g} mode. The other mode around 450 cm^{-1} is therefore identified with the E_g mode.

ization configurations, we examine the Raman tensors for this system:[116]

$$A_{1g}: \begin{pmatrix} a & 0 & 0 \\ 0 & a & 0 \\ 0 & 0 & b \end{pmatrix}, \quad E_g(x): \begin{pmatrix} 0 & d & 0 \\ d & 0 & e \\ 0 & f & 0 \end{pmatrix}, \quad E_g(y): \begin{pmatrix} d & 0 & -e \\ 0 & -d & 0 \\ -f & 0 & 0 \end{pmatrix} \tag{7.1}$$

The A_{1g} mode is observed under parallel scattering configurations as $z(x,x)\bar{z}$ with respect to all three axes. The E_g mode, however, depending on the particular scattering configuration can be observed with parallel as well as orthogonal scattering conditions. This mode is observed for $z(x,x)\bar{z}$ ($E_g(y)$) and $z(x,y)\bar{z}$ ($E_g(x)$) and is only forbidden for the parallel configuration along z, as for $y(z,z)\bar{y}$. In the $c(a,a)\bar{c}$ configuration, both the A_{1g} and the E_g mode should be observed, while in the $c(a,b)\bar{c}$ configuration, only the E_g mode should appear. Setting the polarization configurations correspondingly in the Raman experiment results in the spectra shown in Fig. 7.1. Clearly, the selection rules are well fulfilled and it is straightforward to identify the peak around 450 cm^{-1} as the E_g mode and the peak around 710 cm^{-1} as the A_{1g} mode.

Besides the two main Raman peaks, which should be the only two features according to group theory, additional features are observed in the parallel scattering configuration $c(a,a)\bar{c}$. Among the investigated samples $CuCrO_2$, $PdCrO_2$ and $AgCrO_2$, these features are exclusive to $CuCrO_2$ and are observed for both the single crystal $CuCrO_2$ as well as the polycrystalline sample. Similar results were obtained by Aktas *et al.* [107] for polycrystalline samples of $CuFeO_2$ and $CuCrO_2$, as well as by Pellicer-Porres *et al.* for $CuAlO_2$ and $CuGaO_2$ [104, 105, 117]. Based on *ab initio* calculations for $CuAlO_2$, it is argued that the additional modes originate from non-zero wavevector phonon modes [104]. In ideal single-crystal samples, due to the small momentum of a photon, optical spectroscopy probes excitations approximately at the Γ point of the Brillouin zone. Therefore, the appearance of non-zero wavevector phonon modes could indicate a reduced periodicity of the lattice due to defects, which would enable the lower-symmetry modes. Such defects could be Cu vacancies, misplaced Cr-ions on Cu sites or interstitial oxygen defects [104, 107].

For a systematic analysis of the lattice dynamics effects due to the A-site substitution of $ACrO_2$, we compare the phonon frequencies of the A_{1g} and the E_g mode for the four different samples with A^+=Cu^+ (monocrystalline sample), Cu^+ (polycrystalline sample), Pd^+, and Ag^+. As before with $Eu_{1-x}Ho_xMnO_3$, the spectra are fitted with Lorentzian functions. In addition,the experimental results are compared with shell-model calculations performed with the GULP software package [118]. Since the phonon frequencies are calculated for $T = 0$, we choose a slightly different approach for this comparison than in section 5.2 for $Eu_{1-x}Ho_xMnO_3$. Still, we want to exclude any effects of the multiferroic phase, since these are not represented in the shell-model calculations. Therefore we perform the full temperature-dependent analysis according to the Klemens model (Sec. 2.4) on the obtained spectra. From the fit according to Eq. 2.18, we obtain the intrinsic phonon frequency $\omega_{T=0} = \omega_0 - C$, that each phonon would display for $T \to 0$ if there were not any additional effects such as spin-phonon coupling (SPC) and use this value for graphs in the following comparison. The values for the experimental phonon frequency ω at room temperature and $\omega_{T=0}$ obtained from the Klemens model fit are listed in Table 7.1 to illustrate that this method does not change the qualitative observation, as the phonon softening due to anharmonic decay at room temperature is approximately uniform among the samples and amounts to 2-3 cm^{-1} for the A_{1g} mode and 4-5 cm^{-1} for the E_g mode. Already at the first glance, Table 7.1 shows that the frequencies of both modes of the monocrystalline and the polycrystalline samples of $CuCrO_2$ coincide so well, that they are indistinguishable in this property.

	$\omega(E_g)$, T=300 K [cm^{-1}] exp.	$\omega_{T=0}(E_g)$ [cm^{-1}] Klemens model
$CuCrO_2$ (mono)	456.0	457.9
$CuCrO_2$ (poly)	456.0	458.1
$PdCrO_2$	473.1	476.3
$AgCrO_2$	451.3	454.0
	$\omega(A_{1g})$, T=300 K [cm^{-1}] exp.	$\omega_{T=0}(A_{1g})$ [cm^{-1}] Klemens model
$CuCrO_2$ (mono)	708.6	712.7
$CuCrO_2$ (poly)	708.7	712.7
$PdCrO_2$	703.7	708.4
$AgCrO_2$	652.0	656.8

Table 7.1: Experimentally observed phonon frequencies ω at room temperature and intrinsic frequencies $\omega_{T=0} = \omega_0 - C$ obtained with the Klemens model fit for the A_{1g} and the E_g modes in $ACrO_2$.

	m [u]	ionic radius [Å]	$\angle$ A-O-Cr [°]	electron config.
Cu^+	64	0.46	120.3	[Ar] $3d^{10}$
Pd^+	106	0.54	122.1	[Kr] $4d^8 5s^1$
Ag^+	104	0.67	122.3	[Kr] $4d^{10}$

Table 7.2: Geometric parameters of the $ACrO_2$ sample series

In order to illustrate possible trends among the sample series, the obtained frequencies $\omega_{T=0}$ are plotted versus the atomic mass of the A-site ion (Fig. 7.2b), the ionic radii (Fig. 7.2a) and the A-O-Cr bong angle (Fig. 7.2c). Bond angles are calculated with the structural data from references [21, 119, 120] and the ionic radius is taken from Ref. [68]. These parameters of the geometric structure are listed in Table 7.2. In each graph, the A_{1g} mode is plotted in the left-hand panel, while the E_g mode is plotted in the panel on the right-hand side. Depending on the chosen form of representation, the $PdCrO_2$ sample is either located closer to $AgCrO_2$, which is the case for the plots of frequency versus atomic mass and versus bond angle, or closer to $CuCrO_2$, as is the case for the plot with respect to the ionic radius. While a systematic dependence with respect to the ionic mass is not anticipated as the elongation patterns of both modes consists exclusively of oxygen displacements, also the other two representations do not show a clear tendency, which is a result of the peculiar behavior of the phononic modes in $PdCrO_2$.

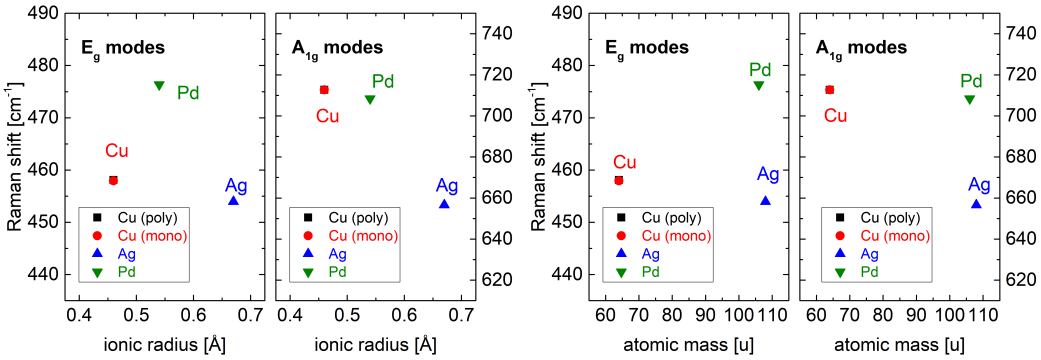

(a) Raman shift vs. ionic radius.

(b) Raman shift vs. mass of the A-ion

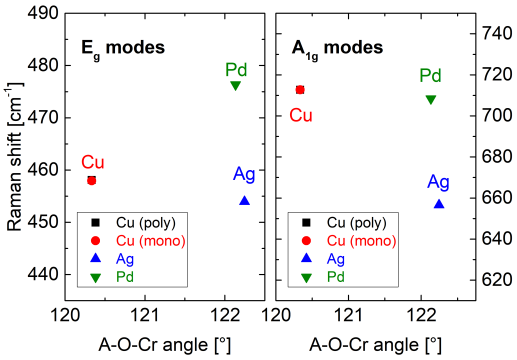

(c) Raman shift vs. bond angle.

Figure 7.2: Experimentally observed Raman shifts for the E_g and A_{1g} modes of $ACrO_2$ versus ionic radius (a), mass of the A-ion (b), and versus the A-O-Cr bond angle (c). The polycrystalline and monocrystalline samples of $CuCrO_2$ coincide perfectly.

For the E_g mode, $CuCrO_2$ and $AgCrO_2$ show very similar mode frequencies, while the $PdCrO_2$ mode frequency is vastly larger (about +20 cm^{-1}). On the other hand, if we consider the A_{1g} modes, this behavior is completely reversed: Here, $CuCrO_2$ and $PdCrO_2$ show comparable frequencies while $AgCrO_2$ shows a much lower frequency (about -55 cm^{-1}) compared to the other two. Similarly like in the $Eu_{1-x}Ho_xMnO_3$ series, one could expect that due to the nearly identical bond angle, $PdCrO_2$ and $AgCrO_2$ would also show a comparable behavior in their lattice dynamics. To further investigate this issue, basic shell model calculations were performed. In the calculation, only the different ionic masses and the ionic radii have been considered. The latter by adjusting the effective radius ρ_0 of the interionic potentials in proportion to the ionic radius extracted from reference [68]. This approach does not claim to be a full numerical treatment, nevertheless it is expected to give

reasonable results for trends when considering the phonon frequencies in the order of replacement of Cu→Pd→Ag. The results of the calculations are shown in Fig. 7.3. For $CuCrO_2$ and $AgCrO_2$, the calculated frequencies for

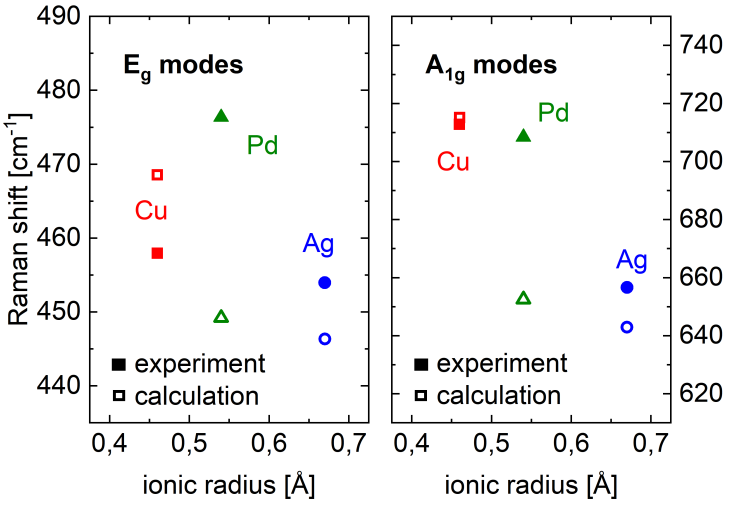

Figure 7.3: Comparison of the experimentally observed Raman shifts with simple shell model calculations. Only effects of ion radii and masses were considered. The general trend for $CuCrO_2$ and $AgCrO_2$ is recreated, however $PdCrO_2$ shows a distinctly different behavior.

the A_{1g} modes fit reasonably well with the experimentally observed values, while for the E_g modes the scale in Fig. 7.3 is offset by a constant for the calculated results. In the order of Cu→Pd→Ag, the calculations show a decrease of mode frequencies for both modes. Clearly, $PdCrO_2$ shows an obviously different behavior for its phonon frequencies in the experimental observations. As this can neither be explained by geometric reasons, i.e. the ionic radius and bond angle, nor with the change in atomic mass, another reason must be responsible. One property that distinguishes Pd^+ from the other two ions is the configuration of valence electrons. Both Cu^+ and Ag^+ have completely filled $3d^{10}$ and $4d^{10}$ configurations, respectively, while Pd^+ has the electron configuration $4d^8 5s^1$. Besides the observations presented here, there is evidence of far larger observed Raman shifts for the E_g mode of $PdCrO_2$ of about 550 cm^{-1} by Glamazda *et al.*, while the reported frequency of 710 cm^{-1} for the A_{1g} mode at 5 K is only marginally different from the results presented in this thesis [17]. This points to possible challenges in sample preparations that need to be overcome, as $PdCrO_2$ samples seem to show very different properties among different research groups. This is of particular interest in future work, as $PdCrO_2$ is not only an interesting

specimen within the multiferroics community, but also under investigation for spin-liquid behavior [18, 121].

7.2 Temperature dependence and spin-phonon coupling

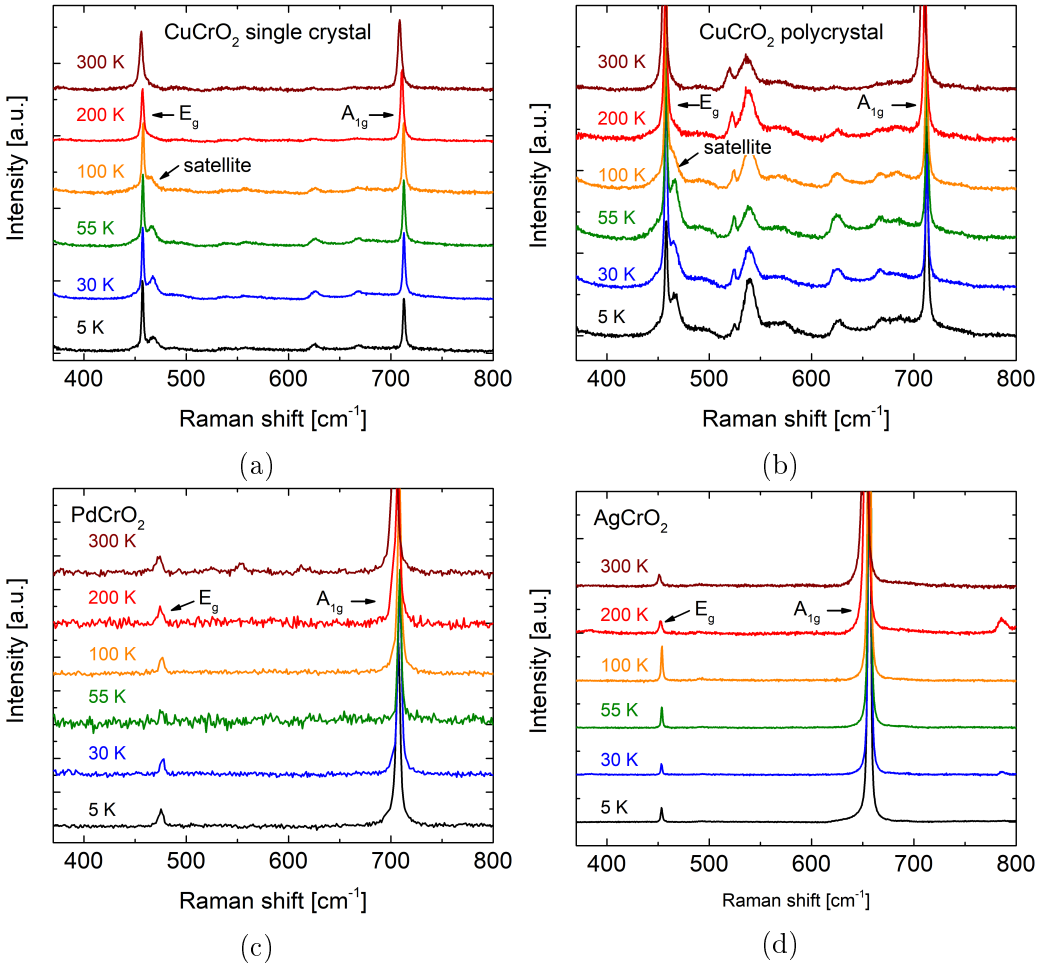

Figure 7.4: Temperature-dependent Raman spectra of the $ACrO_2$ series. (a) single crystal of $CuCrO_2$, (b) polycrystalline $CuCrO_2$, (c) $PdCrO_2$ and (d) $AgCrO_2$.

The temperature-dependent behavior of the phonon frequencies is investigated in the same way as in the case of $Eu_{1-x}Ho_xMnO_3$ with the Horiba LabRAM micro Raman setup equipped with a coldfinger cryostat described in section 3.1. A selection of unpolarized spectra at various temperatures is shown in Fig.7.4. Aside from the initial frequency shift when cooling from 300 K-100 K, as expected from the Klemens model (Sec. 2.4), no obvious changes in the phonon spectra are observed at the lower tempera-

tures, indicating a much smaller spin-phonon coupling (SPC) effect than in $Eu_{1-x}Ho_xMnO_3$. Note, how the polycrystalline sample of $CuCrO_2$ shows much larger intensities for the defect modes, located between the actual phonon modes. Despite this hint to a possible reduction of crystal quality and subsequently the coherence length, the mode frequencies themselves coincide perfectly with those of the monocrystalline sample. The lattice itself seems to be unaltered by the grain size of the polycrystalline sample. For $PdCrO_2$ and $AgCrO_2$ the defect modes do not show up in the spectra at all. The spectra of $CuCrO_2$ show an additional feature at temperatures below 120 K, which is labeled as a "satellite" in Fig. 7.4. It gets more pronounced in intensity and moves further away from the E_g mode as the temperature is reduced. This feature is going to be discussed in detail in Section 7.3, while the main focus of the following discussion are the two phonon modes.
For a more detailed analysis, the A_{1g} and the E_g phonon modes and the satellite peak are fitted with Lorentzian functions for each temperature. Subsequently, the data is fitted with the Klemens model (Eq. 2.18) for $T \geq 100$ K. The result of this analysis is shown in Fig. 7.5. The deviation of the observed frequencies (black squares) from the fit (red lines) is once more attributed to spin-phonon coupling. Clearly, the SPC-induced shift in the investigated

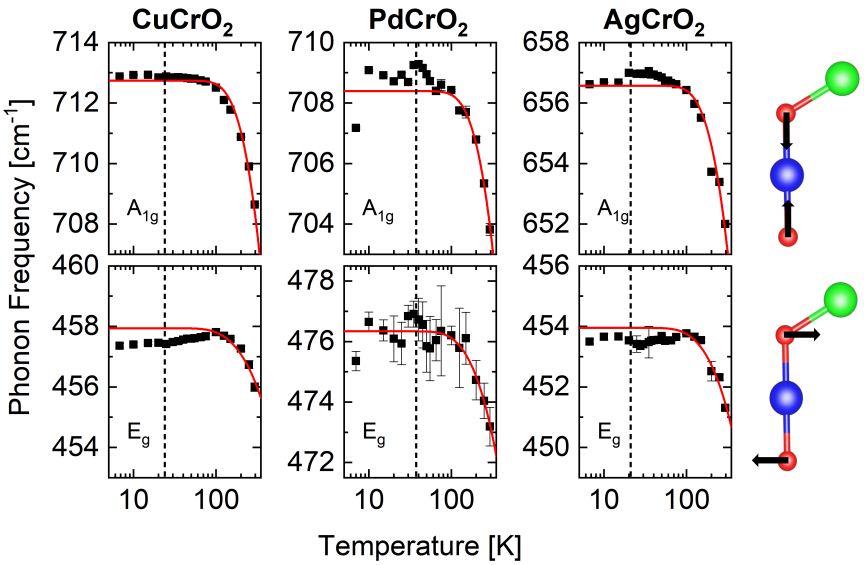

Figure 7.5: Temperature-dependent phonon behavior in the $ACrO_2$ compounds measured by Raman spectroscopy. The onset of SPC above T_N (broken black line) is also here clearly visible as the deviation from the Klemens model fit (red line).

$ACrO_2$ is much weaker than in the $Eu_{1-x}Ho_xMnO_3$ system. The relative shift

SPC shift [‰]	E_g mode	A_{1g} mode
$CuCrO_2$	-1.3	0.3
$PdCrO_2$	-0.2	0.8
$AgCrO_2$	-0.8	0.8

Table 7.3: SPC-induced shift, relative to $\omega_0 - C$ obtained from the Klemens fit.

amounts to only 0.1 % of the phonon frequency, compared to a relative shift in the order of 1 % for the $B_{2g}(1)$ mode in $Eu_{1-x}Ho_xMnO_3$ (see table 7.3). A possible explanation could be the geometry of the phonon modes itself. The $B_{2g}(1)$ mode of the RMnO$_3$ compounds comprises of vibrations of the O(2) ions within the ac plane. With an Mn-O-Mn bond angle of about 146°, the tilt of a single octahedra relative to the ac-plane amounts only to about 17°. For ACrO$_2$, the A-O-Cr angle is about 120°. Therefore, the oxygen displacements of both the A_{1g} and the E_g mode encompass an angle of 30° with respect to the bond towards the magnetic Cr-ion. This means, that the oxygen displacements for the $B_{2g}(1)$ mode in RMnO$_3$ are oriented much more directly at the magnetic Mn-ion and therefore modulate the exchange integral stronger than in ACrO$_2$, where the direction of oxygen displacement and the magnetic Cr-ion encompass a larger angle, which is unfavorable to produce a large effect.

Along the same line, this might explain why the E_g mode shows a stronger SPC-induced shift in $CuCrO_2$ than in the other two compounds, while for the A_{1g} mode, the situation is reversed: Depending on the actual value for the A-O-Cr bond angle, either the A_{1g} or E_g would show the stronger SPC effect. If we consider the hypothetical extreme cases for a 180° A-O-Cr angle, the A_{1g} mode would show the strongest SPC effect, as the oxygen displacements are parallel to Cr-O bond, while from the E_g mode, only minimal SPC shifts would be expected, as the oxygen displacement is perpendicular to the Cr-O bond. The opposite situation would occur for a 90° A-O-Cr angle, where the A_{1g} would show a minimal SPC shift and the E_g mode oxygen displacements would be parallel to the Cr-O bond. In the sample series with A=Cu→Pd→Ag, the A-O-Cr bond angle varies from 120.3° → 122.1° → 122.3°, which would fit to the trend of increasing SPC for the A_{1g} mode, while the SPC for the E_g mode is decreased.

The onset of SPC, visible as a deviation from the Klemens-fit is also observed in ACrO$_2$ at temperatures of about 100 K, indicating local magnetic correlations above T_N for all three compounds. The actual onset of spin correlations might extend to even higher temperatures: Glamazda *et al.* observe

a broadening of the ESR linewidth at temperatures below 220 K in $PdCrO_2$, which they ascribe to the onset of short-range spin correlations [17]. The fact, that this is not visible in the Raman data of Fig. 7.5 in the temperature range of 200 K $\geq T \geq$ 100 K could have multiple reasons. One could be, that the SPC due to spin correlations in the range of 200 K $\geq T \geq$ 100 K are obfuscated with the intrinsic temperature-dependent phonon frequency shift due to anharmonic decay. A second reason is that SPC is not restricted to produce always negative contributions, i.e., a softening of the phonon frequency. This can be seen in the $CuCrO_2$ data in Fig. 7.5, where the E_g mode experiences a shift to smaller frequencies, while the A_{1g} mode is shifted to slightly higher frequencies. In the panel for $AgCrO_2$, the A_{1g} mode shows clearly an increase of mode frequency with respect to the fit in the range of $100 \geq T \geq T_N$ and a subsequent decrease of the mode frequency below T_N. This could indicate, that SPC-effects with opposing signs might be at work, which could also explain the observed minor SPC shift as compared to $Eu_{1-x}Ho_xMnO_3$.

A final remark in this section points towards the datapoint at the lowest temperature (5 K) for $PdCrO_2$ of Fig. 7.5. This might look like a bug in the experiment, as the phonon frequency is abruptly reduced, but has been reproduced. Also the Raman spectra of Glamazda *et al.* show an abrupt shift of the phonon frequency in this temperature range, albeit to a higher frequency [17]. At this point the origin of this observation is not clear as it could be related to a structural change in the lattice, either purely caused by lattice degrees of freedom or also of magnetic origin similar to the magnetostriction mechanism or due to a sudden change in the spin system, which affects the SPC.

7.3 Satellite peak of the E_g mode

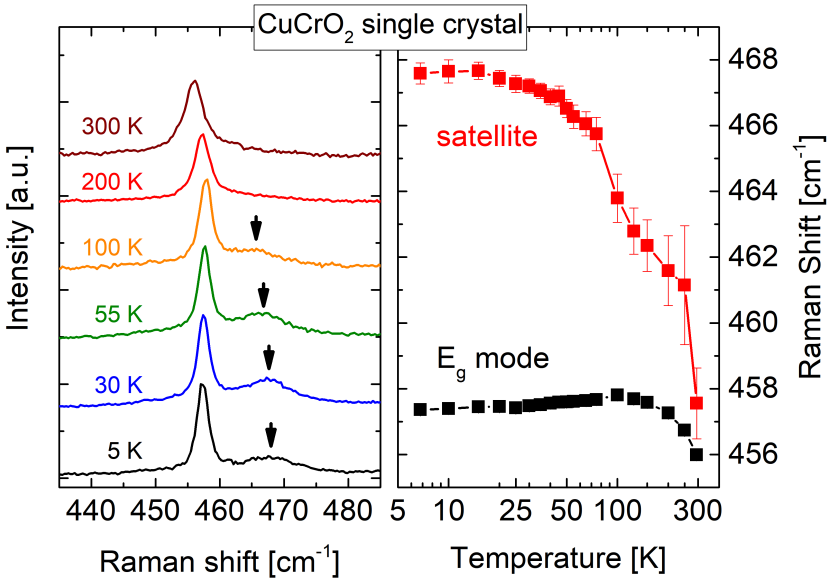

Figure 7.6: A shoulder or satellite peak (black arrow) becomes visible and separates itself from the main E_g phonon peak with decreasing temperature.

A feature already referenced to in the previous section, which is going to be discussed in the following is the development of a satellite peak next to the E_g mode in $CuCrO_2$ while lowering the temperature.

Figure 7.6 shows how the satellite is clearly separated from the main E_g peak below 120 K (left panel). If we follow the peak position in the spectrum versus temperature (Fig. 7.6 right panel) by fitting two Lorentzian lineshapes, it can be traced until room temperature, where it merely shows up as a shoulder to the E_g peak. This is in line with the observation of Aktas *et al.* [107]. However, they point out that the satellite peak appears for parallel and crossed polarization configurations. Unfortunately no spectra are presented in their article. Therefore, they ascribe the same symmetry to the satellite peak as for the E_g phonon mode. In contrast, if we compare our spectra of the two polarization configurations at 5 K shown in Fig. 7.7, the satellite peak is clearly suppressed in crossed polarization, which is the same behavior like for the A_{1g} mode. The appearance of a satellite peak next to the E_g mode was also shown in the isostructural $CuGaO_2$, where it is observed when pressure is applied and was explained to be caused by a structural phase transition [104]. In a similar way, the satellite peak is

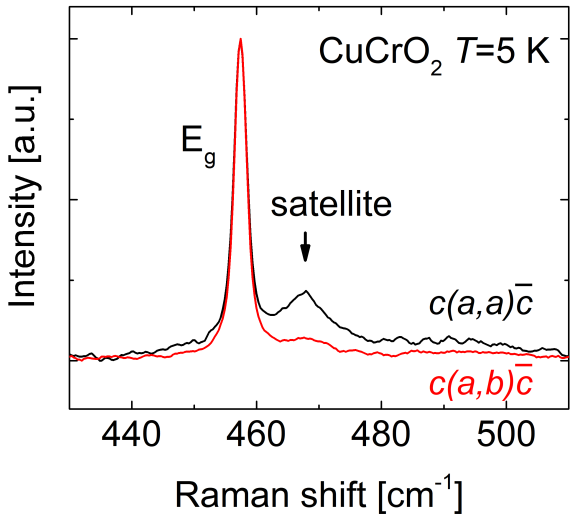

Figure 7.7: Raman spectra of $CuCrO_2$ for parallel and crossed polarization configurations at 5 K. The E_g phonon appears in both configurations, while the satellite peak is strongly suppressed in the crossed configuration.

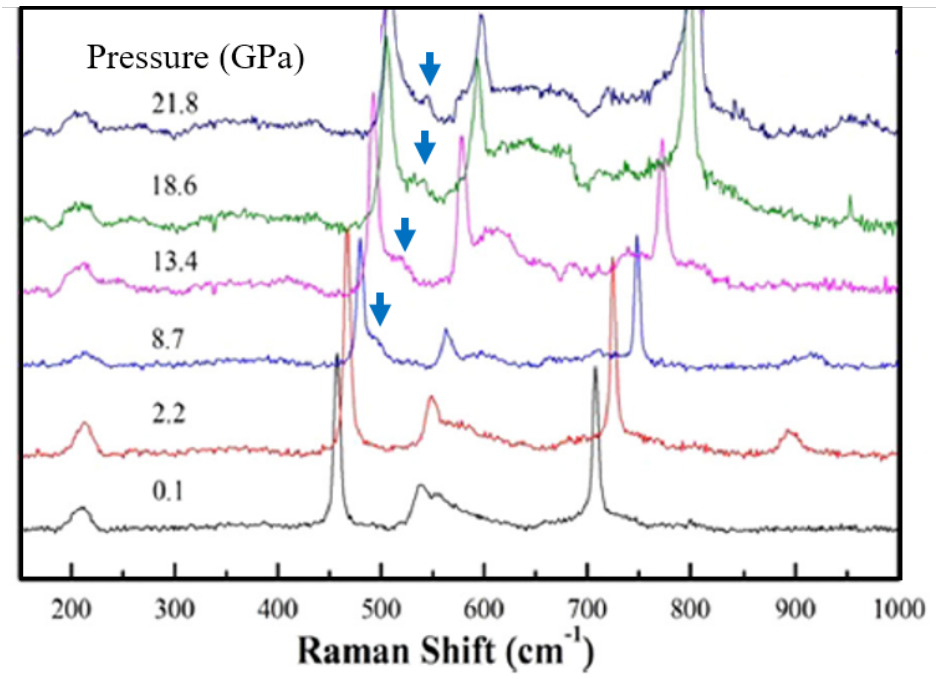

Figure 7.8: Raman spectra of $CuCrO_2$ at room temperature under hydrostatic pressure. The satellite peak, marked by arrows, is clearly distinguishable for 8.7 GPa and above. Adapted from [122].

observed in $CuCrO_2$ at room temperature, when hydrostatic pressure is applied. It is well separated for hydrostatic pressures of 8.7 GPa and above in the spectra shown in Figure 7.8, which were recorded by Garg *et al.* [122]. The appearance of the satellite peak with applied pressure hints at a possible deformation of the triangular lattice. Since the E_g is the mode with in-plane oxygen displacements in the *ab*-plane, it is plausible, that a deformation of the triangular lattice would be accompanied by a splitting of the E_g mode.

A connection between a lattice distortion and the magnetic properties is suggested by Kimura *et al.* [23]. They observe a contraction of the triangular lattice in $CuCrO_2$ parallel to the modulation vector **Q**.

Two scenarios could lead to a lattice distortion coupled to the magnetic phase transition [23]. As discussed in section 6.2, systems with strong geometrical frustration are likely to have a large spin degeneracy. On the other hand it is well known, that degenerate systems are generally unstable, as they can often lower their energy by lifting the degeneracy. The Jahn-Teller deformation (Sec. 4.1.2) is also an example for this, where the degeneracy of the *d* orbitals is lifted by deforming the ligand-bonds, if the *d* orbitals are not fully- or half-filled. In this way, the system in $CuCrO_2$ could lift the spin degeneracy by deforming the triangular lattice, resulting in the incommensurable spin spiral with $q = 0.329$ instead of the 120° order, which would correspond to $q = 1/3$. The second scenario could be, that the incommensurable order would in fact be the energetically most favorable state for the spin system. Then, the spin system could induce a lattice distortion to achieve this state by exchange striction [23, 123, 124].
With this interplay of lattice and spin degrees of freedom, the question arises why the E_g mode splitting does not occur at the magnetic phase transition temperature T_N, since the results of Figure 7.6 show a gradual separation of the satellite from the E_g mode. A possible explanation can be found in the local nature of Raman spectroscopy: magnetic correlations in the $ACrO_2$ system are observed in ESR for temperatures in the order of 200 K (220 K for $PdCrO_2$ [17]). Kimura *et al.* describe, that three possible domains exist for the spin spiral within the *ab*-plane. For the isotropic triangular lattice, the spin spiral modulation vector can point into the three equivalent directions [100], [010] and [110] as shown in Figure 7.9. In the ground state, only the [110] spirals remain, but all three variants of spiral domains would show a lattice deformation parallel to the respective modulation vector. In a similar scenario as in $RMnO_3$, the onset of deformation could be visible in Raman spectroscopy by the appearance of the satellite peak, while all possible domains are present. In contrast, in non-local averaging experiments, the lattice distortion would be obfuscated. In this way the gradual splitting

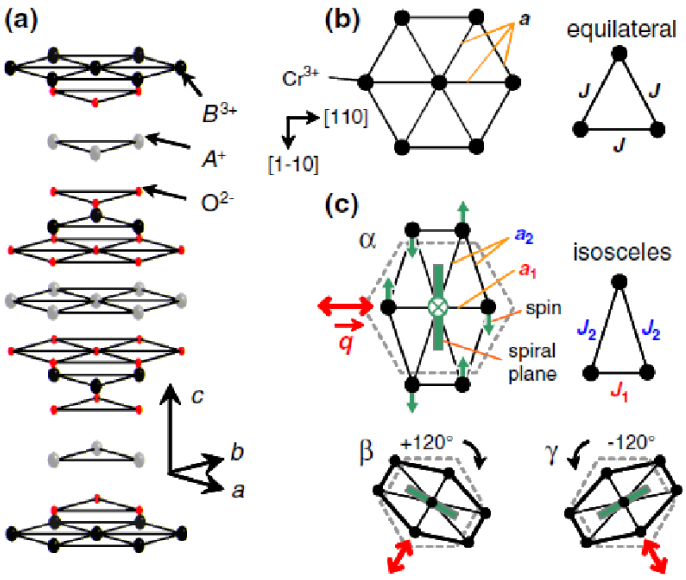

Figure 7.9: Distortion of the isotropic triangular lattice caused by proper-screw spin structure. The bond lengths are shortened parallel to the modulation vector **Q**. The resulting three possible domains are indicated with the labels α, β and γ Adapted from Ref. [23]

of the E_g mode can be explained with the gradual orientation of spin-spiral domains and growth of correlations lengths.
A different approach for explanation of the satellite peak is discussed by Suzuki *et al.* for $LiCrO_2$, which is another a triangular Heisenberg antiferromagnet [22]. They observe a similar "hidden" peak, superimposed with the A_{1g} mode and another broad feature around 350 cm^{-1}, whereas both are present at low temperatures, but can be traced to temperatures up to $\approx$ 150 K. The features are ascribed to a two-magnon scattering process, which also assumes local magnetic correlations at temperatures far above the transition temperature T_N=62 K for $LiCrO_2$ [22, 125]). This is further supported by NMR studies of Alexander *et al.*, who found magnetic correlations for temperatures up to nearly $4 \cdot T_N$ [126].
From the experimental point of view, one should consider if the increase of intensity of a given feature is truly caused by its own temperature dependence or if it is merely a result of a resonance enhancement as the temperature is varied. Such an effect could be the variation of the bandgap energy with the temperature. If the bandgap energy comes close to the laser energy, Raman signals can be enhanced (see chapter 2). To exclude this possibility, the intensities of the E_g mode and the satellite peak are considered by integrating

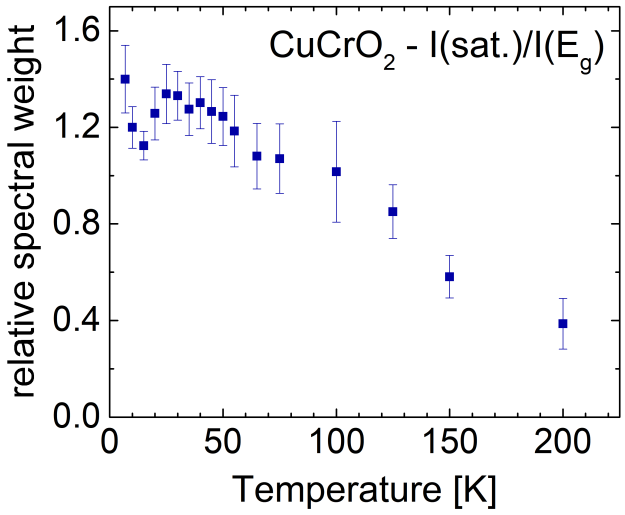

Figure 7.10: Intensity ratio $I(satellite)/I(E_g)$ of the satellite peak with respect to the E_g mode.

their respective area and plotting the intensity ratio of $I(satellite)/I(E_g)$ in Figure 7.10. If the increase of peak intensity would be caused by resonance enhancement, due to the close proximity of both peaks, both, the satellite peak and the E_g mode should experience a similar enhancement. Thus the ratio would be constant. The plot in Fig. 7.10 shows a decrease of spectral weight of the satellite peak relative to the E_g mode as the temperature is increased, indicating that the satellite intensity is not related to resonance enhancement. This supports the notion of a magnetic origin of this peak.

To summarize, no final conclusion about the origin of the satellite peak can be reached at this point. While it seems likely, that the peak is appears due to a deformation of the triangular lattice caused by the magnetic order, it raises the question why no such peaks are observed in $PdCrO_2$ or $AgCrO_2$, which should also exhibit the proper-screw magnetic order. This could be related to the crystalline quality of the samples, as the manufacturing of $CuCrO_2$ samples seems to be under better control, giving consistent Raman spectra among different research groups and sample specimen and also larger single crystal slabs of a few mm size are available. On the other hand the Raman spectra for $PdCrO_2$ can vary wildly, as pointed out in the characterization (section 7.1)

7.4 Lattice dynamics in an external magnetic field

In order to complete the investigation of the lattice dynamics of $A\mathrm{CrO_2}$, the behavior of the two vibrational modes as well as the satellite peak is investigated under the influence of an external magnetic field. For this purpose, the samples are mounted into the Spectromag LHe bath cryostat (see section 3.2). The triple monochromator allows to probe excitations with very low Raman shifts, i.e. with small energy differences with respect to the laser line. This is mandatory to detect any low-lying excitations such as (electro-)magnons. The magnetic-field dependence of the eigenfrequencies

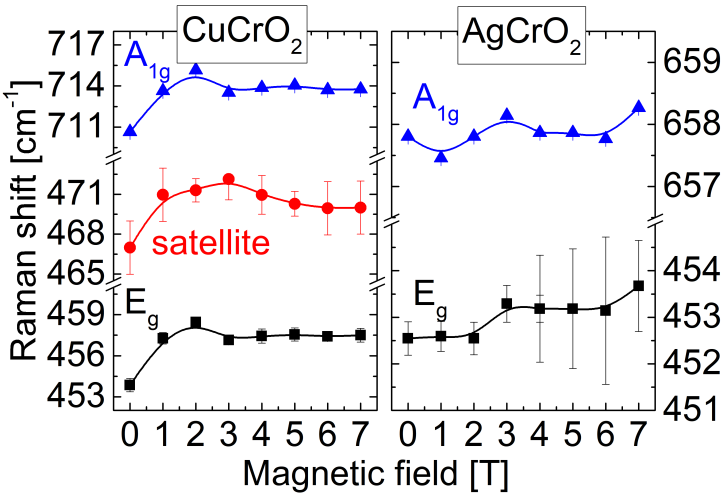

Figure 7.11: Magnetic-field dependence of the $A\mathrm{CrO_2}$ phonons and the satellite peak of $\mathrm{CuCrO_2}$.

of the $A\mathrm{CrO_2}$ phonons and the $\mathrm{CuCrO_2}$ satellite peak is displayed in Figure 7.11. Note, that the $\mathrm{PdCrO_2}$ samples were unsuitable for macroscopic Raman spectroscopy as they were comprised of discontiguous micro crystallites, too small for the spot size of the macro Raman setup. Therefore only $\mathrm{CuCrO_2}$ and $\mathrm{AgCrO_2}$ could be investigated in an external B-field. The $A\mathrm{CrO_2}$ compounds show a more pronounced frequency shift in the magnetic field than the $\mathrm{Eu_{1-x}Ho_xMnO_3}$ compounds. The maximum frequency shift in $\mathrm{Eu_{1-x}Ho_xMnO_3}$ amounts to about $\pm\ 2\,\mathrm{cm^{-1}}$ (see Fig. 5.16), whereas it is up to $5\,\mathrm{cm^{-1}}$ in $A\mathrm{CrO_2}$. The distinct value of magnetic-field-induced shift of up to $5\,\mathrm{cm^{-1}}$ is especially unexpected, as the temperature-dependent SPC-induced shift was much lower than in the $R\mathrm{MnO_3}$ compounds.

While $AgCrO_2$ shows just a weak variation of phonon frequencies with the magnetic field of about $1\,cm^{-1}$ across the whole accessible magnetic-field range of 7 T, $CuCrO_2$ shows a strong increase of phonon frequencies for low magnetic fields of about $5\,cm^{-1}$ until 3 T. Also, it is noted that the E_g and A_{1g} mode behave similar, while the satellite peak behaves slightly different: for magnetic fields $B \geq 3$ T, the frequency of the phonon modes remains constant, while the frequency of the satellite peak is slightly reduced. Since the frequency difference of the satellite peak and the E_g mode gets slightly smaller for the higher fields, this could indicate a slight relaxation of the lattice deformation with magnetic field. Considering the temperature- and magnetic-field dependent results together with the results of pressure-dependent Raman spectroscopy of Garg *et al.* [122] and the spin-dependent $p-d$ hybridization model of Arima [42] one can arrive at the conclusion that in this compound, not only is the ferroelectric order, but also the deformation of the lattice is coupled to the magnetic order. This gives an interesting perspective for future investigations in this compound. If this cross-correlation of magnetization, polarization and deformation is established, one should be able to confirm this by inducing the phonon splitting of the E_g mode in $CuCrO_2$ with the application of a static electric field.

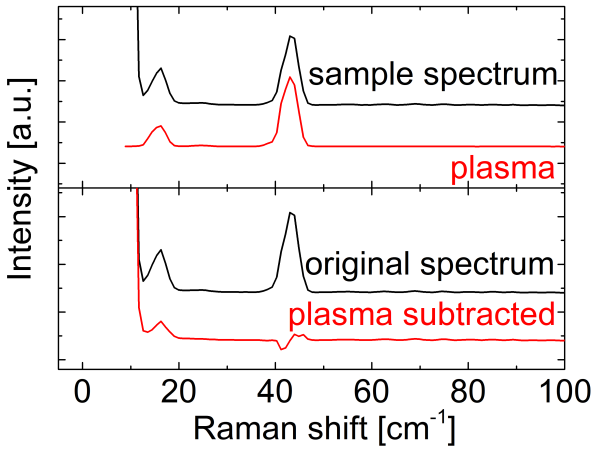

Figure 7.12: Schematical illustration of the subtraction process for the $ACrO_2$ sample series. Plasma lines dominate the spectrum around $20\,cm^{-1}$ and $40\,cm^{-1}$ due to the low optical density of the plasma line filters. An argon plasma spectrum is subtracted to further reduce the plasma line intensity in the final spectrum.

With magnetic order and electric polarization being coupled, these compounds should also show (electro-)magnons. In literature, such data exists

for $LiCrO_2$ [22]. However, the detection on the present samples provided several challenges: in close vicinity to the expected Raman shifts, there exist plasma lines of the Ar and HeNe plasma of the available lasers and commercially available plasmaline cleanup filters suffer of a very low optical density at wavenumbers which correspond to a Raman shift less than $\sim 70\,\mathrm{cm}^{-1}$. It was possible to partially improve the spectra by taking the difference of the sample spectra and the same spectra with detuned laser which only show plasma lines. An example of the subtraction process is given in Figure 7.12. The resulting spectra are shown in Figure 7.13. However, it remains unclear if in these spectra any (electro-) magnons are detected. $CuCrO_2$ shows a feature which appears to be composed of multiple overlapping peaks at around $100\,\mathrm{cm}^{-1}$ and $210\,\mathrm{cm}^{-1}$. These features are not present in $AgCrO_2$. In contrast, $AgCrO_2$ shows a broad structure centered around $61\,\mathrm{cm}^{-1}$, which would be a typical value for (electro-) magnons in $ACrO_2$. Due to the very low signal strengths in this range, no concluding remark can be given at this point in time. It can be beneficial, if not even necessary, to use a tunable laser source and perform resonance Raman spectroscopy to improve the signal yield.

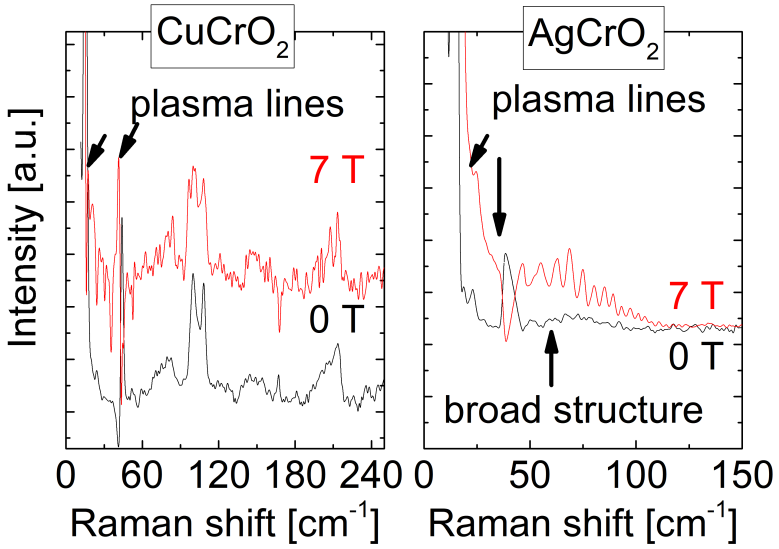

Figure 7.13: Raman spectra of $CuCrO_2$ and $AgCrO_2$ down to very low Raman shifts at different magnetic fields. Despite the subtraction process illustrated in Fig. 7.12, some intensity of the laser plasma lines still remains.

7.5 Summary

To investigate the lattice dynamics of the delafossite $A\mathrm{CrO_2}$ system with respect to the A-site ionic radius, the set of samples with A=Cu, Pd and Ag was considered, which forms a series of decreasing A-site ionic radii. The two Raman-active phonon modes of A_{1g} and E_g symmetry were successfully identified by polarized Raman spectroscopy. To supplement the experimental findings, the phonon frequencies were calculated with shell-model calculations with the GULP software package, which showed that the phonon frequencies should decrease in the order Cu→Pd→Ag. While $\mathrm{CuCrO_2}$ and $\mathrm{AgCrO_2}$ followed this trend, the $\mathrm{PdCrO_2}$ phonon frequencies exceeded the expected frequencies by far. In an attempt to categorize possible causes of this unusual behavior, this trend was examined with respect to the ionic radius, mass and the A-O-Cr bond angle, which did not reveal a systematic dependence of one of these parameters. However, one property that distinguishes the Pd^+ ion from Cr^+ and Ag^+ is the configuration of the valence electrons: Cr^+ and Ag^+ have completely filled d shells with the configuration $3d^{10}$ and $4d^{10}$, respectively, while the Pd^+ ion is in the valence electron configuration $4d^8 5s^1$. With this and the fact that there are reports of even higher phonon frequencies in literature, it appears that synthesis of $\mathrm{PdCrO_2}$ still poses a challenge that needs to be overcome in the future to achieve consistent results [17].
In order to investigate SPC effects in $A\mathrm{CrO_2}$, temperature-dependent Raman spectroscopy was performed. Similar to $\mathrm{Eu}_{1-x}\mathrm{Ho}_x\mathrm{MnO_3}$, or $R\mathrm{MnO_3}$ in general, SPC effects were already observed at temperatures well above T_N, up to about 100 K, indicating the onset of local magnetic correlations. This finding is also supported by ESR linewidth measurements, which indicate local magnetic correlations to even higher temperatures [17]. The SPC strength however, was found to be one order of magnitude weaker than in the $R\mathrm{MnO_3}$ compounds: The relative SPC-induced shift amounts to about 1% in $\mathrm{Eu}_{1-x}\mathrm{Ho}_x\mathrm{MnO_3}$ and to only about 0.1% in $A\mathrm{CrO_2}$. The reason might be the A-O-Cr bond angle of about 120°, which is unfavorable to produce a large SPC effect when the elongation patterns of the A_g and E_g modes are considered.

It was shown, that the sensitivity of the two phonon modes for SPC effects changes in the sample series: for $\mathrm{CuCrO_2}$, the E_g mode showed the stronger SPC effect, while for $\mathrm{AgCrO_2}$, the A_g mode showed the stronger effect. This was successfully explained with geometric reasons by considering how the A-O-Cr bond angle is altered within the three samples: For the extreme case of a bond angle of 180°, it would be expected that the A_{1g} mode shows the

maximum possible SPC effect, while the E_g should not show any effect. In the opposite case of a 90° angle, the role of both modes would be reversed. With an actual angle of about 120°, the bonds are oriented in such a manner, that both modes lead to a similar elongation of the O-Cr bond. Then, the behavior of the SPC strength across the sample series is explained by the change in the bond angle, which leads to a stronger SPC-induced frequency shift for the A_g mode, as the bond angle is increased, while the SPC is weakened for the E_g mode.

In $CuCrO_2$ a satellite peak of the E_g mode was observed. It was shown, that this peak is likely of magnetic origin and either caused by a two-magnon scattering due to local spin correlations, or by a lattice deformation, induced by the spiral spin order via a magnetostrictive mechanism [22, 23]. Also in the second case, local spin correlations are assumed for $T > T_N$, which produce domains with spin spirals along the three possible directions [100], [010] and [110], each with lattice deformations along the respective spiral axes. While no global magnetic structure can be detected, the local nature of Raman spectroscopy could make this distortion visible already in the disordered phase via the observed satellite peak. As the temperature is reduced, the peak gets more pronounced and increasingly separated from the E_g mode, which indicates increased correlation lengths as the long range magnetic order develops. However, it remains unclear why such a peak is not observed in the other samples, $PdCrO_2$ and $AgCrO_2$.

Eventually, the lattice dynamics of $CuCrO_2$ and $AgCrO_2$ in a magnetic field were investigated. Within each sample, all features show a similar behavior as the magnetic field is increased. As also the satellite peak frequency is shifted strongly in the magnetic field, this indicates a lattice deformation caused by the application of the field if the notion of the spin-spiral induced lattice deformation is correct.

Several low-lying features in $CuCrO_2$ and $AgCrO_2$ could be detected, which could correspond to possible magnon or electromagnon excitations. However, the low signal strength, close proximity to plasma lines of the lasers and the lack of clear magnetic-field induced effects poses a challenge to irrevocably identify these features. It might be beneficial to perform resonance Raman spectroscopy to improve the signal strength and at the same time avoid the parasitic laser lines of classical gas lasers.

Chapter 8

Conclusion

In this thesis, coupling effects between the lattice dynamics and magnetic correlations in multiferroic oxides were investigated. For a systematic analysis, two series of samples with distinct magnetoelectric coupling mechanisms were considered. On the one hand, the orthorhombic rare-earth manganites $Eu_{1-x}Ho_xMnO_3$ ($0 \leq x \leq 0.5$) where the magnetoelectric coupling arises due to the inverse DM interaction and on the other hand the delafossite $ACrO_2$ (A= Cu, Pd, Ag), where the spin-dependent $p-d$ hybridization affects the valency of the Cr-O bonds and creates dipole moments with a uniform component. Raman spectroscopy was employed to investigate the lattice dynamics by systematically analyzing the Raman-active vibrational modes with respect to the compound composition, symmetry of the modes and the temperature- and magnetic-field dependence.

Both, the orthorhombic $Eu_{1-x}Ho_xMnO_3$ as well as the $ACrO_2$ delafossites show spin-phonon coupling effects in their temperature-dependent lattice dynamics by a renormalization of their vibration frequency, which is a result of the modulation of the exchange integral caused mainly by the lattice vibrations of oxygen ions which mediate the exchange. The strength of the effect is highly dependent on the particular elongation pattern of each specific mode, whereas the SPC-induced frequency shift observed in $ACrO_2$ is by an order of magnitude smaller than in the $RMnO_3$ compounds (section 5.3 and section 7.2). While the progress of understanding the multiferroic phase and the occurrence of SPC in the $RMnO_3$ compounds is already more advanced than in the delafossite $ACrO_2$, important progress was achieved in the course of this work. For the first time, the $B_{3g}(1)$ mode could be unequivocally identified in the Raman spectrum of $RMnO_3$. With this, the formalism introduced by Granado *et al.* to extract quantitative ac-plane spin-phonon coupling strengths by analyzing the $B_{2g}(1)$ mode frequency was extended to the $B_{3g}(1)$ mode which enabled the evaluation of the AFM coupling strength

along the b-direction, thus giving a complete quantifiable picture of the dominant interactions in $R\mathrm{MnO_3}$ [8]. The observations made on SPC in $R\mathrm{MnO_3}$, supplemented by the infrared activity of the electromagnon at $T \gg T_N$, the conservation of electric polarization even when the sample is heated and analysis of the activation energy for flipping a spin cycloid in dielectric measurements all point towards an activation energy corresponding to about 100 K, which stabilizes the cycloids on a local scale even above T_N and can be consistently explained by the newly introduced pseudospin model, which describes the multiferroic to paramagnetic phase transition as an order-disorder transition of locally correlated spin cycloids [11, 56, 90, 92, 93]. In addition, the violation of Raman selection rules, most likely caused by fluctuations of 90° cycloid domain walls close to the cycloid reorientation temperature in $\mathrm{Eu_{1-x}Ho_xMnO_3}$ underscore the importance of domain wall dynamics and the effectiveness of Raman spectroscopy as a local probe. Within this framework, the intermediate sinusoidal phase is described as a time-averaged distribution of fluctuating spin cycloids with short correlations lengths and can therefore explain the significant magnetic correlations, but absence of ferroelectric polarization in the sinusoidal phase, thus enriching the understanding of the spin dynamics in the broad temperature range of the magnetic phases between the paramagnetic and the cycloidal phase.

Parts of these findings can be applied to the $A\mathrm{CrO_2}$ system, where strong magnetic correlations can be found at even higher temperatures (up to 200 K), with suspected intermediate magnetic phases. By symmetry considerations, the spin spiral can propagate along three possible directions, giving rise to six possible magnetic domains. The onset of the magnetically ordered spin-spiral phase can then be understood in a similar way as for the $R\mathrm{MnO_3}$ system: locally correlated, fluctuating spin spirals, without long-range order at $T \geq T_N$ and once one of the spin-spiral domains starts to dominate, this is percepted as the onset of magnetic order. The idea of a gradual development of the magnetic order, by growing correlations lengths as the temperature is reduced, is supported by the gradual development of the satellite peak observed in $\mathrm{CuCrO_2}$, which is very likely associated with a lattice deformation caused by the spin spiral. It is, however, still unclear why this peak is only observed in $\mathrm{CuCrO_2}$ and not in other $A\mathrm{CrO_2}$ showing the spin-spiral magnetic order as well.

The domain wall dynamics of both systems offer promising approaches for further investigations and eventually applications. For example, it was demonstrated that, depending on the nature of the domain wall boundary, the boundaries can show neutral, enriched or depleted charge carrier con-

centrations. A possible applications is an electronic circuit, which can be erased and rewritten at will by aligning the domains correspondingly [25–27]. Further improving the understanding of the origin and interplay of the microscopic mechanisms, the investigation of the electromagnon and lattice dynamics with Raman as well as infrared/THz spectroscopy will prove crucial to understand how spin- and lattice degrees of freedom and conversely magnetization and polarization couple in the multiferroic systems.

Kapitel 9

Zusammenfassung

In dieser Dissertation wurden Kopplungseffekte zwischen der Gitterdynamik und magnetischen Korrelationen in multiferroischen Oxiden untersucht. Es wurden zwei Probenserien, mit jeweils verschiedenen magnetoelektrischen Kopplungsmechanismen betrachtet. Dies waren zum Einen die orthorhombischen Seltenerdmanganate $Eu_{1-x}Ho_xMnO_3$ ($0 \leq x \leq 0.5$), deren magnetoelektrische Kopplung sich aus der inversen Dzyaloshinskii-Moriya Wechselwirkung ableitet und zum Anderen die $ACrO_2$ (A = Cu, Pd, Ag) Delafossite. Bei Letzteren ergibt sich die magnetoelektrische Kopplung aus der $p-d$ Hybridisierung der Bindungspartner, welche durch den Spin des magnetischen Kupferions beeinflusst wird und sich dadurch auf die Valenz der Cr-O Bindung auswirkt. Die daraus resultierenden Dipolmomente besitzen eine uniforme Komponente und führen somit zur makroskopischen elektrischen Polarisation. Um die Gitterdynamik zu untersuchen, wurde Raman Spektroskopie betrieben und die ramanaktiven Schwingungsmoden des Gitters systematisch bezüglich der Zusammensetzung der Verbindung, der Symmetrie der Moden und der Temperatur- und Magnetfeldabhängigkeit analysiert.

Sowohl die orthorhombischen $Eu_{1-x}Ho_xMnO_3$ als auch die $ACrO_2$ Delafossite zeigen Spin-Phonon Kopplungseffekte in ihrer temperaturabhängigen Gitterdynamik. Dies äußert sich durch eine Renormalisierung der Frequenzen der Schwingungsmoden und resultiert aus der Modulation des Austauschintegrals durch die Gitterschwingungen, insbesondere solcher Schwingungen, bei denen hauptsächlich Sauerstoffionen an der Schwingung beteiligt sind, da diese den Austausch vermitteln. Die Stärke des Effekts hängt hochgradig vom jeweiligen Auslenkungsmuster jeder einzelnen Mode ab, wobei die durch Spin-Phonon Kopplung beobachtete Frequenzverschiebung in $ACrO_2$ etwa um eine Größenordnung geringer ausfällt als in den $RMnO_3$ Verbindungen. Obwohl die multiferroische Phase und das Zustandekommen der Spin-

Phonon Kopplung in $R\mathrm{MnO_3}$ bereits besser verstanden wird als in den relativ neuen $A\mathrm{CrO_2}$ Multiferroika, wurde in dieser Arbeit ein wichtiger Fortschritt erzielt: Erstmals wurde die $\mathrm{B}_{3g}(1)$ Mode im Ramanspektrum von $R\mathrm{MnO_3}$ eindeutig identifiziert. Dadurch konnte ein Formalismus, welcher von Granado *et al.* eingeführt wurde, um die Spin-Phonon Kopplungsstärken in der ferromagnetischen ac-Ebene durch die Analyse der $\mathrm{B}_{2g}(1)$ Mode zu extrahieren, erweitert und auf die $\mathrm{B}_{3g}(1)$ Mode angewandt werden [8]. Dies erlaubt nun zusätzlich die Auswertung der antiferromagnetischen Kopplungsstärke in der b-Richtung und liefert damit einen vollständigen Rahmen zur quantitativen Bewertung der dominanten Wechselwirkungen in $R\mathrm{MnO_3}$. Die Beobachtungen über die Spin-Phonon Kopplung in $R\mathrm{MnO_3}$, unterstützt durch die Infrarotaktivität des Elektromagnons für $T \gg T_N$, die Erhaltung der elektrischen Polarisation, selbst wenn die Probe über die Übergangstemperatur T_N hinweg erhitzt wird und die Analyse der Aktivierungsenergie, welche benötigt wird um den Drehsinn eines Spin Zykloids umzukehren, deuten alle darauf hin, dass die charakteristische Aktivierungsenergie für die Zykloide etwa 100 K entspricht. Das bedeutet, dass die Spin Zykloide selbst oberhalb von $T_N \approx 50\,\mathrm{K}$ lokal stabil bleiben. Dies wird mittels eines neu eingeführten Pseudospin Modells konsistent erklärt, welches den Übergang von der multiferroischen Phase zur paramagnetischen Phase als einen Ordnungs-Unordnungs Übergang lokal korrelierter Spin Zykloide beschreibt [11, 56, 90, 92, 93]. Die Beobachtung der Verletzung der optischen Auswahlregeln im Ramanspektrum nahe der Reorientierungstemperatur der Zykloide in $\mathrm{Eu}_{1-x}\mathrm{Ho}_x\mathrm{MnO_3}$, welche höchstwahrscheinlich durch Fluktuationen der 90° Domänengrenzen verursacht wird, unterstreicht die Wichtigkeit der Domänengrenzendynamik und die Effektivität der Raman Spektroskopie als lokale Sonde. In diesem Rahmen wird die bisher angenommene sinusoidale Phase zwischen der multiferroischen und der paramagnetischen Phase in einer anderen Form erklärt: Anstatt einer statischen sinusartigen Ordnung der Spins wird dieser Zustand nun als Zeitmittel von fluktuierenden Spin Zykloiden mit kurzer Korrelationslänge verstanden. Dadurch werden sowohl die beobachteten signifikanten lokalen magnetischen Korrelationen sowie die Abwesenheit einer makroskopischen Polarisation in der sinusoidalen Phase erklärt und somit das Verständnis der Spindynamik der magnetischen Phasen in dem breiten Temperaturbereich zwischen der zykloidalen (multiferroischen) und paramagnetischen Phase bereichert.

Einige dieser Ergebnisse lassen sich auch auf das $A\mathrm{CrO_2}$ System anwenden, da dort ebenfalls starke magnetische Korrelationen bei noch höheren Temperaturen beobachtet werden können (bis zu 200 K), obwohl sich die Übergangstemperatur zur multiferroischen Phase in einem ähnlichen Tem-

peraturbereich wie in $Eu_{1-x}Ho_xMnO_3$ befindet. Anhand von Symmetriebetrachtungen können die Spin Spiralen in $ACrO_2$ entlang dreier möglicher Richtungen propagieren, wodurch sechs verschiedene magnetische Domänen möglich sind. Die Ausbildung der magnetischen Ordnung kann nun auf eine ähnliche Art und Weise wie im $RMnO_3$ System verstanden werden: Bei Temperaturen $T \geq T_N$ sind die fluktuierenden Spin Spiralen lokal korreliert, ohne langreichweitige Ordnung zu zeigen. Sobald eine Domäne der Spin Spiralen beginnt zu dominieren, wird dies als Ansatz der magnetischen Ordnung angesehen. Die Idee der fortschreitenden Ausbildung der magnetischen Ordnung, hervorgerufen durch ansteigende Korrelationslängen während die Temperatur verringert wird, wird durch die ebenfalls fortschreitende Entwicklung eines Satellitenpeaks unterstützt, welcher in $CuCrO_2$ beobachtet wurde und höchstwahrscheinlich mit einer Deformation des Kristallgitters einhergeht, welche durch die Spin Spirale hervorgerufen wird. Es ist jedoch zur Zeit noch unklar, warum dieser Peak nur in $CuCrO_2$ beobachtet werden kann und nicht in anderen $ACrO_2$ Verbindungen auftritt, die das gleiche magnetische Ordnungsmuster aufweisen.

Die Dynamik der Domänengrenzen beider Systeme bieten vielversprechende Ansatzpunkte für weitere Untersuchungen und möglichen Anwendungen. Zum Beispiel wurde bereits demonstriert, dass Domänengrenzen gegenüber dem restlichen Volumen eine neutrale, erhöhte oder verringerte Ladungsträgerkonzentration aufweisen können, abhängig davon, auf welche Art und Weise die Domänen aufeinander treffen. Als mögliche Anwendung käme ein elektronischer Schaltkreis in Frage, der nach Belieben gelöscht und neu geschrieben werden könnte, indem man die Domänen entsprechend ausrichtet [25–27]. Die weitergehende Verbesserung des Verständnisses über den Ursprung und das Wechselspiel der mikroskopischen Mechanismen und die Untersuchung des Elektromagnons und der Gitterdynamik mittels Raman-, Infrarot- und THz-Spektroskopie wird entscheidend dafür sein um zu verstehen, wie Freiheitsgrade der Spins und des Kristallgitters und entsprechend der Magnetisierung und Polarisierung in den multiferroischen Systemen koppeln.

Appendices

Appendix A

Hubbard model

The Hubbard model offers a very successful approach to the many-body problem given by the N electrons and their mutual correlations in a solid. It is introduced at this point to facilitate the subsequent discussion in section 4.2. Following the deduction outlined in [127], the general Hamiltonian of the many-body problem is given by:

$$H = \sum_{i=1}^{N} \left(\frac{\mathbf{p}_i^2}{2m} + V_I(\mathbf{r}_i) \right) + \sum_{1 \leq i < j \leq N} V_C(\mathbf{r}_i - \mathbf{r}_j) \tag{A.1}$$

where V_I is the periodic potential caused by the ionic lattice and approximated to form a static lattice and V_C is the Coulomb potential acting between the electrons i and j and depends of course on the distance between them. This form is too complex to be solved exactly. Promising approaches therefore contain often mean-field one-particle approximations. Here, an auxiliary potential $V_A(\mathbf{r})$ is added to V_I and subtracted again from V_C in a particular way:

$$V(\mathbf{r}) = V_I(\mathbf{r}) - V_A(\mathbf{r}), \qquad U(\mathbf{r_i}, \mathbf{r_j}) = V_C(\mathbf{r_i} - \mathbf{r_j}) - \frac{1}{N-1}(V_A(\mathbf{r_i}) + V_A(\mathbf{r_j})) \tag{A.2}$$

which results in the Hamiltonian

$$H = \sum_{i=1}^{N} \left(\frac{\mathbf{p}_i^2}{2m} + V(\mathbf{r}_i) \right) + \sum_{1 \leq i < j \leq N} U(\mathbf{r}_i, \mathbf{r}_j). \tag{A.3}$$

The prefactor $1/(N-1)$ is necessary, because V_A is added N times in the first sum with V and is twice subtracted $\frac{N(N-1)}{2}$ times in the sum with U. To write the Hamiltonian (A.3) in the Hubbard form, (A.3) needs to rewritten

in second quantization. For a single particle in a periodic potential $V(\mathbf{r})$ the eigenfunctions of the single-particle Hamiltonian $H_1 = \frac{p^2}{2m}V(\mathbf{r})$ are given by the Bloch functions

$$\phi_{\alpha,\mathbf{k}}(\mathbf{r}) = e^{i\mathbf{k}\mathbf{r}}u_{\alpha\mathbf{k}}(\mathbf{r}) \quad with \quad u_{\alpha\mathbf{k}}(\mathbf{r}+\mathbf{G}) = u_{\alpha\mathbf{k}}(\mathbf{r}) \tag{A.4}$$

where $\mathbf{k}$ is the wavevector and $\mathbf{G}$ is a lattice vector. The eigenvalues are then given by

$$H_1\phi_{\alpha,\mathbf{k}}(\mathbf{r}) = E_1\phi_{\alpha,\mathbf{k}}(\mathbf{r}). \tag{A.5}$$

The Bloch functions are now expressed in terms of Wannier functions

$$\varphi_\alpha(\mathbf{r}) = \frac{1}{\sqrt{N_I}}\sum_{\mathbf{k}}\phi_{\alpha,\mathbf{k}}(\mathbf{r}) \tag{A.6}$$

with N_I the number of ions. The advantages if this way of expression are, that the Wannier functions $\varphi_\alpha(\mathbf{r}-\mathbf{R_i})$ are localized at the lattice positions $\mathbf{R_i}$. This means they are orthogonal for different lattice sites $\mathbf{R_i}$ and $\mathbf{R_j}$ and also different band indices α:

$$\varphi_\alpha(\mathbf{r}-\mathbf{R_i})\cdot\varphi_\beta(\mathbf{r}-\mathbf{R_j}) = \delta_{ij}\delta_{\alpha\beta}. \tag{A.7}$$

Because both $\phi_{\alpha,\mathbf{k}}(\mathbf{r})$ and $\varphi_\alpha(\mathbf{r})$ form complementary bases of the one-particle space, the Bloch functions can be expressed in terms of Wannier functions by inverse Fourier transformation:

$$\phi_{\alpha,\mathbf{k}}(\mathbf{r}) = \frac{1}{\sqrt{N_I}}\sum_{\mathbf{k}}e^{i\mathbf{k}\mathbf{R_i}}\varphi_\alpha(\mathbf{r}-\mathbf{R_i}). \tag{A.8}$$

The creation operators $c^\dagger_{\alpha\mathbf{k},\sigma}$, which create an electron in the Bloch state $\phi_{\alpha,\mathbf{k}}(\mathbf{r})$ with spin σ. With Eq. (A.8), the Wannier creation operators $c^\dagger_{\alpha i,\sigma}$ are then defined by by Fourier transformation of the Bloch creation operators in the following way:

$$c^\dagger_{\alpha i,\sigma} = \frac{1}{\sqrt{N_I}}\sum_{\mathbf{k}}e^{-i\mathbf{k}\mathbf{R_i}}c^\dagger_{\alpha\mathbf{k},\sigma}. \tag{A.9}$$

In order to create a particle in $\mathbf{r}$-space, we need the field operators $\mathbf{\Psi}^\dagger_\sigma$. It creates an electron at the position $\mathbf{r}$ with spin σ. The field operator $\mathbf{\Psi}^\dagger_\sigma$ can then be written as

$$\mathbf{\Psi}^\dagger_\sigma(\mathbf{r}) = \sum_i \phi^*_\alpha(\mathbf{r}-\mathbf{R_i})c^\dagger_{\alpha i\sigma} \tag{A.10}$$

where $\phi_\alpha(\mathbf{r}-\mathbf{R_i})$ is the Wannier function centered at the lattice position $\mathbf{R_i}$. We turn our attention now back to our Hamiltonian in Eq. (A.3). We see, that the left hand side of Eq. (A.3) can be expressed as a sum of single-particle Hamiltonians H_1. All that is left to do, is transform our initial Hamiltonian into its form in second quantization:

$$H = \sum_\sigma \int d\mathbf{r}\Psi^\dagger_\sigma(\mathbf{r})H_1\Psi_\sigma(\mathbf{r}) + \frac{1}{2}\sum_{\sigma,\sigma'}\int d\mathbf{r}d\mathbf{r}'\Psi^\dagger_\sigma(\mathbf{r})\Psi^\dagger_{\sigma'}(\mathbf{r}')U(\mathbf{r},\mathbf{r}')\Psi_{\sigma'}(\mathbf{r}')\Psi_\sigma(\mathbf{r}). \tag{A.11}$$

Eventually, the Hubbard parameters are introduced to simplify Eq. (A.11). The first is the hopping integral t^α_{ij}, which describes the hopping of an electron from site i to site j

$$t^\alpha_{ij} = \int d\mathbf{r}\phi^*_\alpha(\mathbf{r}-\mathbf{R_i})H_1\phi_\alpha(\mathbf{r}-\mathbf{R_j}) \tag{A.12}$$

which can be evaluated with Eq. (A.5) and Eq. (A.6) to $t^\alpha_{ij} = \frac{1}{N_I}\sum_{\mathbf{k}} e^{i\mathbf{k}(\mathbf{R_i}-\mathbf{R_j})}E_{1,\alpha\mathbf{k}}$. The value of t^α_{ij} can be determined with good accuracy by density-functional theory (DFT) calculations. The second parameter is the two-particle interaction parameter $U^{\alpha\beta\gamma\delta}_{ijkl}$

$$U^{\alpha\beta\gamma\delta}_{ijkl} = \int d\mathbf{r}d\mathbf{r}'\phi^*_\alpha(\mathbf{r}-\mathbf{R_i})\phi^*_\beta(\mathbf{r}'-\mathbf{R_j})U(\mathbf{r},\mathbf{r}')\phi_\gamma(\mathbf{r}'-\mathbf{R_j})\phi_\delta(\mathbf{r}-\mathbf{R_i}). \tag{A.13}$$

With Eq. (A.12) and (A.13) and considering only a single electron band (therefore omitting the band index α), the Hamiltonian (A.3) can be rewritten in the well-know form of the Hubbard Hamiltonian:

$$H = \sum_{ij} t_{ij}c^\dagger_{i\sigma}c_{j\sigma} + \frac{U}{2}\sum_i c^\dagger_{i\sigma}c^\dagger_{i\sigma'}c_{i\sigma'}c_{i\sigma}. \tag{A.14}$$

If the overlap of conduction electron wave functions is sufficiently small, it is sufficient to consider only nearest-neighbor hopping and the on-site repulsion of doubly occupied sites:

$$H = \sum_{<ij>} t_{ij}c^\dagger_{i\sigma}c_{j\sigma} + U\sum_i n_{i,+}n_{i-} \tag{A.15}$$

where $n_{i,\pm}$ are particle number operators for spin up (+) or down (-) and $< i,j >$ indicates that the sum runs over nearest neighbors only. There are now three regimes that can be distinguished in this model:

- $t \gg U$: Electron hopping or delocalization dominates, the system is metallic.
- $t \ll U$: On-site repulsion dominates, electrons are localized.
- $U/t \approx 1$: Upon increasing the on-site repulsion the system undergoes metal-insulator transition driven purely by electron-electron interactions: the Mott-Hubbard transition.

Appendix B

Basic principles of Monte Carlo simulation

In the following, an introduction to the Monte Carlo method employed for the calculations in section 5.8 will be given. As outlined by Walter and Barkema, fundamentals as detailed balance and ergodicity are discussed and the Metropolis algorithm is introduced [128].

B.1 Detailed balance and ergodicity

The fundamental idea behind Monte Carlo (MC) simulations is to introduce a small random change to the configuration C_i of a system, which results in a new configuration called a trial configuration. This trial configuration can then be either rejected or accepted. If it is accepted, the trial configuration becomes the next configuration C_{i+1} and will be used in the next iteration. If it is rejected, the configuration remains unchanged and $C_{i+1} = C_i$. This process of advancing through configurations is known as a Monte Carlo move. Two constraints are imposed onto this way of advancing through configurations. The first one is that starting from a configuration with nonzero Boltzmann weight, every other possible configuration of nonzero Boltzmann weight should be reachable in a finite number of steps. This is known as *ergodicity* and ensures that the whole phase space is sampled properly. The second constraint is known as *detailed balance*. Let us consider a pair of configuration states a and b, where the probability to find the system in configuration a is P_a and $W(a \to b)$ is the transition probability from configuration a to b. The probability for the move $a \to b$ and the probability for

the move $b \to a$ are related by:

$$P_a \cdot W(a \to b) = P_b \cdot W(b \to a). \tag{B.1}$$

For example, if a would be an unfavorable (and thus improbable) configuration and b would be much more favorable, the transition rates would be reciprocally related: $W(a \to b)$ is large and $W(b \to a)$ is small. The effect that this condition has, is to ensure stable probabilities P to find the system in a certain configuration. This can be seen by considering $dP_a(t)/dt$ to all states b:

$$\frac{dP_a(t)}{dt} = \sum_{b \neq a} [P_b(t) \cdot W(b \to a) - P_a(t) \cdot W(a \to b)] \tag{B.2}$$

Together with Eq. B.1, each term in the sum of Eq. B.2 cancels out and ensures $dP_a(t)/dt = 0$. The transition probability W for the MC method can be further decomposed into the probability T to propose a trial configuration and the probability A to accept said trial configuration. It is therefore of utmost importance to choose appropriate trial- and acceptance probabilities in a way, that the probability P_a is equal to the Boltzmann weight

$$P_a = \frac{e^{-E_a/k_B T}}{Z} \tag{B.3}$$

where Z is the partition function and E_a is the energy of the configuration a. With Eq. B.3, the detailed balance condition from Eq. B.1 can be written as

$$\frac{T(b \to a) \cdot A(b \to a)}{T(a \to b) \cdot A(a \to b)} = \frac{P_a}{P_b} = e^{\frac{-(E_a - E_b)}{k_B T}} \tag{B.4}$$

B.2 Metropolis algorithm

The approach of the Metropolis algorithm is to choose the trial configuration in such a way that $T(a \to b) = T(b \to a)$. This is suitable for a system with N spins, where one spin of the lattice is selected at random. Then $T = 1/N$ for every trial probability. The detailed balance condition reads then

$$\frac{A(a \to b)}{A(b \to a)} = \frac{P_b}{P_a} = e^{\frac{-(E_b - E_a)}{k_B T}}. \tag{B.5}$$

Since this equation contains only ratios of A, one can include a scaling factor for both acceptance probabilities. For the metropolis algorithm, this is done by setting the larger of the two acceptance probabilities to 1. Thus, there

are two cases to consider for the acceptance probabilities. If $A(b \to a)$ is the larger probability, then Eq. B.5 becomes $A(a \to b) = e^{\frac{-(E_b - E_a)}{k_B T}}$. If $A(a \to b)$ is the larger probability, then it is set to $A(a \to b) = 1$. Therefore, the acceptance probability for the Metropolis algorithm is:

$$A_{met}(a \to b) = min\left[1, e^{\frac{-(E_b - E_a)}{k_B T}}\right]. \tag{B.6}$$

A trial configuration which does not increase the total energy will always be accepted with $(A = 1)$. If the trial configuration raises the total energy, it is only accepted with a probability, which decreases exponentially as the energy difference increases. The steps for the program would then be

1. select a random spin and reorient it
2. calculate the energy difference $E_b - E_a = \Delta E$
3. generate a random number *rand* in the interval [0,1]
4. accept if $\Delta E < 0$ or $rand < e^{(-\Delta E/k_B T)}$

What remains is to choose a suitable representation of the system, i.e., the magnetic lattice, and use a Hamiltonian which captures the main physics of the system to calculate the energy. Here, a classical Heisenberg Hamiltonian is used, given by

$$\mathbf{H}_{Heisenberg} = \sum_{i \neq j} J_{ij} \mathbf{S}_i \cdot \mathbf{S}_j \tag{B.7}$$

where $\mathbf{S}_{i,j}$ are the spin vectors and J_{ij} is the exchange interaction acting between them. The spins are approximated with classical 3D vectors. The approximation is more accurate, the larger the spins are.

Appendix C

Shell-model calculations with GULP

In this section, an introduction to the GULP calculation software will be given by describing in short the method of operation of the algorithm. Numerical details are explained, where it is mandatory for the user to understand the program. For further explanations and sub-algorithms, the inclined reader is referred to Refs. [118, 129]. Informations on how to set up a script for GULP are provided and some basic available options for the simulations are discussed.

C.1 Energy minimization

GULP, which stands for "General Utility Lattice Program" is a program for the symmetry-adapted minimization of a system's energy for bulk materials. [118] It can be used to optimize lattice parameters by minimizing the total potential energy, determining the relative energy of different crystal polymorphs and calculate mechanical properties or also phonon energies, elongation patterns and their relative strengths of activity in the infrared or Raman spectrum. To minimize the energy, the Newton-Raphson method is used, where the search vector $\mathbf{x}$ is calculated as:

$$\mathbf{x} = -\mathbf{H}^{-1}\mathbf{g} \tag{C.1}$$

where $\mathbf{H}$ is the hessian matrix with the second derivatives of the energy E as matrix elements $H_{ij} = \partial^2 E/\partial x_i \partial x_j$ and $\mathbf{g}$ is the gradient vector with $g_i = \partial E/\partial x_i$. The symmetry operations of the considered systems are used to reduce the number of variables needed for the optimization and during

the generation of the hessian, the latter being the major optimization compared to non-symmetry-adapted algorithms. Altogether the computational efficiency is improved up to an order of magnitude. The algorithm determines the optimal step length and searches for a better set of parameters along $\mathbf{x}$. The whole process is repeated until the the change of energy is smaller than the desired limit.

C.2 Long-range potential

In order to determine the actual value for the potential energy of the lattice, the energy calculation is split up into two classes: long-range potentials and interatomic potentials. The long range potential, caused by the ionic charges of the ions, is simply the Coulomb potential. The numerical challenge is that the Coulomb potential decays with distance only as $1/r$, while the number of interactions increases as r^2. To achieve an efficient summation of the electrostatic energy, the Ewald summation is used.[130] This is a particular way of summing up the contributions of Coulomb potentials, by splitting the sum into a sum in real space for short distances of the interacting charges and one in reciprocal space. The optimal distribution between real-space and reciprocal-space summation was derived by Jackson and Catlow, which is controlled by a single parameter and is set by choosing the desired accuracy. A typical recommended value for the accuracy parameter A is given as $A = 10^{-8}$. [118] The user must set charges for each ion in the unit cell. For fully ionic materials as most oxides or halides, one can simply choose the formal charge of the ions, which is often already sufficient to describe the long-range potential. For materials that are not fully ionic, the formal charges can still be used, but to describe the partial covalency, a core-shell model should be provided, where a part of the formal charge is split between two ions and an harmonic spring is that couples the two ions is added to account for effects of polarization. In a typical oxide, one would therefore describe the cations with the full formal charge as a static "core" and the oxygen anion with a modified charge split between core and the covalent shell.

C.3 Interatomic potentials

As for the long-range Coulomb potentials, the charges in each specified core are treated as point charges, further potentials need to be introduced to

describe the short-range repulsive or attractive potentials. For this, several commonly used potential functions like the Morse potential and Lennard-Jones potential, among others, are available. The Lennard-Jones potential in its (12,6) form with $A/r^{12} - B/r^6$ is used where computational efficiency is of essence, as the r^{-12} term can be evaluated by squaring the result for the r^{-6} term. A more realistic potential, which is extensively used is the Buckingham potential, given by

$$Ae^{-r/\rho} - \frac{C}{r^6} \tag{C.2}$$

where the $-\frac{C}{r^6}$ is, like in the Lennard-Jones potential, an attractive term due to dipole-dipole interaction and $Ae^{-r/\rho}$ describes the repulsion at small ionic distances due to the Pauli exclusion principle. A and C are constants given in eV and eV·Å^6 by the user to set the strength of the potentials, while ρ is given in Å and related, but not identical, to the physical ionic radius, as for $r = \rho$ the exponential repulsion has dropped to $1/e$. As the exponential function in Eq. C.2 is finite at $r = 0$, while the $-\frac{C}{r^6}$ diverges this would lead to an attractive potential for very small distances (see Fig. C.1). The result is that the optimization would terminate in the unphysical state where all ions are located at distance zero to each other. The Buckingham potential is therefore not suited for materials with very short ionic distances. In such cases, it is advised to use other potentials like the Lennard-Jones or Morse potential instead, as they do not lead to unphysical energy minima. Note, that the potential minimum for the pure Buckingham potential (red curve in Fig. C.1) is rather shallow. Once the Coulomb potential is added into the consideration (blue curve in Fig. C.1), a clear energy minimum appears. As expected, the Coulomb interaction is the dominant contribution in an ionic bond. All potentials act solely between "species" of ions defined by the user. The term "species" is used in this context to distinguish ions of the same element, but on inequivalent positions within the unit cell, inequivalent charges etc. The Buckingham potential acts between two species. Thus, for the calculations for the $A\mathrm{CrO_2}$ compounds, three types of Buckingham potentials need to be defined:

- between the Ag cores and the O shells
- between the Cr cores and the O shells
- between the O shells and other O shells

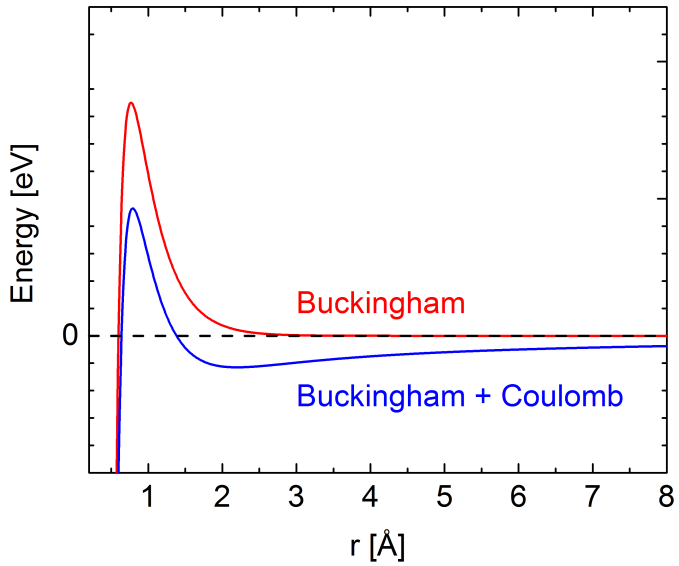

Figure C.1: Exemplary plot of the Buckingham potential (red) used for the core-shell calculations in GULP. For comparison the Buckingham-Coulomb potential (blue) is shown, which includes the Coulomb term for ionic bonds.

C.4 Setting up a GULP input file

In this section we are going to discuss how to set up a basic core-shell model calculation with GULP on the example of $CuCrO_2$. In the first line of the input file, GULP expects commands which tasks should be performed:

```
opti conp phonon noden intensity raman
```

This tells GULP to optimize the geometry at constant pressure, calculate the phonon frequencies, but not the phonon density of state. The keyword *intensity* triggers the output of phonon intensities, but prints only the infrared intensities. Therefore, also the last keyword *raman* must be given to obtain also the Raman intensities. The next lines

```
name
CuCrO2 delafossite
```

define merely the name of the crystal structure, which is useful when reading the output files when several calculations for different systems are performed consecutively. Next, the unit cell is defined by

```
cell
2.98540  2.98540  17.90910  90.0  90.0  120.0
```

```
fractional
Cu core    0.0   0.0   0.0
Cr core    0.0   0.0   0.5
O core     0.0   0.0   0.107920
O shel     0.0   0.0   0.107920
space
R -3 M
```

The unit cell is defined by the lengths of the three base vectors in Å and the three crystallographic angles. The keyword fractional indicates, that the position of the ions are given as fractions of the lattice vectors instead of absolute values in Å. Next, the positions of Cu, Cr, and O are given. Each species must be given at least the "core" position. For oxygen, also an additional position for the shell is given, which will represent the covalency of the bonds. In the space section, the user inputs the symmetry information for the system. This can be done with the Hermann-Mauguin notation, as in the example ($R\bar{3}M$) or as the space group number. In the following part, the ionic charges are specified:

```
species
Cu core   1.0
Cr core   3.0
O  core   0.84819
O  shel  -2.84819
end
```

As discussed in section C.2, the formal charge is a good value for most oxides and is used for the Cu- and Cr-ions. The covalency is expressed by the definition of the O-species by assigning a positive partial charge to the oxygen core and a larger negative charge to the oxygen shell. Of course, the total charge within one unit cell must be zero. Eventually, the interatomic potentials are defined:

```
buck
Cu core O  shel  1217.1  0.24   0.00  0.0 10.0
Cr core O  shel  1717.1  0.2947 0.00  0.0 10.0
O  shel O  shel  22764.0 0.2    27.88 0.0 10.0
spring
O      74.92     1
```

The keyword "buck" indicates the usage of Buckingham potentials. It is specified between which species the potentials should act, for example between the Cu cores and the O shells. The first three numbers are the parameters

for A, ρ and C. Note, that for oxides C is often zero, which is also the default value if not all parameters are given. This is justified by the often neglectably small attractive contribution of the potential compared to the Coulomb potential. In addition, it prevents the unphysical attractive potential for $r \to 0$. The units are eV for A, Å for ρ and eV·Å^6 for C. The last two numbers (0.0 and 10.0) define the minimum and maximum radius for the cutoff. Note, that up to three flags can be set by three additional values, that can be either 1 or 0. If the flag is set, the corresponding potential parameter will be also part of the optimization, which of course only makes sense if there is data available to fit the interatomic potentials to. The "spring" keyword adds an harmonic potential, which acts between the oxygen core and oxygen shell. Eventually, the output is written to a file with

```
dump every out.res
```

whereby "every n" specifies that output is written each n cycle of optimization. In this case the default is used, which is n=1. The calculation is then started by passing the input file via the command line to the GULP programm:

```
gulp < CuCrO2.gin
```

As the crystallographic parameters are often easily available in literature and the charges can often be inferred from formal charges, the true challenge lies in finding appropriate parameters for the different interatomic potentials. Some libraries are available, as for example by Bush *et al.* or Baram and Parker. [132, 133]. However, care must be taken, that the potentials were determined for the same class of materials and not to mix values from different sources. While they might give consistent results for compounds within one library, the parameters can differ too much across different libraries to combine them. The results produced in this way will not be of the highest accuracy, as there are much more advanced methods of modeling interatomic potentials and determining their parameters from *ab initio* calculations or from fits to various structural and mechanical parameters. Nevertheless, they can give a valuable estimation of phonon frequencies and qualitative informations about intensities and elongation patterns.

Bibliography

[1] T. Kimura, T. Goto, H. Shintani, K. Ishizaka, T. Arima, and Y. Tokura, "Magnetic control of ferroelectric polarization," Nature **426**, 55–58 (2003).

[2] D. Khomskii, "Classifying multiferroics: Mechanisms and effects," Physics **2** (2009), 10.1103/physics.2.20.

[3] I. S. Smirnova, "Normal modes of the lamno3 pnma phase: comparison with La_2CuO_4 Cmca phase," Physica B **262**, 247–261 (1999).

[4] M. N. Iliev, M. V. Abrashev, J. Laverdière, S. Jandl, M. M. Gospodinov, Y. Q. Wang, and Y. Y. Sun, "Distortion-dependent Raman spectra and mode mixing in $RMnO_3$ perovskites (R=La, Pr, Nd, Sm, Eu, Gd, Tb, Dy, Ho, Y)," Phys. Rev. B **73**, 064302 (2006).

[5] V. Y. Ivanov, A. A. Mukhin, V. V. Glushkov, and A. M. Balbashov, "Spontaneous reorientation of the electric polarization in $Eu_{1-x}Ho_xMnO_3$ multiferroics," JETP Lett. **97**, 28–33 (2013).

[6] T. Kimura, S. Ishihara, H. Shintani, T. Arima, K. T. Takahashi, K. Ishizaka, and Y. Tokura, "Distorted perovskite with e_g^1 configuration as a frustrated spin system," Phys. Rev. B **68**, 060403 (2003).

[7] S. Issing, F. Fuchs, C. Ziereis, E. Batke, A. Pimenov, Y. V. Ivanov, A. A. Mukhin, and J. Geurts, "Lattice dynamics of $Eu_{1-x}Y_xMnO_3$ (0 <= x <= 0.5) studied by Raman and infrared spectroscopy," European Physical Journal B **73**, 353–360 (2010).

[8] E. Granado, A. García, J. A. Sanjurjo, C. Rettori, I. Torriani, F. Prado, R. D. Sánchez, A. Caneiro, and S. B. Oseroff, "Magnetic ordering effects in the Raman spectra of $La_{1-x}Mn_{1-x}O_3$," Phys. Rev. B **60**, 11879–11882 (1999).

[9] I. E. Dzyaloshinskii, "On the Magneto-Electrical Effect in Antiferromagnets," JETP (1959).

[10] I. E. Dzyaloshinskii, "Theory of helicoidal structures in antiferromagnets. I. nonmetals," Soviet Physics JETP **19**, 960 (1964).

[11] S. Elsässer, M. Schiebl, A. A. Mukhin, A. M. Balbashov, A. Pimenov, and J. Geurts, "Impact of temperature-dependent local and global spin order in $r\mathrm{mno}_3$ compounds for spin-phonon coupling and electromagnon activity," New J. Phys. **19**, 013005 (2017).

[12] S. Elsässer, A. A. Mukhin, A. M. Balbashov, and J. Geurts, "Observation of transient lattice disorder at the onset of multiferroic ordering in $\mathrm{Eu}_{1-x}\mathrm{Ho}_x\mathrm{MnO}_3$ by Raman spectroscopy," Phys. Rev. B **97**, 224307 (2018).

[13] A. Pimenov, T. Rudolf, F. Mayr, A. Loidl, A. A. Mukhin, and A. M. Balbashov, "Coupling of phonons and electromagnons in GdMnO_3," Phys. Rev. B **74**, 100403 (2006).

[14] P. Rovillain, M. Cazayous, Y. Gallais, A. Sacuto, M.-A. Measson, and H. Sakata, "Magnetoelectric excitations in multiferroic TbMnO_3 by Raman scattering," Phys. Rev. B **81**, 054428 (2010).

[15] A. M. Shuvaev, A. A. Mukhin, and A. Pimenov, "Magnetic and magnetoelectric excitations in multiferroic manganites," J. Phys.: Condens. Matter **23**, 113201 (2011).

[16] A. M. Shuvaev, F. Mayr, A. Loidl, A. A. Mukhin, and A. Pimenov, "High-frequency electromagnon in GdMnO_3," The European Physical Journal B **80**, 351–354 (2011).

[17] A. Glamazda, W.-J. Lee, S.-H. Do, K.-Y. Choi, P. Lemmens, J. van Tol, J. Jeong, and H.-J. Noh, "Collective excitations in the metallic triangular antiferromagnet PdCrO_2," Phys. Rev. B **90**, 045122 (2014).

[18] D. Billington, D. Ernsting, T. E. Millichamp, C. Lester, S. B. Dugdale, D. Kersh, J. A. Duffy, S. R. Giblin, J. W. Taylor, P. Manuel, D. D. Khalyavin, and H. Takatsu, "Magnetic frustration, short-range correlations and the role of the paramagnetic fermi surface of PdCrO_2," Scientific Reports **5**, 12428– (2015).

[19] C. W. Hicks, A. S. Gibbs, L. Zhao, P. Kushwaha, H. Borrmann, A. P. Mackenzie, H. Takatsu, S. Yonezawa, Y. Maeno, and E. A. Yelland, "Quantum oscillations and magnetic reconstruction in the delafossite PdCrO_2," Physical Review B **92** (2015), 10.1103/PhysRevB.92.014425.

[20] M. Hemmida, H.-A. K. von Nidda, and A. Loidl, "Traces of Z(2)-vortices in $CuCrO_2$, $AgCrO_2$, and $PdCrO_2$," Journal of the Physical Society of Japan **80**, 053707 (2011).

[21] H. Takatsu and Y. Maeno, "Single crystal growth of the metallic triangular-lattice antiferromagnet $PdCrO_2$," J. Cryst. Growth **312**, 3461–3465 (2010).

[22] M. Suzuki, I. Yamada, H. Kadowaki, and F. Takei, "A Raman scattering investigation of the magnetic ordering in the two-dimensional triangular lattice antiferromagnet $LiCrO_2$," Journal of Physics: Condensed Matter **5**, 4225 (1993).

[23] K. Kimura, T. Otani, H. Nakamura, Y. Wakabayashi, and T. Kimura, "Lattice distortion coupled with magnetic ordering in a triangular lattice antiferromagnet $CuCrO_2$," Journal of the Physical Society of Japan **78**, 113710 (2009).

[24] T. Aoyama, A. Miyake, T. Kagayama, K. Shimizu, and T. Kimura, "Pressure effects on the magnetoelectric properties of a multiferroic triangular-lattice antiferromagnet $CuCrO_2$," Phys. Rev. B **87**, 094401 (2013).

[25] M. Fiebig, T. Lottermoser, D. Fröhlich, A. V. Goltsev, and R. V. Pisarev, "Observation of coupled magnetic and electric domains," Nature **419**, 818–820 (2002).

[26] D. Meier, J. Seidel, A. Cano, K. Delaney, Y. Kumagai, M. Mostovoy, N. A. Spaldin, R. Ramesh, and M. Fiebig, "Anisotropic conductance at improper ferroelectric domain walls," Nature Materials **11**, 284–288 (2012).

[27] D. Meier, "Functional domain walls in multiferroics," J. Phys.: Condens. Matter **27**, 463003 (2015).

[28] W. C. Röntgen, "Ueber die durch Bewegung eines im homogenen electrischen Felde befindlichen Dielectricums hervorgerufene electrodynamische Kraft," Annalen der Physik und Chemie **271**, 264–270 (1888).

[29] P. Debye, "Bemerkung zu einigen neuen Versuchen über einen magnetoelektrischen Richteffekt," Zeitschrift für Physik **36**, 300–301 (1926).

[30] D. N. Astrov, "The magnetoelectric effect in antiferromagnetics," JETP (1960).

[31] G. T. Rado and V. J. Folen, "Observation of the magnetically induced magnetoelectric effect and evidence for antiferromagnetic domains," Phys. Rev. Lett. **7**, 310–311 (1961).

[32] M. Fiebig, "Revival of the magnetoelectric effect," J. Phys. D: Appl. Phys. **38**, R123–R152 (2005).

[33] N. A. Hill, "Why are there so few magnetic ferroelectrics?" The Journal of Physical Chemistry B **104**, 6694–6709 (2000).

[34] N. A. Spaldin and M. Fiebig, "The renaissance of magnetoelectric multiferroics," Science **309**, 391–392 (2005).

[35] Y. Tokura and S. Seki, "Multiferroics with spiral spin orders," Adv. Mater. **22**, 1554–1565 (2010).

[36] T. Kimura, "Spiral magnets as magnetoelectrics," Annu. Rev. Mater. Res. **37**, 387–413 (2007).

[37] P. Kumar, "Multiferroic materials and their properties," Integrated Ferroelectrics **131**, 25–35 (2011).

[38] R. Ramesh and N. A. Spaldin, "Multiferroics: progress and prospects in thin films," Nature Materials **6**, 21– (2007).

[39] C. N. R. Rao, A. Sundaresan, and R. Saha, "Multiferroic and magnetoelectric oxides: The emerging scenario," The Journal of Physical Chemistry Letters **3**, 2237–2246 (2012), pMID: 26295776.

[40] C. Binek and B. Doudin, "Magnetoelectronics with magnetoelectrics," J. Phys.: Condens. Matter **17**, L39 (2005).

[41] A. Shuvaev, V. Dziom, A. Pimenov, M. Schiebl, A. A. Mukhin, A. C. Komarek, T. Finger, M. Braden, and A. Pimenov, "Electric field control of terahertz polarization in a multiferroic manganite with electromagnons," Phys. Rev. Lett. **111** (2013), 10.1103/PhysRevLett.111.227201.

[42] T. Arima, "Ferroelectricity induced by proper-screw type magnetic order," J. Phys. Soc. Jpn. **76**, 073702 (2007), http://dx.doi.org/10.1143/JPSJ.76.073702 .

[43] M. H. Brodsky, E. Burstein, M. Cardona, L. M. Falicov, M. V. Klein, R. M. Martin, A. Pinczuk, A. S. Pine, and Y.-R. Shen, *Light Scattering in Solids I*, 2nd ed., edited by M. Cardona (Springer Verlag, Berlin, 1983).

[44] N. W. Ashcroft and N. D. Mermin, *Festkörperphysik* (Oldenbourg Verlag, München, 2007).

[45] R. Loudon, "The Raman effect in crystals," Adv. Phys. **13**, 423–482 (1964).

[46] P. G. Klemens, "Anharmonic decay of optical phonons," Phys. Rev. **148**, 845–848 (1966).

[47] M. Balkanski, R. F. Wallis, and E. Haro, "Anharmonic effects in light-scattering due to optical phonons in silicon," Phys. Rev. B **28**, 1928–1934 (1983).

[48] T. R. Hart, R. L. Aggarwal, and B. Lax, "Temperature dependence of Raman scattering in silicon," Phys. Rev. B **1**, 638–642 (1970).

[49] W. Baltensperger and J. S. Helman, "Influence of magnetic order in insulators on the optical phonon frequency," Helv. Phys. Acta **41**, 668 (1968).

[50] E. O. Wollan and W. C. Koehler, "Neutron diffraction study of the magnetic properties of the series of perovskite-type compounds $La_{1-x}Ca_xMnO_3$," Phys. Rev. **100**, 545–563 (1955).

[51] Q. Huang, A. Santoro, J. W. Lynn, R. W. Erwin, J. A. Borchers, J. L. Peng, and R. L. Greene, "Structure and magnetic order in undoped lanthanum manganite," Phys. Rev. B **55**, 14987 (1997).

[52] J. Laverdière, S. Jandl, A. A. Mukhin, V. Y. Ivanov, V. G. Ivanov, and M. N. Iliev, "Spin-phonon coupling in orthorhombic RMnO$_3$ (R = Pr, Nd, Sm, Eu, Gd, Tb, Dy, Ho, Y): A Raman study," Phys. Rev. B **73**, 214301 (2006).

[53] P. Rovillain, J. Liu, M. Cazayous, Y. Gallais, M.-A. Measson, H. Sakata, and A. Sacuto, "Electromagnon and phonon excitations in multiferroic $TbMnO_3$," Phys. Rev. B **86**, 014437 (2012).

[54] M. N. Iliev, M. V. Abrashev, V. N. Popov, and V. G. Hadjiev, "Role of Jahn-Teller disorder in Raman scattering of mixed-valence manganites," Phys. Rev. B **67**, 212301 (2003).

[55] S. Elsässer, J. Geurts, A. A. Mukhin, and A. M. Balbashov, "Lattice dynamics and spin-phonon coupling in orthorhombic $Eu_{1-x}Ho_xMnO_3$ ($x \leq 0.3$) studied by Raman spectroscopy," Phys. Rev. B **93**, 054301 (2016).

[56] A. Pimenov, A. A. Mukhin, V. Y. Ivanov, V. D. Travkin, A. M. Balbashov, and A. Loidl, "Possible evidence for electromagnons in multiferroic manganites," Nat. Phys. **2**, 97–100 (2006).

[57] H. Katsura, N. Nagaosa, and A. V. Balatsky, "Spin current and magnetoelectric effect in noncollinear magnets," Phys. Rev. Lett. **95**, 057205 (2005).

[58] H. Katsura, A. V. Balatsky, and N. Nagaosa, "Dynamical magnetoelectric coupling in helical magnets," Phys. Rev. Lett. **98**, 027203 (2007).

[59] A. Pimenov, A. M. Shuvaev, A. A. Mukhin, and A. Loidl, "Electromagnons in multiferroic manganites," J. Phys.: Condens. Matter **20**, 434209 (2008).

[60] Y. Takahashi, Y. Yamasaki, N. Kida, Y. Kaneko, T. Arima, R. Shimano, and Y. Tokura, "Far-infrared optical study of electromagnons and their coupling to optical phonons in $Eu_{1-x}Y_xMnO_3$ ($x = 0.1$, 0.2, 0.3, 0.4, and 0.45)," Phys. Rev. B **79**, 214431 (2009).

[61] R. Valdés Aguilar, M. Mostovoy, A. B. Sushkov, C. L. Zhang, Y. J. Choi, S.-W. Cheong, and H. D. Drew, "Origin of electromagnon excitations in multiferroic $RMnO_3$," Phys. Rev. Lett. **102**, 047203 (2009).

[62] S. Issing, *Correlation between Lattice Dynamics and Magnetism in the Multiferroic Manganites: Korrelation von Kristallgitterdynamik und Magnetismus in den Multiferroischen Manganaten*, Ph.D. thesis (2011).

[63] P. A. Fleury and R. Loudon, "Scattering of light by one- and two-magnon excitations," Phys. Rev. **166**, 514–530 (1968).

[64] F. G. Bass and M. I. Kaganov, "Raman scattering of electromagnetic waves in ferromagnetic dielectrics," JETP **10**, 986 (1960).

[65] HORIBA Jobin Yvon GmbH, *LabRAM HR System - User Manual* (HORIBA Jobin Yvon GmbH, 2004) [Online; 27.03.2013].

[66] M. Johnsson and P. Lemmens, "Handbook of magnetism and advanced magnetic materials, 5 volume set," (Paperbackshop UK Import, 2007) Chap. Crystallography and Chemistry of Perovskites.

[67] M. V. Abrashev, J. Bäckström, L. Börjesson, V. N. Popov, R. A. Chakalov, N. Kolev, R.-L. Meng, and M. N. Iliev, "Raman spectroscopy of $CaMnO_3$: Mode assignment and relationship between Raman line intensities and structural distortions," Phys. Rev. B **65**, 184301 (2002).

[68] R. D. Shannon, "Revised effective ionic radii and systematic studies of interatomic distances in halides and chalcogenides," Acta Crystallographica Section A **32**, 751–767 (1976).

[69] R. Choithrani, M. N. Rao, S. L. Chaplot, N. K. Gaur, and R. K. Singh, "Lattice dynamics of manganites $RMnO_3$ (R=Sm, Eu or Gd): instabilities and coexistence of orthorhombic and hexagonal phases," New J. Phys. **11**, 073041 (2009).

[70] R. Choithrani, M. N. Rao, S. L. Chaplot, N. K. Gaur, and R. K. Singh, "Structural and phonon dynamical properties of perovskite manganites: (Tb, Dy, Ho)MnO_3," J. Magn. Magn. Mater. **323**, 1627 – 1635 (2011).

[71] B. Lorenz, Y. Q. Wang, Y. Y. Sun, and C. W. Chu, "Large magnetodielectric effects in orthorhombic $HoMno_3$ and $YMno_3$," Phys. Rev. B **70**, 212412 (2004).

[72] Y. Tokura and Y. Tomioka, "Colossal magnetoresistive manganites," J. Magn. Magn. Mater. **200**, 1–23 (1999).

[73] M. Abbate, F. M. F. de Groot, J. C. Fuggle, A. Fujimori, O. Strebel, F. Lopez, M. Domke, G. Kaindl, G. A. Sawatzky, M. Takano, Y. Takeda, H. Eisaki, and S. Uchida, "Controlled-valence properties of $La_{1-x}Sr_xFeO_3$ and $La_{1-x}Sr_xMnO_3$ studied by soft-x-ray absorption spectroscopy," Phys. Rev. B **46**, 4511–4519 (1992).

[74] J. B. Goodenough, "Theory of the role of covalence in the perovskite-type manganites [La, M(II)]MnO_3," Phys. Rev. **100**, 564–573 (1955).

[75] J. B. Goodenough, *Magnetism and the Chemical Bond* (Interscience Publishers, 1963).

[76] M. Gross, "Magnetismus," Vorlesungsskript Magnetismus, TU München (2005).

[77] J. A. Alonso, M. J. Martinez-Lopez, M. T. Casais, and M. T. Fernandez-Diaz, "Evolution of the Jahn-Teller Distortion of MnO_6 octahedra in $RMnO_3$ perovskites (R = Pr, Nd, Dy, Tb, Ho, Er, Y): A neutron diffraction study," Inorg. Chem. **39**, 917–923 (2000).

[78] J. van den Brink and D. I. Khomskii, "Multiferroicity due to charge ordering," J. Phys.: Condens. Matter **20**, 434217 (2008).

[79] N. Zhang, S. Dong, F. G. Chang, Z. M. Fu, and J.-M. Liu, "Grain size effect on $GdFeO_3$-type lattice distortion and ferroelectric behavior in $DyMnO_3$," Physica B - Condensed Matter **407**, 3736–3739 (2012).

[80] S. Issing, A. Pimenov, V. Y. Ivanov, A. A. Mukhin, and J. Geurts, "Composition-dependent spin-phonon coupling in mixed crystals of the multiferroic manganite $Eu_{1-x}Y_xMnO_3$ ($0 <= x <= 0.5$) studied by Raman spectroscopy," Phys. Rev. B **81**, 024304 (2010).

[81] S. Issing, A. Pimenov, Y. V. Ivanov, A. A. Mukhin, and J. Geurts, "Spin-phonon coupling in multiferroic manganites $RMnO_3$: comparison of pure (R = Eu, Gd, Tb) and substituted ($R = Eu_{1-x}Y_x$) compounds," European Physical Journal B **78**, 367–372 (2010).

[82] M. N. Iliev, M. V. Abrashev, H. G. Lee, V. N. Popov, Y. Y. Sun, C. Thomsen, R. L. Meng, and C. W. Chu, "Raman spectroscopy of orthorhombic perovskitelike $YMnO_3$ and $LaMnO_3$," Phys. Rev. B **57**, 2872–2877 (1998).

[83] E. T. Heyen, R. Wegerer, E. Schönherr, and M. Cardona, "Raman study of the coupling of crystal-field excitations to phonons in $NdBa_2Cu_3O_{7-\delta}$," Phys. Rev. B **44**, 10195–10205 (1991).

[84] N. Koshizuka and S. Ushioda, "Inelastic-light-scattering study of magnon softening in $ErFeO_3$," Phys. Rev. B **22**, 5394–5399 (1980).

[85] S. Venugopalan and M. Becker, "Raman-scattering study of $LuFeO_3$," J. Chem. Phys. **93**, 3833 (1990).

[86] A. Muñoz, J. Alonso, M. Casais, M. Martínez-Lope, J. Martínez, and M. Fernández, "Study of the incommensurate-commensurate magnetic transition in $HoMnO_3$ perovskite," J. Alloys Compd. **323-324**, 486 – 489 (2001), Proceedings of the 4th International Conference on f-Elements.

[87] A. M. Shuvaev, J. Hemberger, D. Niermann, F. Schrettle, A. Loidl, V. Y. Ivanov, V. D. Travkin, A. A. Mukhin, and A. Pimenov, "Soft-mode behavior of electromagnons in multiferroic manganite," Phys. Rev. B **82**, 174417 (2010).

[88] Z. Chen, M. Schmidt, Z. Wang, F. Mayr, J. Deisenhofer, A. A. Mukhin, A. M. Balbashov, and A. Loidl, "Electromagnons, magnons, and phonons in $Eu_{1-x}Ho_xMnO_3$," Phys. Rev. B **93** (2016), 10.1103/PhysRevB.93.134406.

[89] M. Mochizuki and N. Furukawa, "Microscopic model and phase diagrams of the multiferroic perovskite manganites," Phys. Rev. B **80**, 134416 (2009).

[90] M. Schiebl, A. Shuvaev, A. Pimenov, G. E. Johnstone, V. Dziom, A. A. Mukhin, V. Y. Ivanov, and A. Pimenov, "Order-disorder type critical behavior at the magnetoelectric phase transition in multiferroic $DyMnO_3$," Phys. Rev. B **91**, 224205 (2015).

[91] R. Vilarinho, E. C. Queirós, A. Almeida, P. B. Tavares, M. Guennou, J. Kreisel, and J. A. Moreira, "Scaling spin–phonon and spin–spin interactions in magnetoelectric $Gd_{1-x}Y_xMnO_3$," J. Solid State Chem. **228**, 76–81 (2015).

[92] C. De and A. Sundaresan, "Possible coexistence of cycloidal phases, magnetic field reversal of polarization, and memory effect in multiferroic $R_{0.5}Dy_{0.5}MnO_3$ (R = Eu and Gd)," Appl. Phys. Lett. **107**, 052902 (2015), 10.1063/1.4928126.

[93] M. Schiebl, *Dielectric spectroscopy at the spin-driven ferroelectric phase transition in chiral multiferroic $DyMnO_3$*, Ph.D. thesis, Technische Universität Wien (2016).

[94] G. Lawes, A. P. Ramirez, C. M. Varma, and M. A. Subramanian, "Magnetodielectric effects from spin fluctuations in isostructural ferromagnetic and antiferromagnetic systems," Phys. Rev. Lett. **91**, 257208 (2003).

[95] R. Muralidharan, T.-H. Jang, C.-H. Yang, Y. H. Jeong, and T. Y. Koo, "Magnetic control of spin reorientation and magnetodielectric effect below the spin compensation temperature in $TmFeO_3$," Appl. Phys. Lett. **90**, 012506 (2007).

[96] M. T. Dove, "Theory of displacive phase transitions in minerals," Am. Miner. **82**, 213 (1997).

[97] V. A. Zhirnov, "A contribution to the theory of domain walls in ferroelectrics," J. Exp. Theor. Phys. **35**, 822 (1959).

[98] B. Meyer and D. Vanderbilt, "Ab initio study of ferroelectric domain walls in $PbTiO_3$," Phys. Rev. B **65**, 104111 (2002).

[99] F. Kagawa, M. Mochizuki, Y. Onose, H. Murakawa, Y. Kaneko, N. Furukawa, and Y. Tokura, "Dynamics of multiferroic domain wall in spin-cycloidal ferroelectric $DyMnO_3$," Phys. Rev. Lett. **102**, 057604 (2009).

[100] T. W. B. Kibble, "Topology of cosmic domains and strings," Journal of Physics A: Mathematical and General **9**, 1387–1398 (1976).

[101] T. W. B. Kibble, "Some implications of a cosmological phase transition," Phys. Rep. **67**, 183–199 (1980).

[102] P. Rovillain, M. Cazayous, Y. Gallais, M.-A. Measson, A. Sacuto, H. Sakata, and M. Mochizuki, "Magnetic field induced dehybridization of the electromagnons in multiferroic $TbMnO_3$," Phys. Rev. Lett. **107**, 027202 (2011).

[103] M. P. V. Stenberg and R. de Sousa, "Model for twin electromagnons and magnetically induced oscillatory polarization in multiferroic $RMnO_3$," Phys. Rev. B **80**, 094419 (2009).

[104] J. Pellicer-Porres, A. Segura, E. Martínez, A. M. Saitta, A. Polian, J. C. Chervin, and B. Canny, "Vibrational properties of delafossite $CuGaO_2$ at ambient and high pressures," Phys. Rev. B **72**, 064301 (2005).

[105] J. Pellicer-Porres, A. Segura, E. Martínez, A. M. Saitta, A. Polian, J. C. Chervin, and B. Canny, "Erratum: Vibrational properties of delafossite $CuGaO_2$ at ambient and high pressures [phys. rev. b **72** , 064301 (2005)]," Phys. Rev. B **74**, 139902 (2006).

[106] P. Bruesch and C. Schuler, "Raman and infrared spectra of crystals with α-$NaFeO_2$ structure," Journal of Physics and Chemistry of Solids **32**, 1025–1038 (1971).

[107] O. Aktas, G. Quirion, T. Otani, and T. Kimura, "First-order ferroelastic transition in a magnetoelectric multiferroic: $CuCrO_2$," Physical Review B **88** (2013), 10.1103/PhysRevB.88.224104.

[108] H. Kadowaki, H. Kikuchi, and Y. Ajiro, "Neutron powder diffraction study of the two-dimensional triangular lattice antiferromagnet $CuCrO_2$," J. Phys.: Condens. Matter **2**, 4485–4493 (1990).

[109] D. A. Huse and V. Elser, "Simple variational wave functions for two-dimensional Heisenberg spin-$\frac{1}{2}$ antiferromagnets," Phys. Rev. Lett. **60**, 2531–2534 (1988).

[110] M. Frontzek, G. Ehlers, A. Podlesnyak, H. Cao, M. Matsuda, O. Zaharko, N. Aliouane, S. Barilo, and S. V. Shiryaev, "Magnetic structure of $CuCrO_2$: a single crystal neutron diffraction study," Journal of Physics: Condensed Matter **24**, 016004 (2012).

[111] K. Kimura, H. Nakamura, K. Ohgushi, and T. Kimura, "Magnetoelectric control of spin-chiral ferroelectric domains in a triangular lattice antiferromagnet," Phys. Rev. B **78**, 140401 (2008).

[112] M. F. Collins and O. A. Petrenko, "Review/synthèse: Triangular antiferromagnets," Canadian Journal of Physics **75**, 605–655 (1997).

[113] Y. Tokura, S. Seki, and N. Nagaosa, "Multiferroics of spin origin," Rep. Prog. Phys. **77**, 076501 (2014).

[114] C. Jia, S. Onoda, N. Nagaosa, and J. H. Han, "Bond electronic polarization induced by spin," Phys. Rev. B **74**, 224444 (2006).

[115] C. Jia, S. Onoda, N. Nagaosa, and J. H. Han, "Microscopic theory of spin-polarization coupling in multiferroic transition metal oxides," Phys. Rev. B **76**, 144424 (2007).

[116] M. Cardona and G. Güntherodt, *Light Scattering in Solids II* (Springer Verlag, Berlin, 1982).

[117] J. Pellicer-Porres, D. Martínez-García, A. Segura, P. Rodríguez-Hernández, A. Muñoz, J. C. Chervin, N. Garro, and D. Kim, "Pressure and temperature dependence of the lattice dynamics of $CuAlO_2$ investigated by Raman scattering experiments and ab initio calculations," Physical Review B **74** (2006), 10.1103/PhysRevB.74.184301.

[118] J. D. Gale, "GULP: A computer program for the symmetry-adapted simulation of solids," J. Chem. Soc., Faraday Trans. **93**, 629–637 (1997).

[119] M. Poienar, F. Damay, C. Martin, V. Hardy, A. Maignan, and G. André, "Structural and magnetic properties of $CuCr_{1-x}Mg_xO_2$ by neutron powder diffraction," Phys. Rev. B **79**, 014412 (2009).

[120] A. Kumar, P. Shahi, S. Kumar, K. K. Shukla, R. K. Singh, A. K. Ghosh, A. K. Nigam, and S. Chatterjee, "Raman effect and magnetic

properties of doped $TbMnO_3$," J. Phys. D: Appl. Phys. **46**, 125001 (2013).

[121] D. Boldrin and A. S. Wills, "Anomalous hall effect in geometrically frustrated magnets," Adv. Condens. Matter Phys. **2012**, 1–12 (2012).

[122] A. B. Garg, A. K. Mishra, K. K. Pandey, and S. M. Sharma, "Multiferroic $CuCrO_2$ under high pressure: In situ X-ray diffraction and Raman spectroscopic studies," Journal of Applied Physics **116**, 133514 (2014).

[123] E. Rastelli and A. Tassi, "The rhombohedral Heisenberg antiferromagnet: infinite degeneracy of the ground state and magnetic properties of solid oxygen," Journal of Physics C: Solid State Physics **19**, L423 (1986).

[124] H. Kadowaki, H. Takei, and K. Motoya, "Double-Q 120 degrees structure in the Heisenberg antiferromagnet on rhombohedrally stacked triangular lattice $LiCrO_2$," Journal of Physics: Condensed Matter **7**, 6869 (1995).

[125] J. L. Soubeyroux, D. Fruchart, C. Delmas, and G. L. Flem, "Neutron powder diffraction studies of two-dimensional magnetic oxides," Journal of Magnetism and Magnetic Materials **14**, 159 – 162 (1979).

[126] L. K. Alexander, N. Büttgen, R. Nath, A. V. Mahajan, and A. Loidl, "^{7}Li NMR studies on the triangular lattice system $LiCrO_2$," Phys. Rev. B **76**, 064429 (2007).

[127] F. H. L. Essler, H. Frahm, F. Göhmann, A. Klümper, and V. e. Korepin, *The One-Dimensional Hubbard Model*, 1st ed. (Cambridge University Press, 2005).

[128] J.-C. Walter and G. T. Barkema, "An introduction to Monte Carlo methods," Physica A: Statistical Mechanics and its Applications **418**, 78–87 (2015).

[129] W. H. Press, S. A. Teukolsky, W. T. Vetterling, and B. P. Flannery, *Numerical Recipes*, 3rd ed. (Cambridge University Press, 2007).

[130] P. P. Ewald, "Die Berechnung optischer und elektrostatischer Gitterpotentiale," Annalen der Physik **369**, 253–287 (1921).

[131] R. A. Jackson and C. R. A. Catlow, "Computer Simulation Studies of Zeolite Structure," Molecular Simulation **1**, 207–224 (1988).

[132] T. S. Bush, J. D. Gale, C. R. A. Catlow, and P. D. Battle, "Self-consistent interatomic potentials for the simulation of binary and ternary oxides," J. Mater. Chem. **4**, 831–837 (1994).

[133] P. S. Baram and S. C. Parker, "Atomistic simulation of hydroxide ions in inorganic solids," Philosophical Magazine B **73**, 49–58 (1996).

[134] K. Sedlmeier, S. Elsässer, D. Neubauer, R. Beyer, D. Wu, T. Ivek, S. Tomic, J. A. Schlueter, and M. Dressel, "Absence of charge order in the dimerized kappa-phase BEDT-TTF salts," Phys. Rev. B **86** (2012), 10.1103/PhysRevB.86.245103.

[135] S. Elsässer, D. Wu, M. Dressel, and J. A. Schlueter, "Power-law dependence of the optical conductivity observed in the quantum spin-liquid compound κ-(BEDT-TTF)$_2$Cu$_2$(CN)$_3$," Phys. Rev. B **86**, 155150 (2012).

List of publications and conference contributions

Parts of this thesis were presented in form of posters and talks at national and international conferences and published in scientific journals. This section provides a list of contributions which emerged during this work. For conference contributions, the presenting author is underscored.

Publications

S. Elsässer, A. A. Mukhin, A. M. Balbashov and J. Geurts – Lattice dynamics and spin-phonon coupling in orthorhombic $Eu_{1-x}Ho_xMnO_3$ ($x \leq 0.3$) studied by Raman spectroscopy. Phys. Rev. B **93**, 054301 (2016) [55]

S. Elsässer, M. Schiebl, A. A. Mukhin, A. M. Balbashov, A. Pimenov and J. Geurts – Impact of temperature-dependent local and global spin order in RMnO$_3$ compounds for spin-phonon coupling and electromagnon activity. New Journal of Physics **19**, 013005 (2017) [11]

S. Elsässer, A. A. Mukhin, A. M. Balbashov and J. Geurts – Observation of transient lattice disorder at the onset of multiferroic ordering in $Eu_{1-x}Ho_xMnO_3$ by Raman spectroscopy.
Phys. Rev. B **97**, 224307 (2018) [12]

Conference contributions

S. Elsässer, V. V. Glushkov, A. M. Balbashov and J. Geurts – Raman spectroscopy and spin-phonon coupling of multiferroic $Eu_{1-x}Ho_xMnO_3$. Poster, DPG Frühjahrstagung, Berlin (2015)

S. Elsässer and J. Geurts – Raman spectroscopy with spin-phonon coupling as a quasi-local probe of magnetic order in multiferroic $Eu_{1-x}Ho_xMnO_3$ compounds. Contributed talk, Phonons 2015, Nottingham (2015)

S. Elsässer, Anna Pimenov and J. Geurts – Spin-phonon coupling in $ACrO_2$ (A=Cu, Ag, Pd) studied by Raman spectroscopy. Poster, DPG Frühjahrstagung, Regensburg (2016)

S. Elsässer, M. Schiebl, A. Shuvaev, A. A. Mukhin, J. Geurts and A. Pimenov – Impact of temperature-dependent local and global ordering in $RMnO_3$ for electromagnons and spin-phonon coupling. Poster, DPG Frühjahrstagung, Regensburg (2016)

S. Elsässer, A. A. Mukhin, A. M. Balbashov and J. Geurts – Magnetic correlations in $Eu_{1-x}Ho_xMnO_3$ ($0 \leq x \leq 0.5$) probed by Raman spectroscopy. Poster, DPG Frühjahrstagung, Dresden (2017)

A. Koudinov, A. Knapp, S. Elsässer and J. Geurts – A series of "fractional" peaks in multiple paramagnetic resonance Raman scattering by (Cd,Mn)Te quantum wells. Poster, DPG Frühjahrstagung, Berlin (2018)

Publications and conference contributions preceding this thesis

Publications

K. Sedlmeier, S. Elsässer, D. Neubauer, R. Beyer, D. Wu, T. Ivek, S. Tomic, JA Schlueter and M. Dressel – Absence of charge order in the dimerized κ-phase BEDT-TTF salts. Phys. Rev. B **86**, 245103 (2012)[134]

S. Elsässer, D. Wu, M. Dressel and JA Schlueter – Power-law dependence of the optical conductivity observed in the quantum spin-liquid compound kappa-$(BEDT\text{-}TTF)_2Cu_2(CN)_3$. Phys. Rev. B **86**, 155150 (2012)[135]

Conference contributions

S. Elsässer, J. A. Schlueter and M. Dressel – Searching for the Power-Law Conductivity Inside the Mott Gap in κ-$(ET)_2Cu_2(CN)_3$. Poster, DPG Frühjahrstagung, Berlin (2012)

M. Dressel, K. Sedlmeier, S. Elsässer, D. Neubauer, R. Beyer, D. Wu, T. Ivek, S. Tomic and JA Schlueter – Absence of charge order in the dimerized κ-phase BEDT-TTF salts. Contributed talk, DPG Frühjahrstagung, Regensburg (2013)

Danksagung

Zur Entstehung dieser Dissertation trugen zahlreiche Personen bei, die mich in physikalischer oder anderweitiger Natur unterstützt haben. Dies soll nicht unerwähnt bleiben und daher möchte ich an dieser Stelle, ohne Anspruch auf Vollständigkeit und ohne wertende Reihenfolge, einige Worte des Dankes entrichten:

- An meinen Doktorvater Prof. Dr. Jean Geurts, für die Möglichkeit der Promotion auf diesem hochinteressanten Thema, die stets angenehme Arbeitsatmosphäre in der Gruppe und selbstverständlich dafür, dass er sich immer Zeit für ein Gespräch genommen hat, wenn Unklarheiten bestanden.

- Prof. Dr. Laurens Molenkamp, für die Möglichkeit am Lehrstuhl der Experimentellen Physik III zu arbeiten.

- Der AG Geurts für die gute Zusammenarbeit und gegenseitige Hilfestellung innerhalb und ausserhalb des Labors, insbesondere Alexander Knapp, Benedikt Halbig, Kim-Mario Wolf und Utz Bass.

- Prof. Dr. Andrei Pimenov, Anna Pimenov, Dr. Alexey Shuvaev und Dr. Markus Schiebl vom Institut für Festkörperphysik der TU Wien, sowie Dr. Joachim Deisenhofer vom Lehrstuhl Experimentalphysik V der Universität Augsburg, für die fruchtbaren Diskussionen und die Bereitstellung der Proben.

- Prof. Dr. Vladimir Dyakonov, Dr. Franziska Fuchs und Christian Kasper vom Lehrstuhl Experimentelle Physik VI für die Möglichkeit an Ihrem Raman Setup meine temperaturabhängigen Messungen durchzuführen.

- Die Mitarbeiter der Mechanik- und Elektronikwerkstätten, sowie insbesondere Roland Ebert und Cornelius Ziga von der Heliumverflüssigung für ihr Know-How und dafür, dass sie immer ein Kännchen Helium für mich übrig hatten.

- Enno Krauss, Heiko Groß und Thorsten Feichtner für die Kaffeerunden und die tollen Weihnachtsfilme der EP V.
- Manuel Weber der nie eine Gelegenheit ausließ, mich an seinem einzigartigen Geschmack in Sachen Filme, Musik und Getränke teilhaben zu lassen.
- Meine Eltern und meine Freundin, Katarína Dereníková für ihre Unterstützung und Motivation in den Höhen und Tiefen dieser Arbeit.